

BIOGEOCHEMICAL SIGNATURES IN IRON (OXYHYDR)OXIDE DIAGENETIC
PRECIPITATES: CHEMICAL, MINERALOGICAL
AND TEXTURAL MARKERS

by

Sally Latham Potter-McIntyre

A dissertation submitted to the faculty of
The University of Utah
in partial fulfillment of the requirements for the degree of

Doctor of Philosophy

in

Geology

Department of Geology and Geophysics

The University of Utah

May 2013

Copyright © Sally Latham Potter-McIntyre 2013

All Rights Reserved

The University of Utah Graduate School

STATEMENT OF DISSERTATION APPROVAL

The dissertation of Sally Latham Potter-McIntyre
has been approved by the following supervisory committee members:

<u>Marjorie A. Chan</u>	, Chair	<u>1/25/2013</u> Date Approved
<u>Allan A. Ekdale</u>	, Member	<u>1/25/2013</u> Date Approved
<u>Jack Farmer</u>	, Member	<u>2/15/2013</u> Date Approved
<u>Brian M. Hynek</u>	, Member	<u>3/15/2013</u> Date Approved
<u>Erich U. Petersen</u>	, Member	<u>1/25/2013</u> Date Approved

and by D. Kip Solomon, Chair of
the Department of Geology and Geophysics

and by Donna M. White, Interim Dean of The Graduate School.

ABSTRACT

Diagenetic variables (e.g., microbial influence, sediment composition and fluid chemistry) are investigated to determine the effects on iron redox reactions and iron (oxyhydr)oxide nucleation, cement textures, mineralogy and chemistry. Three individual examinations are conducted in the Colorado Plateau, USA: 1. reservoir fluid chemistry in a natural fossil CO₂ reservoir in the Jurassic Navajo Sandstone exposed in Justensen Flats in the northern San Rafael Swell, 2. concretion formation in the reactive, volcanoclastic Jurassic Brushy Basin Member of the Morrison Formation, and 3. comparative microbial influences in the precipitation of iron (oxyhydroxides) in a modern Ten Mile Graben spring system and the Brushy Basin Member.

Bulk geochemistry in a lithologically controlled, iron (oxyhydr)oxide reaction front in Justensen Flats shows that the precipitating fluid in the reservoir was likely a CO₂- and hydrocarbon-charged fluid and that CO₂ injection into a saline reservoir would result in dolomite precipitation and significantly reduce porosity. Chemical and physical concretion comparisons in the Brushy Basin Member show that reactants are moving via fluid flow in porous host rocks and producing uniform concretion morphologies and mineralogies. In reactive Brushy Basin Member claystone and siltstone lithofacies, reactants are being sourced from abundant ashes reacting with groundwater to create localized diagenetic microenvironments and produce variable concretion mineralogies and morphologies. Variability of fluids on regional to outcrop scales and lithologically

controlled fluid flow and cement precipitation in permeable reservoirs furthers the science of carbon capture and sequestration.

Comparison of modern and 100ka microbial iron (oxyhydr)oxides in tufas at the Ten Mile Graben spring system shows that biosignatures exhibit some degradation and recrystallization on millennial time scales, although biotic features are clearly recognizable. Microbial fossils in the Brushy Basin Member are associated with macroscopic biotic features such as charophyte molds. Biogenic iron (oxyhydr)oxides in modern tufas and Jurassic rocks exhibit two distinct elemental suites that function as biosignatures: 1. C, Fe, and As, and 2. C, S, Se. Biogeochemical markers provide diagnostics for depositional environment, fluid chemistry and potential microbial fossils and/or biosignatures to aid in the exploration of similar iron- and clay-rich sediments on Mars in Gale Crater.

TABLE OF CONTENTS

ABSTRACT.....	iii
ACKNOWLEDGEMENTS.....	vii
INTRODUCTION.....	1
Background.....	1
Purpose of Study.....	2
Applications.....	3
Formations.....	5
Summary of Chapters.....	8
References.....	10
1: IRON PRECIPITATION IN A NATURAL CO ₂ RESERVOIR: JURASSIC NAVAJO SANDSTONE IN THE NORTHERN SAN RAFAEL SWELL, UT, USA....	14
Abstract.....	14
Introduction.....	15
Purpose of Study.....	16
Study Area.....	18
Methods.....	20
Results.....	23
Interpretation and Discussion.....	34
Conclusions.....	40
Acknowledgements.....	41
References.....	41
2: EVALUATING THE ROLE OF ORGANICS, MINERALOGY AND PETROPHYSICAL PROPERTIES ON EARLY DIAGENESIS AND CONCRETION FORMATION IN VOLCANICLASTIC HOST ROCK COMPOSITION.....	46
Abstract.....	46
Introduction.....	47
Purpose of Study.....	49
Study Area.....	50
Methods.....	51
Results.....	54
Interpretation and Discussion.....	72
Conclusions.....	80
References.....	81

3: TEXTURAL AND MINERALOGICAL CHARACTERISTICS OF MICROBIAL FOSSILS ASSOCIATED WITH MODERN AND ANCIENT IRON(OXYHYDR)OXIDES.....	86
Abstract.....	86
Introduction.....	87
Purpose of Study.....	89
Applications to Mars.....	90
Study Area.....	91
Methods.....	93
Results.....	96
Interpretation and Discussion.....	110
Conclusions.....	114
References.....	115
 DISSERTATION CONCLUSIONS.....	 119
 APPENDICES	
 A. SAMPLES.....	 125
 B. X-RAY DIFFRACTION.....	 130
 C. VISIBLE TO NEAR INFRARED REFLECTANCE SPECTROSCOPY.....	 134
 D. QEMSCAN.....	 137
 E. WHOLE ROCK ANALYSIS.....	 148
 F. BRUSHY BASIN MEMBER OF THE MORRISON FORMATION STRATIGRAPHIC SECTIONS.....	 153
 G. LASER ABLATION INDUCED COUPLED MASS SPECTRSCOPY.....	 158
 H. RAMAN SPECTROSCOPY.....	 201

ACKNOWLEDGEMENTS

The work for Chapter 1 was supported in part by a Utah Geological Survey grant (#110398) to Dr. Si-Yong Lee and Dr. Jessica Allen. Much of the applied characterization work was also supported in large part by a U.S. Department of Energy grant (to Dr. Brian J. McPherson) managed by the DOE National Technology Laboratory, project DE-FE0001812. I greatly benefited from participation in several NASA-sponsored short courses and summer workshops that expanded my professional development and exposed me to the breadth and integration of Earth and planetary sciences as well as the challenges in the rapidly growing field of astrobiology.

I extend my gratitude to my committee members, Dr. Marjorie Chan, Dr. Erich Petersen, Dr. Tony Ekdale, Dr. Jack Farmer and Dr. Brian Hynek for their time, support and guidance during this process. I also thank Dr. Brian McPherson for his encouragement and participation as an informal committee member as well as for his financial support for this dissertation. I am especially grateful to my advisor, Margie Chan, whose persistence and commitment to excellence drove me to attain scientific heights that I did not realize I was capable of reaching. I am extremely grateful to my family, Jacquelin Allen, Lillian McIntyre, Alexis McIntyre, James Potter and Andres Aslan for their encouragement and patience. I could not have achieved this without them.

INTRODUCTION

Background

Diagenesis in sedimentary rocks has long been difficult to understand because of the many complexities of physical, chemical and biological influences in small, subsurface pore spaces. In permeable sandstones, the diagenesis is particularly challenging to unravel because these are open systems where multiple fluids and events may be superimposed over a long period of postdepositional history. With new advances in biogeochemistry, we are better poised to understand the role of biomediation in precipitation and preservation of biosignatures in authigenic minerals. Here the focus is on iron (oxyhydr)oxide because iron is the fourth most common element on the surface of the Earth; iron also is prevalent on Mars where we seek to understand similar diagenetic processes and hope to find evidence of extinct or extant life. Any natural ferric iron mineral is typically a comingling of two or more iron oxide and hydrous ferric oxide phases; therefore, the term iron (oxyhydr)oxide is used herein to denote all ferric iron mineral phases.

Diagenesis is the chemical and physical process by which sediment becomes sedimentary rock and includes any fluid-rock interaction as fluids move through the substrate. This process begins at deposition (early diagenesis), and continues during burial (middle diagenesis) through uplift and exposure (late diagenesis). The chemical changes that occur during this process are the result of complex interactions between the

rock, the diagenetic fluids and subsurface biota (primarily microbes), i.e., the biogeochemistry.

Iron is a highly mobile element and is an important constituent in diagenetic biogeochemical redox reactions (Ferris, 2005; Fortin and Langley, 2005; Druschel et al., 2008). The energy released in these redox reactions provides an important energy source for chemoautotrophs (organisms that obtain their energy from the oxidation of inorganic elements such as iron; Ferris, 2005; Fortin and Langley, 2005; Druschel et al., 2008). Iron minerals present as cements in sedimentary rocks can record fluid chemistries and even preserve a record of paleomicrobial fingerprints (Farmer and DesMarais, 1999; Ferris et al., 2000; Cady et al., 2003; Ferris, 2005; Hazen, 2010).

Concretions are cemented mineral masses in sedimentary rocks. Concretions form in a variety of lithologies and exhibit diverse mineralogies. Iron (oxyhydr)oxide concretions are very common and also can preserve a record of the diagenetic biogeochemistry (e.g., Chan et al., 2000, 2001; 2005; Potter and Chan 2011; Potter et al., 2011). In 2004, the MER (Mars Exploration Rover), Opportunity, returned images of hematite spherules (“blueberries”) that have been interpreted as concretions (Grotzinger et al., 2005; McLennan et al., 2005; Chan et al., 2005, 2012; Calvin et al., 2009; Potter et al., 2011). This discovery sparked a renewed interest in the study of terrestrial iron(oxyhydr)oxide concretions and the biogeochemical information preserved by these diagenetic features.

Purpose of Study

This research provides insight into the role geochemically reactive sediments, subsurface microbial life and fluid chemistry play in diagenesis. The central question of

this dissertation is: how do variables such as microbial influence, sediment composition and fluid chemistry affect iron redox reactions and iron (oxyhydr)oxide nucleation, cement textures, mineralogy and chemistry? This research aims to document biogeochemical fingerprints in ancient diagenetic cements to produce a library of diagnostic characteristics. Comparison of modern and ancient microbial iron (oxyhydr)oxide precipitation highlights changes in these mineral phases, textures and chemistry over geologic time. The following questions are answered by this research. 1. What effect does CO₂ and salinity (common components of diagenetic fluids) have on iron (oxyhydr)oxide precipitates? 2. How does reactive host rock composition affect iron (oxyhydr)oxide precipitation? 3. What microscopic and macroscopic characteristics do paleomicrobial influences imprint in ancient iron (oxyhydr)oxide precipitates? 4. How do these paleomicrobial characteristics compare to modern biomediated iron (oxyhydr)oxides?

Modern and ~100ka tufa deposits with iron (oxyhydr)oxide microbial mats are examined and compared with putative microbial features in the Brushy Basin Member to produce a library of recognizable biosignatures consisting of mineral phases, textures and elemental suites. Insights from this research on iron cycling, fluid chemistries, microbial fossils, biosignatures and biota-fluid-rock interactions provide important insights into understanding diagenetic processes.

Applications

Anthropogenic contribution to atmospheric CO₂ is a pressing concern because of its major contribution to global climate change; therefore, much research is focused on

carbon capture and sequestration (CCS; e.g., McPherson and Cole, 2000; Smith et al., 2009; Dubacq et al., 2011; Lu et al., 2011). The Jurassic stratigraphic section of the Colorado Plateau contains three eolian reservoir units (as well as other porous and permeable units) overlain by a thick sequence of late Jurassic and Cretaceous shales that serve as a seal. The Lower Jurassic Navajo Sandstone is one of the eolian units and serves as an important oil, gas or water reservoir in the areas where it occurs in the subsurface (Baer and Rigby, 1978; Parry et al., 2007; Parry et al., 2009; Chidsey et al., 2011). The late Jurassic Brushy Basin Member of the Morrison Formation is part of the seal formations overlying the Middle Jurassic Entrada Sandstone reservoir. This research investigates iron (oxyhydr)oxide precipitation in a fossil CO₂- and hydrocarbon-charged, saline Navajo Sandstone reservoir. This dissertation also investigates the effect that more reactive, volcanoclastic sediments of the Jurassic Brushy Basin Member have on iron mobilization and precipitation. These data provide clues to how fluids move through the subsurface, the timing of precipitation and the complexities of fluid/rock interactions during diagenesis.

The study of biogeochemistry and concretion formation in iron- and clay-rich shales is applicable to Mars geology and the search for microbial extraterrestrial life. Iron oxide is abundant in the surface and near subsurface geology of Mars – present both in the soils and as cements and concretions in the sedimentary rocks. On Earth, iron (oxyhydr)oxide cement precipitation in sedimentary rocks preserves a record of the diagenetic history. Iron oxide spherules in the Burns formation at Meridiani Planum, Mars exhibit striking similarities to Navajo Sandstone concretions (Chan et al., 2005, 2012; Potter et al., 2011). However, a major difference is that the Navajo Sandstone is a

clean quartz arenite, and the Burns formation is a more reactive, volcanoclastic host rock—more similar geochemically to the reactive, volcanoclastic, concretion-bearing Brushy Basin Member of the Morrison Formation. Research into how reactive host rock sediments affect iron precipitation and mobilization and concretion formation will help to better understand diagenetic fluid-rock interactions in the Burns formation on Mars.

One of the thickest stratigraphic sections (~5 km) on Mars is exposed on Mount Sharp in Gale Crater (Milliken et al., 2010; Thomson et al., 2011). This unit is partly composed of clays that formed in a likely nonacidic, lacustrine environment (Cabrol et al., 1999; Milliken et al., 2010; Thomson et al., 2011). The Brushy Basin Member may provide an excellent terrestrial analog for understanding lithological and diagenetic histories of these similar iron- and clay-rich shales on Mars. Iron is abundant on Mars as well as Earth and is likely to be abundant on any rocky planet we investigate in the future; thus, recognizing important biogeochemical signatures is applicable to both terrestrial origin of life studies and the search for extraterrestrial microbial life.

Formations

Lower Jurassic Navajo Sandstone

The Navajo Sandstone represents the largest erg to ever exist on Earth; the unit and its equivalents extend throughout the Colorado Plateau and into Wyoming in the north, Colorado to the east, New Mexico and Arizona to the south and Nevada to the west (Blakey et al., 1988; Blakey, 1994). The unit is a fine-grained, porous and permeable, eolian quartz arenite, known for its dramatic coloration patterns resulting from diagenetic

iron (oxyhydr)oxide mobilization and precipitation (Beitler et al., 2003, 2005; Seiler, 2008, Nielsen and Chan, 2009; Nielsen et al., 2009; Potter and Chan, 2011).

At Justensen Flats in the northern San Rafael Swell in southern Utah, the entire section of the Navajo Sandstone is exposed in three dimensions. Along one fracture face, a lithologically controlled, iron (oxyhydr)oxide reaction front extends into a cross-bed set and abuts a bounding surface at the top. This site is chosen for study because of the exposure as well as the proximity to the modern spring system at Ten Mile Graben which emanates CO₂- and hydrocarbon-charged water from the Navajo Sandstone reservoir that is in the subsurface in this area (Shipton et al., 2004; Heath et al., 2009; Kampmann et al., 2009; Burnside, 2010). The reaction front at Justensen Flats preserves a record of the CO₂- and hydrocarbon-charged fluids involved in the mobilization and precipitation of the iron and provides insight into the likely behavior a supercritical CO₂ fluid would have if injected into this or a similar reservoir.

Brushy Basin Member of the Upper Jurassic Morrison Formation

The Jurassic Brushy Basin Member of the Morrison Formation is a variegated, tuffaceous shale that also extends throughout the Colorado Plateau (Turner and Fishman, 1999; Turner and Peterson, 2004). The depositional environment is interpreted to be a groundwater-fed, ephemeral, alkaline saline lake system named Lake T'oo'dichi' (Turner and Fishman, 1999). A back-arc basin to the west during the Jurassic produced abundant volcanic activity that input copious amounts of volcanic ash into the lake system (Turner and Fishman, 1999; Turner and Peterson, 2004). This ash reacted with the groundwater in the lake, to produce an iron-rich, alkaline saline geochemical system (Turner and

Fishman, 1999; Turner and Peterson, 2004). This unit exhibits diagenetic concretions as well as abundant macroscopic and microscopic biotic influences. Study of this unit provides insight into the role a shale composed of more reactive sediments plays in diagenetic concretion-forming processes. Microbial fossils and fingerprints of biotic interactions are preserved in iron minerals and give clues to complex biogeochemical reactions.

Quaternary Ten Mile Graben Spring System

A modern spring system emanates through faults along Ten Mile Graben in southeastern Utah (Shipton et al., 2004; Heath et al., 2009; Kampmann et al., 2009; Burnside, 2010). Several of the major springs of this system – Crystal Geysir, Big Bubbling Spring and Little Bubbling Spring – are selected for study along with a terrace of ~100ka tufa (Burnside, 2010) near Crystal Geysir. The CO₂- and hydrocarbon-charged, saline and slightly alkaline effluent is derived from the subsurface Navajo Sandstone reservoir that is recharged to the west and northwest at the edge of the San Rafael Swell (Shipton et al., 2004; Heath et al., 2009; Kampmann et al., 2009). This spring system is host to microbially precipitated iron (oxyhydr)oxide mats in the active springs and these mats are preserved in the ancient tufa terraces (Shipton et al., 2004; Burnside, 2010). The iron (oxyhydr)oxides in the ancient mats preserve a record of diagenetic changes of microbial features over geologic time. Study of this unit provides insight into recognition of biosignatures both in ancient terrestrial formations (like the Brushy Basin Member) as well as extraterrestrial iron-rich systems.

Summary of Chapters

Chapter 1

The first chapter, titled “Iron Precipitation in a Natural CO₂ Reservoir: Jurassic Navajo Sandstone in the northern San Rafael Swell, UT, USA,” addresses the effect of a CO₂- and hydrocarbon-charged fluid on iron precipitation and is directly applicable to CCS (carbon capture and storage). Characterization of an iron (oxyhydr)oxide reaction front in a natural, fossil CO₂ reservoir provides insight into the potential behavior an injected CO₂ fluid might exhibit over geologic time on a pore- to outcrop-scale.

Samples from a well-exposed, iron (oxyhydr)oxide reaction front in the Justensen Flats area of the northern San Rafael Swell are collected along a transect to observe paleo-fluid/rock interaction. Synthesis of petrographic, chemical and spectroscopic data shows that CO₂ is consumed by abundant dolomite precipitation and minor clay precipitation that significantly decreases porosity. A comparison of bulk geochemistry in the reaction front is compared to effluent from the nearby Ten Mile Graben spring system that emanates from the subsurface Navajo Sandstone reservoir to show that similar fluids were responsible for precipitation of the reaction front. Published bulk geochemical data from the Navajo Sandstone in Spencer Flat in southern Utah show that reservoir fluid chemistry varies spatially and temporally.

Chapter 2

Chapter 2, titled “Evaluating the Effects of Organics, Mineralogy and Petrophysical Properties on Early Diagenesis and Concretion Formation in Volcaniclastic Host Rock Compositions,” addresses the effects of reactive sediments on iron

precipitation and mobilization and concretion formation. Because iron precipitates record a range of diagenetic clues such as precipitating fluid chemistries and fluid/rock interaction, the broad applications for this chapter include insight into behavior and mobility of fluids in a seal formation as well as clues to the diagenetic history of clay- and iron-rich lacustrine shales on Mars.

Petrography, chemistry and lithology in three main concretion types are documented based on mineralogy: 1. calcite concretions, 2. iron (oxyhydr)oxide concretions, and 3. phosphate concretions. Diagenetic facies cross-cut lithofacies and record meter-scale paleotopography. Concretions are present in all diagenetic facies and several types are typically present within a stratigraphic horizon. Diagenesis in the Brushy Basin Member was largely limited to syndepositional to early diagenetic reactions. The diverse range of concretion mineralogies suggests that that low porosity and permeability sediments and reactive geochemistry create diagenetic microenvironments within the larger lake system.

Chapter 3

Chapter Three, titled “Textural and Mineralogical Characteristics of Microbial Fossils in Modern and Ancient Iron (Oxyhydr)oxides,” addresses the biogeochemistry of iron precipitation and documents microbial fossils in the Jurassic Brushy Basin Member. Modern microbial iron (oxyhydr)oxides and ~100ka tufa terraces from the Ten Mile Graben spring system are compared to document diagenetic changes to microbial features over geologic time. Microbial features are then compared with the Jurassic examples to document microbial fossils, biogenic textures and chemical biosignatures.

Abundant macroscopic biotic features in the Brushy Basin Member (e.g., burrows, charophyte molds, root traces and dinosaur bones) provide a starting place to look for related microbial fossils. Charophyte molds exhibit diatoms and other forms of algal fossils in close association with iron (oxyhydr)oxide spheres. Comparison of chemistry in transects across putative microbial features and subsequent principal component analysis of the data show two diagnostic elemental suites associated with microbial features: 1) C, Fe, As, and 2) C, S, Se.

This dissertation is unified by the evaluation of geologic factors affecting diagenesis and iron cycling. Each chapter addresses different aspects of diagenesis such as diagenetic fluid chemistries, reactive sediments and microbial interaction in mineral precipitation. Appendices contain all raw data, tables and measured sections.

References

- Baer, J. L., and Rigby, J. K., 1978. Geology of the Crystal Geyser and environmental implications of its effluent, Grand County, Utah. *Utah Geology*, 5, 125-130.
- Beitler, B., Chan, M.A., Parry, W.T., 2003. Bleaching of Jurassic Navajo Sandstone on Colorado Plateau Laramide highs; Evidence of exhumed hydrocarbon supergiants? *Geology*, 31, 1041-1044.
- Beitler, B., Parry, W.T., Chan, M.A., 2005. Fingerprints of fluid flow; chemical diagenetic history of the Jurassic Navajo Sandstone, southern Utah, U.S.A. *Journal of Sedimentary Research*, 75, 547-561.
- Blakey, R., Peterson, F., Kocurek, G., 1988. Syntheses of late Paleozoic and Mesozoic eolian deposits of the Western Interior of the United States. *Sedimentary Geology*, 56, 3-125.
- Blakey, R., 1994. Paleogeographic and tectonic controls on some Lower and Middle Jurassic erg deposits, Colorado Plateau Mesozoic systems of the Rocky Mountain region, USA.

- Burnside, N.M., 2010. U-Th dating of travertine on the Colorado Plateau: Implications for the leakage of geologically stored CO₂. Department of Geographical and Earth Sciences. University of Glasgow, Glasgow.
- Cady, S. L., J. D. Farmer, et al., 2003. Morphological biosignatures and the search for life on Mars. *Astrobiology*, 3, 351-368.
- Calvin, W.M., Shoffner, J.D., Johnson, J.R., Knoll, A.H., Pockock, J.M., Squyres, S.W., Weitz, C.M., Arvidson, R.E., Bell, J.F., III, Christensen, P.R., de Souza, P.A., Jr., Farrand, W.H., Glotch, T.D., Herkenhoff, K.E., Jolliff, B.L., Knudson, A.T., McLennan, S.M., Rogers, A.D., Thompson, S.D., 2008. Hematite spherules at Meridiani; results from MI, Mini-TES, and Pancam. *Journal of Geophysical Research*, 113.
- Chan, M.A., Parry, W.T., Bowman, J.R. 2000. Diagenetic hematite and manganese oxides and fault-related fluid flow in Jurassic sandstone, southeastern Utah. *AAPG Bulletin*, 84, 1281–310.
- Chan, M.A., Beitler, B., Parry, W.T., Ormö, J., Komatsu, G., 2004. A possible terrestrial analogue for hematite concretions on Mars. *Nature*, 429, 731–4.
- Chan, M.A., Bowen, B.B., Parry, W.T., Ormö, J., Komatsu G., 2005. Red rock and red planet diagenesis: comparison of Earth and Mars concretions. *GSA Today*, 15, 8.
- Chan, M.A., Potter, S.L., Bowen, B.B., Parry, W.T., Barge, L.M., Seiler, W., Bowman, J.R., 2012. Characteristics of Terrestrial Ferric Oxide Concretions and Implications for Mars, in: Grotzinger, J.P., Milliken, R.E. (Ed.), *Sedimentary Geology of Mars*. SEPM Special Publication 102.
- Chidsey, T.C. Jr., Hartwick, E. E., Johnson, K. R., Schelling, D. D., Sbarra, R., Sprinkel, D. A., Vrona, J. P. and Wavrek, D. A., 2011. Petroleum geology of Providence oil field, central Utah thrust belt. In: *Sevier thrust belt: northern and central Utah and adjacent areas* (eds. Sprinkel, D.A., Yonkee, W.A., and Chidsey, T.C., Jr.): Utah Geological Association Publication 40, p. 213-231.
- Druschel, G.K., Emerson, D., Sutka, R., Suchecki, P., & Luther, G.W., 2008. Low oxygen and chemical kinetic constraints on the geochemical niche of neutrophilic iron(II) oxidizing microorganisms. *Geochimica et Cosmochimica Acta*, 72, 3358-3370.
- Dubacq, B., Kampmann, N., Assayag, N., Wigley, M., Bickle, M., 2011. CO₂ degassing and groundwater mixing in the Navajo Aquifer, Green River, Utah. *Mineralogical Magazine*, 75, 786-786.

- Farmer, J.D., Des Marais, D.J., 1999. Exploring for a record of ancient Martian life. *Journal of Geophysical Research*, 104, 26-26,995.
- Ferris, F.G., 2005. Microbial mineral transformations in the Fe(II)-Fe(III)-H₂O system. *Geochimica et Cosmochimica Acta*, 69, Suppl., pp.454.
- Ferris, F.G., Hallberg, R.O., Lyven, B., Pedersen, K., 2000. Retention of strontium, cesium, lead and uranium by bacterial iron oxides from a subterranean environment. *Applied Geochemistry*, 15, 1035-1042.
- Fortin, D., and Langley, S., 2005. Formation and occurrence of biogenic iron-rich minerals. *Earth-Science Reviews*, 72, 1-19.
- Grotzinger, J., 2005. Stratigraphy and sedimentology of a dry to wet eolian depositional system, Burns Formation, Meridiani Planum, Mars. *Earth and Planetary Science Letters*, 240, 11-72.
- Hazen, R.M., 2010. Evolution of Minerals. *Scientific American*, March, 58-65.
- Heath, J. E., Lachmar, T. E., Evans, J. P., Kolesar, P. T., and Williams, A. P., 2009. Hydrogeochemical characterization of leaking, carbon dioxide-charged fault zones in east-central Utah, with implications for geological carbon storage. *Geophysical Monograph*, 183, 147-158.
- Kampmann, N., Bickle, M., Becker, J., Assayag, N., and Chapman, H., 2009. Feldspar dissolution kinetics and Gibbs free energy dependence in a CO₂-enriched groundwater system, Green River, Utah. *Earth and Planetary Science Letters*, 284, 473-488.
- Lu, P., Fu, Q., Seyfried, W.E., Jr., Hereford, A., Zhu, C., 2011. Navajo Sandstone-brine-CO₂ interaction; implications for geological carbon sequestration. *Environmental Earth Sciences*, 62, 101-118.
- McLennan, S., Bell, J.F., III, Calvin, W.M., Christensen, P.R., Clark, B.C., De Souza, P.A., Farmer, J.D., Farrand, W.H., Fike, D.A., Gellert, R., Ghosh, A., Glotch, T.D., Grotzinger, J., Hahn, B., Herkenhoff, K.E., Hurowitz, J.A., Johnson, J.R., Johnson, S.S., Jolliff, B.J., Klingelhoefer, G., Knoll, A.H., Learner, Z., Malin, M.C., McSween, H.Y., Pockock, J.M., Ruff, S.W., Soderblom, L.A., Squyres, S.W., Tosca, N.J., Watters, W.A., Wyatt, M.B., Yen, A., 2005. Provenance and diagenesis of the evaporite-bearing Burns Formation, Meridiani Planum, Mars. *Earth and Planetary Science Letters*, 240, 95-121.
- McPherson, B.J. and Cole, B.S., 2000. Multiphase CO₂ flow, transport and sequestration in the Powder River Basin, Wyoming, USA. *Journal of Geochemical Exploration*, 69-70, 65-69.

- Nielsen, G., Chan, M.A., and Petersen, E.U., 2009. Diagenetic coloration facies and alteration history of the Jurassic Navajo Sandstone, Zion National Park and vicinity, southwestern Utah: in Tripp, B.T., Krahulec, K., and Jordan, J.L., eds., Utah Geological Association Publication 38, Geology and Geological Resources and Issues of Western Utah, CD-ROM.
- Nielsen, G., and Chan, M.A., 2009. Mapping, architecture, and spatial correlation of diagenetic coloration facies, Jurassic Navajo Sandstone, Snow Canyon State Park, southwestern Utah, in Tripp, B.T., Krahulec, K., and Jordan, J.L., eds., Utah Geological Association Publication 38, Geology and Geological Resources and Issues of Western Utah, CD-ROM
- Parry, W., Forster, C., Evans, J., Bowen, B., and Chan, M., 2007. Geochemistry of CO₂ sequestration in the Jurassic Navajo Sandstone, Colorado Plateau, Utah. *Environmental Geosciences*, 14, 91-109.
- Parry, W.T., Chan, M.A. and Nash, B.P., 2009. Diagenetic characteristics of the Jurassic Navajo Sandstone in the Covenant oil field, central Utah thrust belt. *AAPG Bulletin*, 93, 1039-1061.
- Potter, S.L., Chan, M.A., 2011. Joint controlled fluid flow patterns and iron mass transfer in Jurassic Navajo Sandstone, Southern Utah, USA. *Geofluids*, 11, 184-198.
- Potter, S.L., Chan, M., Petersen, E., Dyar, M.D., Sklute, E., 2011. Characterization of Navajo Sandstone Concretions: Mars comparison and criteria for distinguishing diagenetic origins. *Earth and Planetary Science Letters*, 301, 444-456.
- Seiler, W.M., 2008. Jurassic Navajo Sandstone of Coyote Buttes, Utah/Arizona: Coloration and diagenetic history, preservation of a dinosaur trample surface, and a terrestrial analog to Mars, *Geology and Geophysics*. University of Utah, Salt Lake City.
- Shipton, Z. K., Evans, J. P., Kirschner, D., Kolesar, P. T., Williams, A. P., and Heath, J., 2004. Analysis of CO₂ leakage through "low-permeability" faults from natural reservoirs in the Colorado Plateau, east-central Utah. *Geological Society Special Publications*, 233, p. 43-58.
- Smith, H. J., Fahrenkamp-Uppenbrink, J., and Coontz, R., 2009. Carbon capture and sequestration. *Science*, 325, 1641.

CHAPTER 1

IRON PRECIPITATION IN A NATURAL CO₂ RESERVOIR: JURASSIC NAVAJO SANDSTONE IN THE NORTHERN SAN RAFAEL SWELL, UT, USA

Sally L. Potter-McIntyre, Jessica L. Allen, Si-Yong Lee, Weon Shik Han, Marjorie A.
Chan and Brian J. McPherson

Published: Geofluids, January, 2013, doi: 10.1111/gfl.12014

Abstract

Diagenetic iron (oxyhydr)oxide minerals are common precipitates expected in CO₂ reservoirs and these minerals record fluid flow for application to carbon capture and sequestration (CSS). Multiple mineralogy and spectroscopy analyses on a pore- to meter-scale characterize a well-exposed, lithologically controlled, iron (oxyhydr)oxide reaction front in the Jurassic Navajo Sandstone. Dolomite is the most prevalent cement (up to 23 area%), followed by only several percent or less of iron (oxyhydr)oxides, kaolinite, illite and gypsum cements. Bulk geochemistry based on diagenetic mineralogies in the reaction front is compared to the water chemistry from nearby modern spring effluent emanating from the Navajo Sandstone to conclude that similar fluids (i.e., CO₂-charged, saline waters containing hydrocarbons) are responsible for the precipitation. A second comparison of bulk geochemistry and diagenetic mineralogies of the reaction front with

data from other abundant Navajo Sandstone concretions in the Spencer Flat region (in south central Utah) show that reservoir fluids likely vary spatially and temporally in the porous and permeable Navajo Sandstone. CO₂ injection into porous and permeable, quartz arenite, saline aquifers will likely result in minor clay and abundant dolomite precipitation that will significantly decrease porosity.

Introduction

Carbon capture and sequestration (CCS) is garnering much interest recently as a means of mitigating anthropogenic contributions to rising atmospheric CO₂ levels (e.g., McPherson and Cole, 2000; Smith et al., 2009; Dubacq et al., 2011; Lu et al., 2011). The Jurassic Navajo Sandstone is examined for its potential as a sequestration reservoir due to its excellent reservoir qualities (e.g., high permeability and porosity), its widespread areal extent across the Colorado Plateau, and its clean and mature quartz arenite mineralogy (consisting of ~95% quartz and ~5% K-feldspar: Baer and Rigby, 1978; Parry et al., 2007; Potter, 2009). Here we document the mineralogy and chemistry of cement precipitates in an inferred fossil CO₂ reservoir to predict the geochemical effects that addition of supercritical CO₂ might have on a reservoir of similar lithology. This study addresses the questions:

1. Was the Navajo Sandstone in the San Rafael Swell a natural CO₂ reservoir during burial diagenesis?
2. What were the types of precipitating reservoir fluids during burial diagenesis?
3. What are the effects of adding CO₂ to a reservoir on mineralogy, chemistry and porosity?

The Jurassic Navajo Sandstone is the largest ancient erg known to exist on Earth (Blakey, 1988; Blakey et al., 1994). The unit and its equivalents extend north-south from Wyoming to New Mexico and east-west from Nevada to Colorado (Blakey, 1988, Blakey et al., 1994). Regional reservoir properties are well-studied (e.g., Linnert, 1988; Chan et al., 2000; Beitler et al., 2003, 2005; Bowen et al., 2007) and previous works proposed that during post-Laramide (70-50Ma until uplift and exposure), the Navajo Sandstone was a “supergiant” hydrocarbon reservoir (Beitler et al., 2003). Iron (oxyhydr)oxide precipitation in more specific regional areas has also been documented (Eichhubl et al., 2004; Parry et al., 2004, 2007; Seiler, 2008; Nielsen et al., 2009; Nielsen and Chan, 2009; Potter and Chan, 2011). Currently, where the Navajo Sandstone is in the subsurface, it serves as an important aquifer in southern Utah and as a hydrocarbon reservoir in central Utah. In the Providence Oil Field (north of the Covenant Oil Field; Figure 1.1), both CO₂ and hydrocarbons are produced from the Navajo Sandstone (Chidsey et al., 2011). In the northern San Rafael Swell and into eastern Utah, the Navajo Sandstone is a modern CO₂ reservoir (Baer and Rigby, 1978; Parry et al., 2007; Heath et al., 2009; Burnside, 2010; Figure 1.1). This reservoir charges cold CO₂ geysers and springs along the Little Grand Wash and Salt Wash fault systems near Green River, Utah as well as at Woodside Dome and Farnham Dome (Allis et al., 2001; Parry et al., 2007; Kampmann et al., 2008; Figure 1.1).

Purpose of Study

This study examines mineralogy and geochemistry of cement in samples collected along vertical and horizontal transects of a diagenetic, iron (oxyhydr)oxide-bearing

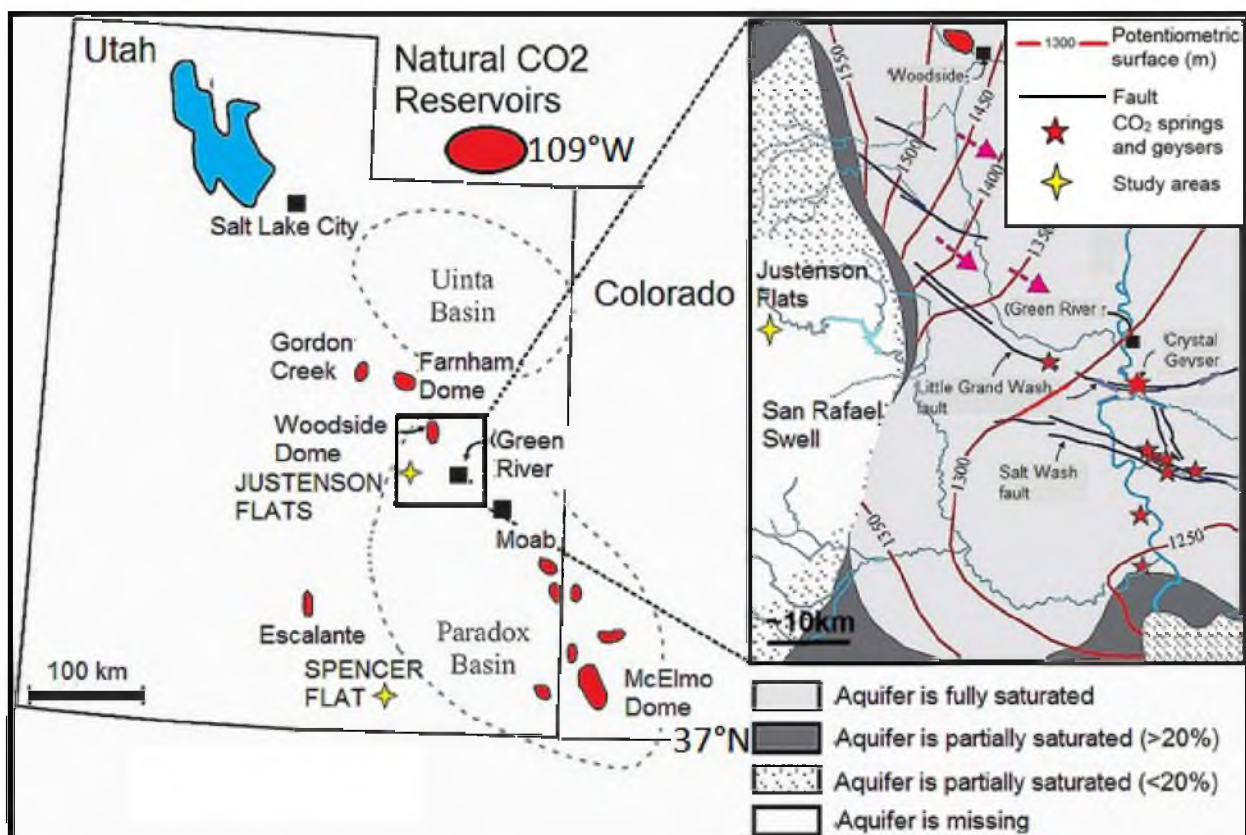


Figure 1.1. Map of Ten Mile Graben fault system (including Little Grand Wash and Salt Wash fault areas) and modern potentiometric surface of CO₂-charged, water reservoir (aquifer) in the Navajo Sandstone (modified from Allis et al., 2001 and Kampmann et al., 2009). The % saturation refers to saturation of aquifer with water.

reaction front to determine changes along the front on a pore-scale to meter-scale (Figure 1.2). This feature is interpreted as a reaction front due to the precipitation of iron (oxyhydr)oxide cements in a bleached sandstone in a roll front geometry (similar to a uranium roll front). The results from this study produce a thorough interpretation of the diagenetic history of this reaction front to apply towards understanding past and potentially future diagenetic reservoir fluids in the Navajo Sandstone in the northern San Rafael Swell. We also examine the spatial and temporal variation in reservoir fluid chemistry through a porous and permeable medium.

Study Area

The entire Navajo Sandstone section is expressed in Justensen Flats in the northern San Rafael Swell, the central site for this study (Figure 1.1). Eroded fracture faces expose the unit in three dimensions and make this well-suited for detailed evaluation and analyses. A ~45m long, colorful, diagenetic interval of iron (oxyhydr)oxide cemented sandstone exhibits a roll front geometry (Figure 1.2). This roll front extends into the “bleached” or white sandstone where the iron has, in large part, been removed by a reducing fluid (see Chan et al., 2000; Beitler et al., 2003, 2005; Bowen et al., 2007 for discussion of “bleached” sandstone). The roll front is herein interpreted to be a reaction front where an oxidizing fluid infiltrated the reservoir that was filled with a Fe²⁺-bearing reducing fluid (Chan et al., 2000; Beitler et al., 2003, 2005; Bowen et al., 2007).

Comparative field sites of the Little Grand Wash and Salt Wash fault systems are located southeast of Green River, Utah (Figure 1.1) where modern CO₂-charged, saline

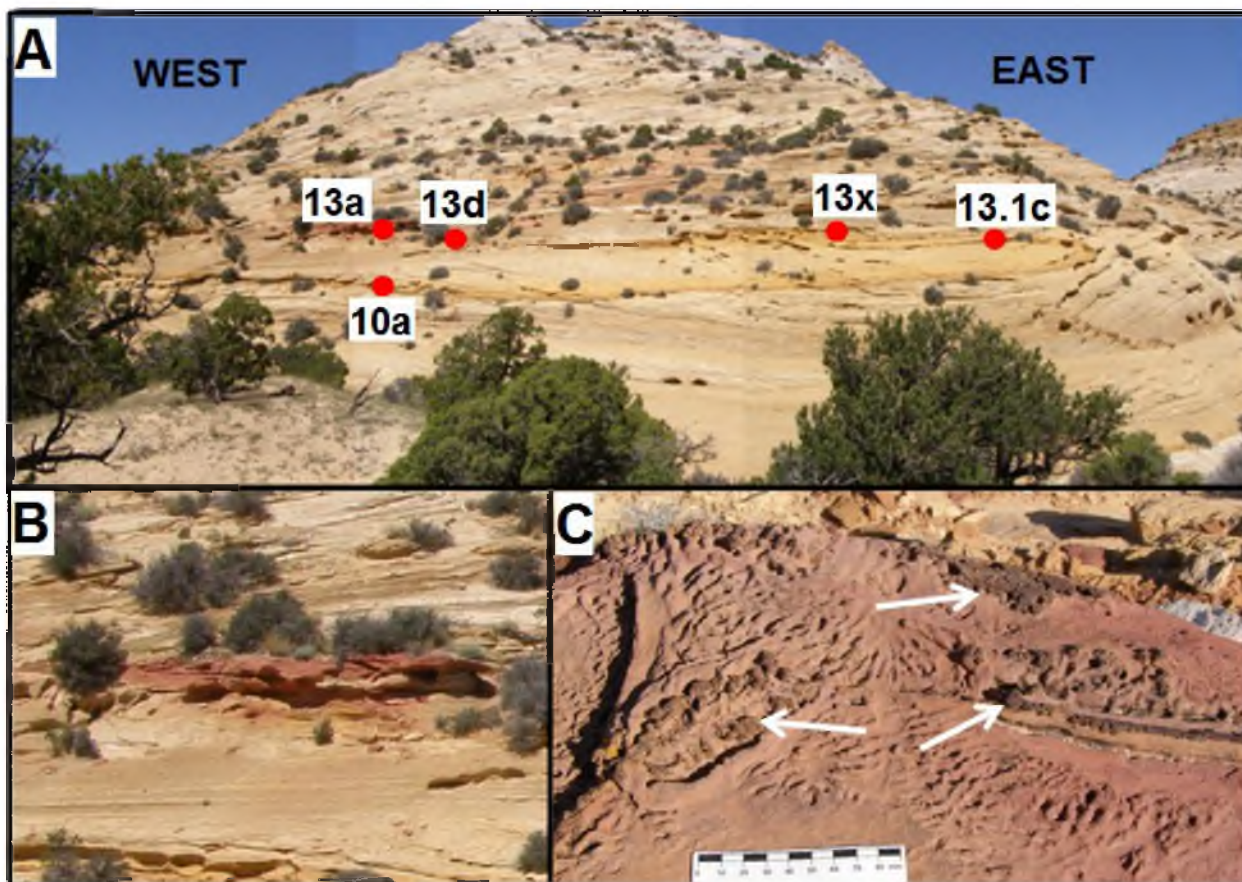


Figure 1.2. Reaction front in Justensen Flats in northern San Rafael Swell. A. The front initiated from the left side of the photo and proceeded to the right. Note the roll front geometry. Arrows mark horizontal and vertical transects that were sampled. Numbers denote samples used in QEMSCAN analysis. B. Close up of the red ledge at the initiating end of the reaction front. C. Colliform concretions (arrows) and wrinkle features on the top of the red ledge.

water emanates in cold springs and geysers along faults from the subsurface Navajo Sandstone reservoir (Shipton et al., 2004). The source of the spring salinity is the underlying Pennsylvanian Paradox Formation (Wilkinson et al., 2008; Heath et al., 2009; Kampmann et al., 2009). The source of the CO₂ is likely decarbonation of Paleozoic marine carbonates (Shipton et al., 2004; Heath et al. 2009; Kampmann et al., 2009). The chemistries of these springs provide a baseline for understanding what kinds of mineralogies precipitate from CO₂-charged fluids.

The Navajo Sandstone is well-exposed in Spencer Flats in Grand Staircase Escalante National Monument of southern Utah (Figure 1.1) and contains abundant spheroidal iron (oxyhydr)oxide concretions along with other concretion geometries (Potter and Chan, 2011). This comparison of three different Navajo Sandstone localities is used to examine spatial variation in diagenetic fluid chemistry.

Methods

Navajo Sandstone samples at Justensen Flats were collected every meter along the top of the reaction front in a horizontal transect (n=30) beginning at the red ledge. Samples (n=5) were also taken every meter in a vertical transect beginning at the bottom and ending at the red ledge (Figure 1.2). Polished thin sections were prepared from three of the vertical transect samples and ten samples from the horizontal transect. Two of the slides were stained with Alizarin red to differentiate calcite from dolomite.

Three sandstone samples from the vertical transect (bottom, middle and 1 m below the top) and nine samples from the horizontal transect (from roughly every three meters) were selected for X-ray diffraction (XRD) analysis (Table 1.1) using a Rigaku

Table 1.1. Comparison of results from XRD (X), Vnir spectroscopy on prepared XRD slides (VS) and Vnir spectroscopy on hand sample (VH). * denotes hand sample taken from nearby the XRD slide sample analyzed rather than the same sample. Vertical transect samples are 10Jn and horizontal transect samples are 13Jn.

Sample	Illite	Kaolinite	Goethite	Hematite	Lepidocrocite	Dolomite	Fe Dolomite	Gypsum
10Jnb	X, VH	X, VH	X, VS		VS	X	VS	
10Jnd	X, VH	X, VH	X, VS	X	VS, VH	X	VH	
10Jne	X, VH	X, VH	X, VS		VS, VH	X	VH	
13Jna	X, VH	X, VH	VS, VH	X	VH	X		
13Jnd*	X	X, VH	X, VS, VH	X		X		X
13Jng	X, VH	X, VH	X, VS, VH	X	VS	X	VS, VH	X
13Jnj*	X, VH	X, VH	VS, VH	X	VS	X	VS	X
13Jnq	X	X, VH	X, VS, VH	X	X, VS	X	VS, VH	X
13Jnw	X, VH	X, VH	X, VS, VH	X	VS	X	VS, VH	X
13Jnz*	X	X, VH	X, VS, VH	X	VS, VH	X		X
13Jn1D*	X	X, VH	X, VS, VH	X	VS	X	VS	X

2000V x-ray spectrometer with a copper anode x-ray tube at a rate of 2° per minute scanning speed. The air-dried, oriented samples (<2 μm size fraction) were analyzed from 2-30° 2θ (except for samples SRS13Jnj, SRS13Jnq and SRS13Jn1D that were analyzed from 2-50 °2θ to detect iron (oxyhydr)oxide phases and dolomite). The slides were then vapor glycolated for 12 hours at 60°C and analyzed from 2-50°2θ to determine if smectite or interstratified illite/smectite clays were present.

An ASD FieldSpec 3 visible to near infrared (Vnir) reflectance spectrometer was used to obtain spectra on the prepared XRD slides (n=12) as well as rock samples (n=18). The same rock samples as the XRD slides were used when available; rock samples from the nearest meter were used when the same samples were not available. Spectra were compared with USGS standards (Clark et al., 2007). This spectroscopy technique is effective for differentiating iron oxide mineral phases and clay minerals in sandstones because the iron oxides and clays absorb light in the visible to near infrared spectrum, but quartz and feldspars do not (Bowen et al., 2007; Seiler, 2008; Potter et al., 2011).

QEMSCAN (Quantitative Elemental Mineralogy using SCANNing electron microscope), a Zeiss scanning electron microscope with four Bruker high-speed energy dispersive detectors, was used to make mineralogical maps of the entire thin sections (n=6) at a 10μm pixel spacing (Armitage et al., 2010). The results are given in area % because these are two-dimensional mineral images. Whole rock analysis was performed by ALS Chemex in Reno, NV on three samples from the vertical transect and ten samples from the horizontal transect.

This study uses two approaches. 1. Bulk geochemistry from the cements in the reaction front at Justensen Flats is compared with water chemistry from the modern

springs emanating from the modern Navajo Sandstone reservoir to determine possible paleo fluid chemistry that precipitated the reaction front. 2. Bulk geochemistry from Justensen Flats is compared to bulk geochemistry of cement mineralogy in the Navajo Sandstone exposed in Spencer Flats to compare spatial variation of likely precipitating fluid chemistries (Figure 1.1).

Results

Field Study

The Justensen Flats field site exhibits two stratigraphic units in ascending order: 1. a bottom unit forms the contact with the underlying Kayenta Formation and is characterized by soft-sediment deformation, and 2. an upper unit forms the contact with the overlying Carmel Formation and consists of high-angle cross-bed sets. Both units are bleached (i.e., the original hematite grain coatings have been removed by a reducing fluid; Beitler et al., 2003). Cross-bed sets typically range between 1.5 and 10 m thick and are internally composed of grainflow laminae and wind ripple laminae. In the bleached, cross-bedded upper unit, an iron (oxyhydr)oxide reaction front is ~5 m high and extends for ~45 m; it is contained within a ~10 m cross-bed set (Figure 1.2). The reaction front initiated in the western part of the host rock and moved east in a roll front geometry, similar to a uranium roll front. The top of the reaction front abuts a bounding surface and extends below through a high-angle cross-bed set. At the top of the initiating end is a ~30 cm thick, well cemented, red ledge (Munsell color 5R4/6 – 5R 2/6; Figure 1.2). The top of the ledge exhibits colloform iron (oxyhydr)oxide concretions and a wrinkled weathering surface where there was likely more carbonate cement (Figure 1.2). The rest

of the reaction front is outlined in yellowish-brown cement (Munsell color 5YR 5/6 to 10YR 6/6) with an interior relatively depleted of iron (oxyhydr)oxide cement. In Justensen Flats, the Navajo Sandstone is exposed in three dimensions due to the presence of opening-mode fractures that have eroded. The reaction front is exposed along the face of a fracture.

X-Ray Diffraction

Clay and carbonate cement mineralogies are similar between samples. Herein, only the 2-50 °2θ spectra are discussed because glycolation produced no change in the spectra (i.e., no interstratified clays are detected). All samples from the vertical and horizontal transects (Figure 1.3; Table 1.1) show illite (~10.2Å, 5.0Å), kaolinite (3.6Å) and dolomite (2.9Å, 2.0Å) peaks. The top two samples from the vertical transect show minor hematite (~2.7Å, 2.5Å).

Iron (oxyhydr)oxides are also present in all of the samples analyzed. In the horizontal transect, all samples contain goethite (broad peaks at 2.47Å, 2.7Å,) and hematite (sharp peak at 2.7Å, 2.5Å) except Sample 13Jna – the sample from the red ledge – and Sample 13Jnj. The only iron (oxyhydr)oxide phase detected in the red ledge (Sample 13Jna) is hematite and goethite is the only iron mineral phase detected in Sample 13Jnj; however, these samples produced very low intensity spectra. Lepidocrocite (3.2Å) is detected in Sample 13Jnq along with hematite and goethite. All of the samples except SRS13Jna (the red ledge) contain gypsum which produces a sharp and intense first order peak that overlaps the second order quartz peak at a d-spacing of ~4.3Å and a peak at ~7.2Å.

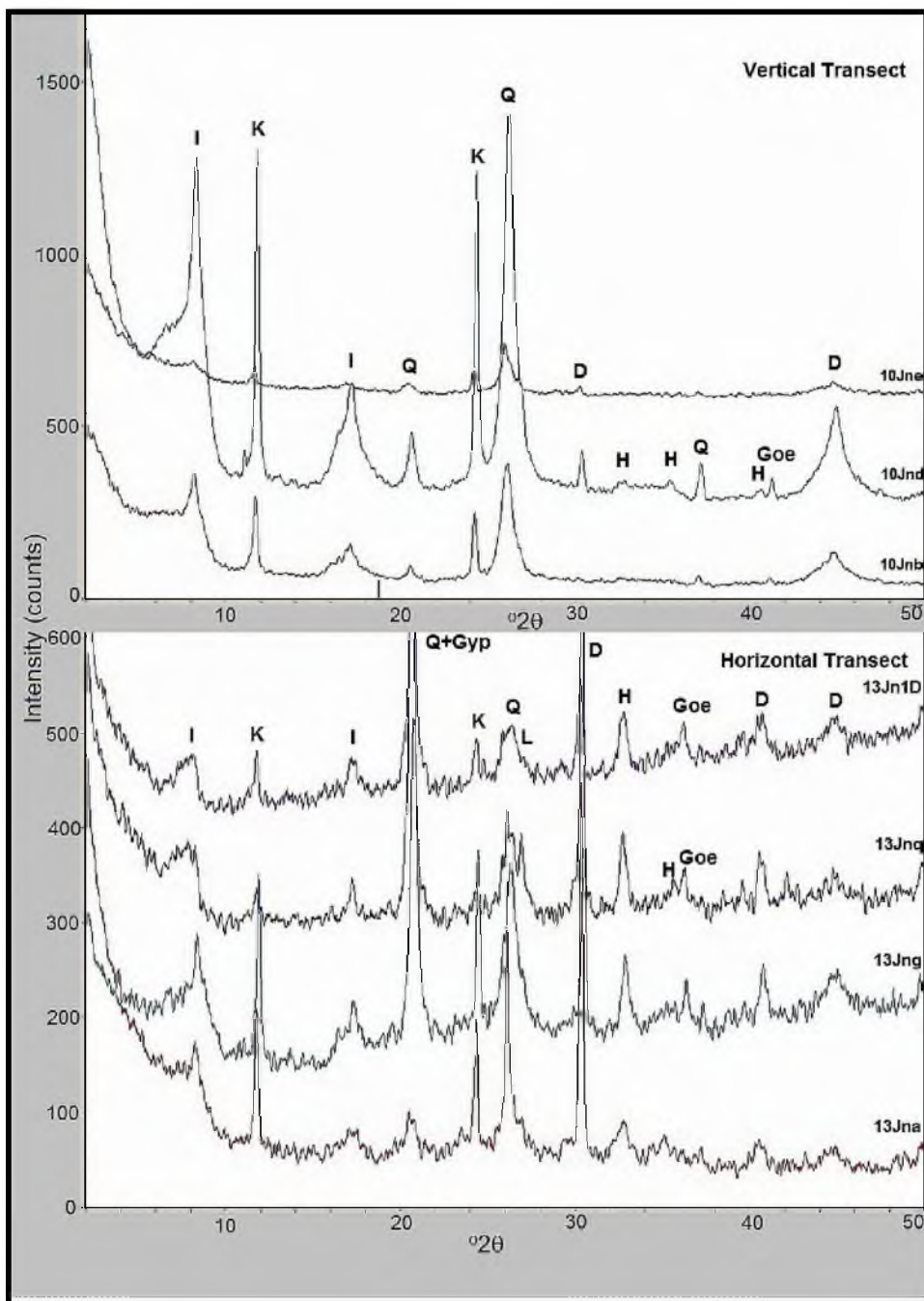


Figure 1.3. XRD data selected samples in vertical (top) and horizontal (bottom) transects. I= illite, K = kaolinite, Q = quartz, Gyp = gypsum, L = lepidocrocite, H = hematite, Goe = goethite, D = dolomite.

Visible to Near Infrared (Vnir) Reflectance Spectroscopy

Vnir reflectance spectra were taken on the oriented clay slides for XRD and their original hand sample for the majority of specimens (Table 1.1; Figure 1.4). Iron (oxyhydr)oxide phases are differentiated based on the adsorption minima between 800-900nm, shoulders at 630nm as well as the water/hydroxyl features at 1400nm, 1900nm and 2200nm. Goethite is present in all of the slides from both the vertical and horizontal transects. Lepidocrocite is present in the slides from the vertical transect and lepidocrocite is present in all of the slides from the horizontal transect except for two from the originating (west) end of the transect (13Jna, d). Dolomite was not detected in the slides because the diagnostic Vnir spectral features are at longer wavelengths than we examined; however, a ferroan dolomite feature is present at ~435nm in the top of the vertical transect (Samples 10Jnb) and in the terminating (east) end of the horizontal transect (13Jng-w and 13Jn1D). Ferroan dolomite was not easily detectable with XRD, but it was seen with the petrographic microscope (see petrography results). Illite and kaolinite were not detected on any of the clay smear slides. This is likely because the water/hydroxyl features of goethite interfere with kaolinite and illite features at the same wavelengths and darker materials typically dominate reflectance spectra, so the iron (oxyhydr)oxides may overshadow the clays in the reflected spectra (Clark, 1995). Another likely contributing factor is that reflectance is decreased in larger grain sizes (Clark, 1995). The slides contain the <2 μ m fraction and the iron (oxyhydr)oxides in these

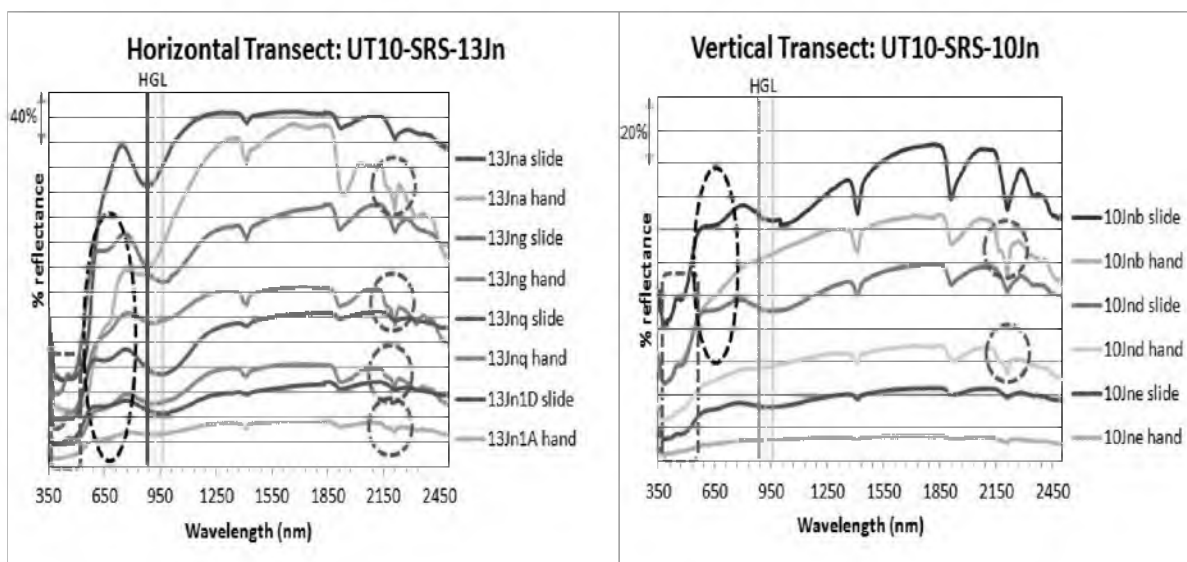


Figure 1.4. Vnir reflectance spectroscopy data from the horizontal and vertical transects. H = hematite, G = goethite, L = lepidocrocite. Dashed rectangle shows ferroan dolomite feature, dashed oval shows goethite/lepidocrocite shoulders and dashed circles shows kaolinite feature.

samples may be, in large part, the more amorphous, finer grained particles that reflect more light than the clays. Also, hematite was detected on the slides with XRD but not with spectroscopy, possibly because the smaller grain size of the more amorphous particles reflect more light than the larger hematite particles.

In hand sample, kaolinite is in all samples in the vertical transect by the presence of a distinct shoulder at 1900nm. Illite is probably present in the vertical transect samples because of the depth of the minima at 1400nm. Lepidocrocite and ferroan dolomite were detected in middle (10Jnd) and bottom (10Jne) samples in the vertical transect.

In the horizontal transect, kaolinite is detected in all hand samples; illite is present in all except 13Jnq, 13Jnw (13Jnz slide equivalent) and 13Jn1A (13Jn1D slide equivalent). Goethite was identified in all samples. Lepidocrocite was detected in 13Jna,

13Jnd and 13Jn1A. Ferroan dolomite is present in 13Jng, 13Jnq and 13Jnw (13Jnz slide equivalent).

Petrography

Petrographic analysis shows abundant carbonate cements (dolomite) that did not stain with Alizarin red (used to detect calcite). Euhedral rhombohedra of dolomite with concentric outlines of iron are common (Figure 1.5). Dissolution features of dolomite rhombohedrons are present (Figure 1.5). Herein, we refer to the rhombohedra with iron as dolomite although it is possibly ankerite and Vnir reflectance spectroscopy detects ferroan dolomite. Further study using microprobe would be required to pinpoint the exact mineral phase.

Diffuse, fine-grained iron oxides are abundant throughout all of the samples and are commonly nucleated on feldspar grains. Kaolinite blebs and illite rims on quartz grains are present. Minor amounts of gypsum cement are also visible.

QEMSCAN

QEMSCAN analysis (Figure 1.6; Table 1.2) shows that the most abundant cement is dolomite (8.5 - 23.2 area %). Wind ripple laminae have higher dolomite area percentages and lower porosity than grain flow lamina (Table 1.2). All the iron (oxyhydr)oxide phases (e.g., hematite, goethite, lepidocrocite, etc.) are grouped as “Fe oxides”. Iron oxides range from 1.3 to 2.9 area %. Kaolinite (2.2 - 4.5 area %) and illite (0.9 - 1.7 area %) are also identified. Gypsum is present in minor amounts along the horizontal transect (0.02 - 1.6 area %). In the sample at the bottom of the vertical transect

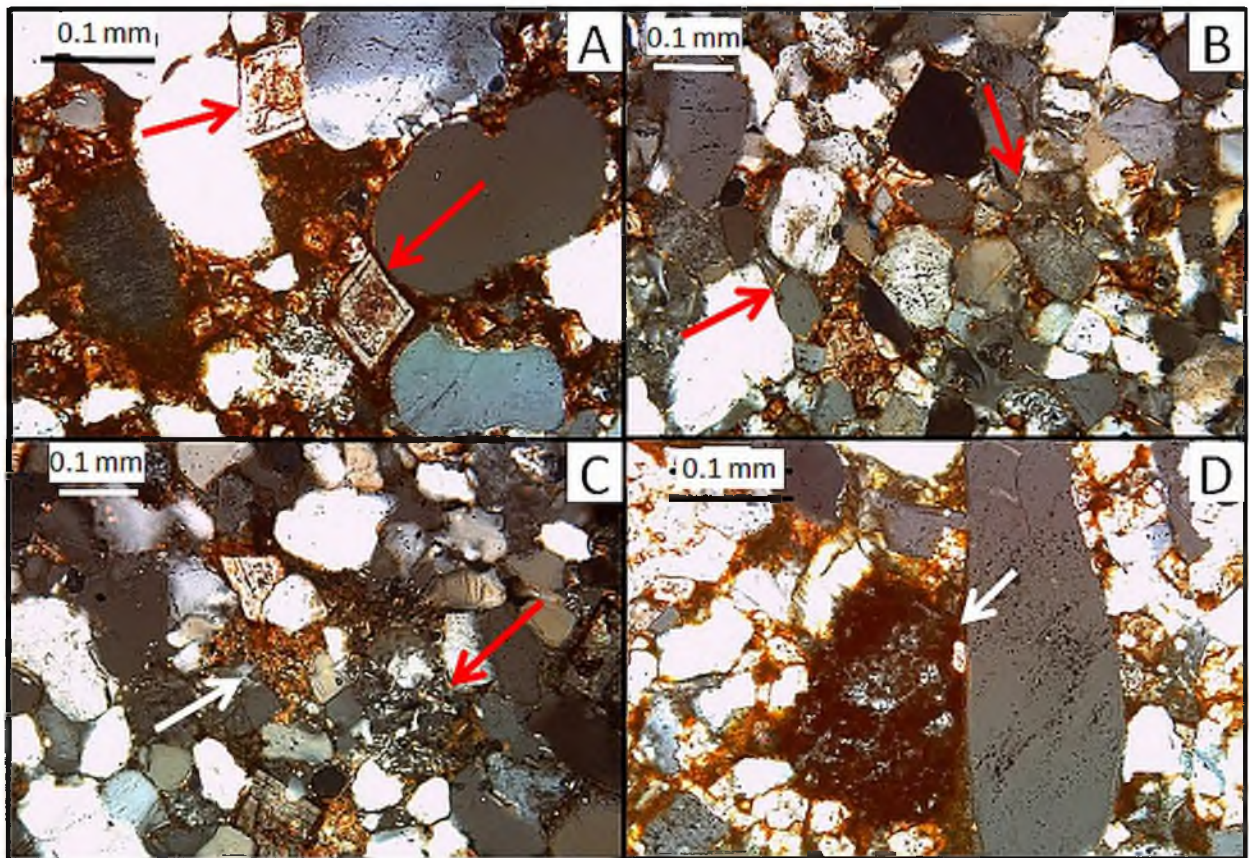


Figure 1.5. Cement petrography. A. Dolomite or ankerite rhombohedrons (arrows). Note multiple generations of precipitation outlined with iron. B. Illite rims (arrows) are abundant around quartz grains. C. Fine-grained, discrete iron (oxyhydr)oxide cement (white arrow) and kaolinite (red arrow). D. Iron oxide/ oxyhydroxide nucleated on a feldspar grain (arrow).

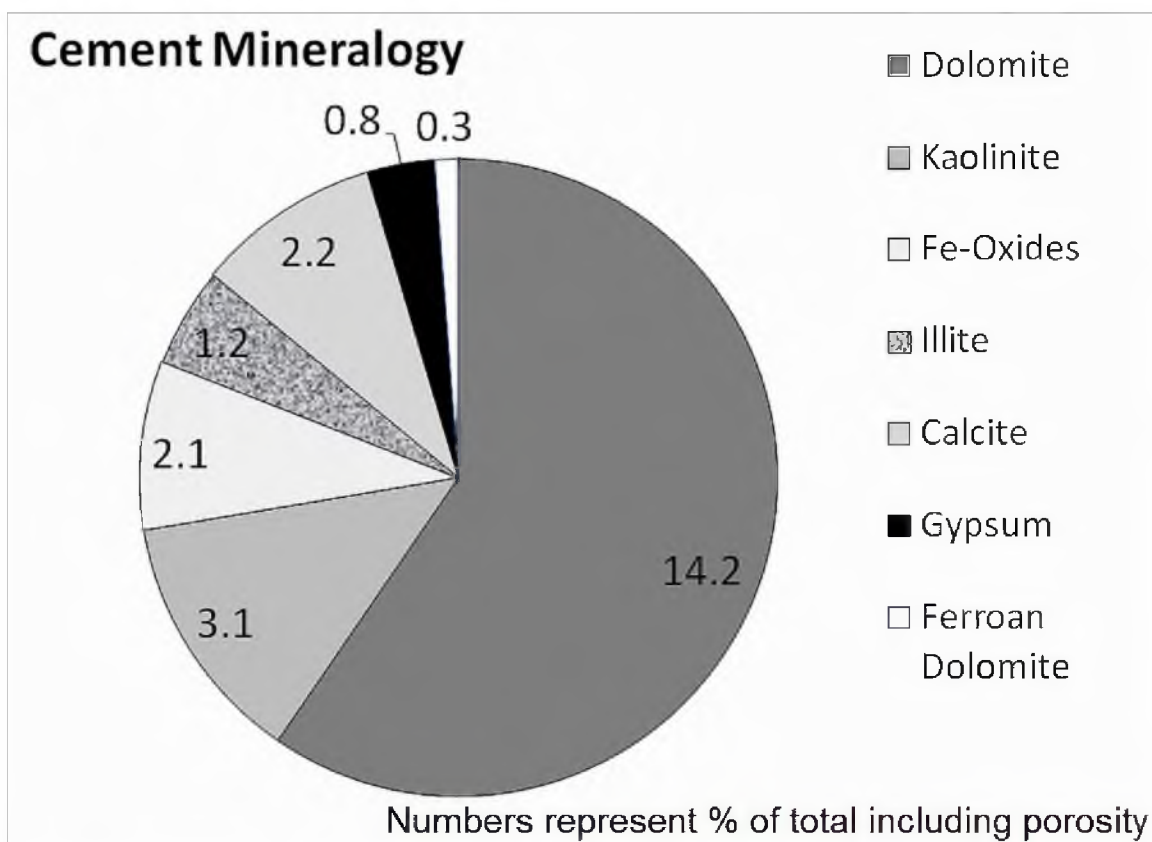


Figure 1.6. QEMSCAN results showing area percent of total for cement minerals.

Table 1.2. Area % of minerals reported by QEMSCAN.

	10Jna	13Jna	13Jnd	13Jnx	13Jn1C
Quartz	67.8	48.3	68.1	60.2	55.5
Dolomite	12.0	23.2	8.5	10.4	17.1
Porosity	11.4	1.7	13.4	3.6	4.0
Other	7.2	11.6	6.5	10.8	10.4
Orthoclase	5.5	5.6	7.8	5.3	5.3
Kaolinite	3.7	2.5	4.5	2.4	2.2
Fe-Oxides	1.4	2.9	1.3	2.3	2.5
Illite	1.2	0.9	1.7	1.2	1.0
Calcite	0.0	3.0	0.1	4.6	3.4
Gypsum	0.0	1.2	0.0	1.6	1.3
Plagioclase	0.8	0.7	1.0	0.9	0.8
Fe Dolo.	0.4	0.1	0.3	0.1	0.4

(Sample 10Jna), only trace amounts of gypsum are present (0.002 area %). Average porosity is 6.8%.

Whole Rock Analysis (WRA)

In the vertical transect, calcium and magnesium concentrations (reported as CaO and MgO, respectively) are highest at the bottom (CaO = 0.80 wt.% ; MgO = 4.53 wt.%) and decrease at the top (CaO = 1.51 wt.%; MgO = 0.99 wt.%; Table 1.3). Iron (reported as Fe₂O₃) increases from the bottom to the top of the transect (bottom = 1.81 wt.%; top = 7.05 wt.%). Calcium also increases along the horizontal transect from the originating end (3.98 wt.%) to the terminating end (10.85 wt.%). Likewise, magnesium increases along the horizontal transect (2.59 to 5.14 wt.%). Iron decreases along the transect with the highest values at the originating end (3.52 wt.%) decreasing to 2.10 wt.% at the terminating end. An inverse relationship exists between the abundances of iron and calcium and magnesium (Fig. 1.7) such that calcium and magnesium increase along the horizontal transect as iron decreases. Calcium and magnesium are well correlated (correlation coefficient = 0.92). Iron and calcium -0.55 and iron and magnesium -0.56 are slightly negatively correlated.

We examined bulk geochemistries of effluent from the springs and geysers along the Little Grand Wash and Salt Wash fault systems (Heath et al., 2009), with diagenetic mineralogies of the Navajo Sandstone in Justensen Flats and the Navajo Sandstone in Spencer Flat (Potter, 2009) to compare and contrast precipitating fluid chemistries. A comparison of water chemistry from the Little Grand Wash and Salt Wash springs and geysers (Figure 1.1) with whole rock analysis from Justensen Flats shows a high

Table 1.3. Whole Rock Analysis for San Rafael Samples, Spencer Flat (30 host rock samples) and water chemistry (as percent of total dissolved solids) for the modern springs and geysers in the Ten Mile Graben fault systems.

SAMPLE	wt.%	wt.%	wt.%	wt.%	wt.%	ppm	ppm	ppm
San Rafael Swell								
Vertical Transect	Fe2O3	CaO	MgO	MnO	SrO	U	As	Zn
UT10-SRS-10Jn a	1.81	10.80	4.53	0.16	0.01	0.76	10.60	77
UT10-SRS-10Jn c	1.39	1.67	1.09	0.03	0.01	0.67	6.20	23
UT10-SRS-10Jn e	7.05	1.51	0.99	0.09	0.01	0.54	11.60	27
Horizontal Transect								
UT10-SRS-13Jn a	3.52	3.98	2.59	0.10	0.00	0.64	15.40	58
UT10-SRS-13Jn d	3.46	3.05	2.06	0.10	0.01	0.51	10.30	53
UT10-SRS-13Jn g	2.17	6.43	4.24	0.15	0.01	0.63	17.20	69
UT10-SRS-13Jn j	3.87	5.45	3.19	0.14	0.01	0.62	41.60	69
UT10-SRS-13Jn m	2.73	5.62	3.66	0.12	0.01	0.49	20.70	60
UT10-SRS-13Jn p	2.10	5.12	3.21	0.11	0.01	0.53	9.20	53
UT10-SRS-13Jn s	2.00	8.54	3.25	0.10	0.01	0.68	10.70	51
UT10-SRS-13Jn v	2.00	7.30	4.31	0.14	0.01	0.92	18.90	71
UT10-SRS-13Jn y	1.90	10.15	4.82	0.15	0.01	0.89	11.90	77
UT10-SRS-13Jn 1b	2.10	10.85	5.14	0.16	0.01	1.18	7.70	73
Average	2.78	6.19	3.31	0.12	0.01	0.70	14.77	58
Spencer Flat	Fe2O3	CaO	MgO	MnO	SrO	U	As	Zn
Average (n=30)	0.75	0.02	0.08	0.01	0.00	0.37	4.52	8.21
Modern Springs	%Fe	%Ca	%Mg	%Mn	%Sr			
Crystal Geyser	0.02	245.83	0.74	0.00	0.04			
Small Bubbling Spr.	0.02	190.63	1.33	0.01	0.07			
Big Bubbling Spr.	0.02	295.83	0.90	0.00	0.06			
Ten Mile Geyser	0.04	534.78	0.82	0.00	0.06			
Pseudo Ten Mile	0.01	260.87	0.78	0.00	0.05			
Torrey's Spring	0.03	283.33	1.04	0.00	0.05			
Tumbleweed Geyser	0.01	260.00	0.59	0.00	0.03			
Average	0.02	202.70	0.89	0.00	0.05			

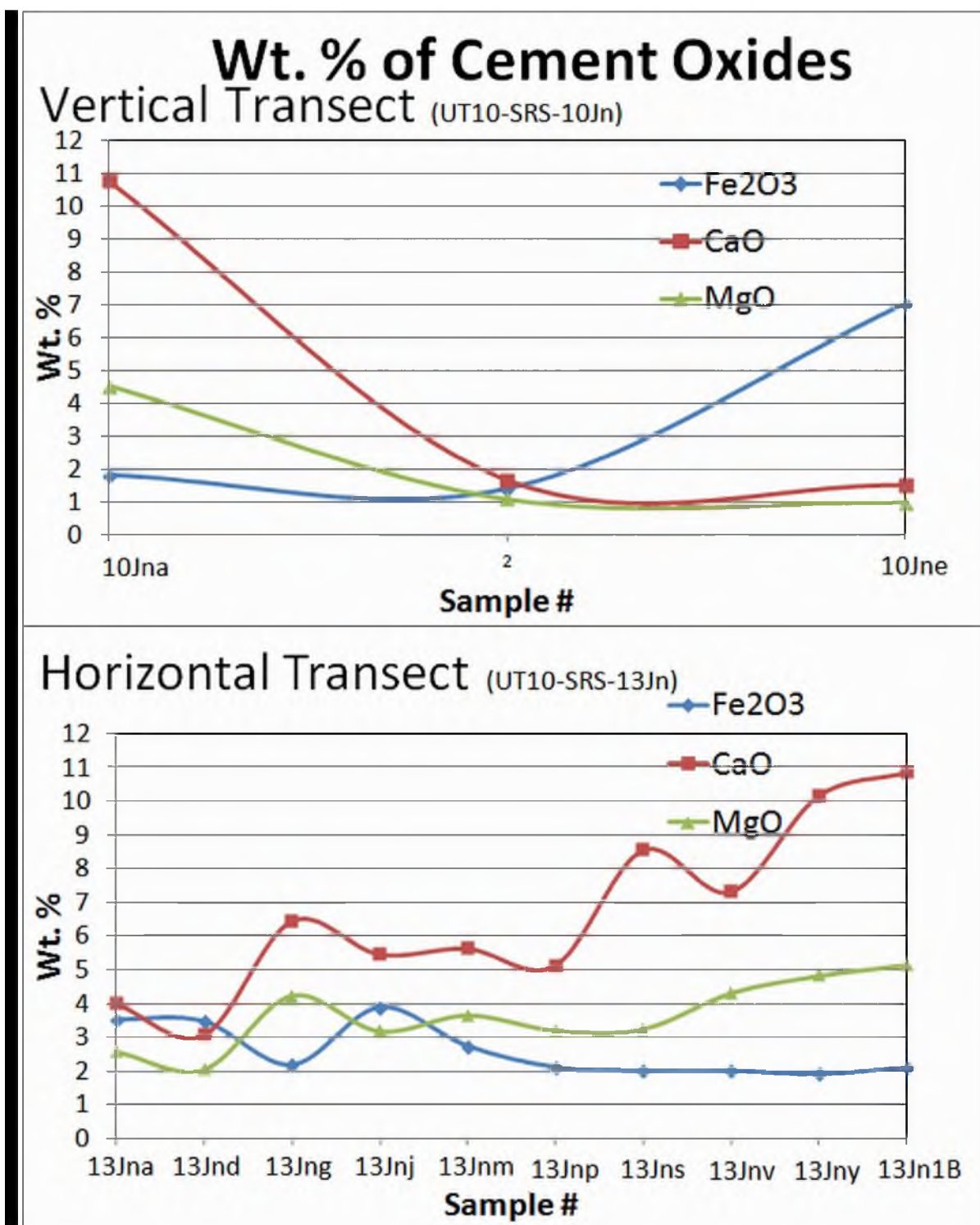


Figure 1.7. Graphs of wt. % from vertical and horizontal transects showing inverse relationship between iron and calcium/ magnesium concentrations (reported as oxides).

correlation coefficient (0.89) between the elements: calcium, magnesium, iron, manganese and strontium. This was calculated by averaging the data from the springs and geysers published by Heath et al. (2009) and averaging the values from the whole rock analysis from this report for those elements. When the values are normalized, calcium is a greater percentage of the water chemistry (75%) than the WRA (50%) and iron is less prevalent in the water (1%) than the WRA (22%; Figure 1.8). Magnesium is similar in both the water (23%) and the WRA (27%). Manganese is 1% in the WRA and negligible in the water; Strontium is 1% in the water and negligible in WRA. The bulk geochemistry from Justensen Flats shows a much better correlation to the effluent from the Little Grand Wash/ Salt Wash fault systems (0.89), than to the Spencer Flat data (0.10; Table 1.3; Figure 1.8). The constituents from the Little Grand Wash/ Salt Wash fault systems are negatively correlated with the Spencer Flat data (-0.32). We acknowledge that comparing bulk geochemistry to water chemistry is simplistic; however, the approach broadly demonstrates similarities and differences between the bulk geochemistries of Justensen Flats and Spencer Flat and the water chemistry of the springs in the Little Grand Wash/ Salt Wash fault system.

Interpretation and Discussion

Diagenetic CO₂ Reservoir

The Justensen Flats reaction front is located along a fracture and abuts a bounding surface along the top. Iron (oxyhydr)oxide cements (as well as gypsum and dolomite) are concentrated heavily along the top of the reaction front and this suggests that fluids pooled along the less permeable bounding surface (interdune surface) at the top of the

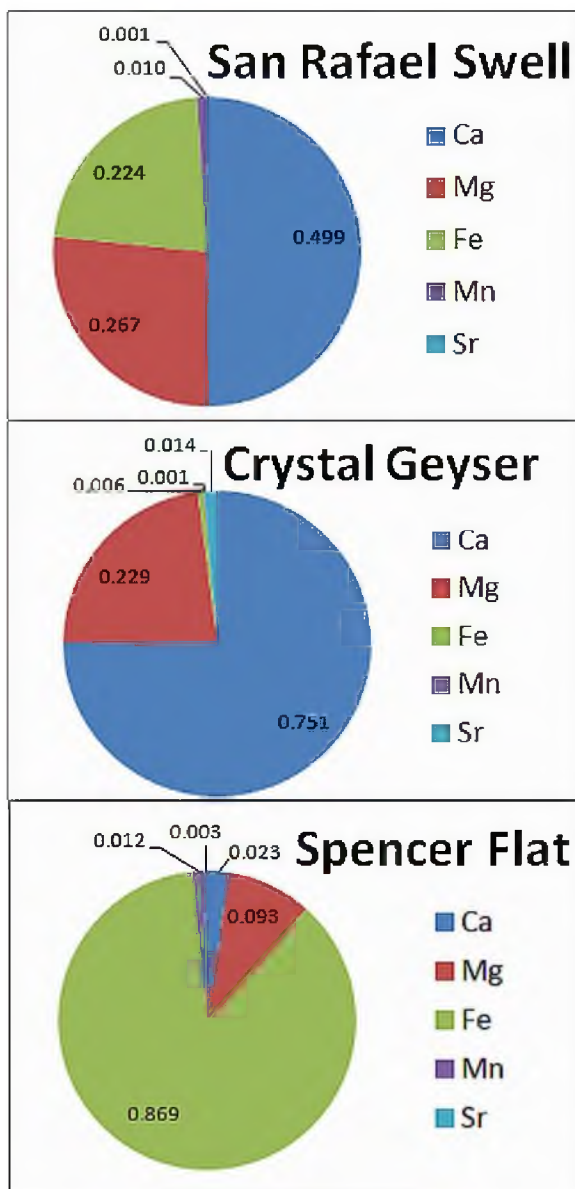


Figure 1.8. Normalized constituents of the Navajo Sandstone in San Rafael Swell (from whole rock analysis), and in Spencer Flat (WRA, Potter, 2009) and Crystal Geysir (water chemistry, Heath et al., 2009). Constituents are normalized to 100% and numbers represent percent of total.

cross-bed set. Therefore, the reaction front is lithologically controlled such that fluids moved upward through the subsurface along a cross-bed set and were limited or stopped by a finer-grained first-order bounding surface (interdune surface) at the top. This upward movement of fluids suggests that these precipitating fluids were less dense than water (i.e., possibly hydrocarbons).

Gypsum is an evaporite mineral that likely precipitated during early diagenesis in a hypersaline interdune setting because it is concentrated along the bounding surface (Parry et al., 2009). Some of the dolomite present in these samples are likely synsedimentary to early diagenetic minerals as well because sand grains seem to be compacted around the large euhedral crystals (Figure 1.5A). However, a likely genesis for some of the abundant dolomite, as well as the kaolinite and illite, is precipitation within a CO₂-charged reservoir (Parry et al., 2007). The Navajo Sandstone is a CO₂ reservoir to both the west and east of the study area (Shipton et al., 2004; Chidsey et al., 2011); CO₂-charged waters emanate from the formation at nearby Farnham Dome, Woodside Dome and Crystal Geyser (Shipton et al., 2004; Parry et al., 2007). At Crystal Geyser, results of geochemical modeling of water chemistry (see Shipton et al., 2004 for model) show that waters are saturated with respect to aragonite, calcite, dolomite, fluorite and gypsum.

Results of geochemical modeling (see Parry et al., 2007 for model) show that saline waters reacting with CO₂-charged Farnham Dome water would produce muscovite (as a proxy for illite) and then kaolinite as the K-feldspar begins to dissolve by the reaction:



This reaction consumes acid, buffers the solution and, when the fluid is saturated with respect to dolomite (as these reservoir fluids were), dolomite is precipitated (Parry et al., 2007).

Petrographic analysis shows euhedral dolomite rhombohedrons with iron outlines around multiple generations of carbonate precipitation. Ferroan dolomite is detected with Vnir reflectance spectroscopy and QEMSCAN. Ferroan dolomite is also present in Navajo Sandstone cores from the Covenant Oil Field and has been interpreted as iron sourced from early diagenetic grain coatings, mobilized, and subsequently incorporated into dolomite (Parry et al., 2009). Therefore, it is likely that although some of the dolomite is an evaporative mineral precipitated syndepositionally during early diagenesis, the majority precipitated as a later phase during burial diagenesis.

Precipitating Reservoir Fluids and Timing

At springs and geysers along the Little Grand Wash and Salt Wash fault systems, hydrocarbons (a chemical reductant) are present in the waters that emanate from the Navajo Sandstone and there is also an oil seep along Little Grand Wash fault (Shipton et al., 2004). A comparison of effluent from the Little Grand Wash and Salt Wash springs and geysers with bulk geochemistry from Justensen Flats shows a high correlation coefficient (0.89) between the elements calcium, magnesium, iron, manganese and strontium. The high correlation and the similarity of chemical composition, along with the saturation with respect to dolomite, suggest that similar fluids, i.e., CO₂- and hydrocarbon-charged, saline fluids, precipitated the minerals in the San Rafael Swell roll front.

In slightly reducing conditions, the dolomite and gypsum could persist while iron is reduced and mobilized, particularly if there was a relatively high $p\text{CO}_2$ that would lower pH (iron is mobilized more easily in circumneutral to acidic fluids; Drever, 1997). Indeed, there is an inverse relationship between the iron and the calcium and magnesium as reported in whole rock analysis (WRA) in the horizontal transect. The iron decreases along the transect as the calcium and magnesium increases. It is likely that although iron has been incorporated into the dolomite, some iron remained in solution and as dolomite dissolved as acidic fluids permeated the reservoir, more iron was put into solution. The mobilized iron precipitated in a late-stage, oxidizing reaction front when meteoric, oxidizing water infiltrated along the fracture and diffused through the cross-bed set. Cements precipitated sequentially (Figure 1.9): 1. symsedimentary to early diagenetic evaporite precipitation of gypsum and minor dolomite (evidenced by compaction of grains around euhedral crystals; Figure 1.5A), 2. during middle diagenesis, infiltration of CO_2 - and hydrocarbon-charged, saline, reducing fluid precipitated illite, kaolinite and more dolomite (evidenced by multiple generations of precipitation; Figure 1.5A); small amounts of iron remained in solution, and 3. oxidizing meteoric water infiltrated along fracture and precipitated iron (oxyhydr)oxides in a lithologically controlled reaction front during middle to late diagenesis.

Porosity and Mineralogy of a CO_2 Reservoir

The reaction front in this study is located along a porous and permeable cross-bed set and has a roll front geometry. It likely precipitated according to the two fluid model

EVENT					
Deposition	[Solid black bar]				
Dolomite and gypsum precipitate	[Solid black bar]				
Laramide Orogeny	[Dashed line]				
CO ₂ , hydrocarbon-charged fluid infiltrates	[Dashed line]				
Carbonate, clays precipitate	[Dashed line]				
Meteoric water infiltrates	[Dashed line]				
Reaction front precipitates	[Dashed line]				
DIAGENETIC STAGE	early	middle		middle-late	late
PERIOD	Jurassic		Tertiary		Quaternary

Figure 1.9. Paragenetic diagram of diagenetic dolomite, clay and iron (oxyhydr)oxide precipitation, as well as tectonic and fluid flow events in Justensen Flats.

(e.g., Chan et al., 2000; Parry et al., 2004) where an oxidizing fluid diffuses into an iron-bearing reducing fluid and precipitates iron (oxyhydr)oxides. The greatest amount of iron was precipitated at the vanguard of the front, supported by WRA data that show a decrease in iron wt% over the length of the reaction front. There is a high concentration of hematite in the red ledge, as shown by XRD data, and the yellowish brown cement contains both hematite and goethite.

The presence of kaolinite and illite suggests that K-feldspar dissolution has occurred. CO₂ would drive the pH down and increase the dissolution of K-feldspar (Parry et al., 2007). However, K-feldspar is only ~5 wt.% of the Navajo Sandstone (Parry et al., 2007) and the dissolution of dolomite under acidic conditions would produce bicarbonate, consume H⁺ and buffer the acid. Therefore, although the precipitation of

clay minerals has occurred, it has not done so in sufficient amounts to significantly affect porosity and permeability in the unit based on QEMSCAN and petrography data. The Navajo Sandstone typically exhibits ~20-25% porosity (Lindquist, 1988; Potter, 2009). Porosity in the fossil reservoir at Justensen Flats is significantly less (6.8%) and pore space is primarily filled by dolomite evidenced in QEMSCAN analysis.

Conclusions

The reaction front in the Justensen Flats area of the San Rafael Swell represents a late stage diagenetic event where an oxidizing fluid diffused into a CO₂-charged reservoir. The reservoir fluid was likely reducing due to the presence of hydrocarbons (present in modern Navajo Sandstone reservoir fluids both to the east and west of the study area). The reducing fluid contained some ferrous iron. Some iron was already incorporated into an earlier dolomite phase and was not available to precipitate as iron (oxyhydr)oxide. Illite, kaolinite and dolomite likely precipitated from the dissolution of K-feldspar in CO₂-charged waters, although the small amount of K-feldspar has not produced enough of these clays to significantly affect reservoir porosity and permeability. Dolomite precipitation significantly reduced original porosity.

Our new comparative study shows a marked contrast in the mineralogy and chemistry between the northern San Rafael Swell region and the southern Utah region of previous studies (Table 1.1). The Navajo Sandstone in the Grand Staircase Escalante National Monument (GSENM) typically lacks calcite or dolomite (except in sabkha/wadi deposits) and gypsum. We suggest that the calcite and dolomite precipitated from a

locally CO₂-charged aquifer in the northern San Rafael Swell region that differs significantly from the precipitating fluid chemistries in southern Utah.

In the San Rafael Swell, dolomite (with iron) precipitated independently of the iron oxide/ oxyhydroxide phases and has not subsequently oxidized to Fe³⁺ phases. This study shows that the chemistry of reservoir fluids varies substantially both spatially and temporally in the porous and permeable Navajo Sandstone.

Our results suggest that CO₂ injection into a saline sandstone aquifer would precipitate abundant dolomite, particularly if enough feldspar was present to buffer the acidity and abundant calcite and magnesium were in solution.

Acknowledgements

This work was supported in part by a Utah Geological Survey grant (#110398) to Si-Yong Lee and Jessica Allen. This work was also supported in large part by a U.S. Department of Energy grant (to Brian J. McPherson) managed by the DOE National Technology Laboratory, project DE-FE0001812. The authors thank William T. Parry for his help with the manuscript and interpreting the XRD data and E.U. Petersen for providing guidance with the manuscript. We acknowledge Peter Mozley and an anonymous reviewer for insightful critiques that refined the manuscript.

References

- Allis, R.G., Chidsey, T., Gwynn, W., Morgan, C., White, S.P., Adams, M. and Moore, J., 2001, Natural CO₂ reservoirs on the Colorado Plateau and Southern Rocky Mountains: candidates for CO sequestration, Proc. 1st National Conference on Carbon Sequestration, May 14-17, 2001, Washington DC.
- Armitage P.J., Worden R.H., Faulkner D.R., Aplin A.C., and Butcher A.R., 2010, Diagenetic and sedimentary controls on porosity in Lower Carboniferous fine-grained

- lithologies, Krechba Field, Algeria: A petrological study of a caprock to a carbon capture site: *Marine and Petroleum Geology*, v. 27, p. 1395-1410.
- Baer, J. L., and Rigby, J. K., 1978, Geology of the Crystal Geysers and environmental implications of its effluent, Grand County, Utah: *Utah Geology*, v. 5, no. 2, p. 125-130.
- Beitler, B., Chan M.A. and Parry W.T. 2003, Bleaching of Jurassic Navajo Sandstone on Colorado Plateau Laramide highs; Evidence of exhumed hydrocarbon supergiants?: *Geology*, v. 31, no. 12, p. 1041-1044.
- Beitler, B., Parry, W. T., and Chan, M. A., 2005, Fingerprints of fluid flow; chemical diagenetic history of the Jurassic Navajo Sandstone, southern Utah, U.S.A: *Journal of Sedimentary Research*, v. 75, no. 4, p. 547-561.
- Blakey, R.C., Peterson, F. and Kocurek G., 1988, Synthesis of late Paleozoic and Mesozoic eolian deposits of the western interior of the United States: *Sedimentary Geology*, v. 56, p. 3-125.
- Blakey, R.C., 1994, Paleogeographic and tectonic controls on some lower and middle Jurassic erg deposits, Colorado Plateau. In: *Mesozoic Systems of the Rocky Mountain Region, U.S.A.* (eds. M.V. Caputo, J.A. Peterson & K.J. Franczyk) SEPM, Rocky Mountain Section, pp.273-298.
- Bowen, B., Martini, B. A., Chan, M. A., and Parry, W. T., 2007, Reflectance spectroscopic mapping of diagenetic heterogeneities and fluid-flow pathways in the Jurassic Navajo Sandstone: *AAPG Bulletin*, v. 91, no. 2, p. 173-190.
- Burnside, N. M., 2010, U-Th dating of travertines on the Colorado Plateau: implications for the leakage of geologically stored CO₂. PhD Thesis: University of Glasgow, 290 p.
- Chan, M., Parry, W. T., and Bowman, J. R., 2000, Diagenetic hematite and manganese oxides and fault-related fluid flow in Jurassic sandstones, southeastern Utah: *AAPG Bulletin*, v. 84, no. 9, p. 1281-1310.
- Chidsey, T.C. Jr., Hartwick, E. E., Johnson, K. R., Schelling, D. D., Sbarra, R., Sprinkel, D. A., Vrona, J. P. and Wavrek, D. A., 2011, Petroleum geology of Providence oil field, central Utah thrust belt. In: *Sevier thrust belt: northern and central Utah and adjacent areas* (eds. Sprinkel, D.A., Yonkee, W.A., and Chidsey, T.C., Jr.): Utah Geological Association Publication 40, p. 213-231.
- Clark, R. N., 1995, Reflectance Spectra in Ahrens, T. J., ed., AGU Reference Shelf 3, *Rock Physics and Phase Relations, A Handbook of Physical Constants*: Washington, American Geophysical Union, p. 178-188.

- Clark, R.N., Swayze, G.A., Wise, R., Livo, E., Hoefen, T., Kokaly, R. and Sutley, S.J., 2007, USGS digital spectral library splib06a: U.S. Geological Survey, Digital Data Series 231.
- Drever, J.I., 1997. The geochemistry of natural waters : surface and groundwater environments Upper Saddle River, NJ: Prentice Hall, 436 p.
- Dubacq, B., Kampmann, N., Assayag, N., Wigley, M., Bickle, M., 2011, CO₂ degassing and groundwater mixing in the Navajo Aquifer, Green River, Utah: *Mineralogical Magazine*, v. 75, p. 786-786.
- Eichhubl, P., Taylor, W. L., Pollard, D. D., and Aydin, A., 2004, Paleo-fluid flow and deformation in the Aztec Sandstone at the Valley of Fire, Nevada; evidence for the coupling of hydrogeologic, diagenetic, and tectonic processes: *Geological Society of America Bulletin*, v. 116, no. 9-10, p. 1120-1136.
- Heath, J. E., Lachmar, T. E., Evans, J. P., Kolesar, P. T., and Williams, A. P., 2009, Hydrogeochemical characterization of leaking, carbon dioxide-charged fault zones in east-central Utah, with implications for geological carbon storage: *Geophysical Monograph*, v. 183, no. 0065-8448, 0065-8448, p. 147-158.
- Kampmann, N., Bickle, M., Becker, J., Assayag, N., and Chapman, H., 2009, Feldspar dissolution kinetics and Gibbs free energy dependence in a CO₂-enriched groundwater system, Green River, Utah: *Earth and Planetary Science Letters*, v. 284, no. 3-4, p. 473-488.
- Lindquist, S. J., 1988, Practical characterization of eolian reservoirs for development: Nugget Sandstone, Utah-Wyoming thrust belt: *Sedimentary Geology*, v. 56, p. 315-339.
- Lu, P., Fu, Q., Seyfried, W.E., Jr., Hereford, A., Zhu, C., 2011, Navajo Sandstone-brine-CO₂ interaction; implications for geological carbon sequestration: *Environmental Earth Sciences*, v. 62, p. 101-118.
- McPherson, B.J. and Cole, B.S., 2000, Multiphase CO₂ flow, transport and sequestration in the Powder River Basin, Wyoming, USA: *Journal of Geochemical Exploration*, v. 69-70, p. 65-69.
- Nielsen, G., Chan, M.A., and Petersen, E.U., 2009, Diagenetic coloration facies and alteration history of the Jurassic Navajo Sandstone, Zion National Park and vicinity, southwestern Utah: in Tripp, B.T., Krahulec, K., and Jordan, J.L., eds., *Utah Geological Association Publication 38, Geology and Geological Resources and Issues of Western Utah*, CD-ROM.

- Nielsen, G., and Chan, M.A., 2009, Mapping, architecture, and spatial correlation of diagenetic coloration facies, Jurassic Navajo Sandstone, Snow Canyon State Park, southwestern Utah, in Tripp, B.T., Krahulec, K., and Jordan, J.L., eds., Utah Geological Association Publication 38, Geology and Geological Resources and Issues of Western Utah, CD-ROM
- Parry, W. T., Chan, M. A., and Beitler, B., 2004, Chemical bleaching indicates episodes of fluid flow in deformation bands in sandstone: AAPG Bulletin, v. 88, no. 2, p. 175-191.
- Parry, W., Forster, C., Evans, J., Bowen, B., and Chan, M., 2007, Geochemistry of CO₂ sequestration in the Jurassic Navajo Sandstone, Colorado Plateau, Utah: Environmental Geosciences, v. 14, no. 2, p. 91-109.
- Parry, W.T., Chan, M.A. and Nash, B.P., 2009, Diagenetic characteristics of the Jurassic Navajo Sandstone in the Covenant oil field, central Utah thrust belt: AAPG Bulletin, v. 93, p. 1039-1061.
- Potter, S. L., 2009, Characterization of Navajo Sandstone Hydrous Ferric Oxide Concretions Master's thesis: University of Utah, 180 p.
- Potter, S. L., and Chan, M. A., 2011, Joint controlled fluid flow patterns and iron mass transfer in Jurassic Navajo Sandstone, Southern Utah, USA: Geofluids, v. 11, no. 2, p. 184-198.
- Potter, S. L., Chan, M., Petersen, E., Dyar, M. D., and Sklute, E., 2011, Characterization of Navajo Sandstone Concretions: Mars comparison and criteria for distinguishing diagenetic origins: Earth and Planetary Science Letters, v. 301, p. 444-456.
- Seiler, W. M., 2008, Jurassic Navajo Sandstone of Coyote Buttes, Utah/Arizona: Coloration and diagenetic history, preservation of a dinosaur trample surface, and a terrestrial analog to Mars: Master's thesis: University of Utah, 238 p.
- Shipton, Z. K., Evans, J. P., Kirschner, D., Kolesar, P. T., Williams, A. P., and Heath, J., 2004, Analysis of CO₂ leakage through "low-permeability" faults from natural reservoirs in the Colorado Plateau, east-central Utah: Baines, S.J. and Worden, R.H. (eds), Geological Society, London Special Publications, v. 233, no. 0305-8719, p. 43-58.
- Smith, H. J., Fahrenkamp-Uppenbrink, J., and Coontz, R., 2009, Carbon capture and sequestration: Science, v. 325, no. 5948, p. 1641.
- Wilkinson M., Gilfillan, S.M., Haszeldine, S.R., Ballentine, C.J., 2008, Plumbing the depths: Testing natural tracers of subsurface CO₂ origin and migration, Utah, USA.

In Carbon dioxide sequestration in geological media, 59, J. C. M. Grobe, Pashin, and R. L., Dodge (eds.). AAPG Studies.

CHAPTER TWO

EVALUATING THE ROLE OF ORGANICS, MINERALOGY AND PETROPHYSICAL PROPERTIES ON EARLY DIAGENESIS AND CONCRETION FORMATION IN VOLCANICLASTIC HOST ROCK COMPOSITION

Sally L. Potter-McIntyre, Marjorie A. Chan and Brian J. McPherson

Submitted: Journal of Sedimentary Research

Abstract

The Brushy Basin Member of the Jurassic Morrison Formation was deposited in an ephemeral alkaline saline lake system with copious input of volcanic ash that resulted in a highly reactive chemical system during early diagenesis. Three broad diagenetic facies defined by iron oxidation states are interpreted: oxidized, intermediate and reduced. Diagenetic facies reflect controls of original, depositional, meter-scale paleotopography; oxidized facies represent shallow water to subaerial conditions and reduced facies reflect deeper water deposition. Three categories of concretions are characterized based on mineralogy: carbonate, iron (oxyhydr)oxide and phosphate concretions. Comparisons of concretion and host rock chemistry show that most concretion examples are enriched in calcium, iron and manganese by ~ 100%, but only carbonate concretions in more permeable, relatively coarse-grained sandstone channels

are greatly enriched (>>100%) in calcium, manganese and strontium relative to the host rock. Variation in concretion mineralogy and morphology within the Brushy Basin Member suggests alkaline saline fluid chemistries create diagenetic microenvironments within a larger lake system to affect concretion precipitation. However, petrophysical properties of porosity and permeability are more important factors affecting concretion size, morphology, and even mineralogy than host rock composition. Diagenetic fluid-rock interactions in volcanoclastic sediments reacting with alkaline saline fluids can be quite spatially variable, even on an outcrop scale. Broader diagenetic questions of iron cycling and concretion formation on a pore- to outcrop-scale are illuminated for both Earth and Mars in similar volcanoclastic, iron-rich sediments of the Burns formation.

Introduction

Concretions are cemented mineral masses that form in sedimentary rocks during diagenesis. Cement mineralogies include ferric and ferrous iron minerals, carbonate minerals, quartz and apatite. Concretions form in a variety of lithologies and host rock compositions from fine- to coarse-grained clastic rocks and in chemical sedimentary rocks (Clifton, 1957; Raiswell, 1976; Coleman and Raiswell, 1981, 1995; Selles-Martinez, 1996; Chan et al., 2000; Raiswell et al., 2000; Seilacher, 2001; Mozley and Davis, 2005; Lyons et al., 2007; Potter et al., 2011). Concretion geometries range from spherical/spheroidal forms to irregular masses to elongate pipes (Chan et al., 2000; Potter and Chan, 2011). Although small (mm-scale) spheroidal forms are the most common, concretions and concretionary masses vary in size from millimeters to meters in diameter (Chan et al., 2000; 2011; Potter and Chan, 2011; Potter et al., 2011).

Carbonate concretions have been intensely studied and two end member models describe growth (e.g., Raiswell et al., 2000). Radial growth occurs when a nucleus – such as organic matter or a smaller mineral mass – provides a kinetically favorable site to initiate crystal growth. Concretions then grow in a radially expansive manner. Radial concretions typically exhibit concentric layers. Pervasive growth in both carbonate and iron (oxyhydr)oxide concretions results when crystals nucleate concurrently either throughout the concretion or in just the rinds (as in some concretions with depleted centers; Potter et al., 2011). This concurrent nucleation of crystals sets the radius of the concretion and some porosity is retained. Subsequent precipitation events partially or completely fill the retained porosity (Dickson and Barber, 1976; Hudson, 1978; Jordan et al., 1992; Huggett, 1994; Raiswell et al., 2000; Potter et al., 2011). Pervasive growth concretions exhibit multiple generations of isopachous cement under petrographic examination (Feistner, 1989; Mozley, 1989; Raiswell et al., 2000; Seilacher, 2001; Potter et al., 2011). These two models of radial and pervasive are end members and concretions can grow by a combination of these mechanisms and may also result from precursor minerals where rinds of a set radius may be partly determined by the amount of reactants (e.g., iron) available from the altered or "consumed" precursor mineral (Chan et al., 2012).

Concretions are prevalent throughout the geologic record on Earth and concretion formation is likely a common process when solute-rich waters move through sedimentary rocks on other planets as well. In 2004, the Mars Exploration Rover, Opportunity, returned images of putative hematite concretions ("blueberries") in the Burns formation at Meridiani Planum, Mars (Squyres et al., 2004; Grotzinger et al., 2005; McLennan et

al., 2005). Although, nonconcretion chemical analog models were proposed to explain the spherules (e.g., Mauna Kea spherules produced by acid sulfate precipitation; Morris et al., 2005; Golden et al., 2008), the nonconcretion models do not exhibit abundant physical similarities to the features observed on Mars (see Potter et al., 2011 for elaboration). Comparative studies of the Navajo Sandstone concretions with the Mars spherules show a preponderance of physical similarities and a physical formation model for both terrestrial and martian concretions is proposed (Chan et al., 2004, 2005; Potter et al., 2011; Chan et al., 2012). However, the Navajo Sandstone host rock is a clean quartz arenite and the Burns formation is a sulfate-rich sandstone with acidic fluids, so the question remains, “How does a chemically reactive host rock composition affect concretion formation?” Sulfate-rich sandstones are uncommon on Earth, but this new study examines concretions in a chemically reactive host rock where fluid-rock interactions may have a great effect on concretion formation processes to better understand diagenetic complexities. The Brushy Basin Member provides an excellent analog formation for the study of early diagenesis in an iron-rich shale that records the action of alkaline saline fluid chemistries reacting with clastic sediments and volcanic ash.

Purpose of Study

The purpose of this research is to detail specific factors, such as reactive sediments, organic influences and grain size that affect concretion formation and iron mobilization and precipitation. Three main questions are investigated:

1. What effect does host rock composition have on concretion mineralogy and formation?

2. What are the relationships between concretion formation and organic influences such as burrows, root traces and dinosaur bones?
3. What effect do host rock properties – petrophysical characteristics such as grain size, porosity and permeability – have on sphericity, size and distribution of concretions?

We document authigenic minerals associated with macroscopic organic features and diagenetic facies, paying particular attention to the iron-bearing minerals. Although macroscopic organic features are not present on Mars, these obvious and clearly defined features in the Brushy Basin Member provide a starting place to characterize organic influence on iron precipitation.

Herein, this study examines concretion sizes, morphologies and mineralogies. We characterize the distribution of concretions, compare stratigraphic distribution of organics and concretions, and interpret timing of diagenetic features. Lastly, we compare the Brushy Basin Member concretions, the Navajo Sandstone concretions from southern Utah and the Burns formation concretions at Meridiani Planum, Mars to evaluate the effects of mineralogical and physical host rock composition on concretion formation.

Study Area

The Brushy Basin Member of the Jurassic Morrison Formation ranges from ~45 to 120 m thick and is a widespread, fine-grained unit that covers the Colorado Plateau and extends from New Mexico in the south to Wyoming in the north; equivalent strata extend into Canada (Turner and Peterson, 2004). On the Colorado Plateau, the upper part of the unit is interpreted as ephemeral, alkaline saline lake deposits (Turner and Fishman, 1991). A volcanically active back-arc basin existed to the west during deposition and

copious input of volcanic ash resulted in chemically reactive, siliceous tuffaceous sediments (Turner and Fishman, 1991; Peterson, 1994; Turner and Peterson, 2004).

Altered clay mineral zones present in tuffs have a bull's eye pattern centering on the Four Corners region of the Colorado Plateau (Turner and Fishman, 1991; Figure 2.1). From margin to center, the clay mineral zones are smectite, clinoptilolite, analcime and albite (Table 2.1). These zones represent early diagenetic alteration in an alkaline, saline, groundwater-fed lake system named Lake T'oo'dichi' with the most intensive alteration of ashes occurring in the basinal center (Turner and Fishman, 1991). Clay mineral zones occur in altered tuffs, but these clay mineral assemblages are typically not present in the abundant siltstone and claystone lithofacies (Turner and Fishman, 1999).

Methods

Eight outcrops from the basinal center to the periphery of ancient Lake T'oo'dichi' deposits were studied and sampled (Figure 2.1). Four stratigraphic sections (35 to 60 m thick) were measured in detail. Particular attention was paid to the stratigraphic context and size of concretions as well as obvious, macroscopic biological influences (e.g., bioturbation, dinosaur and plant fossils, reduction halos/ root traces, charophyte molds). Concretion (n=42) and host rock samples (n=66) were collected for comparisons of mineralogy, petrophysical characteristics and chemical analysis. Representative samples (n=37) were powdered and analyzed with a Rigaku x-ray diffractometer from 2-65 °2θ to determine mineralogy. Oriented samples were not analyzed because the clay mineralogy has already been extensively studied (Turner and Fishman, 1991).

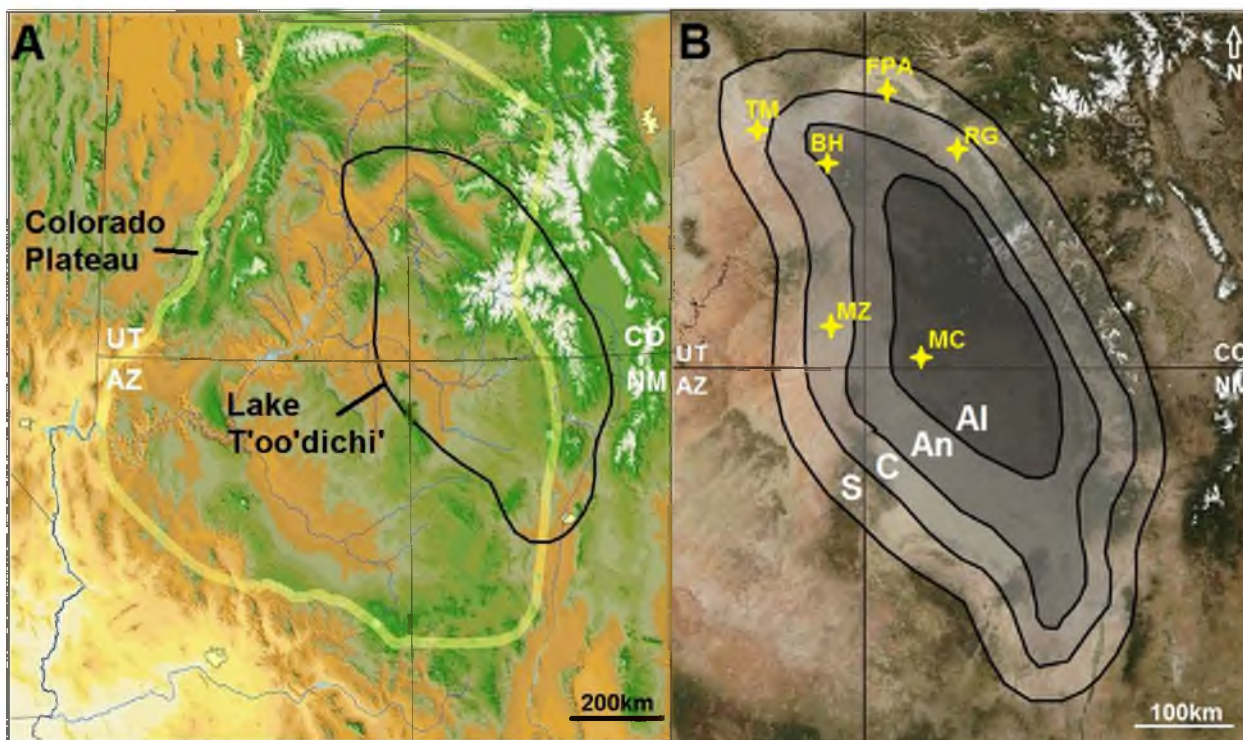


Figure 2.1. Study area of the upper Brushy Basin Member of the Morrison Formation. A. Colorado Plateau with outline of interpreted alkaline saline, paleo Lake T'oo'dichi'. B. Map shows outline of Lake T'oo'dichi' and study sites (in yellow font). TM = Ten Mile Graben, FPA = Fruita Paleo Area (representing outcrops at Fruita Paleo Area and Callison Quarry), BH = Blue Hills, RG = Rattlesnake Gulch, MZ = Montezuma Creek, MC = McElmo Canyon. Sections were measured at MZ, FPA and two sections were measured at BH.

Table 2.1. Lithofacies, clay mineral zones, and diagenetic facies. Munsell rock colors are given in parentheses.

FACIES	NAME	DESCRIPTION
Lithofacies	Siltstone	Laminated and/or bioturbated
	Claystone	Tuffaceous laminated to massive
	Sandstone	Cross-bedded to massive
Clay Mineral Zones* (present only in tuffs)	Smectite	2-25 cm thick lenses of greenish gray to white tuff
	Clinoptilolite	Distinctive orange-pink tuffs
	Analcime +/- K feldspar	Grayish green to dark green tuff
	Albite	Well-indurated, grayish green to pale orange-brown tuff
Diagenetic Facies	Oxidized	Dark red (5R3/4, 2/6) to purple (5P2/2) siltstone and claystone
	Intermediate	Interbedded gray (5Y6/1), orange (10YR8/6), light red (10R6/6) and
	Reduced	Green (5G7/2, 7/4, 6/6) to gray (10G8/2, N6) siltstone, claystone and sandstone

*From Turner and Fishman (1999)

QEMSCAN (Quantitative Evaluation of Minerals using Scanning electron microscope) produced mineralogical images of samples. Two samples of carbonate concretion-bearing rock (MC1, RG1), one sample of a phosphate concretion (MZ18) and the adjacent host rock (MZ17) and one sample of a claystone with mineralized, 1 by 2 mm charophyte molds (MZ3) were selected for analysis. Approximately 5 by 8 mm areas of the five polished thin sections were evaluated. Samples MZ17 and MC1 were analyzed at a 2 µm pixel spacing, samples MZ3 and MZ18 were analyzed at a 5 µm pixel spacing, and sample RG1 was analyzed at a 3 µm pixel spacing. Minor adjustments were made to the Species Identification Protocol (SIP) created for mudrocks by FEI (the QEMSCAN software company) to better identify minerals typically present in the Brushy Basin

Member (identified via XRD and from the literature) such as albite, clinoptilolite and analcime. A generic zeolite definition was added to capture zeolites that did not classify as clinoptilolite or analcime.

Whole rock analysis (WRA) was performed by ALS Chemex on concretion (n=25) and host rock (n=16) samples. Statistical methods (discussed in Results) tested for similarities and differences between chemistries of different facies and between concretions and host rock samples.

Results

Measured Sections

Throughout the four measured sections (Appendix F; Table 2.1), lithologies are fairly homogenous with grain sizes predominately ranging between clay and silt. Siltstone and claystone lithofacies are the most common. The siltstone facies contain clay and are typically tuffaceous and laminated. A bioturbated, massive siltstone lithofacies is present. Likewise, the claystone facies contain some silt, are also typically tuffaceous and laminated, and bioturbation that destroys primary bedding produces a massive claystone lithofacies. Local fine sand lenses are between ~1-5 m in length, are less than 2 m high and are typically cross-bedded. Some sandstone lenses are bioturbated and massive. Poorly developed paleosols are present in the upper parts of some sections, but are not common. Paleosols are typified by slickensides and blocky structures.

The variegated coloration of the Brushy Basin Member indicates the important role of iron in diagenetic reactions. Diagenetic facies are broadly classified as reduced, oxidized or intermediate based on iron oxidation state; however, measured section

diagrams show detailed schematic rock colors (Table 2.1). Reduced facies are green to gray colors (see Table 2.1 for Munsell colors). Oxidized facies are dark red to very dusky purple in color. Intermediate facies are typically interbedded and contain light olive gray, pale yellowish orange, moderate reddish orange or grayish yellow rocks. Diagenetic facies are not laterally persistent and vary horizontally within an outcrop cutting across primary lithofacies (Figure 2.2).

Diagenetic facies exhibit specific types of bioturbation. Large burrows and root traces are mostly present in the oxidized facies and exhibit reduction halos; however, some root traces with oxidized halos are present in the reduced facies. Charophyte molds (most common in the reduced facies) are present in all of the study areas and are preserved with mineral fill (see below for mineralogy).

Petrophysical Characteristics and Mineralogy

Petrographic analysis shows the primary composition of the claystone lithofacies consists of a clay-sized, zeolitic matrix; the siltstone lithofacies has the same matrix, however, it contains silt-sized clasts (Figure 2.3). Detrital grains include quartz, feldspars and biotite. Shards of volcanic ash (~0.1 – 0.3 mm in length) are abundant. Shard morphology ranges from fairly pristine glass fragments with discrete edges to altered and diffuse masses (Figure 2.3).

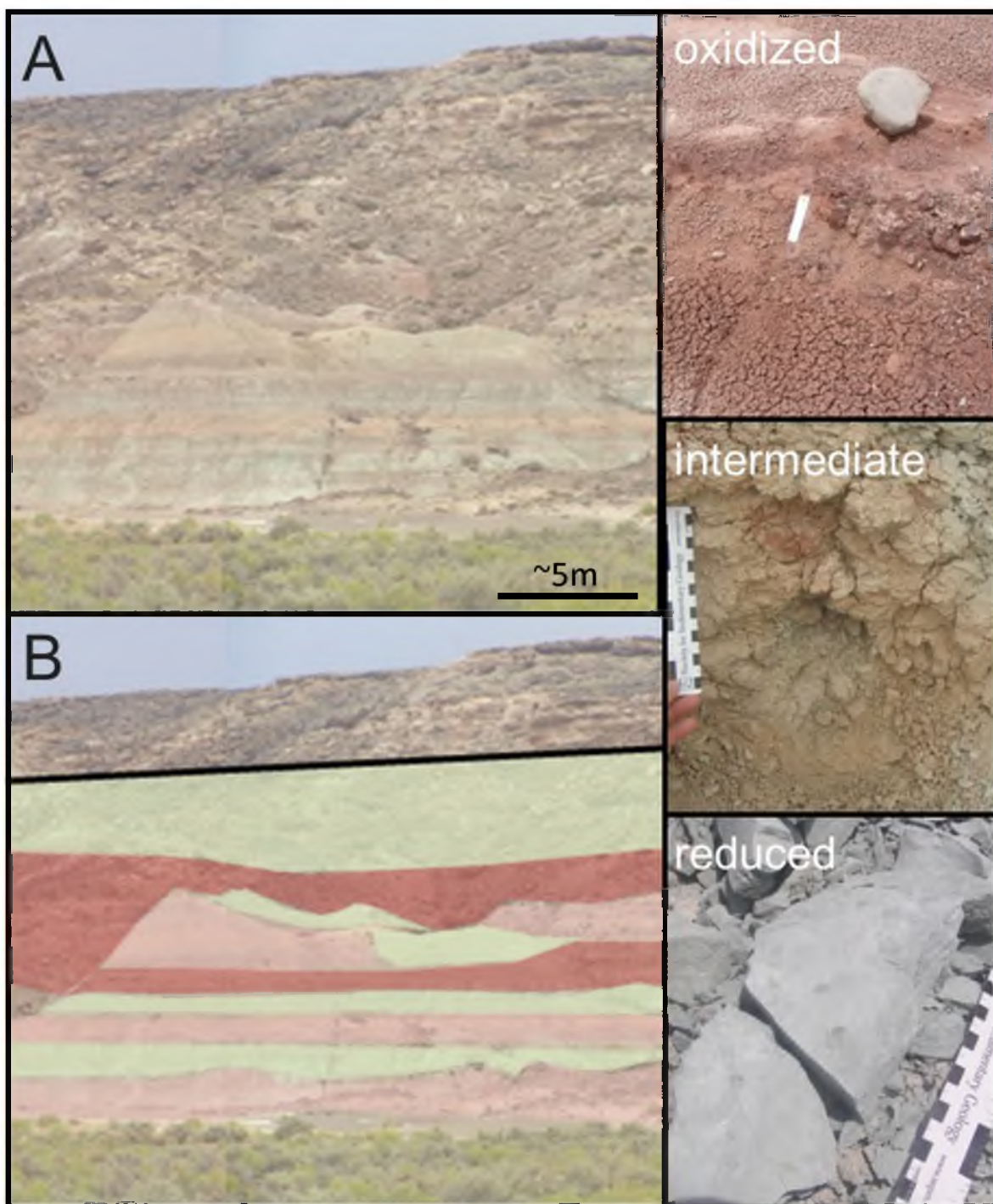


Figure 2.2. Blue Hills study area (A) and diagenetic facies (B). Red = oxidized, pink = intermediate, green = reduced. Outcrop photos of the diagenetic facies are shown on right.

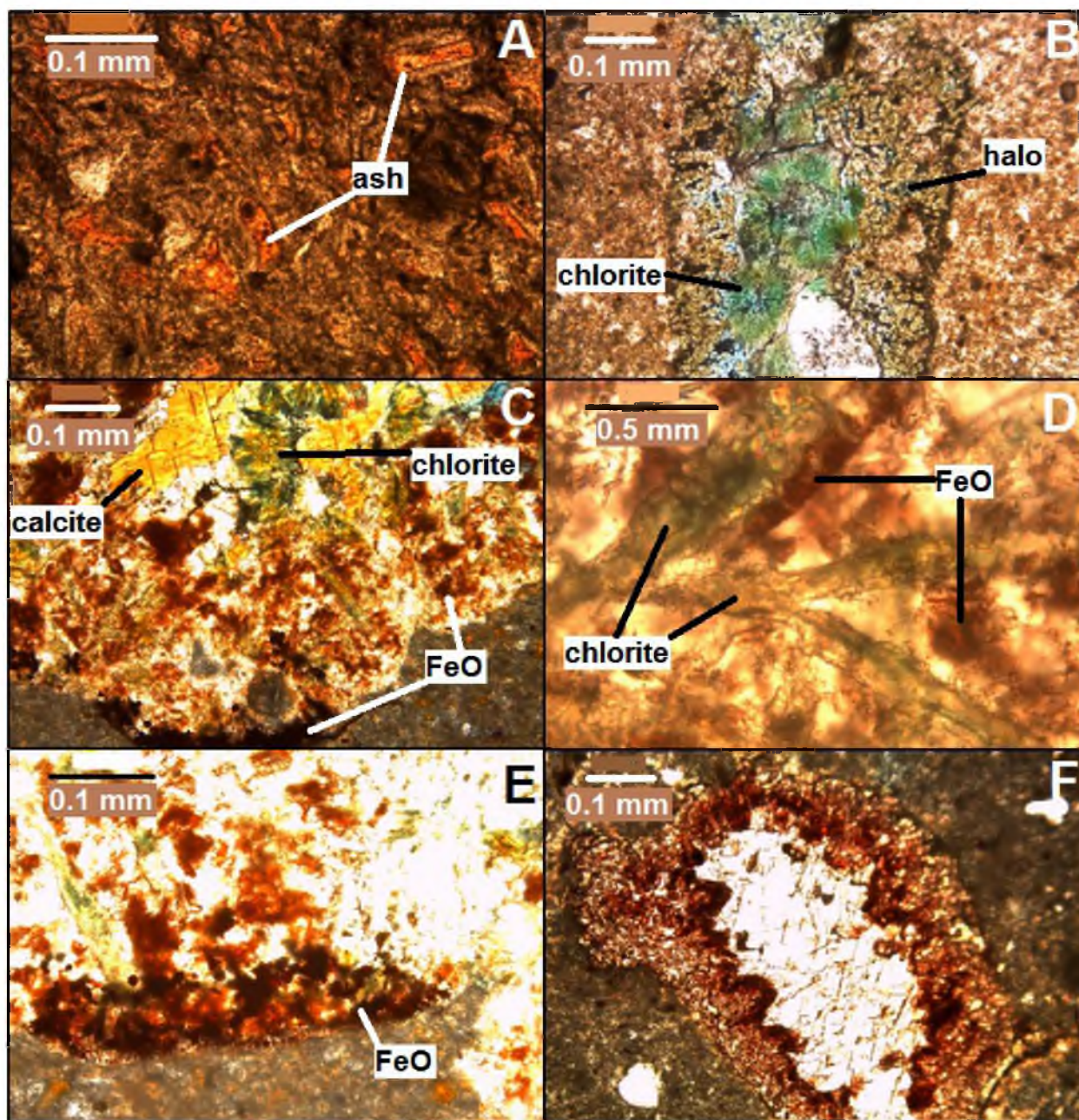


Figure 2.3. Petrographic thin sections of the Brushy Basin Member. A. Volcanic ash shards. B. Vug containing acicular chlorite and surrounded by a reduction halo. C. Vug with acicular chlorite, calcite, and both diffuse and spheroidal iron (oxyhydr)oxide. D. Iron (oxyhydr)oxide overprinted on chlorite laths. E. Iron (oxyhydr)oxide spheres along edge of vug. F. Vug contain a rim of iron (oxyhydr)oxide and filled with albite.

Vugs (charophyte molds) are common and are filled with minerals such as anhedral (massive) albite and calcite (Figure 2.3). Euhedral chlorite commonly overprints both albite and calcite; crystals exhibit either radiating acicular or lath-shaped habits (Figure 2.3). Iron (oxyhydr)oxides in diffuse to granular forms or in euhedral spheres typically rim the vugs (Figure 2.3). Thin iron (oxyhydr)oxide coatings overprint some chlorite laths (Figure 2.3).

QEMSCAN images show maps of *in situ* mineralogy; area percent of minerals and porosity are also reported (Figure 2.4, Table 2.2). Porosity is 2-4% in the siltstone lithofacies (MZ17, MZ18) and 12- 17% in the sandstone lithofacies (MC1, RG1). The porosity in the claystone sample with the charophyte molds is 0.3% (MZ3).

Authigenic minerals reported with QEMSCAN are albite, analcime, apatite, barite, calcite, chlorite, clinoptilolite, iron (oxyhydr)oxides, kaolinite and smectites (Figure 2.4). Quartz, feldspars and biotite are classified as detrital. We acknowledge that authigenic quartz overgrowths are visible with a petrographic microscope, and lenses of silcretes are present in the section at Ten Mile Graben; however, quantification of authigenic versus detrital quartz with QEMSCAN is not possible.

Chemistry

Host rock samples and concretion samples are grouped according to oxidized, reduced and intermediate diagenetic facies for statistical analysis (Table 2.3). Single factor ANOVA (analysis of variance) compares the variance between two or more

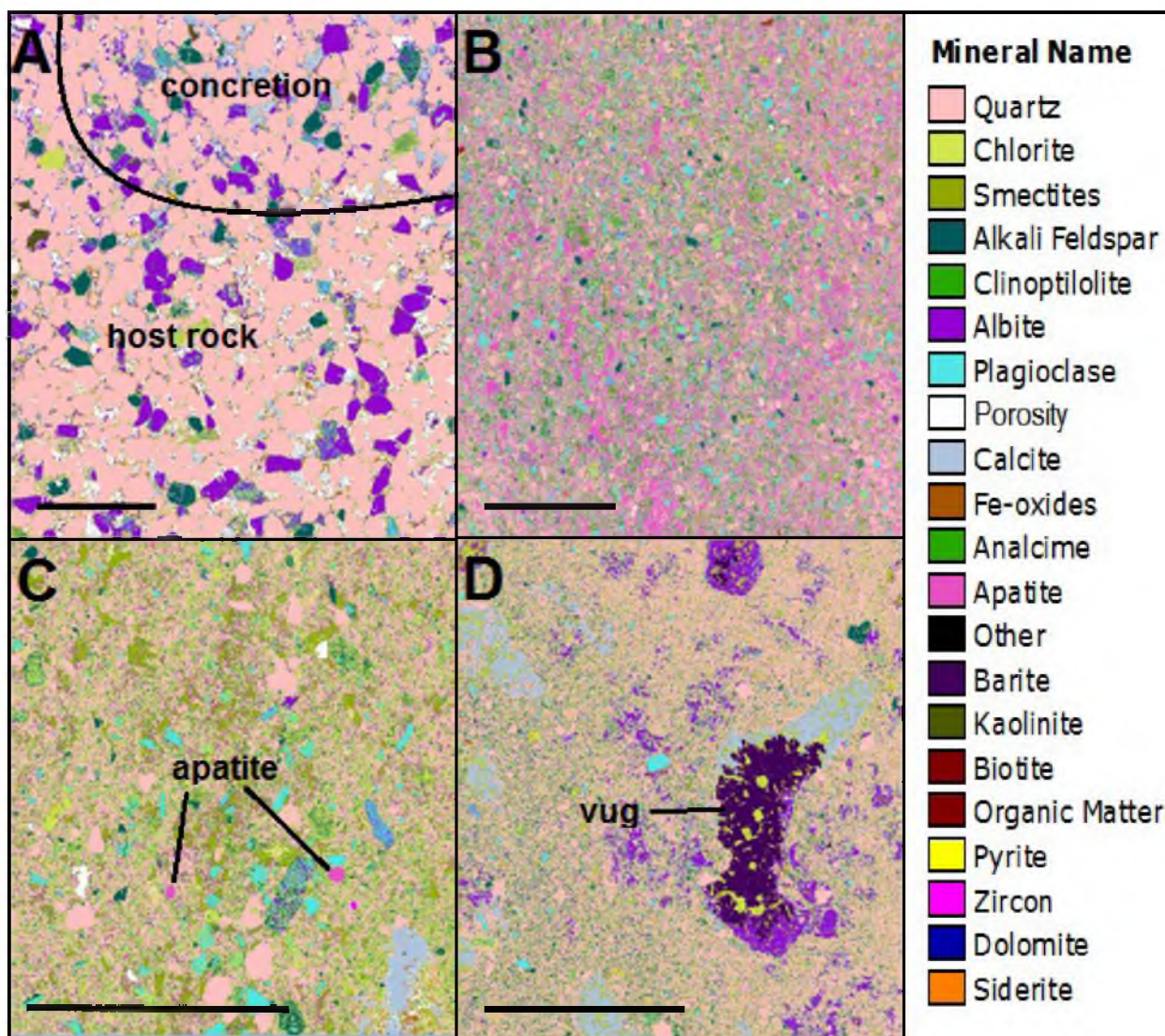


Figure 2.4. QEMSCAN images. Scale bars = 1 mm. A. Carbonate concretion-bearing sandstone (Sample MC1). Black line delineates carbonate cemented concretion from host rock. B. Phosphate concretion (Sample MZ18). Apatite is bright pink color. C. Phosphate concretion-bearing host rock (Sample MZ17). Note discrete apatite grains in bright pink. D. Vug-bearing rock (Sample MZ3). Vug is filled with barite (dark purple), calcite (light blue) and chlorite (green laths).

Table 2.2. Area % of minerals and porosity reported by QEMSCAN.

Carbonate concretion-bearing rocks				Phosphate concretion-bearing rocks				Vug-bearing rock	
RG1		MC1		MZ17		MZ18		MZ3	
Quartz	73.49	Quartz	64.60	Quartz	48.07	Quartz	33.42	Quartz	52.26
Porosity	17.38	Albite	13.37	Chlorite	21.15	Apatite	20.05	Chlorite	15.43
Albite	10.70	Porosity	11.79	Smectites	6.71	Chlorite	14.19	Alkali Feldspar	8.02
Chlorite	5.72	Chlorite	5.20	Alkali Feldspar	6.69	Alkali Feldspar	8.86	Albite	8.01
Alkali Feldspar	3.08	Plagioclase	4.18	Clinoptilolite	6.44	Plagioclase	8.68	Clinoptilolite	4.91
Clinoptilolite	2.55	Alkali Feldspar	3.27	Albite	5.72	Calcite	6.09	Plagioclase	4.33
Plagioclase	1.94	Fe-oxides	3.00	Plagioclase	3.99	Smectites	4.06	Fe-oxides	2.35
Calcite	1.10	Calcite	2.46	Porosity	1.96	Porosity	3.63	Smectites	2.16
Smectites	0.43	Clinoptilolite	1.63	Calcite	0.67	Fe-oxides	2.32	Calcite	1.78
Barite	0.31	Smectites	1.54	Fe-oxides	0.35	Albite	1.81	Barite	0.56
Kaolinite	0.25	Kaolinite	0.44	Analcime	0.07	Clinoptilolite	0.21	Porosity	0.27
Fe-oxides	0.16	Barite	0.18	Apatite	0.06	Analcime	0.11	Biotite	0.08
Biotite	0.08	Apatite	0.04	Other	0.04	Other	0.10	Analcime	0.05
Analcime	0.08	Analcime	0.04	Barite	0.02	Biotite	0.08	Pyrite	0.02
Apatite	0.06	Biotite	0.01	Kaolinite	0.01	Barite	0.02	Apatite	0.02
Other	0.04	Organic Matter	0.01	Biotite	0.01	Organic Matter	0.01	Organic Matter	0.02
Organic Matter	0.02	Other	0.01	Organic Matter	0.01	Kaolinite	0.00	Other	0.01

Table 2.3. Statistical comparison of oxidized, intermediate and reduced diagenetic facies with concretions from the same facies using one-way analysis of variance (ANOVA).

OXIDIZED		INTERMEDIATE		REDUCED	
Groups	P-value	Groups	P-value	Groups	P-value
Al₂O₃		Al₂O₃		Al₂O₃	
Host rock	0.01	Host rock	0.13	Host rock	0.01
Concretions		Concretions		Concretions	
Fe₂O₃		Fe₂O₃		Fe₂O₃	
Host rock	0.88	Host rock	0.19	Host rock	0.29
Concretions		Concretions		Concretions	
CaO		CaO		CaO	
Host rock	0.27	Host rock	0.37	Host rock	0.43
Concretions		Concretions		Concretions	
MgO		MgO		MgO	
Host rock	0.06	Host rock	0.04	Host rock	0.08
Concretions		Concretions		Concretions	
Na₂O		Na₂O		Na₂O	
Host rock	0.00	Host rock	0.23	Host rock	0.83
Concretions		Concretions		Concretions	
K₂O		K₂O		K₂O	
Host rock	0.32	Host rock	0.01	Host rock	0.00
Concretions		Concretions		Concretions	

datasets; a P value <0.05 suggests the datasets are different. We compare host rock diagenetic facies based on amounts of selected elements (iron, aluminum, calcium and manganese) because they are commonly present in clays and because iron, calcium and manganese are typically mobile elements and aluminum is relatively immobile.

Diagenetic facies show no statistically significant difference in variance based on amounts of iron, calcium or manganese. However, a difference in aluminum content between the diagenetic facies is apparent. A subsequent T-test shows a statistical difference between aluminum content in the oxidized and reduced facies (P value [two tailed] = 0.03), but no difference between the aluminum content in the oxidized and intermediate facies (P value [two tailed] = 0.39) or between the intermediate and reduced facies (P value [two tailed] = 0.22).

Weight percent of major oxides plus barium and strontium were averaged for the host rock samples in the oxidized, intermediate and reduced facies. Concretions were grouped according to the diagenetic facies in which they are present (i.e., oxidized concretions are present in oxidized host rock; intermediate concretions are present in intermediate host rock, etc.) Weight percent of the same elements in concretion samples were averaged. Carbonate concretions were grouped separately and compared to reduced host rock because they are typically present only in the reduced diagenetic facies.

Chemical species normalized to aluminum (as a proxy for clay content) and expressed in scatterplots determine enrichment or depletion of species in concretions relative to the host rock (Figure 2.5). In the oxidized facies, aluminum behaves coherently with strontium and sodium; concretions are slightly enriched ($<50\%$) in magnesium. Oxidized concretions are $\sim 100\%$ (two times) enriched in barium and

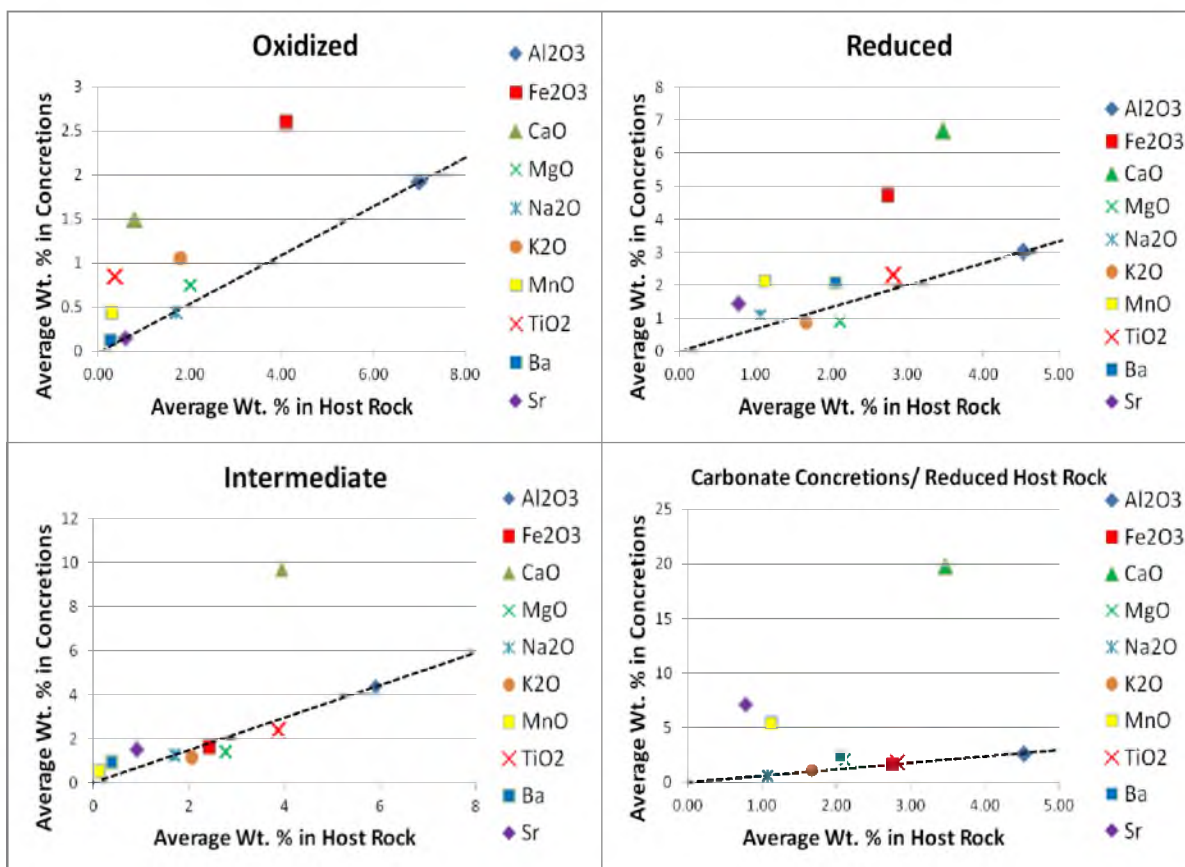


Figure 2.5. Major ion concentration in concretions versus host rock normalized to aluminum concentration to indicate enrichment/ depletion of elements in concretions relative to the host rock for three diagenetic facies (oxidized, reduced, intermediate). Blue lines indicate 50%; red line indicates 100%.

potassium and > 100% enriched in calcium, iron, manganese and titanium. In the intermediate facies, aluminum behaves coherently with sodium and titanium; iron, magnesium and potassium are <50% depleted. Intermediate concretions are ~100% enriched in manganese, barium and strontium and >100% enriched in calcium. In the reduced facies, potassium and magnesium are slightly depleted (<50%); titanium is slightly enriched (<50%). Reduced concretions are 50% enriched in sodium and barium and >100% enriched in calcium, iron, manganese and strontium. Carbonate concretions compared to reduced host rock exhibit coherence between aluminum, iron, sodium, potassium and titanium; concretions are ~50% enriched in magnesium and barium and >>100% enriched in calcium, manganese and strontium.

Concretions

Concretions are present in all outcrops in this study including sections that were not measured (Montezuma Creek, Blue Hills, Fruita Paleo Area, Ten Mile Graben, Rattlesnake Gulch, McElmo Canyon; Figure 2.1). Three main categories of concretions are documented based on mineralogy (Table 2.4): 1. carbonate concretions, 2. iron (oxyhydr)oxide concretions, and 3. phosphate concretions. These broad categories are further divided into subtypes based on size (small = 1-10 mm; large = 10-100 mm; mega = 100-500 mm). Concretion mineralogy and size vary within an outcrop and even within a stratigraphic horizon such that more than one main category and/or subtype is typically present in an outcrop. Latitudinal ridges on spheroidal concretions (formed along bedding) and self-organized spacing are rare; concretions are typically either clustered (~50% of occurrences) or isolated.

Table 2.4. Concretion types based on mineralogy and size. Subtype is based on color, degree of cementation or morphology.

	Type	Subtype	Detailed Mineralogy	Diagenetic Facies	Location	Size	Morphology
Carbonate	Small	Friable	illite, kaolinite, albite, hematite, siderite, calcite	Reduced sandstone	EC, MC, BH, FP	1mm-10mm	spheroidal
		Well-cemented	calcite, high Mg calcite, dolomite	Reduced siltstone and sandstone	BH, TM, FP	2-10mm	spheroidal to tubular
	Large	Brown	calcite, clinoptilolite	Intermediate claystone	BH	100-120mm	spheroidal to irregular
		White	siderite, analcime, smectite, clinoptilolite	Intermediate claystone	BH	<30mm	spheroidal to oblong
		Green	chlorite, calcite	Reduced claystone	BH	<100mm	spheroidal
Iron (oxyhydr)oxide	Large	Rind	hematite, illite/smectite	Reduced sandstone	FP	30-40mm	spheroidal to elongate
		Green	goethite, ferrihydrite, smectite, clinoptilolite	Intermediate claystone	BH	<100mm	spheroidal to irregular
	Mega	Mega	hematite, goethite, calcite, albite, chlorite	Intermediate siltstone	FP	<500mm	circular
Phosphate	Small	Dark Red	hydroxyl apatite, phosphosiderite, hematite, clinoptilolite, smectite, illite	Reduced and intermediate siltstone	MZ	3-8 mm	spheroidal
	Large	Red	goethite, phosphosiderite, analcime, smectite, clinoptilolite	Intermediate claystone	BH	<70mm	spheroidal to irregular

Carbonate Concretions

Carbonate concretions are the most common; they are present in all outcrops studied and exhibit the most diversity in terms of distribution, morphology, size and companion mineralogy (Table 2.4; Figure 2.6). They are yellowish brown (5YR 5/6, 4/4, 3/4) and spheroidal to elongate. The main cement type is calcite but siderite and hematite are also detected with xray diffraction (XRD). Carbonate concretions are typically associated with reduced facies. Other authigenic host rock minerals include illite, kaolinite, chlorite and albite. Calcite concretions are split into two subtypes based on size: 1. Small concretions are 1-10 mm in diameter, and 2. Large concretions are up to 120 mm diameter.

1. Small concretions: The most common small calcite concretion is weakly cemented and weathers flat along the host rock surface. These friable concretions are 1-10 mm in diameter and spheroidal in shape. This concretion type is concentrated along more permeable, relatively coarser-grained lamina in cross-bedded sandstones and is present in outcrops from the basinal center to the exterior of Lake T'oo'dichi'. This type of concretion has variable mineralogies that include calcite, hematite and siderite. Doublets and triplets (conjoined forms) are present. Concretions exhibit digitate ferroan carbonate cements and euhedral albite laths (Figure 2.7). Some of the ferroan carbonate occurs in spheroidal to irregular blebs. Diffuse iron-rich cement (iron (oxyhydr)oxide and ferroan carbonate) also coats grains and other cement minerals. Grain size of the host rock is silt to fine sand. Well-cemented small concretions weather out of the host rock and collect in

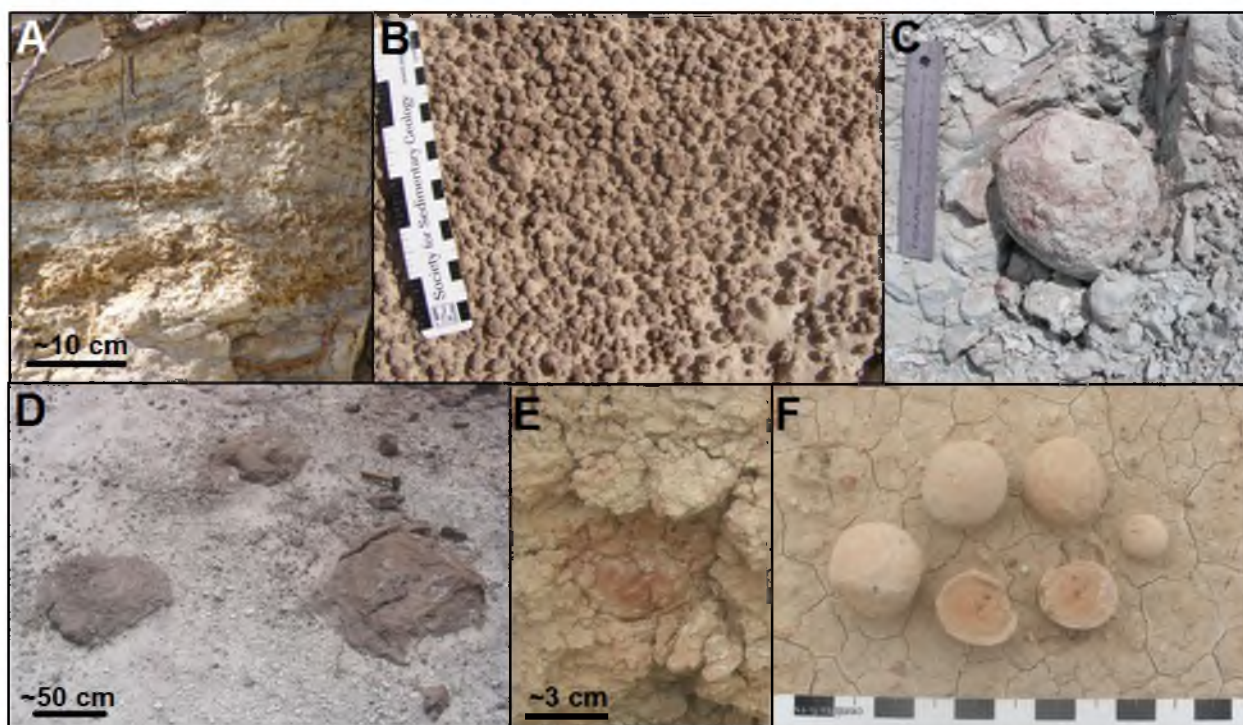


Figure 2.6. Carbonate concretions in the Brushy Basin Member. A. Friable concretions occur along permeable lamina in silty sandstone channel lenses. B. Well-cemented concretions weathered out of host rock and collected in topographic low. C. Large concretion in burrowed green siltstone. D. Mega concretions at Fruita Paleo Area. E. Brown claystone concretion. F. White siderite claystone concretion with apparent nuclei (dark spots in centers) and radial (concentric) growth.

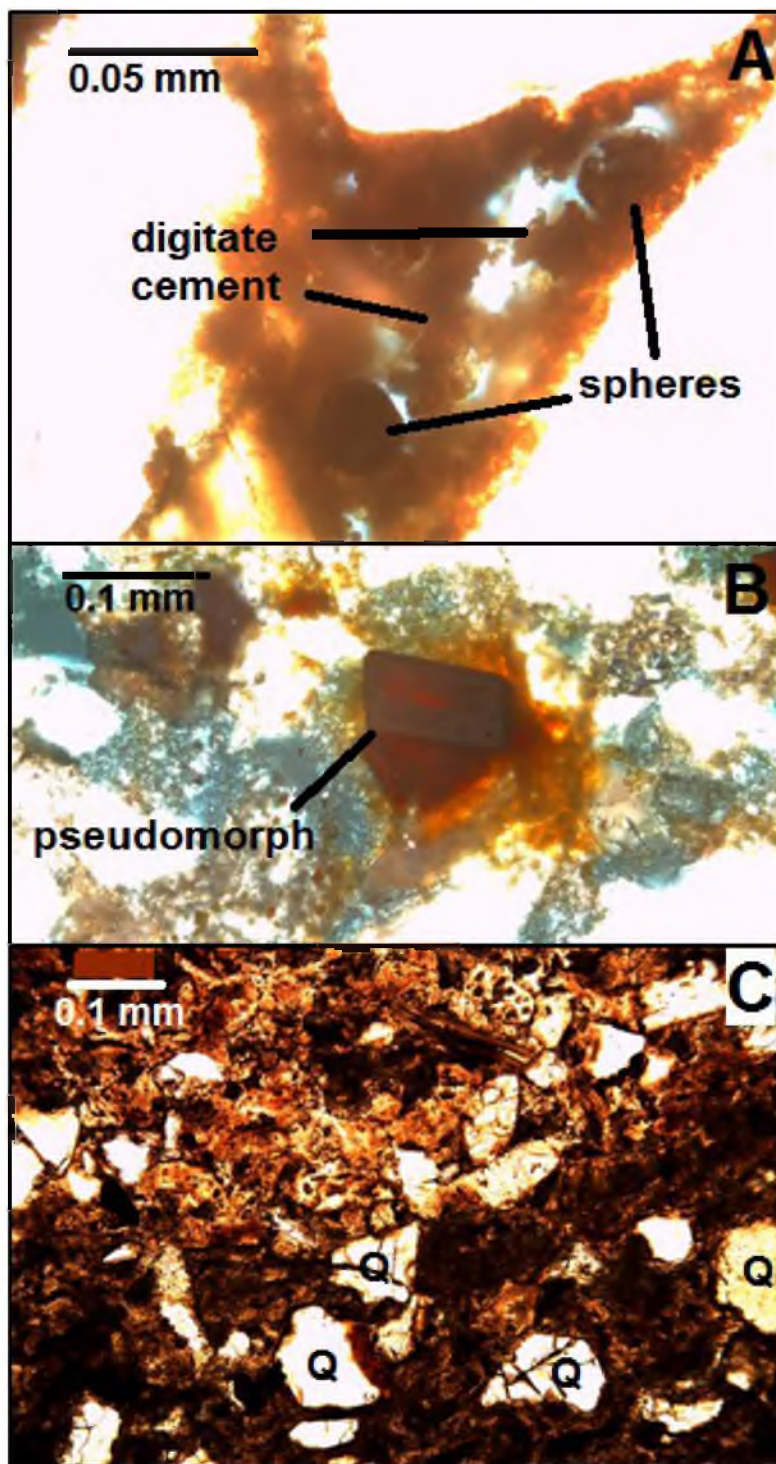


Figure 2.7. Concretion photomicrographs. A. Carbonate concretion in silty sandstone channel exhibits iron carbonate spheroids and digitate cement. B. Iron (oxyhydr)oxide concretion with hematite after pyrite pseudomorphs and diffuse cement. C. Well-cemented phosphate concretion with hydroxyl apatite and iron phosphate (dark cements). Q indicates quartz grains.

topographic lows. These are 2-10 mm in diameter and range in shape from spheroids to elongate tubules up to 3 cm long. They typically exhibit a radiating crystal habit visible in hand sample. These concretions are typically clustered in 0.5-1 m lenses directly above or below more resistant and permeable siltstone or sandstone ledges. They are composed of calcite, high magnesium calcite and dolomite. One collection of weathered out, spheroidal concretions has a mean aspect ratio of 1.20 (n=300). Doublets and triplets (conjoined forms) are present, along with concretions weathered out of the outcrop with adhered host rock still attached. Elongate concretions occur in bioturbated outcrops and preserve burrows.

2. Large concretions: These concretions range from 10-100 mm in diameter and are commonly present in the burrowed, tuffaceous claystone lithofacies and the reduced and intermediate diagenetic facies in the Blue Hills study area (the analcime clay mineral zone of Lake T'oo'dichi'; Turner and Fishman, 1991). These are either moderate reddish brown (10R 4/6), yellowish gray (5Y 8/1) or green (5G 7/2). The brown concretions are spheroidal to irregular and 100-120 mm diameter. The yellowish gray concretions are <30 mm diameter, and spheroidal to elongate. They commonly have obvious nuclei and concentric zonation of 1-2 mm shells. The green concretions are up to 100 mm in diameter, spheroidal and well-cemented and are only present in the reduced facies.

Iron (Oxyhydr)oxide Concretions

Iron (oxyhydr)oxide concretions are characterized as large concretions (up to 100 mm diameter) or mega concretions (up to 0.5 m diameter; Figure 2.8).



Figure 2.8. Iron (oxyhydr)oxide concretions. A. Brushy Basin Member concretion in “Ceratasaurus channel” at Fruita Paleo Area. B. Brushy Basin Member green claystone concretion.

1. Large concretions: Large concretions are present in Fruita Paleo Area in the northern margin of the smectite clay mineral zone of Lake T’oo’dichi’. These concretions are located in a reduced channel sandstone. The reddish brown (10R 4/6) concretions are 30-40 mm in diameter and spheroidal to elongate with ~2 mm rinds and interiors relatively depleted of cement. Halos of iron (oxyhydr)oxide surround the concretions. Some halos are equidistant from the entire concretion and some halos are elongate although elongate halos do not exhibit a preferred map orientation. These concretions are hematite identified by XRD; however, this subtype exhibits iron (oxyhydr)oxide after pyrite pseudomorphs as well as granular iron (oxyhydr)oxide cement (Figure 2.7).

Other large concretions are light green (5G 7/4), <100 mm in diameter, spheroidal to irregular shaped, and contain goethite and ferrihydrite. These concretions are present in the same claystone lithofacies and intermediate diagenetic facies as the large calcite

concretions (in the Blue Hills study area). This subtype contains euhedral iron (oxyhydr)oxide volcanic ash shards and zeolites.

3. Mega concretions: This subtype is also present in Fruita Paleo Area. These are up to 0.5 m in diameter, well-cemented and circular. They are associated with reduced, intermediate and oxidized host rock and are moderate to dark reddish brown (10R 4/6 to 3/4) color. The mineralogies are hematite and calcite determined by XRD.

Phosphate Concretions

Apatite and iron phosphate concretions are present in the Montezuma Creek (clinoptilolite clay mineral zone) and Blue Hills (analcime clay mineral zone) sections in the intermediate facies (Figure 2.9). All of the phosphate concretions are typically solidly cemented with ferroan hydroxyl apatite and iron phosphate identified by XRD (Figure 2.7). Some diffuse iron (oxyhydr)oxide cement is also present. The Montezuma Creek concretions contain both iron phosphate and hydroxyl apatite. These concretions are located in a reaction front directly above burrows and fossilized dinosaur bones. They are dark reddish brown (10R 3/4), 3-8 mm in diameter and spheroidal. Another phosphate concretion collection in the Blue Hills study area contains goethite and iron phosphate identified by XRD.

These reddish orange (10R 6/6) concretions are present in the claystone lithofacies and intermediate diagenetic facies with large iron (oxyhydr)oxide and calcite concretions. These phosphate concretions are up to 70 mm in diameter, spheroidal to irregularly-shaped and at least one example has burrows throughout the concretion.

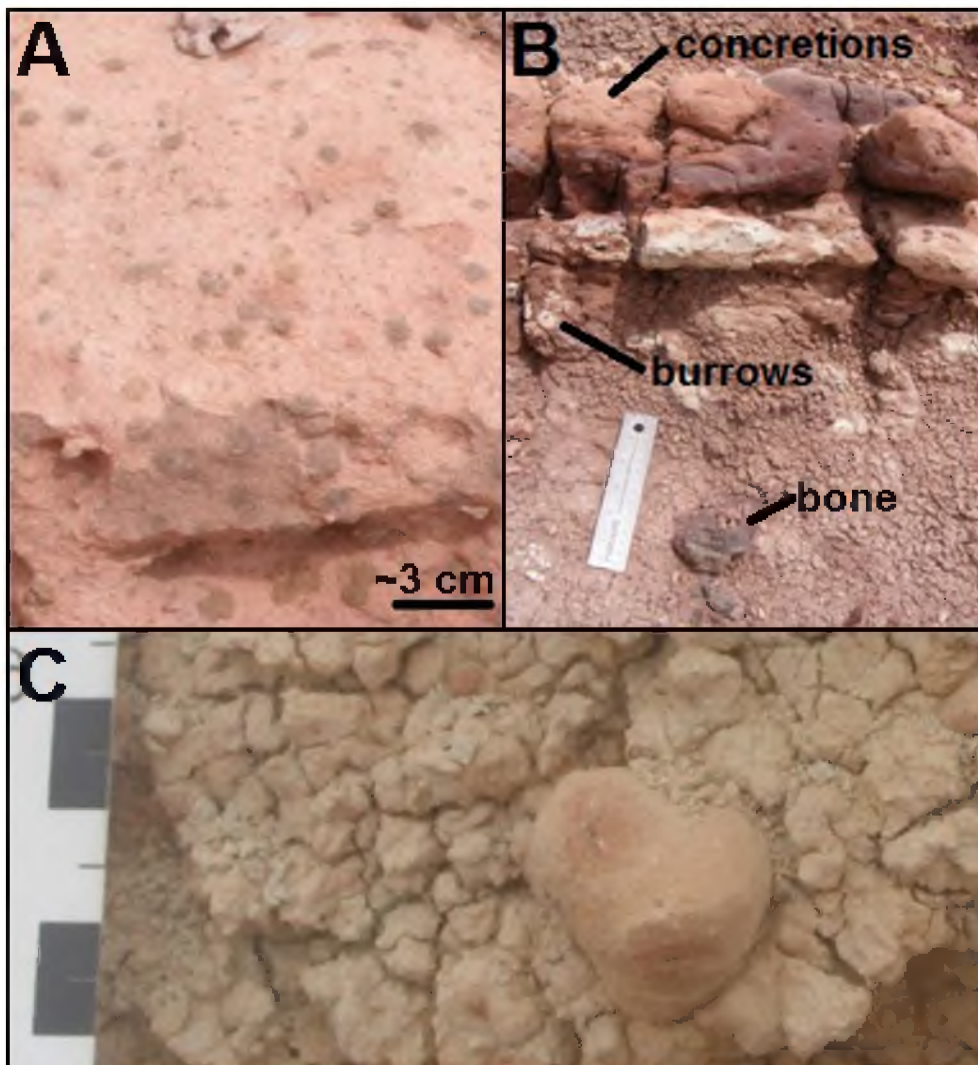


Figure 2.9. Phosphate concretions in the Brushy Basin Member. A. Concretions containing hydroxyl apatite and iron phosphate. These are present in a reaction front (B.) directly above burrows and fossilized bones at Montezuma Creek. C. Red claystone concretion from Blue Hills locality.

Interpretation and Discussion

Lithofacies and Diagenetic Facies

Field observations of siltstones, claystones and localized sandstone lenses are consistent with an ephemeral lacustrine interpretation of the upper Brushy Basin Member (Turner and Fishman, 1991). Laminated and bioturbated siltstones and claystones were likely deposited in meters to 10s of meters of water in an ephemeral groundwater-fed salt flat/ lake. Locally present cross-bedded sandstones are interpreted as stream channels where occasional floodwaters fed the lake. Paleosols are present but poorly developed; blocky texture is common and slickensides are observed in one horizon at the Blue Hills location on the margin of Lake T'oo'dichi'. Sparse paleosols developed during times of nondeposition on topographic highs that were above water level.

Diagenetic facies (oxidized, reduced and intermediate) are localized, and not laterally persistent even within an outcrop (Figure 2.2), and they exhibit important differences in bioturbation features. Oxidized and intermediate facies are typically burrowed with reduction halos and mottles suggesting the presence of roots and burrowing animals. The reduced facies typically has only small 1-2 mm charophyte molds rather than larger burrows and root traces – more typical of subaqueous environments with extreme chemistries (i.e., not neutral) that limit the diversity of biota (Turner and Peterson, 2004). Diagenetic facies are interpreted as early diagenetic processes and oxidized facies represent shallow water to subaerial deposition. Reduced facies are interpreted to represent deeper water environments (Figure 2.10).

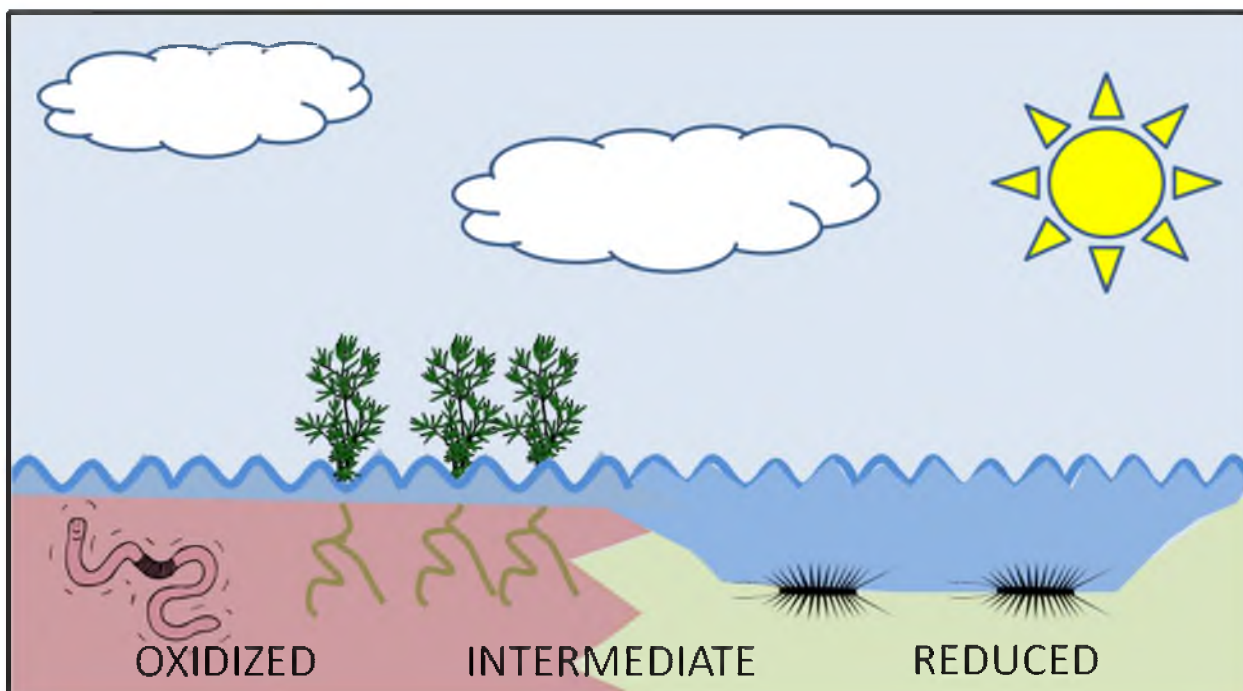


Figure 2.10. Schematic representation of diagenetic facies during early diagenetic conditions. (Figures are not to scale, but rather represent different biogeochemical influences.) Water depth was variable and on the scale of ~0-3 m depth for the shallows and likely up to ~ 10 m depth for the deeper waters.

Comparison of Host Rock Mineralogy and Concretion Mineralogy

In most concretion examples, similar elements (such as iron, calcium, manganese) are enriched by ~100% relative to the host rock even though mineralogy is varied. This suggests outcrop-scale concretion formation mechanisms produced a diversity of minerals from similar elements. Because the elements that participated in the reactions are similar (predominantly iron, calcium and manganese), the precipitation mechanisms were likely very sensitive to fluid chemical differences such as pH, Eh and salinity and likely also sensitive to microbial interaction. Concretion formation chemistry is therefore both inconsistent and complex, even within a formation and on spatial scales of meters or less.

Most Brushy Basin Member concretions are enriched relative to the host rock in certain elements, but only calcite concretions are >> 100% enriched in calcium, magnesium and strontium - highly mobile elements. Friable calcite concretions are present along more permeable lamina in channel sandstones and siltstones. Well-cemented calcite concretions are typically concentrated along lithological boundaries between more permeable sandstones and less permeable siltstones. This suggests that more permeable horizons have the ability to permit more rapid transport of reactants and to allow for a higher concentration of reactants, even if diffusion is the main transport process (Mozley and Davis, 1996). Conversely, similarities in chemistry between concretions and host rock in the more fine-grained portions of the unit suggest reactants are being sourced locally to form concretions. The presence of calcite concretions at lithofacies boundaries where discrete porosity and permeability differences exist supports

the hypothesis that reactants do not travel far into the finer-grained material, but instead precipitate diagenetic minerals as soon as they are concentrated in the finer material.

Although concretions are present in all outcrops examined for this study, they are most common and more varied in terms of mineralogy and morphology in the smectite, clinoptilolite and analcime zones documented by Turner and Fishman (1991), i.e, the outer three rings of the basin in the bull's-eye pattern that forms Lake T'oo'dichi' (Figure 2.1). Concretions in the analcime zone are the most varied and include four different types (calcite, siderite, iron (oxyhydr)oxide and iron phosphate) in the same claystone lithofacies. This suggests that the overall diagenetic reactions are strongly influenced by extreme fluid chemistries, but localized pockets of reactions responsible for concretion formation may be affected by many factors such as fluid chemistry, restricted sources of reactants and microbial communities. The concretions present in the most altered, basin center (albite zone) are in a sandstone lens interpreted as a channel sand that was deposited during a period when the lake was very low or dessicated. Therefore, these concretions may not have been subjected to the same intense chemical alteration as the deeper water facies; however, further work is needed to more thoroughly examine concretions in the basinal center.

Organics and Concretion Formation

Concretions - particularly carbonate concretions – are commonly thought to rely on the reduction of organic carbon by microbial action to initiate nucleation (Raiswell and Fisher, 2000; Mozley and Davis, 2005). In the Brushy Basin Member, only phosphate concretions seem to have a direct relationship to macroscopic organics. These

are present directly above dinosaur bones and burrows in relatively permeable horizons. Phosphate concretions are not nucleated directly on bones or burrows; however, they do contain hydroxyl apatite (detected with XRD) and the host rock contains fine-grain size clasts of apatite (detected with QEMSCAN). It is likely that reactants for these concretions were sourced from nearby bone fragments. Some calcite concretions in Fruita Paleo Area preserve burrows.

Most of the concretions examined exhibit pervasive growth features rather than obvious radial growth patterns. Although most of the concretions do not exhibit true isopachous cements (indicative of pervasive growth), cements are inwardly digitate in many pore spaces. The concentric zonation indicative of radial growth is not observed. One exception is the large yellowish gray carbonate concretions (BH17) present in the claystone lithofacies that have an obvious nucleus (a dark spot of unidentified mineralogy in the center of the concretions; Figure 2.6F) and have grown radially outward from the center. Even though pervasive growth is the likely dominant mechanism controlling concretion precipitation, it is probable that organics are responsible for initiating conditions for precipitation. Evidence for this is: 1. the lack of self organized spacing that is typical of pervasive growth concretions (Potter et al., 2011), 2. differences in mineralogy of concretions within a stratigraphic horizon and outcrop, and 3. precipitation in an organic-rich formation.

Comparison of Brushy Basin Member, Navajo Sandstone and Mars Concretions

Hematite spherules in Meridiani Planum, Mars (dubbed “blueberries”) are interpreted as diagenetic concretions that formed in a porous and permeable, eolian sandstone (informally named the Burns formation; Grotzinger et al., 2005; McLennan et al., 2005). They exhibit many similar physical characteristics with the Navajo Sandstone concretions; however, the Burns formation is composed of ~25% magnesium sulfate sand – a soluble and chemically reactive substrate (Grotzinger, 2005; Squyres, 2004). In this sense, the Burns formation is much more similar to the chemically reactive host rock of the Brushy Basin Member than the relatively inert Navajo Sandstone.

The Brushy Basin Member of the Morrison Formation is predominately a clayey siltstone with local fine-grained sandstone. Both the Navajo Sandstone and the Burns formation are fine-grained sandstones (Grotzinger et al., 2005; McLennan et al., 2005; Potter et al., 2011). The Brushy Basin Member is composed predominately of quartz, feldspars, zeolites and altered volcanic ash. The Navajo Sandstone is a clean quartz arenite and the Burns formation is composed of sulfate sands and basaltic sands (Grotzinger et al., 2005; McLennan et al., 2005; Potter et al., 2011). All three units exhibit documented diagenetic facies, i.e., outcrop- to regional-scale mineralogical, chemical, physical and color differences (Beitler et al., 2003; 2005; McLennan et al., 2005).

Physical concretion characteristics tend to be more similar between the Navajo Sandstone and the Burns formation than in the Brushy Basin Member (Figure 2.7, Table 2.5). Concretions in both the Navajo Sandstone and the Burns formation are spheroidal

Table 2.5. Comparison of concretion and host rock features. FeO represents iron (oxyhydr)oxide. Mars data from Calvin et al., 2009.

	Brushy Basin	Navajo Ss	Mars
Host Rock Characteristics			
Grain size	silt, clay, local fine sand	fine sand	fine sand
Composition	quartz, zeolites, altered volcanic ash	quartz arenite	sulfate, basaltic
Depositional environment	alkaline, saline lake	eolian	eolian
Diagenetic Facies	present	present	present
Concretion Physical Characteristics			
Spheroidal geometry (mean aspect ratio)	1.2	1.1	1.06
Irregular geometry	present	occasional	rare
Latitudinal ridges or furrows	rare	present	rare
Doublets or triplets	present	present	present
Adhered host rock	present	present	present
Self-organized spacing	rare	present	present
Concretion Mineralogical Characteristics			
Cement mineralogy	three types: carbonate, FeO, phosphate	hematite, goethite, nanophase FeO, kaolinite	nanophase FeO, jarosite
Chemistry significantly different from host rock	no (except in permeable lenses)	X	X
Precursor cements	pyrite (in one example)	FeO	goethite
Radial crystal growth	in some calcite concretions	no	X

(McLennan et al., 2005; Calvin et al., 2008; Potter et al., 2011), and Brushy Basin Member concretions are typically more irregularly shaped. Spheroidal concretions in the Brushy Basin Member (mean aspect ratio = 1.20) are less spheroidal than the Navajo Sandstone (mean aspect ratio = 1.10; Potter et al., 2011) and the Burns formation (mean aspect ratio = 1.06; McLennan et al., 2005). In all three units, latitudinal ridges (formed along bedding) are present, although they are rare in both the Brushy Basin and the Burns formation (Calvin et al., 2008). Doublets and triplets are present in all three units as are concretions weathered out with adhered host rock (McLennan et al., 2005; Calvin et al., 2008; Potter et al., 2011). Both the Navajo Sandstone and the Burns formation concretions exhibit self-organized spacing between adjacent concretions (McLennan et al., 2005; Potter et al., 2011); however, this is rare in the Brushy Basin Member concretions likely due to finer-grained, clay-rich sediments restricting the movement of fluid.

Chemical and mineralogical characteristics are also more similar between the Navajo Sandstone and the Burns formation than the Brushy Basin Member. Brushy Basin Member concretion mineralogy is quite variable with three main concretion types present: carbonate, iron (oxyhydr)oxide and phosphate. Both the Navajo Sandstone and the Burns formation are predominately iron (oxyhydr)oxide (Grotzinger et al., 2005; McLennan et al., 2008; Potter et al., 2011). The Navajo Sandstone and Burns formation concretions are greatly enriched in iron relative to the host rock and slightly enriched in nickel (Morris et al., 2006; Potter et al., 2011). In most examples, the Brushy Basin Member concretions are slightly enriched in magnesium and calcium, but otherwise the chemistry in the

concretions and host rock are quite similar. Only in more porous and permeable lenses are concretions greatly enriched relative to the host rock in calcium, manganese and strontium.

The Navajo Sandstone concretions show consistent physical characteristics comparable to the Mars concretions and physical similarities between the Navajo Sandstone and the Burns formation suggest similar formation mechanisms (Potter et al., 2011). Despite differences in the host rock mineralogies, comparison between the Navajo Sandstone and the Burns formation implies that highly mobile reactant transport in porous and permeable media forms a concretion with the physical features observed in both examples (e.g., spheroidal, well-cemented, chemically and mineralogically distinct from the host rock). These similarities are present even though the precipitation reaction is water limited on Mars and iron limited in the Navajo Sandstone (Calvin et al., 2008; Potter et al., 2011) and even though the sediments in the Burns formation are chemically reactive sulfates and the Navajo Sandstone is relatively inert (Grotzinger et al., 2005; McLennan et al., 2005; Calvin et al., 2008; Potter et al., 2011). In the geochemically reactive sediments of the Brushy Basin Member, however, the physical features are quite different (e.g., irregular geometry, chemically and mineralogically similar to host rock).

Conclusions

The influence that reactive volcanoclastic host rock has on diagenetic alkaline saline fluid-rock interactions is extremely spatially variable, even within an outcrop and single stratigraphic horizons. The broad application is to show how seal formations may have inconsistent flow paths even in what may seem to be a laterally homogenous shale.

This can have important implication for diagenetic microenvironments interacting with reducing fluids such as hydrocarbons, or acidic fluids such as injected supercritical CO₂. These data also are applicable to understanding the role of more reactive sediments and fluid interactions on Mars to determine the diagenetic history of the Burns formation.

Five important implications result from this research: 1. Concretions in the Brushy Basin Member – a host rock of volcanoclastic mudrock – exhibit a broad range of mineralogies, sizes, morphologies and distribution. 2. Diagenetic facies formed during early diagenesis and reflect low relief paleotopography in the original alkaline saline lake setting. 3. Concretions can form via reactants sourced from directly adjacent host rocks in low porosity rocks or from greater distances in higher porosity rocks. 4. Extreme fluid chemistries combined with localized factors encourage a diverse range of concretion mineralogies and morphologies. 5. Host rock porosity and permeability affects both physical and chemical properties to a greater degree than host rock chemistry. In summary, reactive host rock compositions affect diagenetic iron precipitation both physically and chemically, creating diverse concretion mineralogies and morphologies. However, petrophysical host rock properties also exert controls on physical and chemical characteristics of concretion formation.

References

- Beitler, B., Chan, M.A., Parry, W.T., 2003. Bleaching of Jurassic Navajo Sandstone on Colorado Plateau Laramide highs; Evidence of exhumed hydrocarbon supergiants? *Geology* 31, 1041-1044.
- Beitler, B., Parry, W.T., Chan, M.A., 2005. Fingerprints of fluid flow: Chemical diagenetic history of the Jurassic Navajo Sandstone, southern Utah, U.S.A. *Journal of sedimentary research* 75, 547-561.

- Blakey, R., 1994. Paleogeographic and tectonic controls on some Lower and Middle Jurassic erg deposits, Colorado Plateau, Mesozoic systems of the Rocky Mountain region, USA, 273 p.
- Blakey, R., Peterson, F., Kocurek, G., 1988. Syntheses of late Paleozoic and Mesozoic eolian deposits of the Western Interior of the United States. *Sedimentary Geology*, 56, 3-125.
- Boles, J.R., 1982. Active albitization of plagioclase, Gulf Coast Tertiary. *American Journal of Science*, 282, 165-180.
- Calvin, W.M., Shoffner, J.D., Johnson, J.R., Knoll, A.H., Pockock, J.M., Squyres, S.W., Weitz, C.M., Arvidson, R.E., Bell, J.F., III, Christensen, P.R., de Souza, P.A., Jr., Farrand, W.H., Glotch, T.D., Herkenhoff, K.E., Jolliff, B.L., Knudson, A.T., McLennan, S.M., Rogers, A.D., Thompson, S.D., 2008. Hematite spherules at Meridiani; results from MI, Mini-TES, and Pancam. *Journal of Geophysical Research*, 113.
- Chan, M., Parry, W.T., Bowman, J.R., 2000. Diagenetic hematite and manganese oxides and fault-related fluid flow in Jurassic sandstones, southeastern Utah. *AAPG Bulletin*, 84, 1281-1310.
- Chan, M., Parry, W., Beitler, B., Ormo, J., Komatsu, G., 2004. A possible terrestrial analogue for haematite concretions on Mars. *Nature*, 429, 731-734.
- Chan, M., Bowen, B., Parry, W., Ormo, J., Komatsu, G., 2005. Red rock and red planet diagenesis; comparisons of Earth and Mars concretions. *GSA Today*, 15, 4-10.
- Chan, M.A., Potter, S.L., Bowen, B.B., Parry, W.T., Barge, L.M., Seiler, W., Petersen, E.U., Bowman, J.R., 2012. Characteristics of terrestrial ferric oxide concretions and implications for Mars. *SEPM Special Publication No. 11*, 253-270.
- Clifton, H., 1957. The carbonate concretions of the Ohio Shale. *The Ohio Journal of Science*, 57, 114-124.
- Coleman, M., Raiswell, R., 1995. Source of carbonate and origin of zonation in pyritiferous carbonate concretions; evaluation of a dynamic model. *The American Journal of Science*, 295, 282-308.
- Coleman, M.L., Raiswell, R., 1981. Carbon, oxygen and sulphur isotope variations in concretions from the upper Lias of N.E. England. *Geochimica et Cosmochimica Acta*, 45, 329-340.

- Dickson, J.A.D., Barber, C., 1976. Petrography, chemistry and origin of early diagenetic concretions in the lower Carboniferous of the Isle of Man. *Sedimentology*, 23, 189-211.
- Feistner, K.W.A., 1989. Petrographic examination and re-interpretation of concretionary carbonate horizons from the Kimmeridge Clay, Dorset. *Journal of the Geological Society*, 146, 345-350.
- Gold, P.B., 1987. Textures and geochemistry of authigenic albite from Miocene sandstones, Louisiana Gulf Coast. *Journal of Sedimentary Petrology*, 57, 353-362.
- Golden, D.C., Ming, D.W., Morris, R.V., Graff, T.G., 2008. Hydrothermal synthesis of hematite spherules and jarosite: Implications for diagenesis and hematite spherule formation in sulfate outcrops at Meridiani Planum, Mars. *American Mineralogist*, 93, 1201-1214.
- Grotzinger, J., 2005. Stratigraphy and sedimentology of a dry to wet eolian depositional system, Burns Formation, Meridiani Planum, Mars. *Earth and Planetary Science Letters*, 240, 11-72.
- Helmold, K.P. and van de Kemp, P.C., 1984. Diagenetic mineralogy and controls on albitization and laumontite formation in Paleogene arkoses, Santa Ynez Mountains, California, in McDonald, D.A. and Surdam, R.C., eds. *Clastic diagenesis: American Association of Petroleum Geologists memoir*, 37, 239-276.
- Hudson, J.D., 1978. Concretions, isotopes, and the diagenetic history of the Oxford Clay (Jurassic) of central England. *Sedimentology*, 25, 339-367.
- Huggett, J.M., 1994. Diagenesis of mudrocks and concretions from the London Clay Formation in the London Basin. *Clay Minerals*, 29, 693-707.
- Jordan, M.M., Aplin, A.C., Curtis, C.D., Coleman, M.L., 1992. Access of pore waters to carbonate precipitation sites during concretion growth. *Proceedings International Symposium on Water Rock Interaction*, 1239-1242.
- Loope, D.B., Kettler, R.M., Weber, K.A., 2010. Follow the water; connecting a CO₂ reservoir and bleached sandstone to iron-rich concretions in the Navajo Sandstone of south-central Utah, USA. *Geology (Boulder)*, 38, 999-1002.
- Lyons, T., Raiswell, R., Robinson, A., Scott, C., Chu, X., Li, C., Love, G., Sessions, A., Gill, B., 2007. Carbonate concretions as a window to the evolving chemistry of the early ocean and atmosphere. *Geochimica et Cosmochimica Acta*, 71, A606.
- McLennan, S., Bell, J.F., III, Calvin, W.M., Christensen, P.R., Clark, B.C., De Souza, P.A., Farmer, J.D., Farrand, W.H., Fike, D.A., Gellert, R., Ghosh, A., Glotch, T.D.,

- Grotzinger, J., Hahn, B., Herkenhoff, K.E., Hurowitz, J.A., Johnson, J.R., Johnson, S.S., Jolliff, B.J., Klingelhofer, G., Knoll, A.H., Learner, Z., Malin, M.C., McSween, H.Y., Pockock, J.M., Ruff, S.W., Soderblom, L.A., Squyres, S.W., Tosca, N.J., Watters, W.A., Wyatt, M.B., Yen, A., 2005. Provenance and diagenesis of the evaporite-bearing Burns Formation, Meridiani Planum, Mars. *Earth and Planetary Science Letters*, 240, 95-121.
- Merino, E., 1975. Diagenesis in Tertiary sandstones from Kettleman North Dome, California, I. Diagenetic mineralogy. *Journal of Sedimentary Petrology*, 45, 320-336.
- Milliken, K.L., Land, L.S., Loucks, R.J., 1981. History of burial diagenesis determined from isotopic geochemistry, Frio Formation, Brazoria County, Texas. *American Association of Petroleum Geologists Bulletin*, 65, 1397-1413.
- Morris, R., Ming, D.W., Graff, T.G., Arvidson, R.E., Bell, J.F., Squyres, S.W., Mertzman, S.A., Gruener, J.E., Golden, D.C., Le, L., Robinson, G.A., 2005. Hematite spherules in basaltic tephra altered under aqueous, acid-sulfate conditions on Mauna Kea volcano, Hawaii; possible clues for the occurrence of hematite-rich spherules in the Burns Formation at Meridiani Planum, Mars. *Earth and Planetary Science Letters*, 240, 168-178.
- Morris, R.V., Klingelhofer, G., Schroeder, C., Rodionov, D.S., Yen, A., Ming, D.W., de Souza, P.A., Jr., Wdowiak, T., Fleischer, I., Gellert, R., Bernhardt, B., Bonnes, U., Cohen, B.A., Evlanov, E.N., Foh, J., Guetlich, P., Kankeleit, E., McCoy, T.J., Mittlefehldt, D.W., Renz, F., Schmidt, M.E., Zubkov, B., Squyres, S.W., Arvidson, R.E., 2006. Mössbauer mineralogy of rock, soil, and dust at Meridiani Planum, Mars; Opportunity's journey across sulfate-rich outcrop, basaltic sand and dust, and hematite lag deposits. *Journal of Geophysical Research*, 111.
- Mozley, P., 1989. Complex compositional zonation in concretionary siderite; implications for geochemical studies. *Journal of Sedimentary Petrology*, 59, 815-818.
- Mozley, P.S., Davis, J.M., 1996. Relationship between oriented calcite concretions and permeability correlation structure in an alluvial aquifer, Sierra Ladrones Formation, New Mexico. *Journal of Sedimentary Research*, 66, 11-16.
- Mozley, P., Davis, J.M., 2005. Internal structure and mode of growth of elongate calcite concretions; evidence for small-scale, microbially induced, chemical heterogeneity in groundwater. *Geological Society of America Bulletin*, 117, 1400-1412.
- Peterson, F., 1994. Sand dunes, sabkhas, streams, and shallow seas; Jurassic paleogeography in the southern part of the Western Interior Basin Mesozoic systems of the Rocky Mountain region, USA. *SEPM (Society for Sedimentary Geology)*, Rocky Mountain Section, Denver, CO, United States (USA).

- Potter, S.L., Chan, M., Petersen, E., Dyar, M.D., Sklute, E., 2011. Characterization of Navajo Sandstone Concretions: Mars comparison and criteria for distinguishing diagenetic origins. *Earth and Planetary Science Letters*, 301, 444-456.
- Potter, S.L., Chan, M.A., 2011. Joint controlled fluid flow patterns and iron mass transfer in Jurassic Navajo Sandstone, Southern Utah, USA. *Geofluids*, 11, 184-198.
- Raiswell, R., 1976. The microbiological formation of carbonate concretions in the upper Lias of NE England. *Chemical Geology*, 18, 227-244.
- Raiswell, R., Fisher, Q.J., Cope, J.C.W., Curtis, C.D., 2000. Mudrock-hosted carbonate concretions; a review of growth mechanisms and their influence on chemical and isotopic composition. *Journal of the Geological Society of London*, 157, 239-251.
- Seilacher, A., 2001. Concretion morphologies reflecting diagenetic and epigenetic pathways. *Sedimentary Geology*, 143, 41-57.
- Seiler, W.M., 2008. Jurassic Navajo Sandstone of Coyote Buttes, Utah/Arizona: Coloration and diagenetic history, preservation of a dinosaur trample surface, and a terrestrial analog to Mars, *Geology and Geophysics*. University of Utah, Salt Lake City.
- Selles Martinez, J., 1996. Concretion morphology, classification and genesis. *Earth Science Reviews*, 41, 3-4.
- Squyres, S.W., 2004. In situ evidence for an ancient aqueous environment at Meridiani Planum, Mars. *Science*, 306, 1709-1714.
- Turner, C.E., Fishman, N.S., 1991. Jurassic Lake T'oo'dichi'; a large alkaline, saline lake, Morrison Formation, eastern Colorado Plateau. *Geological Society of America Bulletin*, 103, 538-558.
- Turner, C.E., Peterson, F., 2004. Reconstruction of the Upper Jurassic Morrison Formation extinct ecosystem; a synthesis. *Sedimentary Geology*, 167, 309-355.

CHAPTER 3

TEXTURAL AND MINERALOGICAL CHARACTERISTICS OF MICROBIAL FOSSILS ASSOCIATED WITH MODERN AND ANCIENT IRON (OXYHYDR)OXIDES

Sally L. Potter-McIntyre, Marjorie A. Chan and Brian J. McPherson

Submitted: Astrobiology

Abstract

Iron (oxyhydr)oxide microbial mats in modern to ~100ka tufa terraces are present in a cold spring system along Ten Mile Graben, southeastern Utah, USA. Mats exhibit morphological, chemical and textural biosignatures and show diagenetic changes that occur over millennial scales. The Jurassic Brushy Basin Member of the Morrison Formation in the Four Corners region of the USA also exhibits comparable microbial fossils and preserved biosignatures in the lacustrine unit.

Both the modern spring system and Brushy Basin Member represent alkaline, saline, groundwater-fed systems and preserve diatoms and other similar algal forms with cellular elaboration. Two distinct suites of elements (1) C, Fe, As and, 2) C, S, Se are associated with microbial fossils in modern and ancient rocks and may be potential markers for biosignatures. The presence of 6-line ferrihydrite (detected via XRD) in ~100ka fossil microbial mats suggests this thermodynamically unstable mineral may also be a potential biomarker.

One of the most extensive sedimentary records on Mars is exposed in Gale Crater and consists of nonacidic, lacustrine clays and sulfates. These terrestrial iron (oxyhydr)oxide examples are a valuable analog because of similar iron- and clay-rich host rock compositions and will help to: 1) document specific biomediated textures, 2) demonstrate how biomediated textures might persist or respond to diagenesis over time, 3) understand diagenetic processes in a nonacidic, saline lacustrine environment such as the sedimentary rocks in Gale Crater, and 4) provide a ground truth library of textures to explore and compare in extraterrestrial iron oxides where future explorations hope to detect past evidence of life.

Introduction

Biosignatures are preserved fingerprints of life interacting with fluid and rock, particularly where microbes enhance mineral precipitation during deposition and/or early diagenesis (Farmer and Des Marais, 1999; Banfield et al., 2000 2001; Cady, 2001, 2009; Cady et al., 2003; Westall, 2008; Schopf et al., 2010). Three types of biosignatures are typically recognized: 1. morphological microfossils that retain the carbonaceous remains of cells, 2. microbially influenced sedimentary structures such as stromatolites and chemofossils that include biominerals, and 3. isotopic signatures or concentrations of trace elements specific to sequestration by microbes (Cady et al., 2003; Westall, 2008).

Establishing biogenicity of putative morphological microbial fossils can often be challenging (Farmer and DesMarais, 1999; Cady, et al., 2003; Schopf et al., 2010). The following criteria have been proposed to show biogenicity (Cady, 2001):

1. Features must occur in a thin section in order to show they are not modern contaminants.
2. The features must occur in sedimentary or low grade metamorphic rocks.
3. Microfossils must be larger than the smallest known extant organisms (~0.01 μ m).
4. The features must be composed of kerogen to show they contain organic carbon.
5. The features must occur with others of similar morphology.
6. The features must be hollow to show a biotic structure.
7. The features must show cellular elaboration.

If the features do not meet or only meet criteria 1-4, they are considered pseudofossils.

Possible fossils meet criteria 1-5 and probable fossils meet all six criteria (Cady, 2001).

Preservation of biosignatures occurs by many different methods and in many different settings, such as banded iron formations, tufas, clay rich shales and water laid pyroclastics (Allison and Briggs, 1991; Farmer and Des Marais, 1999; Cady, 2001; Campbell et al., 2004; Kolo et al., 2009; Rainey and Jones, 2010). Permineralization by iron preserves cell structure during early diagenesis (Parenteau et al., 2010) and three-dimensional preservation of microbial fossils also occurs in concretions (Berner, 1968; Allison and Pye, 1994). Shallow evaporative, high salinity environments are particularly well suited for preservation of microbial fossils (Knoll, 1984; Vogel et al., 2009; 2010). However, preservation of any type of microbial fossil or chemical/textural biosignature depends on the degree of alteration during diagenesis and factors such as exposure to diagenetic fluids (Cady, 2001; Westall, 2008).

Iron (oxyhydr)oxide minerals have outstanding capability to preserve biogenetic fingerprints, both by permineralization of cell structure (Cady and Farmer, 1996; Konhauser et al., 2003; Rancourt et al., 2005; Westall, 2008; Parenteau et al., 2010) and by preserving diagnostic trace element configurations and/or kinetically unusual mineral phases (Westall, 2008; Chan et al., 2009). The Brushy Basin Member has excellent biosignature preservation potential due to its iron- and clay-rich composition.

Purpose of Study

The purpose of this study is to compare modern iron (oxyhydr)oxide microbial precipitates (tufas) at a cold spring along Ten Mile Graben in southeastern Utah, with ~100ka tufa examples from the same spring to determine potential diagenetic changes over millennial scales. Diagnostic morphological and chemical similarities are documented and then compared to features in the Jurassic Brushy Basin Member of the Morrison Formation to distinguish differences and/or similarities with ancient biosignatures in an alkaline saline lacustrine shale. Despite different depositional settings, both of these formations are alkaline, saline, groundwater-fed systems. The modern spring system provides a starting point to recognize biosignatures because of the documented presence of microbial mats (Shipton et al., 2004; Burnside, 2010) as well as a published age for ancient tufas from the same spring system (Burnside, 2010).

The Brushy Basin Member preserves distinctive alkaline saline Lake T'oo'dichi' sediments and is chosen for this study because of the hypersaline geochemistry and alkaline early diagenetic mineral alteration patterns (Turner and Fishman, 1999). Although so-called "extremophiles" – such as halophiles - likely inhabited the water and

subaqueous sediments, abundant bioturbation features (e.g., charophyte molds, root traces, burrows and dinosaur bones) suggest that macroscopic biota was abundant in interbeds where paleosols developed and/or when water chemistries were circumneutral (Turner and Peterson, 2004).

Applications to Mars

One of the most extensive sedimentary stratigraphic sections (~5 km thick) on Mars is exposed in Mount Sharp at Gale Crater (Milliken et al., 2010; Thomson et al., 2011). The unit is partly composed of clays that likely formed in a nonacidic, lacustrine environment (Cabrol et al., 1999; Milliken et al., 2010; Thomson et al., 2011). The Brushy Basin Member may provide an excellent terrestrial analog for understanding lithological, diagenetic and biogeochemical histories of these similar iron- and clay-rich shales on Mars.

The study of extremophiles is of increasing importance in the search for extraterrestrial life (e.g., Rothschild and Manzielli, 2000) because any life that existed on Mars would be or would have been extreme compared to Earth standards. These terrestrial iron (oxyhydr)oxide examples will: 1) document specific biomediated textures and mineral phases from a water-deposited, alkaline saline analog unit, 2) show how these textures and minerals might persist or respond to diagenesis over time, and 3) provide a ground truth library of textural and mineralogical biogenic fingerprints to explore and compare in extraterrestrial iron oxides.

Study Area

Ten Mile Graben

A CO₂- and hydrocarbon-charged cold spring system consisting of three major springs, Crystal Geyser, Big Bubbling Spring and Little Bubbling Spring, emanates along Ten Mile Graben fault system south of Green River, UT (Figure 3.1). This system was chosen for study because modern microbial precipitates of travertine and iron (oxyhydr)oxide are present in the water around the spring source (Shipton et al., 2004; Burnside, 2010). Also, ancient tufas from the same system form terraces along the fault system that are <400ka, established by U-Th dating (Burnside, 2010); therefore, it is possible to compare modern samples with diagenetically altered (and accurately dated) ancient examples of microbially precipitated iron (oxyhydr)oxides. For this study, we use modern examples from Big Bubbling Spring and Little Bubbling Spring and samples from an ancient ~100ka tufa terrace at Crystal Geyser (Figure 3.1). The remote modern spring sample locations were chosen to limit anthropogenic interference with microbial mats.

Morrison Formation, Brushy Basin Member

The Jurassic Brushy Basin Member of the Morrison Formation is a variegated shale formation that extends across the Colorado Plateau in the western US. The Morrison Formation is renowned for its dinosaur remains, particularly the preservation of large sauropods (e.g., Chure, 1994; Evans and Chure, 1998; Henrici, 1998). The entire Morrison Formation was deposited over a period of 7 million years from 155-148Ma (Kowallis et al., 1998; Turner and Peterson, 2004). The Brushy Basin Member is capable

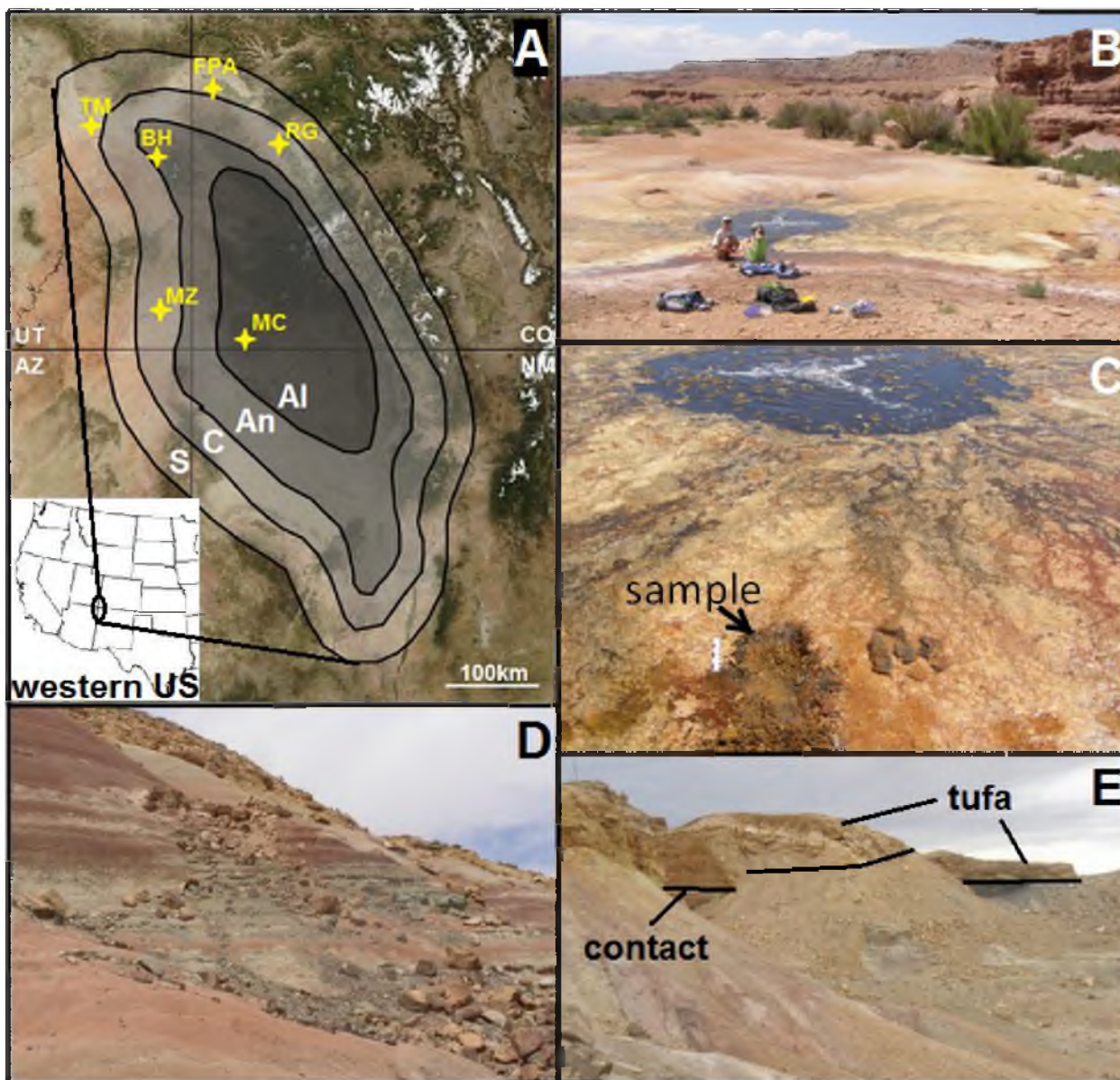


Figure 3.1. Study areas. A. Lake T'oo'dichi centered on the Four Corners region of the western U.S. Bull's eye pattern are clay mineral zones with increasing alteration basinward (S = smectite; C = clinoptilolite; An = analcime; Al = albite). Study sites are marked in yellow (TM = Ten Mile Graben; FPA = Fruita Paleo Area; BH = Blue Hills; RG = Rattlesnake Gulch; MZ = Montezuma Creek; MC = McElmo Canyon). B. Big Bubbling Spring in Ten Mile Graben. C. Sample site in partially lithified microbial mat near the source of Big Bubbling Spring; unlithified sample was collected directly from vent. Scale bar is 15 cm long. D. Brushy Basin Member outcrop in Montezuma Creek exhibiting variegated coloration. Outcrop shown in photo is ~15 m. E. Terraces of tufa deposits (~100ka) at Crystal Geyser in Ten Mile Graben Terraces are 3-5 m high.

of preserving paleobiological information because it is a clay-rich shale, one of the most optimal environments for preserving microbial fossils (Farmer and Des Marais, 1999).

The upper part of the Brushy Basin Member was deposited in a groundwater-fed, ephemeral, alkaline saline lake system named Lake T'oo'dichi' that was centered on the Four Corners region (Turner and Fishman, 1991; Figure 3.1). A back-arc basin existed to the west and associated volcanics supplied copious amounts of ash to the depositional basin (Turner and Fishman, 1999; Turner and Peterson, 2004). Clay mineralogy has been extensively documented and clay mineral zones (present in tuffs) form a bull's-eye pattern showing increasing early diagenetic alteration to the basinal center (Turner and Fishman, 1991; Figure 3.1). The clay mineral zones are – from margin to center - smectite, clinoptilolite, analcime and albite. The Morrison is well known for preserving extensive flood plain, lacustrine and fluvial deposits and has been extensively studied for the rich paleoecological information it preserves about the late Jurassic. The stratigraphic context is so well-documented, it allows for more detailed, pore-to outcrop-scale diagenetic analysis presented in this study.

Methods

Partially lithified samples about 10 cm thick were collected with a shovel from Big Bubbling Spring and Little Bubbling Spring (Figure 3.1). An unlithified sample was collected from the vent at Big Bubbling Spring. Lithified samples from an ~100ka tufa at Crystal Geyser were selected for the presence of preserved iron (oxyhydr)oxide bands (Figure 3.1). Outcrops of Brushy Basin Member (n=6) were selected for exposure and location from Lake T'oo'dichi' basin center to margin (Figure 3.1). Representatives

samples of concretions (n=42) and host rock (n=66) were collected from six locations for mineralogical, petrographical and chemical analysis.

Polished thin sections were prepared and examined (modern tufas, n=5; ancient tufas, n=1; Brushy Basin Member, n=53) to identify possible biogenic textural features and to select a smaller number of appropriate samples (n=9) and sites for further analyses (Table 3.1 shows the nine representative samples, associated clay mineral facies and analyses performed). Due to the presence of abundant microbial features in the modern spring samples, we focused on a select sample set. High resolution images were made of selected spots on one ancient tufa sample and three Brushy Basin Member samples using an FEI NanoNova Scanning Electron Microscope (SEM).

Representative samples of the Brushy Basin Member (n=4) were selected for HF (hydrofluoric acid) dissolution because of the presence of possible microbial precipitates in obvious burrows or ~1 mm by 3 mm vugs (interpreted as small burrows or charophyte

Table 3.1. Representative Brushy Basin Member samples selected for further analyses, the analyses performed and associated clay mineral zones of Turner and Fishman (1991).

Sample	Clay Min. Zone	QEM-SCAN	ICP-MS	SEM	HF+SEM
CO11-MC-1Jmb	Albite	X			
UT11-BH-28Jmb	Analcime				X
UT11-MZ-3Jmb	Clinoptilolite	X	X	X	
UT11-MZ-4Jmb	Clinoptilolite		X		X
UT11-MZ-17Jmb	Clinoptilolite	X		X	X
UT11-MZ-18Jmb	Clinoptilolite	X			
UT11-MZ-29Jmb	Clinoptilolite		X	X	
UT11-EC-2Jmb	Clinoptilolite		X		
UT11-RG-1Jmb	Clinoptilolite	X			

molds; Turner and Peterson, 2004). Bioturbated pieces of samples (<0.25 g) were disaggregated and dissolved in hydrofluoric acid. The slurry was decanted, rinsed with water and allowed to air dry on microscope slides. Slides of the slurry were examined with reflected light microscope and SEM to detect the presence of cells or other carbonaceous material. The slurry technique was chosen over an *in situ* detection technique (i.e., Raman spectroscopy) because the fluorescence of the materials overwhelmed the Raman spectra despite experimentation with multiple techniques and wavelengths rendering this an unsuitable analytical technique for the Brushy Basin Member samples.

X-ray diffraction (XRD) spectra allowed determination of mineralogy. Modern tufa samples (n=4) were air-dried and powdered, then analyzed from 2-65°2 θ . Powdered samples from the Brushy Basin Member (n=29) were also analyzed from 2-65°2 θ . QEMSCAN (Quantitative Elemental Mineralogy using SCANNing electron microscope) produces mineralogical images of entire thin sections (n=6) at 10 μ m pixel spacing.

Whole rock analysis, performed by ALS Chemex in Reno, NV, allowed identification of trace element concentrations and was also used to select target elements for further analyses. One sample from Little Bubbling Spring and four samples from Big Bubbling Spring were analyzed. A total of 55 samples from the Brushy Basin Member were selected for analysis.

Laser Ablation Induced Coupled Mass Spectroscopy (LA-ICP-MS) produced spectra to identify main and trace elemental configurations across possible biological targets. Transects of 1600 μ m were made across possible biological features and possible biomediated mineral structures (e.g., spheres) identified with petrography. Targets (n=8)

on two modern tufa samples and targets (n=3) on one ancient tufa sample were chosen along with targets (n=19) on four Brushy Basin Member samples. Trace element choices were identified with WRA. Principal component analysis (PCA) was used to identify correlations between elements.

Results

Ten Mile Graben Samples

Iron-rich mats preserved in modern Big and Little Bubbling Spring and ancient Crystal Geyser tufas show similar morphologies in petrographic microscopy (Figure 3.2); however, some early diagenetic alteration and recrystallization is observed in the ancient example (Figure 3.2). In the modern mat, microbial stalks consist of slightly rounded segments < 1 mm in length. The stalks and surrounding iron (oxyhydr)oxides are diffuse and fairly amorphous. In the ancient tufa sample, microbial stalks appear more rigid and the exterior is well-defined; however, the segmented morphology is still apparent. Modern microbial mats also exhibit microbial features and fossils visible with SEM (Figure 3.3). Microbial filaments and iron (oxyhydr)oxide framboids (a biomediated mineral habit; Cavalazzi et al., 2012; Table 3.2) are identified. In unlithified sediment collected from the vent of the modern spring, diatom tests are present (Table 3.2; Figure 3.3).

In the modern tufa samples (n=3), the main minerals identified with XRD are aragonite and calcite; quartz, halite, hematite, 6-line ferrihydrite and illite/ smectite are also present. In the unlithified sample from the spring vent, the minerals present are aragonite, calcite, 6-line ferrihydrite, and quartz.

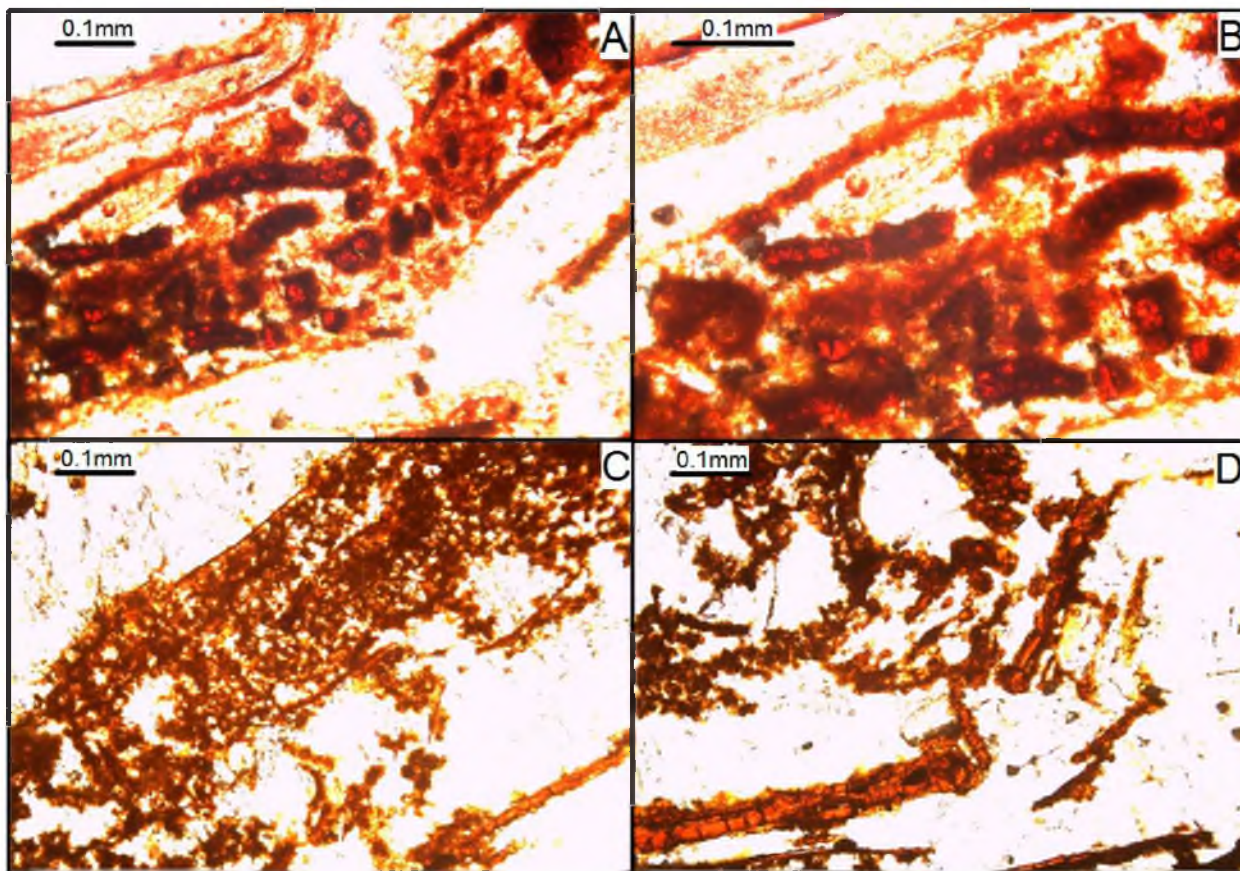


Figure 3.2. Photomicrographs (plane light) of modern (A., B.) and ancient (C., D.) tufas with iron (oxyhydr)oxides from Ten Mile Graben. A. and B. Big Bubbling Spring partially lithified sample exhibiting segmented algal stalks encrusted with iron (oxyhydr)oxides. C. and D. Ancient tufa from near Crystal Geyser exhibiting similar features, but with a higher degree of crystallinity than the modern example.

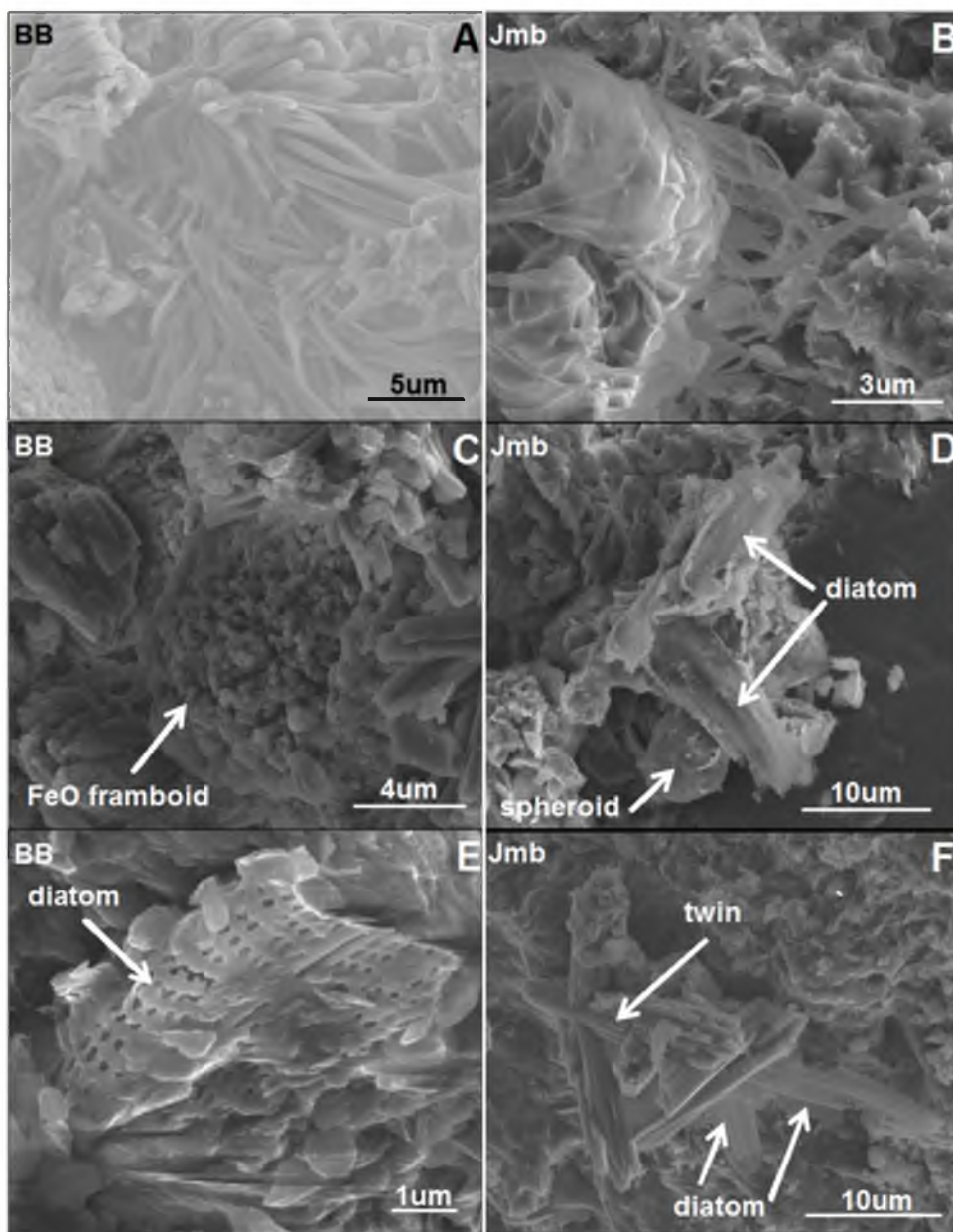


Figure 3.3. SEM images of morphological microbial fossils; left column is modern samples from Big Bubbling Spring (BB) and right column is comparative Brushy Basin Member samples (Jmb). A. and B. Filaments in modern and ancient samples. C. Modern iron (oxyhydr)oxide framboid. D. Ancient diatom tests and iron (oxyhydr)oxide spheroid. E. Modern diatom test. F. Ancient diatom tests and unidentified twinned mineral.

Table 3.2. Observed biosignature features, descriptions and criteria (from Cady, 2001) supporting biogenicity.

Description	Samples	Analytical Method	1. Thin Section/Rock	2. Sed. host rock	3. Size	4. Carbon	5. Others w/ Similar Morphology?	6. Hollow?	7. Cellular Elaboration?	Biogenic?
Segmented stalks coated w/ FeO	Modern and ancient tufas	Petrography	Yes	Yes	0.2-0.3 mm	Yes	Yes	Not observed	Yes	Probable
Branching filaments with equal width	Modern tufas, Jmb	SEM	Yes	Yes	1 μ m wide	?	Yes	Not observed	Not observed	Possible
Frambooidal FeO habit	Modern tufas	SEM	Yes	Yes	10 μ m	?	Yes	No	N/A	Possible
Siliceous, fenestral tests	Modern unlithified sediments, Jmb	SEM	Yes	Yes	~4 μ m wide	?	Yes	No	Not observed	Probable
Spheroidal FeO along edges of vugs; associated with diatoms	Jmb (thin sections, hand samples)	SEM	Yes	Yes	~5 μ m diam.	Yes	Yes	No	N/A	Probable
Rectangular algal forms with internal cellular structures (plastids)	Jmb (HF dissolved sample)	SEM	No	Yes	~10 by 25 μ m	?	Yes	Yes	Yes	Possible
Oval form with radiating segments and central globular structure	Jmb (HF dissolved sample)	SEM	No	Yes	20 by 25 μ m	?	Yes	Yes	Yes	Possible

Brushy Basin Member Samples

The Brushy Basin Member has many macroscopic biogenic features such as charophyte molds (vugs), burrows, petrified wood and dinosaur bones (Figure 3.4). These macroscopic features provided clues to begin the search for microscopic biogenic features and associated biogenic mineral textures using a petrographic microscope. Petrographic analysis indicates that elongate charophyte molds (~ 1 mm wide by 3 mm long) are typically filled with massive calcite or albite (Figure 3.5). Chlorite is also commonly present in charophyte molds and exhibits lath and/ or radiating acicular habits that overprint the massive calcite/ albite fill. Laths typically radiate inward from the edges of charophyte molds and radiating acicular habits are common in the centers. Edges of charophyte molds commonly have reduction halos (Figure 3.5) and iron (oxyhydr)oxide spheroids are clustered along the edges in some examples (Table 3.2). Features observed with SEM in the Brushy Basin Member including filamentous structures, spheroids and diatom fossils (Table 3.2; Figure 3.3). Diatom tests are present along the interior edge of a charophyte mold directly abutting an unidentified twinned mineral in one example and spheroids of iron (oxyhydr)oxide in another example (Figure 3.3). Slurry from charophyte molds and burrows in Brushy Basin Member samples (n=4) dissolved in HF and examined with SEM show fossil algal microbes (~30 μm long) and cellular internal structures (0.5 μm long) that are likely plastids (major organelles found in the cells of plants and algae; Table 3.2; Figure 3.6).

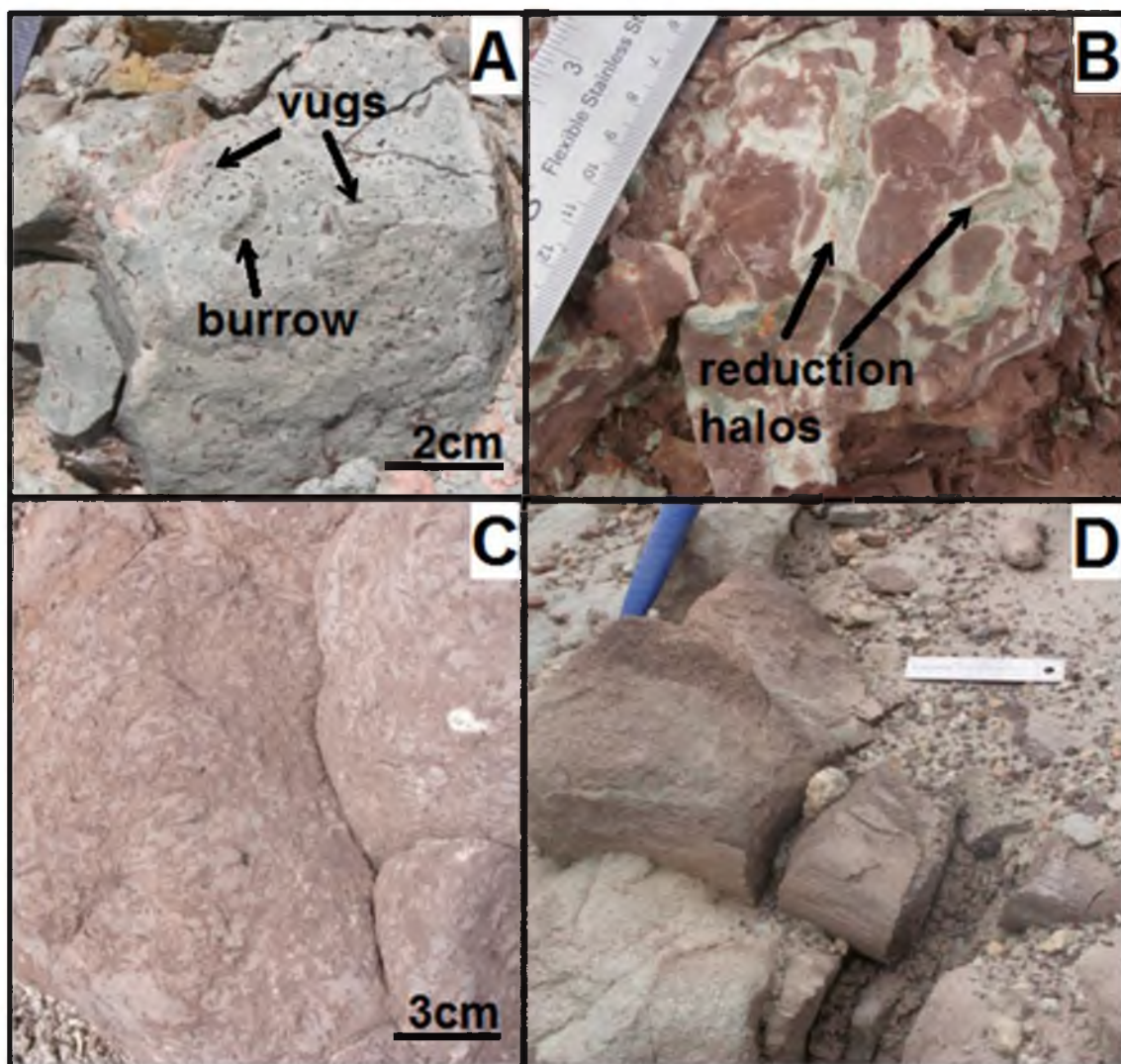


Figure 3.4. Macroscopic biosignatures (trace fossils and permineralized bones) in the Jurassic Brushy Basin Member. A. Vugs (interpreted as charophyte molds or larvae hatches) and burrows. B. Reduction halos around root traces. C. Highly burrowed horizon. D. Fossilized dinosaur femur; scale is 12 cm.

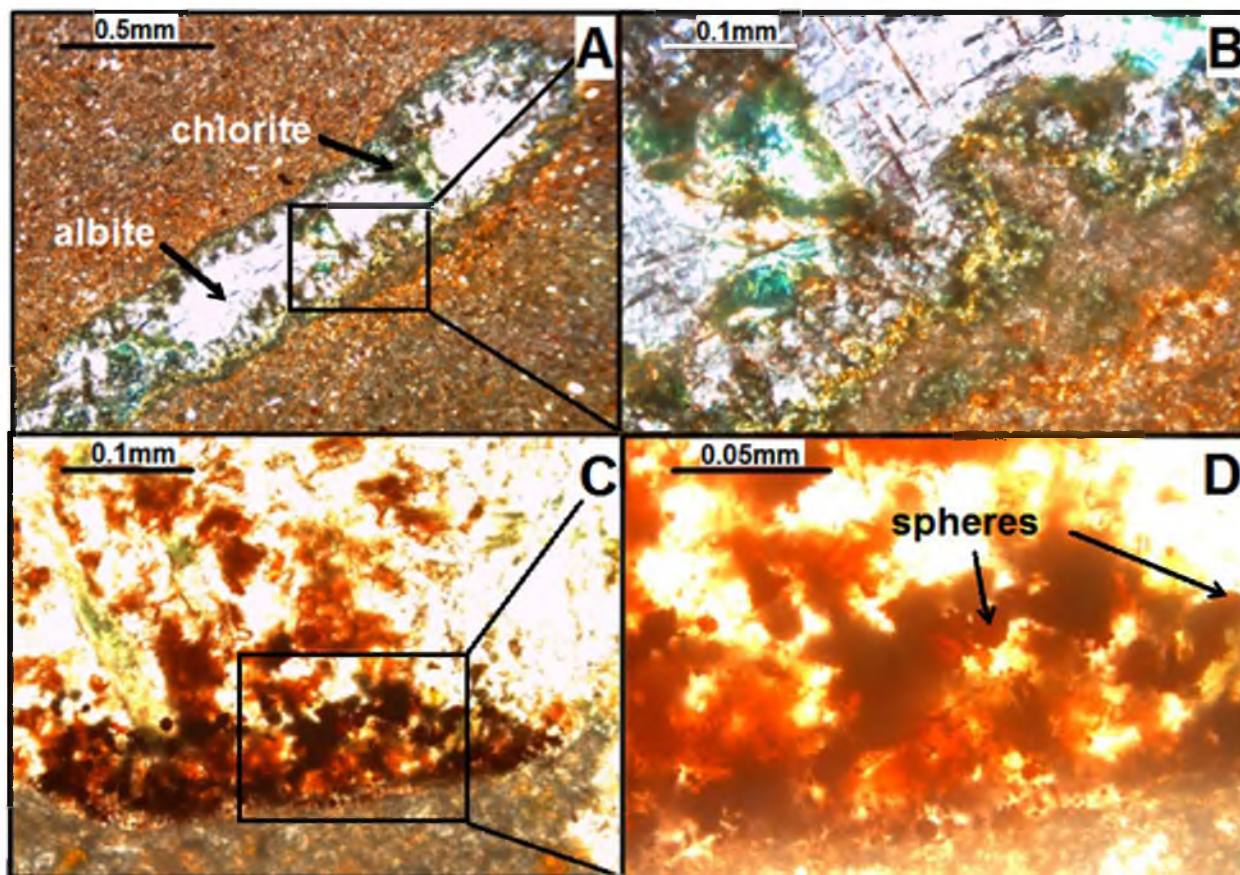


Figure 3.5. Petrographic examples of authigenic minerals in Brushy Basin Member samples. A. Albite and chlorite filled charophyte mold. B. Inset of view A. C. Spheroidal iron (oxyhydr)oxides along edge of charophyte mold. D. Inset of view C. diagnostic minerals are present only in tuffs and not in the more common siltstone/

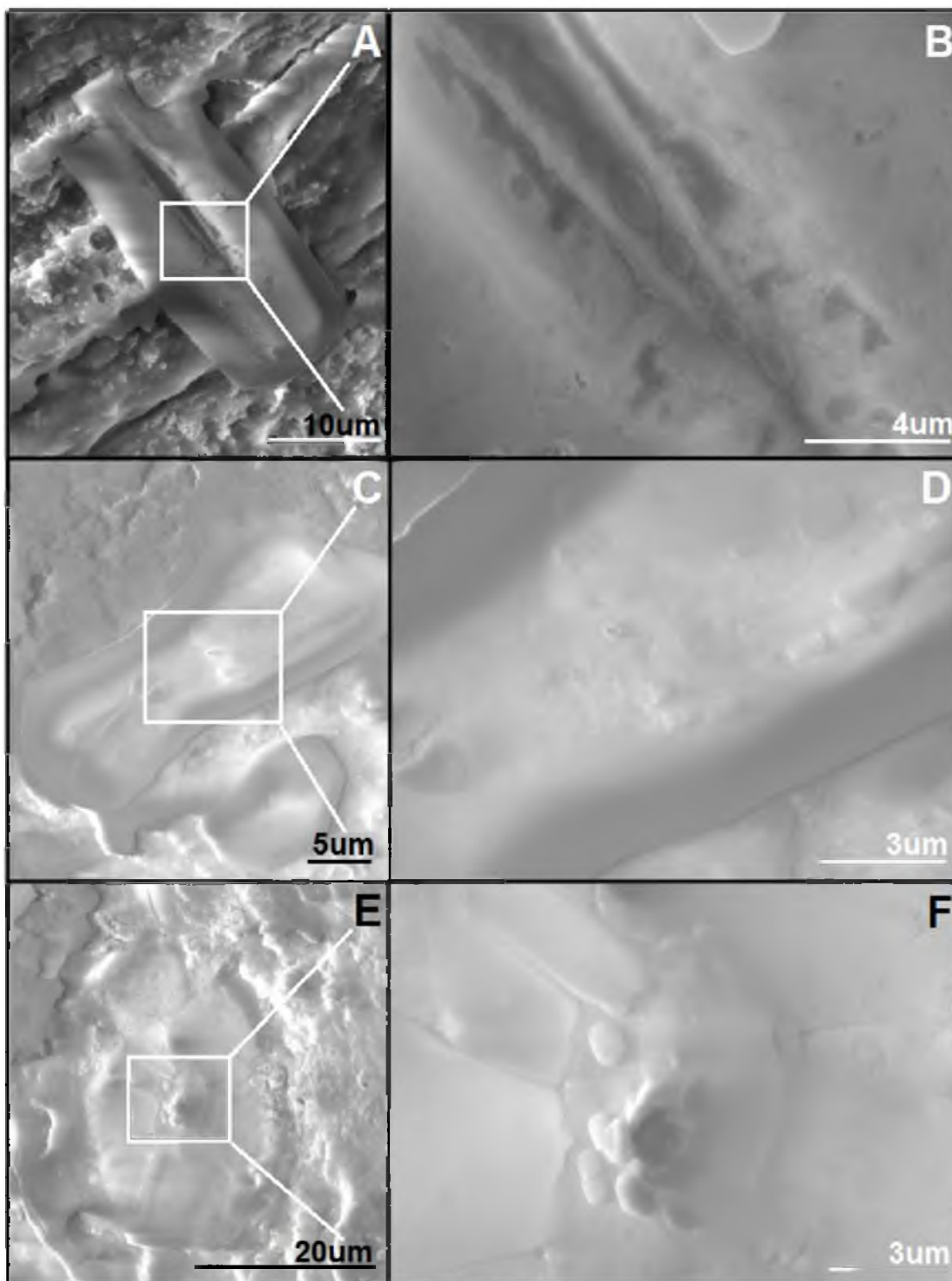


Figure 3.6. SEM images showing cellular elaboration in sample MZ4 dissolved in HF. A. Rectangular alga and B. inset showing internal structure. C. Rectangular alga and D. inset showing internal structure (likely plastids). E. Circular alga and F. inset showing internal structure similar to internal structure of views C. and D.

The Brushy Basin Member samples analyzed with XRD (n=29 from all clay mineral zones) show that clays are dominated by smectite, but illite, illite/ smectite, clinoptilolite, chlorite, analcime and kaolinite are also present. Iron minerals are dominated by goethite and hematite, but 6-line ferrihydrite and siderite are also present. Iron phosphate, apatite and calcite are common. The clay minerals in samples do not typically correlate with the clay mineral zones of Lake T'oo'dichi' because those claystone facies analyzed in this study (Turner and Fishman, 1999).

Area percent mineralogy reported by QEMSCAN (Table 3.3) shows detrital minerals such as quartz, feldspars and biotite. Authigenic minerals include albite, barite, calcite, chlorite, clinoptilolite, analcime, apatite and iron (oxyhydr)oxides. Porosity ranges from 17% in a sandstone sample (RG1) to 0.3% in a claystone sample (MZ3). Trace amounts of organic matter are detected (0.01-0.02 area%; Table 3.3). Organic carbon classification with QEMSCAN is based on brightness value as well as unusually high counts of carbon. In sample MZ3, charophyte molds are filled with barite, calcite, chlorite and albite (Figure 3.7). Iron (oxyhydr)oxide is present throughout the sample as well as in charophyte molds. Small amounts of organic matter are also present throughout the sample (Figure 3.7).

Principal Component Analysis (PCA) and Correlation of Trace Elements

Principal Component Analysis (PCA) is compiled for LA-ICP-MS transects across modern tufa samples ($n_{\text{transects}}=8$), an ancient tufa sample ($n_{\text{transects}}=3$) and four Brushy Basin Member samples ($n_{\text{transects}}=8$). In four transects across two modern tufa samples, carbon correlates with iron (Table 3.4). Carbon correlates with iron in three

Table 3.3. Area % mineralogy reported by QEMSCAN on Brushy Basin Member samples from McElmo Canyon (MC), Rattlesnake Gulch (RG) and Montezuma Creek (MZ).

Mineral Name	MC1	RG1	MZ17	MZ18	MZ3
Albite	13.37	10.70	5.72	1.81	8.01
Alkali Feldspar	3.27	3.08	6.69	8.86	8.02
Analcime	0.04	0.08	0.07	0.11	0.05
Apatite	0.04	0.06	0.06	20.05	0.02
Barite	0.18	0.31	0.02	0.02	0.56
Biotite	0.01	0.08	0.01	0.08	0.08
Calcite	2.46	1.10	0.67	6.09	1.78
Chlorite	5.20	5.72	21.15	14.19	15.43
Clinoptilolite	1.63	2.55	6.44	0.21	4.91
Fe-oxides	3.00	0.16	0.35	2.32	2.35
Kaolinite	0.44	0.25	0.01	0.00	0.00
Organic Matter	0.01	0.02	0.01	0.01	0.02
Other	0.01	0.04	0.04	0.10	0.01
Plagioclase	4.18	1.94	3.99	8.68	4.33
Porosity	11.79	17.38	1.96	3.63	0.27
Pyrite	0.00	0.00	0.00	0.00	0.02
Quartz	64.60	73.49	48.07	33.42	52.26
Smectites	1.54	0.43	6.71	4.06	2.16

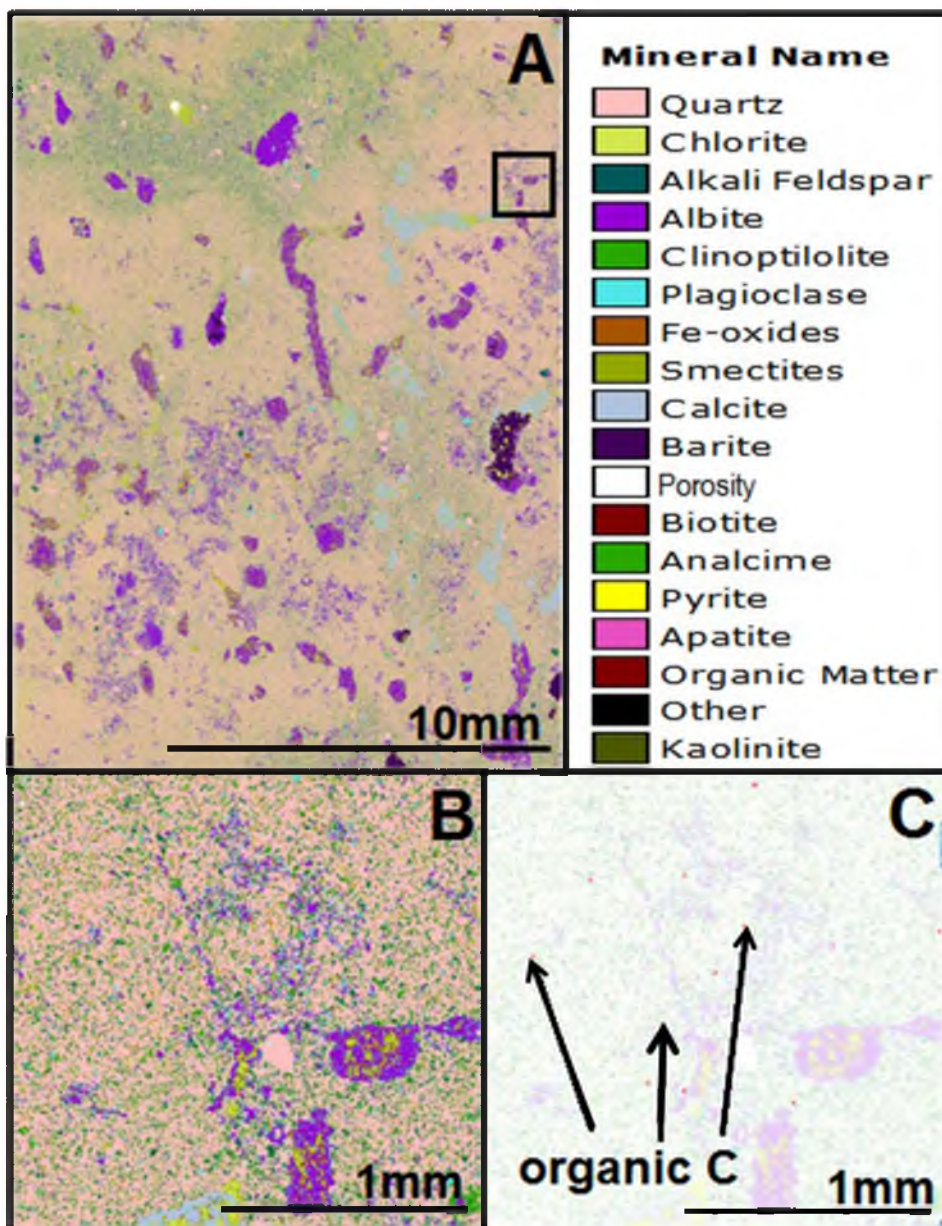


Figure 3.7. QEMSCAN image of charophyte molds and organic carbon in Brushy Basin Member. A. Image of sample MZ3 at $5\mu\text{m}$ pixel spacing. Square shows area of views B. and C. B. Close up of square in A. C. Image showing only organic carbon pixels (red) overlain on view B.

Table 3.4. Three groups of elemental correlations from PCA of LA-ICP-MS transects. Tufa samples are in red font and Jmb samples are in blue font.

C, Fe Correlation		C, S, Se Correlation		Anomalous		
Sample #	Other Corr. Elements	Sample #	Other Corr. Elements	Sample #	Elements Corr. w/ C	Other Corr. Elements
LB1 MSD1	none	BB2 MSD 3	none	BB2 MSD1	Na	none
BB2 MSD2	Cu, Na, Ni, Al	MZ4 1	As, Ni, P, U	LB1 MSD2	Mn	none
BB2 MSD4	As, Ba, Ca, Mn, Na, P, S, Sr, U	MZ3 1	P, U	LB1 MSD3	Cu	Ca, Ni, Si
BB2 MSD5	As, Ba, Mn	EC2 1	none	MZ3 2	Mn, Si	As, Cu, Ni, S
CG1 AT1	As, Na, Si, U	EC2 2	As, P	MZ29 3	Al, Na	Si
CG1 AT2	As, Na, Mn, U	EC2 3	As, Ba, P			
CG1 AT3	Mn, Ni, S	EC2 4	none			
MZ29 1	As, Cu, Na, Ni					
MZ29 2	Cu, Ni					

transects across one ancient tufa sample as well as in a spheroidal iron (oxyhydr)oxide precipitate inside a charophyte mold in a Brushy Basin Member sample (MZ29; Figure 3.8). Arsenic is also typically correlated with carbon and iron in these samples.

In one transect of a modern tufa sample, carbon correlates with sulfur and selenium. These elements also correlate in five transects across three possible biogenic features in three Brushy Basin Member samples (MZ3, MZ4 and EC2). Phosphorous typically correlates with sulfur and selenium as well.

A third group of anomalous correlations with carbon is present. A transect across one modern tufa sample and another transect across one Brushy Basin Member sample show a correlation between carbon and sodium. Transects across single modern tufa and Brush Basin Member samples show carbon correlated with manganese. A transect across one modern tufa sample shows carbon correlated with copper. In three out of these five transects, silicon also correlates with carbon.

In summary, microbial features in modern and ancient tufas are similar enough to recognize the features after ~100ka of diagenetic alteration, although some recrystallization is observed in the ancient examples. Diatoms and algae are present in the tufa mats. Charophyte molds in Brushy Basin Member samples exhibit mineral fill with lath and acicular chlorite habits as well as spheroidal iron (oxyhydr)oxide habits along the edges. Fossil diatoms and algal forms are associated with the spheroidal iron (oxyhydr)oxide mineral habits. QEMSCAN shows small amounts of organic carbon associated with the charophyte molds and 6-line ferrihydrite is detected with XRD in modern and ancient samples. Two distinct elemental suites are associated with microbial

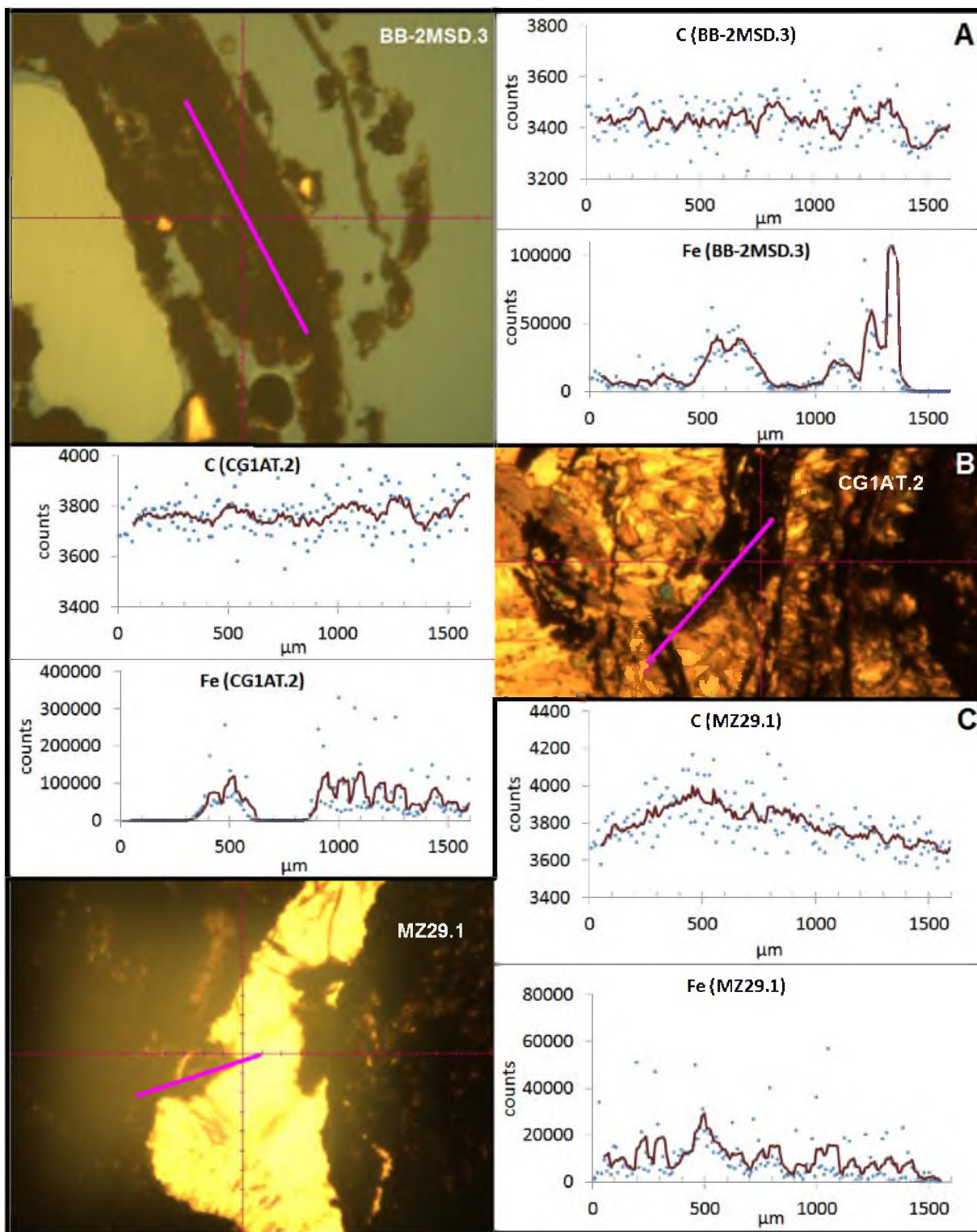


Figure 3.8. LA-ICP-MS data for modern (A.) and ancient (B.) tufas and Brushy Basin Member sample (C.). Blue dots are actual counts and dark brown line shows a five period moving average. Pink lines on photomicrographs show transect for laser ablation and are all ~ 1600 μm in length.

features in both the modern and ancient tufas and the Brushy Basin Member samples: 1) C, Fe, As, and 2) C, S, Se.

Interpretation and Discussion

Interpretation of Modern and Ancient Tufas and Brushy Basin

Member Features

Iron-rich mats contain microbial fossils in both the modern and ancient tufas (Table 3.2); however, some degradation is observed in the ancient examples (Figure 3.2). In the modern mats, cyanobacteria exhibit well-developed segments with amorphous iron (oxyhydr)oxides precipitated on and around them. In the ancient tufa samples, the segmented cyanobacteria fossils are present, although they are smaller than the modern features and the iron (oxyhydr)oxides appear to have recrystallized to larger crystals (less amorphous) via Ostwald ripening (Lifshitz and Slyozov, 1961; Sultan and Ortoleva 1993; Ortoleva 1982; Müller and Ross 2003). High-resolution SEM analysis of modern tufas shows fibrous, branching microbial fossils associated with framboidal structures that are probable biomediated iron (oxyhydr)oxide habits (Table 3.2; Figure 3.3; Cavalazzi et al., 2012). Diatoms are present in the unlithified sample from the spring vent (Table 3.2; Figure 3.3).

In the Brushy Basin Member, macroscopic bioturbation features (such as charophyte molds and burrows) provide a starting point to investigate microscopic biosignatures using the reasoning that in the presence of organic matter such as roots, feces or other animal matter, microbes will utilize the organic carbon as an energy source. Suspected paleomicrobial features in charophyte molds are spheroidal iron

(oxyhydr)oxide precipitates along the edges and reduction halos (Figure 3.5). SEM images show branching filaments similar in morphology to modern tufas (Table 3.2). Degraded diatoms present in close proximity to iron (oxyhydr)oxide spheroids and twinned minerals suggests that spheroids may be a biomediated mineral habit (Table 3.2; Figure 3.3). Both the filaments and the diatoms are present along the edges of charophyte molds. Dissolution in HF of the siliceous portion of the rocks with charophyte molds reveals many algal fossils with cellular elaboration (Table 3.2).

Biogenicity of Jurassic Brushy Basin Member Features

The first requirement for proving biogenicity of putative microbial fossils is that potential features must occur in a thin section in order to show they are not modern contaminants (Cady, 2001; Westall, 2008). Most of these microbial features – such as diatoms and suspected biomineral habits – do occur in thin section. However, careful dissolution of the charophyte molds reveals other types of algal microbial fossils (Table 3.1). Although it is possible that algal microbial features present in the slurry are modern contaminants, diatoms present in thin section suggest that these other forms of algae associated with the diatoms are likely fossil algae as well.

The second requirement is that microbial features must occur in sedimentary or low grade metamorphic rocks (Cady, 2001) and the Brushy Basin Member is a lacustrine volcanoclastic mudrock (Turner and Fishman, 1991). The third requirement is that microfossils must be larger than the smallest known extant organisms ($\sim 0.01\mu\text{m}$; Cady et al., 2001). The features in the Brushy Basin Member are all $\geq 10\mu\text{m}$.

The fourth requirement of biogenicity is that features must be composed of kerogen (Cady, 2001). Raman spectroscopy has been unable to detect kerogen because, despite experimentation with multiple wavelengths and types of Raman spectroscopy, fluorescence overwhelms the signal on most samples. Organic phosphorous was detected with Raman spectroscopy in one sample that was collected directly above a fossilized dinosaur bone. Carbonaceous material is visible with reflected light microscope in slurry from all dissolved samples (see Table 3.1 for samples dissolved with HF). Carbon signals from LA-ICP-MS increase over the putative forms as would be expected if they were carbonaceous and minor amounts of organic carbon are detected with QEMSCAN. Although kerogen is not directly detected, the combination of multiple lines of evidence suggests that these features are likely carbonaceous.

The fifth requirement is that multiple features with similar morphology are present and the feature is not an isolated, lone form (Cady, 2001). Diatoms, twisted stalks, filaments, and rectangular and circular algal forms with internal structures are quite common in the samples examined (Table 3.2; Figures 3.3, 3.5, 3.6). Clusters of spheroids are present in macroscopic biogenic features (charophyte molds) and spheroids are associated with diatom fossils. This supports an interpretation of a biomediated mineral habit for the spheroids (Banfield et al., 2001; Bonny and Jones, 2007; Table 3.2).

The sixth criterion is that the features must be hollow and some algal examples show hollow interiors imaged with SEM (Table 3.2; Figure 3.6). Lastly, the seventh requirement is that features must show cellular elaboration. All of the algal features, such as the diatoms and the rectangular and oval algal forms, show cellular details (Table 3.2; Figure 3.3, 3.6). These features completely meet six of the seven criteria for proving

biogenicity and even though kerogen has not been detected, these features are likely carbonaceous. Thus, these features are classified as probable microfossils (Table 3.2).

Mineralogical and Chemical Biosignatures

Mineralogy in the modern (unlithified and lithified) and ancient tufas are similar and contain disordered, kinetically-favored mineral phases such as 6-line ferrihydrite and aragonite. In the modern unlithified sample, only disordered phases (6-line ferrihydrite and aragonite) are present. Finally, some of the Jurassic Brushy Basin Member samples contain 6-line ferrihydrite. In lab bench experiments, ferrihydrite is very unstable and recrystallizes to more stable phases over the course of days or weeks (Cornell and Schwertmann, 1996; Kukkadapu, 2003). However, organic polymers retard the recrystallization process (Chan et al., 2009) and therefore, the presence of 6-line ferrihydrite in lithified tufas and ancient rocks can function as a potential biosignature indicator (Chatellier and Fortin, 2004; Kennedy et al., 2004; Schwertmann et al., 2005; Chan et al., 2009).

Microbial fossils along the edges of charophyte molds show evidence of microbial mediation of minerals. The close association of unusual crystal habits (spheroids) with algal fossils, such as diatoms, suggests that these mineral habits formed via biomediation because crystal growth in the presence of organic ligands can alter the stability of crystallographic surfaces (Mann et al., 1993; Albeck et al., 1996; Banfield et al., 2001; Chan et al., 2009)

Distinct trace element suites are recognized as a means of identifying biosignatures because organisms sequester trace elements during their lifetime and these

suites can be preserved in minerals (Banfield, 2001; Ferris, 2005). Correlation of elements from LA-ICP-MS in transects across putative biogenic features suggests that two suites of trace element associations can function as biosignature indicators. The first is a correlation of carbon and iron. These elements are also commonly correlated with arsenic. The second suite is carbon, sulfur and selenium. These elements are commonly correlated with phosphorous.

Conclusions

Diatoms and other algal fossils show degradation and some recrystallization of the iron (oxyhydr)oxides that precipitate on and around algal stalks; however, the morphological features are clearly recognizable on millennial time scales. Similar diatoms and algal fossils are present in the Brushy Basin Member and these features meet all seven of the criteria supporting biogenicity in ancient rocks. Other possible biosignatures that occur in both the modern and ancient examples include biomediated spheroidal iron (oxyhydr)oxides and the presence of more amorphous iron (oxyhydr)oxides such as 6-line ferrihydrite. Modern and ancient examples exhibit chemical biosignatures of two suites of elements (1) C, Fe, As and, 2) C, S, Se) that may be unique to sequestration by microbes and can serve as markers for potential biosignatures.

As the study of Gale Crater on Mars progresses, biosignatures in iron (oxyhydr)oxides such as framboids, spheroids, diagnostic trace element suites and more amorphous mineral phases can serve as markers for possible preserved biosignatures where future explorations hope to detect past evidence of life. These terrestrial examples:

1) show that biosignatures as well as bona fide microbial fossils are preserved in Jurassic rocks, 2) show how microbial iron (oxyhydr)oxide precipitates persist and recrystallize to more stable forms during diagenesis, and 3) provide a ground truth library of mineral textures, phases and trace element configurations to explore and compare in extraterrestrial iron (oxyhydr)oxides (e.g., in similar clay-rich shales in Gale Crater on Mars).

References

- Albeck, S., Addadi, L., and Weiner, S., 1996. Regulation of calcite crystal morphology by intracrystalline acidic proteins and glycoproteins. *Connective Tissue Research*, 35, 419-424.
- Allison, P.A., Briggs, D.E.G., 1991. *Taphonomy of nonmineralized tissues*. Plenum Press, New York, NY, New York, NY, United States (USA).
- Allison, P.A., Pye, K., 1994. Early diagenetic mineralization and fossil preservation in modern carbonate concretions. *Palaios*, 9, 561-575.
- Banfield, J.F., Moreau, J.W., Chan, C.S., Welch, S.A., and Little, B., 2001. Mineralogical biosignatures and the search for life on Mars. *Astrobiology*, 1, 447-465.
- Berner, R. A., 1968. Calcium carbonate concretions formed by the decomposition of organic matter. *Science*, 1, 195-197.
- Burnside, N.M., 2010. U-Th dating of travertines on the Colorado Plateau: implications for the leakage of geologically stored CO₂. PhD thesis, University of Glasgow, UK.
- Cady, S.L., 2001. Paleobiology of the Archean. *Advances in Applied Microbiology*, 50, 3-35.
- Cady, S.L. and Farmer, J.D. 1996. Fossilization processes in siliceous thermal springs: trends in preservation along thermal gradients, p. 150-173. In Bock, G.R. and Goode, J.A. (eds.), *Evolution of Hydrothermal Ecosystems on Earth (and Mars?)*, Ciba Foundation Symposium 202. John Wiley and Sons, Chichester.
- Cady, S.L., Farmer, J.D., Grotzinger, J.P., Schopf, J.W., Steele, A., 2003. Morphological biosignatures and the search for life on Mars. *Astrobiology*, 3, 351-368.

- Campbell, K.A., Bundle, T.F., Browne, P.R.L., 2004. Late Pleistocene siliceous sinter associated with fluvial, lacustrine, volcanoclastic and landslide deposits at Tahunaatara, Taupo volcanic zone, New Zealand. *Transactions of the Royal Society of Edinburgh: Earth Sciences*, 94, 485-501.
- Cavalazzi, B., Barbieri, R., Cady, S.L., George, A.D., Gennaro, S., Westall, F., Lui, A., Canteri, R., Rossi, A.P., Ori, G.G., Taj-Eddine, K., 2012. Iron-framboids in the hydrocarbon-related Middle Devonian Hollard Mound of the Anti-Atlas mountain range in Morocco: Evidence of potential microbial biosignatures. *Sedimentary Geology*, 263-264, 183-193.
- Chan, C.S., Fakra, S.C., Edwards, D.C., Emerson, D., Banfield, J.F., 2009. Iron oxyhydroxide mineralization on microbial extracellular polysaccharides. *Geochimica et Cosmochimica Acta*, 73, 3807-3818.
- Châtellier, X., and Fortin, D., 2004. Adsorption of ferrous ions onto *Bacillus subtilis* cells. *Chemical Geology*, 212, 209– 228.
- Chure, D.J., 1994. *Koparion douglassi*, a new dinosaur from the Morrison Formation (upper Jurassic) of Dinosaur National Monument; the oldest *troodontid* (*theropoda: Maniraptora*). *Geology Studies*, 40, 11-15.
- Cornell, R.M., Schwertmann, U., 1996. The iron oxides; structure, properties, reactions, occurrence and uses, VCH Verlagsgesellschaft, Weinheim, Federal Republic of Germany (DEU), p. 573.
- Evans, S.E. and Chure, D.C., 1998. *Paramacellodid* lizard skulls from the jurassic morrison formation at Dinosaur National Monument, Utah. *Journal of Vertebrate Paleontology*, 18, 99-114.
- Farmer, J.D., Des Marais, D.J., 1999. Exploring for a record of ancient Martian life. *Journal of Geophysical Research*, 104, 26,977-26,995.
- Henrici, A.C., 1998. A new pipoid anuran from the late Jurassic Morrison Formation at Dinosaur National Monument, Utah. *Journal of Vertebrate Paleontology*, 18, 321-332.
- Kennedy C.B., Scott S.D., and Ferris F.G., 2004. Hydrothermal phase stabilization of 2-line ferrihydrite by bacteria. *Chemical Geology*, 212, 269–277.
- Knoll, A. H., Exceptional preservation of photosynthetic organisms in silicified carbonates and silicified peats, *Philos. Trans. R. Soc. London, Ser. B*, 311, 111-122, 1984.

- Kolo, K., Konhauser, K., Krumbein, W.E., van Ingelgem, Y., Hubin, A., 2009. Microbial dissolution of hematite and associated cellular fossilization by reduced iron phases; a study of ancient microbe-mineral surface interactions. *Astrobiology*, 9, 777-796.
- Konhauser, K.O., Jones, B., Reysenbach, A. & Renaut, R.W. 2003, Hot spring sinters: keys to understanding Earth's earliest life forms. *Canadian Journal of Earth Sciences/Revue Canadienne des Sciences de la Terre*, 40, 1713-1724.
- Kowallis, B.J., Christiansen, E.H., Deino, A.L., Peterson, F., Turner, C.E., Kunk, M.J., Obradovich, J.D., 1998. The age of the Morrison Formation. *Modern Geology*, 22/1– 4, 235– 260.
- Kukkadapu, R.K., 2003. Transformation of 2-line ferrihydrite to 6-line ferrihydrite under oxic and anoxic conditions. *American Mineralogist*, 88, 11-12.
- Lifshitz I.M., Slyozov V.V. 1961. The kinetics of precipitation from supersaturated solid solutions. *Journal of Physics and Chemistry of Solids*, 19, 35–50.
- Mann, S., Archibald, D.D., Didymus, J.M., Douglas, T., Heywood, B.R., Meldrum, F.C., and Reeves, N.J., 1993. Crystallization at inorganic-organic interfaces – biominerals and biomimetic synthesis. *Science*, 260, 1286-1292.
- Milliken, R.E., Grotzinger, J.P., Thomson, B.J., 2010. Paleoclimate of Mars as captured by the stratigraphic record in Gale Crater. *Geophysical Research Letters*, 37, Citation L04201.
- Müller, S.C., Ross J., 2003. Spatial structure formation in precipitation reactions. *Journal of Physical Chemistry A*, 107, 7997–8008.
- Ortoleva, P., 1982. Solute reaction mediated precipitate patterns in cross gradient free systems. *Zeitschrift für Physik B: Condensed Matter*, 49, 149–56.
- Parenteau, M.N., Cady, S.L., 2010. Microbial biosignatures in iron-mineralized phototrophic mats at Chocolate Pots Hot Springs, Yellowstone National Park, United States. *Palaios*, 25, 97-111.
- Rainey, D.K., and Jones, B., 2010. Preferential soft-tissue preservation in the Hot Creek carbonate spring deposit, British Columbia, Canada. *Sedimentary Geology*, 227, 20-36.
- Rancourt, D.G., Thibault, P., Mavrocordatos, D. & Lamarche, G. 2005, Hydrous ferric oxide precipitation in the presence of nonmetabolizing bacteria; constraints on the mechanism of a biotic effect. *Geochimica et Cosmochimica Acta*, 69, 553-577.

- Schwertmann U., Wagner F., and Knicker H., 2005. Ferrihydrite humic associations: magnetic hyperfine interactions. *Soil Science Society of America Journal*, 69, 1009–1015.
- Sultan R, Ortoleva, P., 1993. Periodic and aperiodic macroscopic patterning in two precipitate post-nucleation systems. *Physica D*, 63, 202–12.
- Thomson, B.J., Bridges, N.T., Milliken, R., Baldrige, A., Hook, S.J., Crowley, J.K., Marion, G.M., de Souza Filho, C.R., Brown, A.J., Weitz, C.M., 2011. Constraints on the origin and evolution of the layered mound in Gale Crater, Mars using Mars Reconnaissance Orbiter data. *Icarus*, 214, 413-432.
- Turner, C.E., Fishman, N.S., 1991. Jurassic Lake T'oo'dichi'; a large alkaline, saline lake, Morrison Formation, eastern Colorado Plateau. *Geological Society of America Bulletin*, 103, 538-558.
- Turner, C.E., Peterson, F., 2004. Reconstruction of the Upper Jurassic Morrison Formation extinct ecosystem; a synthesis. *Sedimentary Geology*, 167, 309-355.
- Westall, F., 2008. Morphological Biosignatures in Early Terrestrial and Extraterrestrial Materials. *Space Science Reviews*, 135, 95-114.

DISSERTATION CONCLUSIONS

The central question of this dissertation is: how do variables such as microbial influence, sediment composition and fluid chemistry affect iron redox reactions and iron (oxyhydr)oxide nucleation, cement textures, mineralogy and chemistry? The overarching goals are to better understand biomediation in diagenetic iron mobilization and precipitation, to better recognize how biosignatures are preserved in iron (oxyhydr)oxides and to unravel the diagenetic histories recorded in concretions. To answer these questions and accomplish these tasks, the research is segregated into three parts that individually examine: 1. reservoir fluid chemistry in a putative natural CO₂ reservoir, 2. concretion formation in reactive, volcanoclastic host rock, and 3. comparative microbial influences in the precipitation of iron (oxyhydroxides) in a modern spring system and the Jurassic Brushy Basin Member – a formation with abundant macroscopic biotic influence. The Jurassic stratigraphic section on the Colorado Plateau is largely composed of three eolian reservoir units – the Navajo Sandstone is the middle unit. Overlying this reservoir is a thick sequence of shales that range in age from late Jurassic to Tertiary. The Brushy Basin Member is the basal part of these shales that function as a seal for the underlying Jurassic reservoir.

An important outcome of this research is documentation of the effects of a CO₂-charged diagenetic fluid on cement precipitation on a pore- to outcrop-scale. Addition of CO₂ to a saline reservoir would precipitate dolomite in amounts to significantly reduce porosity. The average reported porosity in the Navajo Sandstone is ~20-25%; the porosity

in the Justensen Flats study area is ~7% and petrography shows the pore space is typically filled with dolomite. Clays also precipitate; however, due to the low K-feldspar component (~5 wt.%) in the Navajo Sandstone, clays are not produced in enough abundance to significantly reduce porosity in this unit.

Another important outcome is the finding that reservoir fluids are quite spatially variable. Comparison of the Navajo Sandstone in Justensen Flats in eastern Utah with Spencer Flat in southern Utah shows regional-scale fluid variability. In volcanoclastic shales, concretions record the variability of fluid/ rock interactions on outcrop-scales and even within stratigraphic horizons. In these reactive sediment compositions, reactants for concretion formation are sourced from localized diagenetic microenvironments and concretions themselves are quite variable, both in geometry and mineralogy. These concretions also are quite similar chemically to the adjacent host rock.

Fluid flow and precipitation of cements can be lithologically controlled even in porous and permeable media, as evidenced by the reaction front in Justensen Flat. The front is well cemented where it abuts a less porous and permeable bounding surface on top. Further evidence of lithologic control comes from the mineralogical and morphological uniformity of the concretions in the porous sandstone lenses in the Brushy Basin Member suggesting that reactants in porous lithologies move via fluid flow and are being sourced from relatively greater distances than concretions formed locally in claystone and siltstone lithofacies. Understanding the variability of reservoir fluids as well as the effect of CO₂-charged fluid in a saline reservoir has application for providing better parameters for predictive modeling of supercritical CO₂ injection for sequestration and enhanced oil recovery.

Diagenesis in the fine-grained Brushy Basin Member is limited to early diagenesis and the diagenetic facies record meter-scale paleotopography. Diagenetic microenvironments are due to the presence of reactive sediments and variable amounts of oxygen related to water depth. Diversity in macroscopic trace fossils reflects the environment, and shallow water to subaerial environments exhibit greater biodiversity recorded in trace fossils. Conversely, deeper water reduced facies exhibit mostly charophyte molds – remnants of microbial algae – and suggest a relatively extreme geochemical environment that limited the diversity of life.

Navajo Sandstone iron (oxyhydr)oxide concretions exhibit striking physical similarities with hematite concretions in the Burns formation at Meridiani Planum, Mars. Both the Burns formation and the Navajo Sandstone are fine-grained eolian sandstones; however, the Burns formation is a chemically reactive, volcanoclastic and sulfate sandstone and the Navajo Sandstone is a relatively inert, quartz arenite. The question remains as to how the reactive volcanoclastic sediment of the Burns formation affected concretion formation. This research shows that reactive, volcanoclastic host rock provides an abundant and accessible source of reactants, but that inherent petrophysical properties (e.g., porosity, grain size) may affect concretion morphology to a greater degree than chemical properties.

A third major result of this research is the contribution to understanding the effects of diagenesis on microbial fossils preserved in iron (oxyhydr)oxides. Comparison of modern microbial iron (oxyhydr)oxide mats from the Ten Mile Graben spring system with ~100ka tufas from the same spring system shows that although microbial fossils exhibit degradation and recrystallization on millennial time scales, microbial features are

still clearly distinguishable. Microbial fossils and their close association with macroscopic trace fossils are documented in the Jurassic Brushy Basin Member of the Morrison Formation. Thus, both the modern and the Jurassic examples suggest that preservation potential in diagenetic minerals is good, and that biosignature evidence may persist for long periods of geologic time, despite burial and other conditions.

Microbial features from modern and ancient tufas and from the Brushy Basin Member all exhibit distinct chemical, mineralogical and morphological biosignatures. Data from LA-ICP-MS show two diagnostic chemical suites associated with microbial features: 1) C, Fe, As, and 2) C, S, Se. X-ray diffraction also detects 6-line ferrihydrite in both modern and ancient iron (oxyhydr)oxides. The presence of the unstable iron (oxyhydr)oxide phase suggests that the mineral phase itself may function as a biosignature due to the presence of organic compounds that retard or block recrystallization to more stable phases. Spheroids and framboids present in close association with microbial fossils are likely also biosignatures.

Iron is the fourth most common element on the surface of the Earth and Mars is also iron-rich. It is likely that any rocky planet we discover and study may also have iron. This research helps to interpret the history of rock-fluid-biota interactions that iron precipitates record in sedimentary rocks. Important considerations are: variability of diagenetic fluids on an outcrop to regional scale; the diagenetic microenvironments responsible for concretion formation in shales; and subtle original paleotopography recorded in fine-grained (less permeable) shales. These factors influence the iron (oxyhydr)oxide mineralogy and contribute to the body of knowledge necessary to interpret similar rocks on Mars, such as the Burns formation.

In Gale Crater on Mars, one of the thickest stratigraphic sections (~5 km) is exposed. These rocks are composed of iron- and clay-rich smectites in the lower section and sulfates in the upper section. The Brushy Basin Member is a similar iron- and clay-rich shale. Results from this Brushy Basin Member research on paleo Lake T'oo'dichi may be invaluable to interpret the depositional environment and paleotopography at Gale Crater – likely an alkaline saline lacustrine system. The library of diagnostic biotic fingerprints produced by this study may aid in the search for microbial fossils in sedimentary rocks on Mars.

It is acknowledged that no terrestrial analog is a perfect match for any Mars geology for two principal reasons. The first is that the extraterrestrial chemistry is extreme compared to Earth standards. For instance, the diagenetic fluid responsible for the precipitation of the hematite concretions was likely an acidic fluid that mobilized the iron as Fe^{3+} rather than a reducing fluid like in the Navajo Sandstone, although the end products (hematite concretionary masses) are strongly similar. The second is that Earth has had life for at least 3.8 Ga and this life has participated in and affected the chemical reactions responsible for mineral precipitation. It is estimated that more than half of the mineral species on Earth are present because of life. Although Mars may have had life, biotic interactions have not occurred on the grand scale we encounter on Earth. Studying abiotic reactions on Mars may augment our future investigations about biotic interactions on Earth.

To summarize, a better understanding of diagenesis and the biogeochemistry of the Navajo Sandstone and the Brushy Basin Member has important implications for CO_2 capture and sequestration by showing the following: 1. reservoir fluids exhibit spatial

variability on regional to outcrop scales; 2. diagenetic processes are limited to early stages in mudrocks; 3. cement precipitation is lithologically controlled, even in porous units; and 4. CO₂ fluids in a saline reservoir will precipitate dolomite and significantly reduce porosity. These findings have broad application for model parameters to understand and predict past, present and future subsurface fluid flow.

Understanding biogeochemical processes and the preservation of biosignatures has important implications for the future study of Mars and the search for extraterrestrial life by showing the following: 1. two distinct elemental suites are associated with microbial fossils: C, Fe, As, and C, S, Se, 2. unstable and metastable iron (oxyhydr)oxide phases can function as biosignatures, 3. spheroids and framboids can function as biosignatures, and 4. biosignatures preserved in iron (oxyhydr)oxides exhibit some degradation and recrystallization on millennial scales; however, features are still present and clearly discernible. This research identifies biogeochemical markers in the Jurassic Brushy Basin Member of the Morrison Formation to discern depositional environment, fluid chemistry and potential microbial fossils and/or biosignatures to apply to the exploration of similar iron- and clay-rich sediments on Mars. The library of diagnostic iron (oxyhydr)oxide biotic fingerprints produced by this research may possibly help answer one of humanity's weightiest questions, "Are we alone?"

APPENDIX A

SAMPLES

Appendix A lists samples collected for this research and includes some specimens that were not analyzed. The formation, age and sample locations are given along with a brief description of the sample and the analyses performed. Formation abbreviations are as follows: Jn = Jurassic Navajo Sandstone, MSD = modern spring deposits from Ten Mile Graben fault system, AT = ancient tufa terraces from Ten Mile Graben fault system, Jebb = Jurassic Entrada Formation, Board Beds Member, Je = Jurassic Entrada Formation, Jw = Jurassic Wanakah Formation, Jmt = Jurassic Morrison Formation, Tidwell Member, Jmb = Jurassic Morrison Formation, Brushy Basin Member, Kbc = Cretaceous Burro Canyon Formation.

Analysis abbreviations are as follows: XRD = x-ray diffraction, WRA = whole rock analysis, LA-ICP-MS = laser ablation induced coupled mass spectroscopy, SEM = scanning electron microscope, HF = dissolution in hydrofluoric acid and evaluation with reflected light microscope, HF+SEM = dissolution with hydrofluoric acid and evaluation with a scanning electron microscope.

SAMPLE #	FM	LATITUDE	LONGITUDE	NOTES/ROCK DESCRIPTION	THIN SECTION	XRD	WRA	QEM-SCAN	LA-ICP-MS	SEM	HF	SEM
UT10-SRS-10Jn	Jn	N38° 50.473'	W 110° 54.201	vertical transect of rxn front from brown on the bottom to red on top.								
	a				X		X	X				
	b					X						
	c				X		X					
	d					X						
	e				X	X	X					
	f											
UT10-SRS-13Jn	Jn	N38° 50.473'	W 110° 54.201	horizontal transect along top of rxn from every 1 m. 30 total sampled								
	a			red	X	X	X	X				
	d			red	X	X	X	X				
	g			red	X	X	X					
	j			red	X	X	X					
	m			brown	X	X	X					
	p			brown	X		X	X				
	q			brown		X						
	s			brown	X		X					
	t			brown		X						
	v			brown	X		X					
	w			brown		X						
	x			brown	X			X				
	y			brown			X					
	z			brown		X						
	1b			brown			X					
	1c			brown	X			X				
	1d			brown		X						
UT10-BB-1MSD	MSD	N38° 52.260'	W 110° 06.690	wet modern spring deposits of iron/ travertine. Sample taken ~2.5 m from source and 1 m from edge of red surrounding source.					X			
UT10-BB-2MSD	MSD	N38° 52.260'	W 110° 06.690	dry sample from edge of wet/dry transition					X			
UT10-LB-1MSD	MSD	N38° 52.359'	W 110° 06.994	hard iron/ travertine coliform texture	X		X	X				
UT10-CG-1AT	ancient travertine terrace	N38.93708°	W 110.13138°	ancient travertine; iron-rich layers. Some vein-filling calcite with iron bands are present but this sample is	X		X		X	X		
UT10-CG-2AT	ancient travertine terrace	N38.93708°	W 110.13138°	ancient travertine; iron-rich layers. Some vein-filling calcite with iron bands are present but this sample is		X						
CO11-EC-1Jebb	Jebb	N 38° 42.634'	W108° 16.683'	Host rock	X							
CO11-EC-1Jeef	Je	N 38° 42.634'	W108° 16.683'	typical earthy facies host rock	X							
CO11-EC-4Jw	Jw	N 38° 42.634'	W108° 16.683'	algal structure - stromatolite?	X		X					
CO11-EC-5Jw	Jw	N 38° 42.634'	W108° 16.683'	micrite	X		X					
CO11-EC-10Jmt	Jmt	N 38° 42.634'	W108° 16.683'	mounded carbonate structures; algal	X		X					
CO11-DT-3Jw	Jw	N 38° 39.356"	W107° 51.832'	red mudrock with blocky structure	X		X					
CO11-SP-2Jwbc	Jw	N 37° 59.923'	W107° 59.643'	Bilk Creek Sandstone with dense	X		X					
CO11-MC-1Jmb	Jmb	N 37° 19.287'	W108° 40.808'	Fe nodules in ss/ siltstone (lapilli?)	X	X	X	X				
CO11-MC-2Jmb	Jmb	N 37° 19.287'	W108° 40.808'	Fe nodules (lapilli?) in channel along		X						

SAMPLE#	RM	LATITUDE	LONGITUDE	NOTES/ROCK DESCRIPTION	THIN SECTION	XRD	WRA	QEM-SCAN	LA-ICP-MS	SEM	HF-SEM
UT11-MZ-1Jmb	Jmb	N 37° 19.341'	W109° 19.663'	Spheroidal FeO nodules within	X	X	X				
UT11-MZ-2Jmb	Jmb	N 37° 19.341'	W109° 19.663'	green tuffaceous siltstone with red	X	X	X				
UT11-MZ-3Jmb	Jmb	N 37° 19.341'	W109° 19.663'	green tuffaceous siltstone with clear	X	X	X	X	X	X	
UT11-MZ-4Jmb	Jmb	N 37° 19.341'	W109° 19.663'	vugs with earthy hematite in green	X		X		X		X
UT11-MZ-5Jmb	Jmb	N 37° 19.341'	W109° 19.663'	vein or crack with FeO fill;	X						
UT11-MZ-6Jmb	Jmb	N 37° 19.341'	W109° 19.663'	rxn front with red to black overprinting clinoptilolite facies	X						
.001	Jmb			black	XRD	X					
.002	Jmb			red	XRD	X					
UT11-MZ-7Jmb	Jmb	N 37° 19.341'	W109° 19.663'	small channel sand with green	X	X	X				
UT11-MZ-8Jmb	Jmb	N 37° 19.341'	W109° 19.663'	possible petrified wood with lots of	X						
UT11-MZ-14Jmb	Jmb	N 37° 19.341'	W109° 19.663'	dark purple ss/ siltstone; bioturbated	X	X	X				
UT11-MZ-15Jmb	Jmb	N 37° 19.341'	W109° 19.663'	white siltstone with concretion freckles	X	X	X				
UT11-MZ-16Jmb	Jmb	N 37° 19.341'	W109° 19.663'	petrified wood?							
UT11-MZ-17Jmb	Jmb	N 37° 19.341'	W109° 19.663'	lower mottled siltstone with concretions	X	X	X			X	X
17Jmb-a	Jmb			concretions	X						
17Jmb-b	Jmb			elongate stringers; charophyte?	X			X			
UT11-MZ-18Jmb	Jmb	N 37° 19.341'	W109° 19.663'	reaction front zonation with	X	X	X	X			
UT11-MZ-19Jmb	Jmb	N 37° 19.341'	W109° 19.663'	clinoptilolite nodule with hematite inclusion?	X						
UT11-MZ-21Jmb	Jmb	N 37° 19.341'	W109° 19.663'	clinoptilolite siltstone	X	X	X				
UT11-MZ-22Jmb	Jmb	N 37° 19.341'	W109° 19.663'	clino-siltstone facies with possible lapilli	X	X	X				
UT11-MZ-23Jmb	Jmb	N 37° 19.341'	W109° 19.663'	grey nodule with darker center	X	X	X				
UT11-MZ-24Jmb	Jmb	N 37° 19.341'	W109° 19.663'	possible analcime							
UT11-MZ-25Jmb	Jmb	N 37° 19.341'	W109° 19.663'	dark red siltstone	X		X				
UT11-MZ-27Jmb	Jmb	N 37° 19.341'	W109° 19.663'	tan lens of reduced clay; host rock for petrified wood	X		X				
UT11-MZ-28Jmb	Jmb	N 37° 19.341'	W109° 19.663'	red, bioturbated siltstone	X	X	X				
UT11-MZ-29Jmb	Jmb	N 37° 19.341'	W109° 19.663'	mottled dark red siltstone; burrowed and mineralized with lots of zeolites	X	X	X		X		
UT11-BB-1msd	MSD	N 38° 52.260'	W110° 06.688'	black mud from spring		X				X	
UT11-BB-2msd	MSD	N 38° 52.260'	W110° 06.688'	all three samples have white bubbly							
.001	MSD			FeO microbial mat	X	X	X			X	
.002	MSD			sandier than .001 with black mat at	X	X	X				
.003	MSD			FeO-rich with white crust and black	X		X			X	
UT11-BB-5msd	MSD	N 38° 52.260'	W110° 06.688'	case hardened older deposit from	X	X	X				
UT11-BH-1Jmb	Jmb	N 38° 43.046'	W109° 41.530'	clustered, dense, localized		X					
UT11-BH-4Jmb	Jmb	N 38° 43.046'	W109° 41.530'	concretionary masses in green		X					
UT11-BH-5Jmb	Jmb	N 38° 43.046'	W109° 41.530'	light red siltstone with green mottles	X	X	X				
UT11-BH-6Jmb	Jmb	N 38° 43.046'	W109° 41.530'	green siltstone with calcite cemented		X					
UT11-BH-7Jmb	Jmb	N 38° 43.046'	W109° 41.530'	light red siltstone with green mottles		X					

SAMPLE #	FM	LATITUDE	LONGITUDE	NOTES/ROCK DESCRIPTION	THIN SECTION	XRD	WRA	QEM-SCAN	ICP-MS	SEM	HF	HF+ SEM
UT11-BH-9Jmb	Jmb	N 38° 43.046'	W109° 41.530'	concretions from red siltstone with green mottles	X		X					
UT11-BH-11Jmb	Jmb	N 38° 43.046'	W109° 41.530'	<10 cm Fe carbonate spheroidal concretions		X						
.001	Jmb			concretion	X		X					
.002	Jmb			host rock	X	X						
.003	Jmb			concretion?		X						
UT11-BH-12Jmb	Jmb	N 38° 43.046'	W109° 41.530'	purple nodule (analcime?)			X					
UT11-BH-14Jmb	Jmb	N 38° 43.189'	W109° 42.163'	green nodules from lower nodular unit;	X	X	X					
UT11-BH-15Jmb	Jmb	N 38° 43.189'	W109° 42.163'	red nodules from lower nodular unit;	X	X	X					
UT11-BH-16Jmb	Jmb	N 38° 43.189'	W109° 42.163'	brown nodules from lower nodular unit; <12 cm diam	X	X	X					
UT11-BH-17Jmb	Jmb	N 38° 43.189'	W109° 42.163'	white spheroids <3 cm diam with	X	X	X					
UT11-BH-18Jmb	Jmb	N 38° 43.189'	W109° 42.163'	6 cm diam nodule with clustered	X	X	X					
UT11-BH-19Jmb	Jmb	N 38° 43.189'	W109° 42.163'	host rock from nodular zone			X					
UT11-BH-23Jmb	Jmb	N 38° 43.189'	W109° 42.163'	reduction halos around white core in red with green mottles siltstone facies	X		X					
UT11-BH-24Jmb	Jmb	N 38° 43.189'	W109° 42.163'	nodules in burrowed host rock (light	X		X					
UT11-BH-27Jmb	Jmb	N 38° 43.189'	W109° 42.163'	burrowed nodule; light red	X		X					
UT11-BH-28Jmb	Jmb	N 38° 43.189'	W109° 42.163'	red with green mottles; dark cores	X		X					X
UT11-BH-31Jmb	Jmb	N 38° 43.189'	W109° 42.163'	purple claystone with white mottles	X		X					
UT11-TM-2Jmb	Jmb	N 38° 51.130'	W109° 59.156'	black chert	X		X					
UT11-TM-3Jmb	Jmb	N 38° 51.130'	W109° 59.156'	carbonate sabkha	X		X					
UT11-TM-4Jmb	Jmb	N 38° 50.998'	W109° 59.522'	spherical concretions	X		X					
UT11-TM-5Jmb	Jmb	N 38° 51.130'	W109° 59.156'	siltstone nodule from grey siltstone	X	X	X					
UT11-EC-1Jmb	Jmb	N 38° 45.693'	W108° 14.580'	microconcretions in green siltstone at	X	X	X					
UT11-EC-2Jmb	Jmb	N 38° 45.693'	W108° 14.580'	green siltstone with red mineralized voids 1-2 mm wide < 5mm long; either charophytes or altered volcanic glass	X		X		X			
UT11-BD-1Jmw	Jw	N 38° 50.345'	W108° 22.559'	porous limestone with black specks and algal laminae; some chert : iron veins	X							
UT11-BH-32Jmb	Jmb	N 38° 43.046'	W109° 41.530'	host rock with carbonate concretions	X		X					
UT11-BH-33Jmb	Jmb	N 38° 43.046'	W109° 41.530'	calcite ledges with concretions on top								
.001	Jmb			host rock ledge	X		X					
.002	Jmb			calcite	X		X					
UT11-RG-1Jmb	Jmb	N 38° 45.693'	W108° 14.580'	green grey siltstone with Fe/	X	X	X	X				
UT11-RG-1Kbc	Kbc	N 38° 45.693'	W108° 14.580'	FeCO3 and FeO concretions in Burro								
.001	Kbc			calcite	X		X					
.002	Kbc			FeO concretion	X		X					
UT11-RG-2Kbc	Kbc	N 38° 45.693'	W108° 14.580'	FeO pseudomorphs after pyrite in concretions on planolites burrows	X	X	X					

SAMPLE#	FM	LATITUDE	LONGITUDE	NOTES/ROCK DESCRIPTION	THIN SECTION	XRD	WRA	QEM-SCAN	LA-ICP-	SEM	HF	HF+SEM
UT11-FP-1Jmb	Jmb	N 39° 09.126'	W108° 45.353'	FeO/ FeCO# from lower red with green mottles facies		X						
UT11-FP-2Jmb	Jmb	N 39° 09.126'	W108° 45.353'	FeO concretion freckles in biotubated green siltstone from red/ green	X	X	X					
UT11-FP-3Jmb	Jmb	N 39° 09.126'	W108° 45.353'	carbonate concretions; spheroidal and	X	X	X					
UT11-FP-5Jmb	Jmb	N 39° 09.126'	W108° 45.353'	megaconcretions	X	X	X					
UT11-FP-7Jmb	Jmb	N 39° 09.126'	W108° 45.353'	carbonate concretion in channel sandstone and med grained host rock; larger but morphologically	X	X	X					
UT11-FPQ-1Jmb	Jmb	N 39° 08.885'	W108° 46.253'	tabular to cylindrical concretions also								
.001	Jmb			purple nodule	X		X					
.002	Jmb			Black circular nodule	X		X					
UT11-FPQ-2Jmb	Jmb	N 39° 08.885'	W108° 46.253'	FeO concretions in green silt sonte "Ceratesaurus channel"		X						
.001	Jmb			concretion	X		X					
.002	Jmb			host rock			X					
UT07-MR-1Jn	Jn			FeO cemented, pelleted burrows	X	X						

APPENDIX B

X-RAY DIFFRACTION

Appendix B lists minerals identified with XRD along with formation name and a brief sample description. XRD analysis was performed at the University of Utah on a Rigaku x-ray diffractometer. The $<2 \mu\text{m}$ fraction of the Jurassic Navajo Sandstone samples was separated and oriented on glass slides. All other samples were analyzed using a random-oriented powder mount. Sample locations are listed in Appendix A.

Mineral abbreviations are as follows: I/S = interstratified illite/ smectite, Ill = illite, Smec = smectite, Kaol = kaolinite, An = analcime, Chl = chlorite, Alb = albite, Goe = goethite, Hem = hematite, Lepid = lepidocrocite, Ferri = ferrihydrite, Sid = siderite, Apa = apatite, FePhos = iron phosphate, Cal = calcite, Dolo = dolomite, MnO = manganese oxide, Gyp = gypsum.

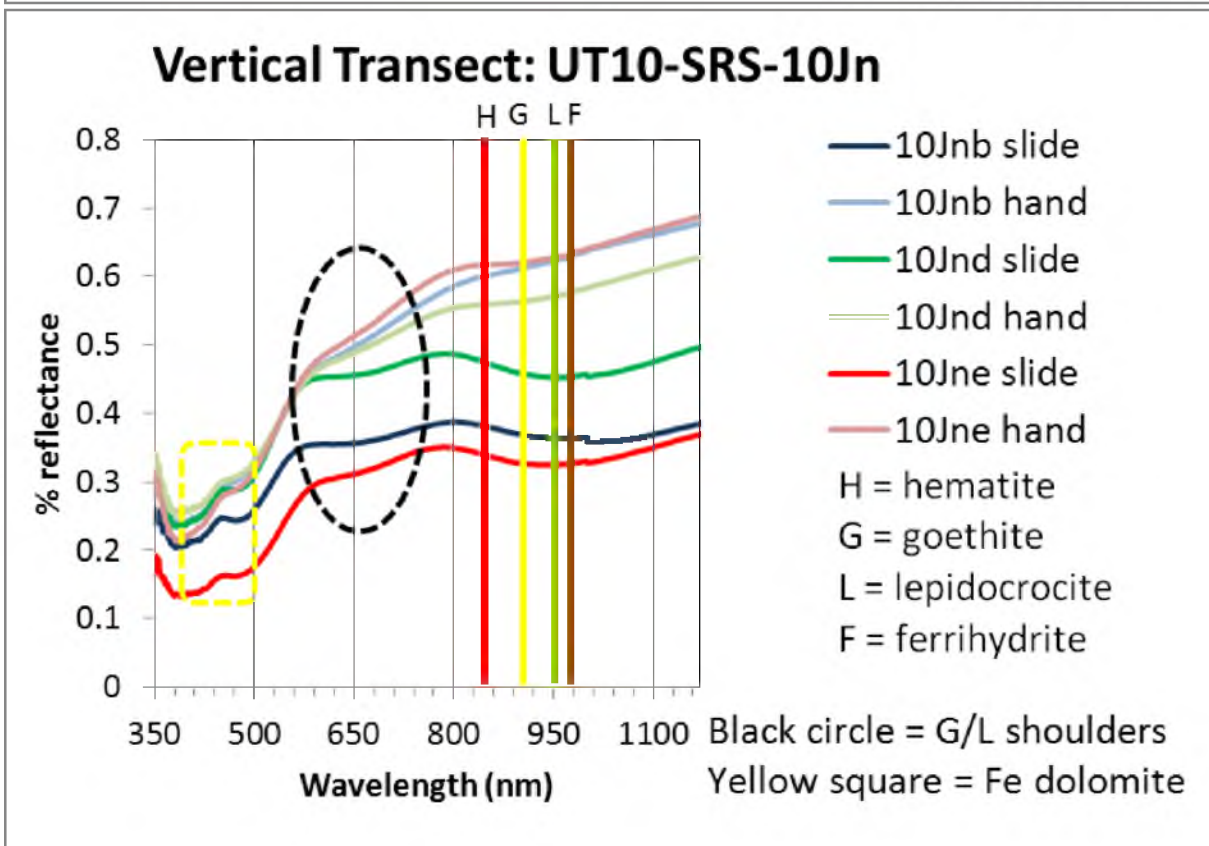
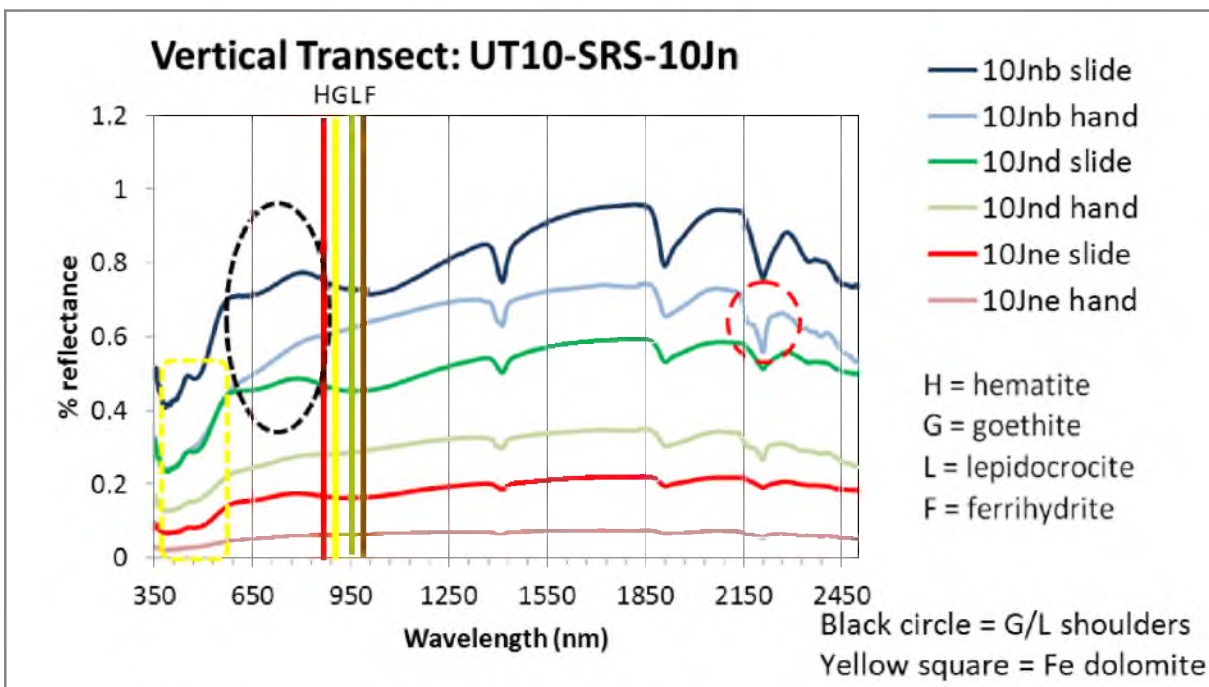
McElmo Canyon																				
Sample #	Formation	Description	I/S	Ill.	Smec.	Kaol.	Clinop.	An.	Chl.	Alb.	Goe.	Hem.	Lepid.	Ferri.	Sid.	Apa.	FePhos	Cal.	Dolo.	MnO
O11-MC-1Jmb	Jmb	Fe nodules in ss/ siltstone	X			X				X		X						X		
O11-MC-2Jmb	Jmb	Fe nodules in channel along bedding	X							X	?				X			X		
Montezuma Creek																				
Sample #	Formation	Description	I/S	Ill.	Smec.	Kaol.	Clinop.	An.	Chl.	Alb.	Goe.	Hem.	Lepid.	Ferri.	Sid.	Apa.	FePhos	Cal.	Dolo.	MnO
JT11-MZ-1Jmb	Jmb	Spheroidal FeO nodules within clinoptilolite facies; ~4 cm diam			X					X		minor					X			
JT11-MZ-2Jmb	Jmb	siltstone with red chert stringers 0.5 - 2 mm wide			X	X											X			
JT11-MZ-3Jmb	Jmb	green tuffaceous siltstone with clear analcime stringers	X			X		X									X			
JT11-MZ-6Jmb	Jmb	rxn front with red to black overprinting clinoptilolite facies																		
.001	Jmb	black	X			X						X				X	X			X
.002	Jmb	red	X				X							?			X			
JT11-MZ-7Jmb	Jmb	small channel sand with green reduction halos	X			X		X									X	X		
T11-MZ-14Jmb	Jmb	dark purple ss/ siltstone; bioturbated			X				X		X	X					X			
T11-MZ-15Jmb	Jmb	white siltstone with concretion freckles	X		X			X				minor					X			
T11-MZ-17Jmb	Jmb	lower mottled siltstone with concretions			X		X										X			
T11-MZ-18Jmb	Jmb	reaction front zonation with concretions			X	X	X					X					X	X		
T11-MZ-21Jmb	Jmb	clinoptilolite siltstone			X		X										X			
T11-MZ-22Jmb	Jmb	clino-siltstone facies with possible lapilli			X		X										X			
T11-MZ-23Jmb	Jmb	grey nodule with darker center				X		X	X								X			X
T11-MZ-28Jmb	Jmb	red, bioturbated siltstone			X							minor					X			
T11-MZ-29Jmb	Jmb	mottled dark red siltstone			X							X					X			

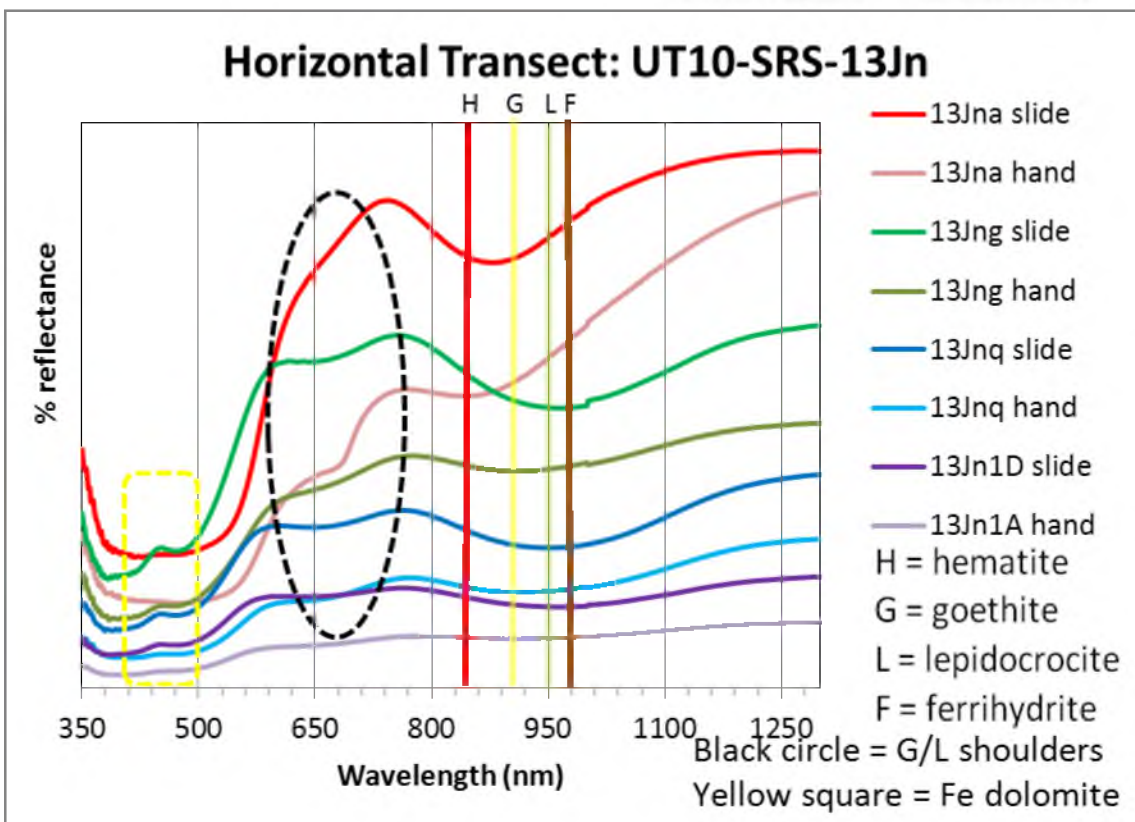
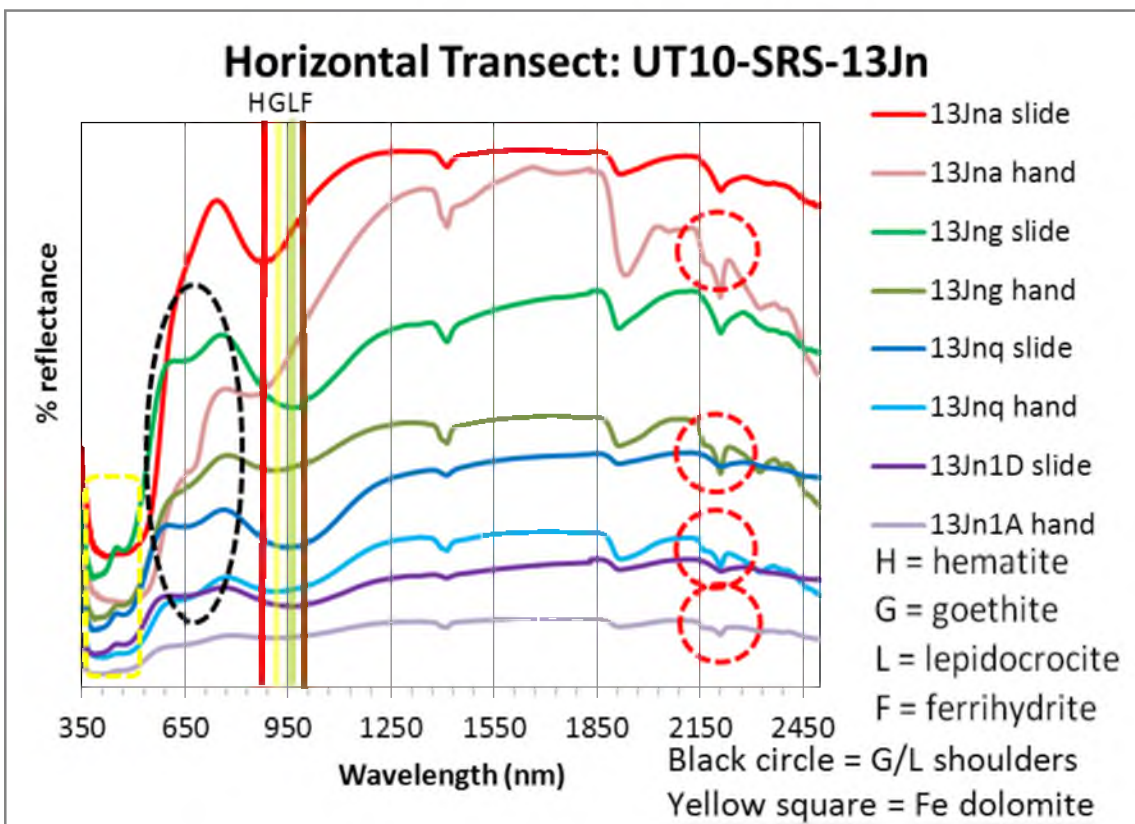
APPENDIX C

VISIBLE TO NEAR INFRARED REFLECTANCE SPECTROSCOPY

Visible to near infrared (Vnir) reflectance spectroscopy produces spectra with characteristic minima to identify minerals. An ASD Field Spec Pro was used in the laboratory to obtain spectra on XRD slides and the same hand samples of Jurassic Navajo Sandstone. If the hand sample was not available, the nearest hand sample was used for comparison. Spectra are compared with standards from the USGS spectral library (Clark, R.N., Swayze, G.A., Wise, R., Livo, E., Hoefen, T., Kokaly, R., Sutley, S.J., 2007, USGS digital spectral library splib06a: U.S. Geological Survey, Digital Data Series 231).

Spectra collected from the XRD slide and the matching hand sample are presented in the same graph and are organized by vertical transect samples and horizontal transect samples. The entire spectrum is presented in the first graph followed by a graph showing only the iron (oxyhydr)oxide and ferroan dolomite minima. Lines indicate minima for iron (oxyhydr)oxide phases and are labeled H (hematite), G (goethite), L (lepidocrocite) and F (ferrihydrite). Black dashed circles show the goethite and lepidocrocite shoulders, yellow dashed boxes show ferroan dolomite minima and red dashed circles indicate kaolinite minima.



















APPENDIX D

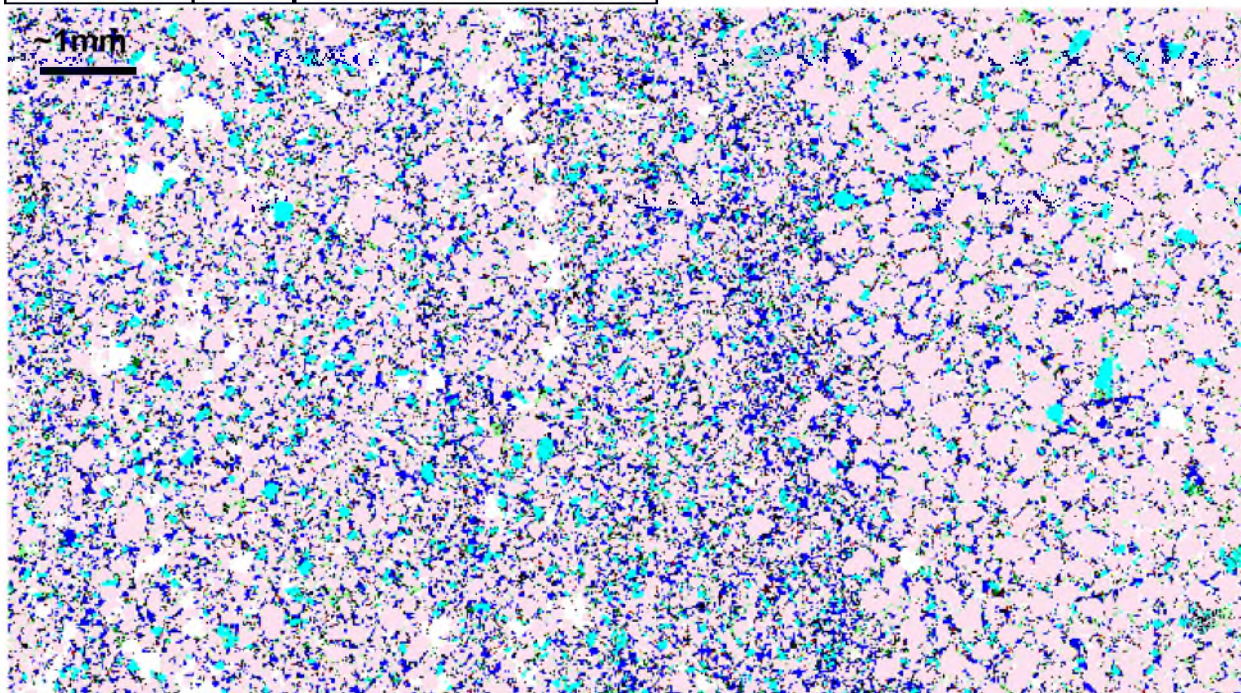
QEMSCAN

This table presents all QEMSCAN images made for this research. Analysis was performed at the Energy and Geoscience Institute at the University of Utah. A species identification protocol (SIP) written specifically for shales by FEI (the QEMSCAN software company) was used to identify minerals. Slight changes were made to the SIP to better identify specific zeolites (such as clinoptilolite and analcime) present in the Brushy Basin Member samples and identified in the literature and with XRD. Vertical dark blue lines in sample 10Jna, 10Jnd, 13Jnx and 13Jn1C are fine-grained, wind ripple laminae where dolomite cements are concentrated.

Jurassic Navajo Sandstone Samples

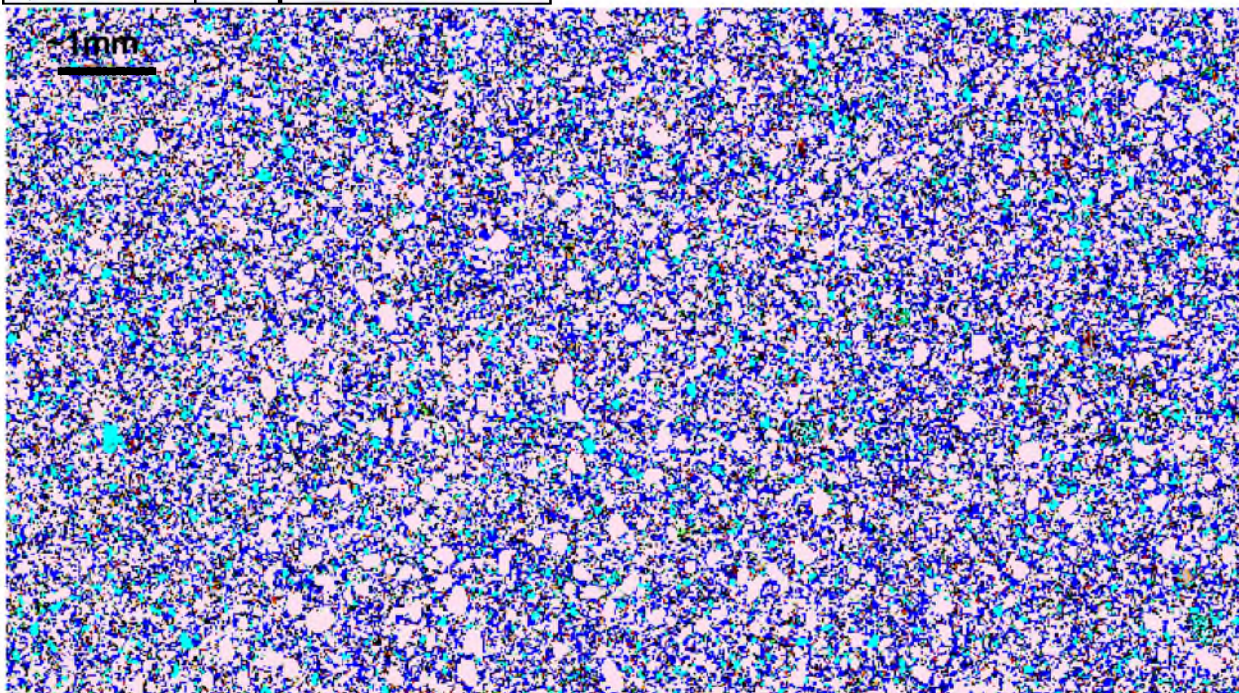
10Jna

Mineral Name	Area%	Mineral Name	
Quartz	67.78		Quartz
Dolomite	11.97		Dolomite
Porosity	11.41		Porosity
Other	7.21		Other
Orthoclase	5.46		Orthoclase
Kaolinite	3.68		Kaolinite
Fe-Oxides	1.36		Fe-Oxides
Illite	1.22		Illite
Plagioclase	0.82		Plagioclase
Fe Dolomite	0.41		Ferroan Dolomite
Barite	0.04		Barite
Siderite	0.02		Siderite
Apatite	0.02		Apatite
Zircon	0.02		Zircon



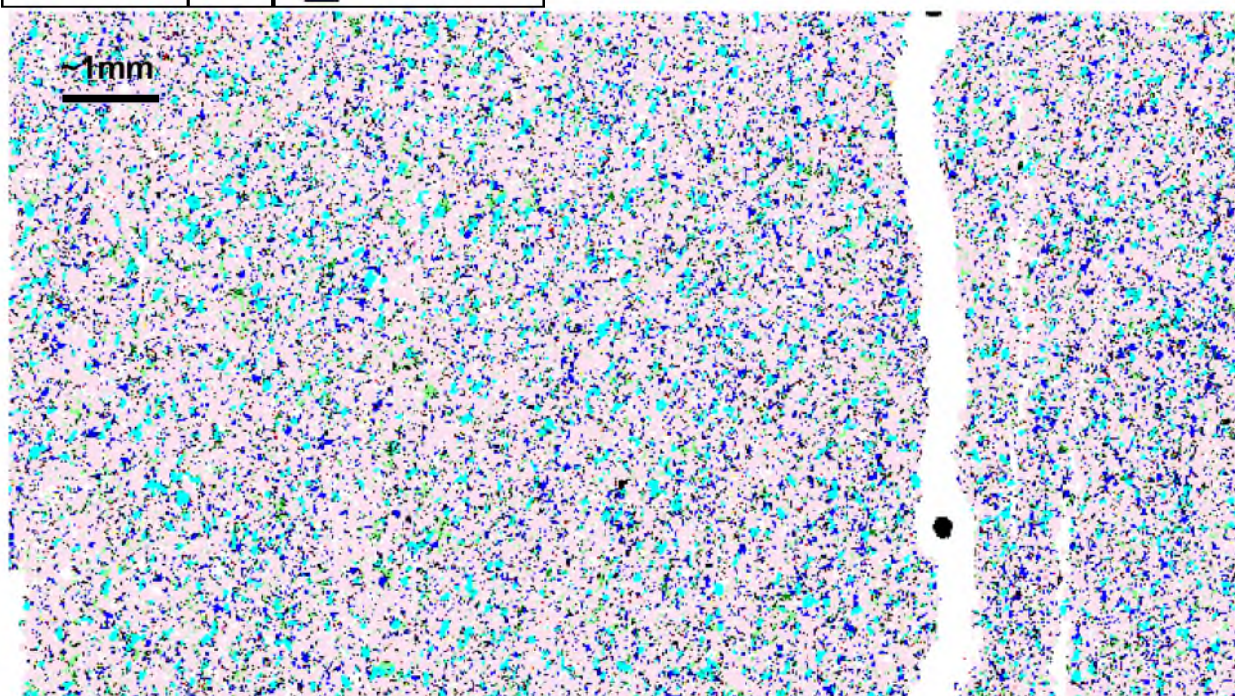
13Jna

Mineral Name	Area%	Mineral Name
Quartz	48.29	Quartz
Dolomite	23.20	Dolomite
Other	11.58	Other
Orthoclase	5.62	Orthoclase
Calcite	3.03	Calcite
Fe-Oxides	2.86	Fe-Oxides
Kaolinite	2.48	Kaolinite
Porosity	1.69	Porosity
Gypsum?	1.17	Gypsum?
Illite	0.89	Illite
Plagioclase	0.71	Plagioclase
Fe Dolomite	0.10	Ferroan Dolomite
Barite	0.04	Barite
Zircon	0.03	Zircon
Apatite	0.02	Apatite



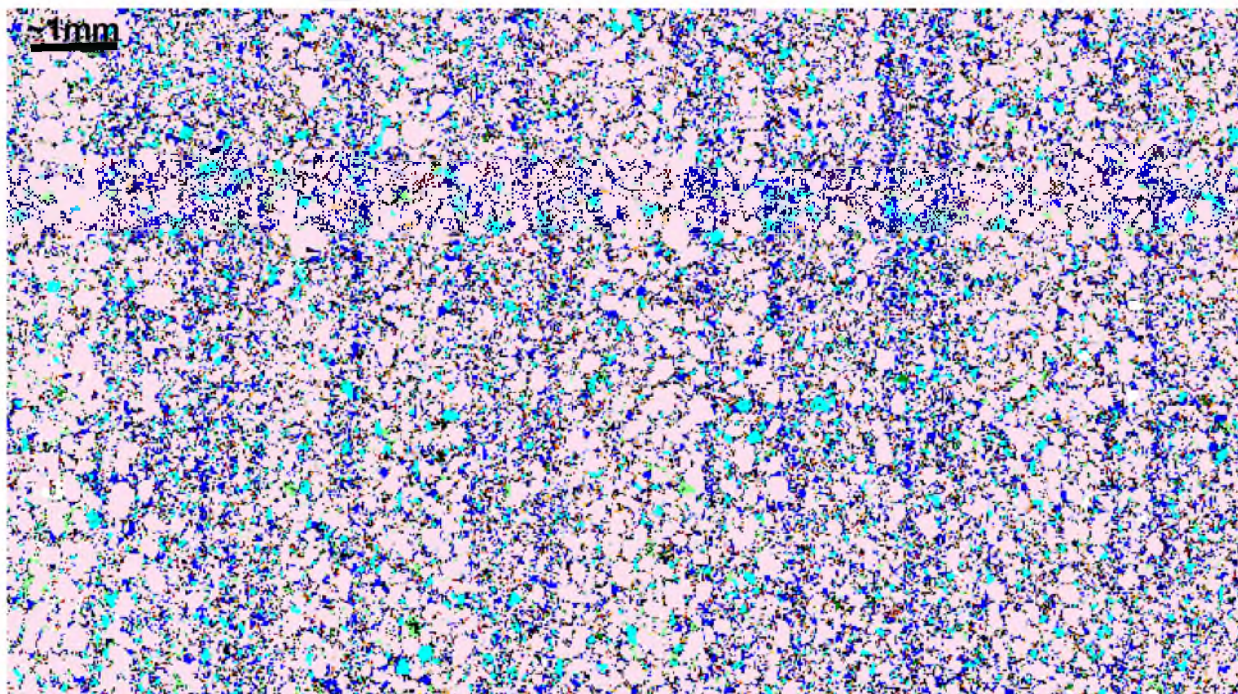
13Jnd

Mineral Name	Area%	Mineral Name
Quartz	68.13	Quartz
Porosity	13.44	Porosity
Dolomite	8.52	Dolomite
Orthoclase	7.81	Orthoclase
Other	6.47	Other
Kaolinite	4.51	Kaolinite
Illite	1.71	Illite
Fe-Oxides	1.27	Fe-Oxides
Plagioclase	1.00	Plagioclase
Fe Dolomite	0.34	Ferroan Dolomite
Calcite	0.14	Calcite
Barite	0.04	Barite
Gypsum?	0.02	Gypsum?
Siderite	0.01	Siderite
Apatite	0.01	Apatite
Zircon	0.01	Zircon



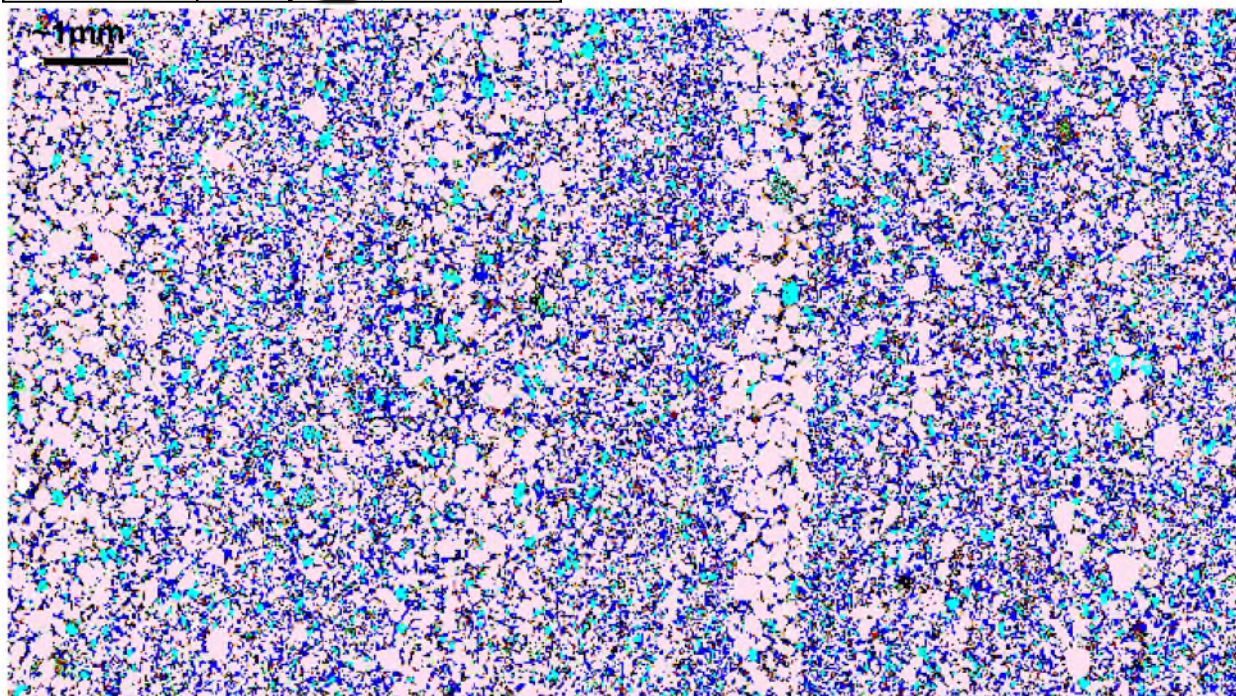
13Jnx

Mineral Name	Area%	Mineral Name
Quartz	60.17	Quartz
Other	10.82	Other
Dolomite	10.39	Dolomite
Orthoclase	5.29	Orthoclase
Calcite	4.63	Calcite
Porosity	3.59	Porosity
Kaolinite	2.41	Kaolinite
Fe-Oxides	2.30	Fe-Oxides
Gypsum?	1.60	Gypsum?
Illite	1.24	Illite
Plagioclase	0.90	Plagioclase
Fe Dolomite	0.15	Ferroan Dolomite
Barite	0.07	Barite
Siderite	0.02	Siderite
Zircon	0.02	Zircon
Apatite	0.02	



13Jn1C

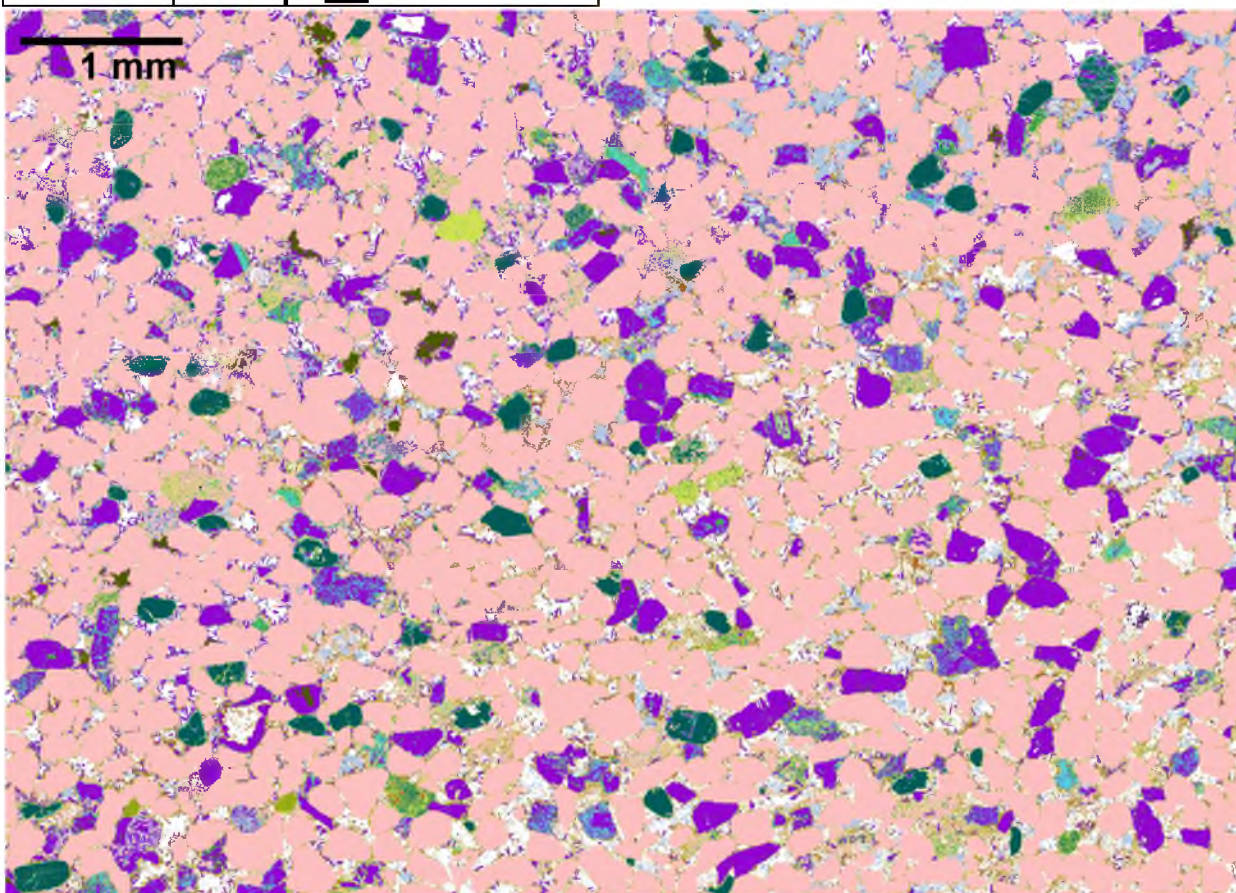
Mineral Name	Area%	Mineral Name
Quartz	55.54	Quartz
Dolomite	17.08	Dolomite
Other	10.37	Other
Orthoclase	5.32	Orthoclase
Porosity	4.01	Porosity
Calcite	3.42	Calcite
Fe-Oxides	2.47	Fe-Oxides
Kaolinite	2.19	Kaolinite
Gypsum?	1.28	Gypsum?
Illite	0.97	Illite
Plagioclase	0.77	Plagioclase
Fe Dolomite	0.44	Ferroan Dolomite
Barite	0.04	Barite
Zircon	0.02	Zircon
Siderite	0.02	Siderite
Apatite	0.01	Apatite



Jurassic Morrison Formation - Brushy Basin Member Samples

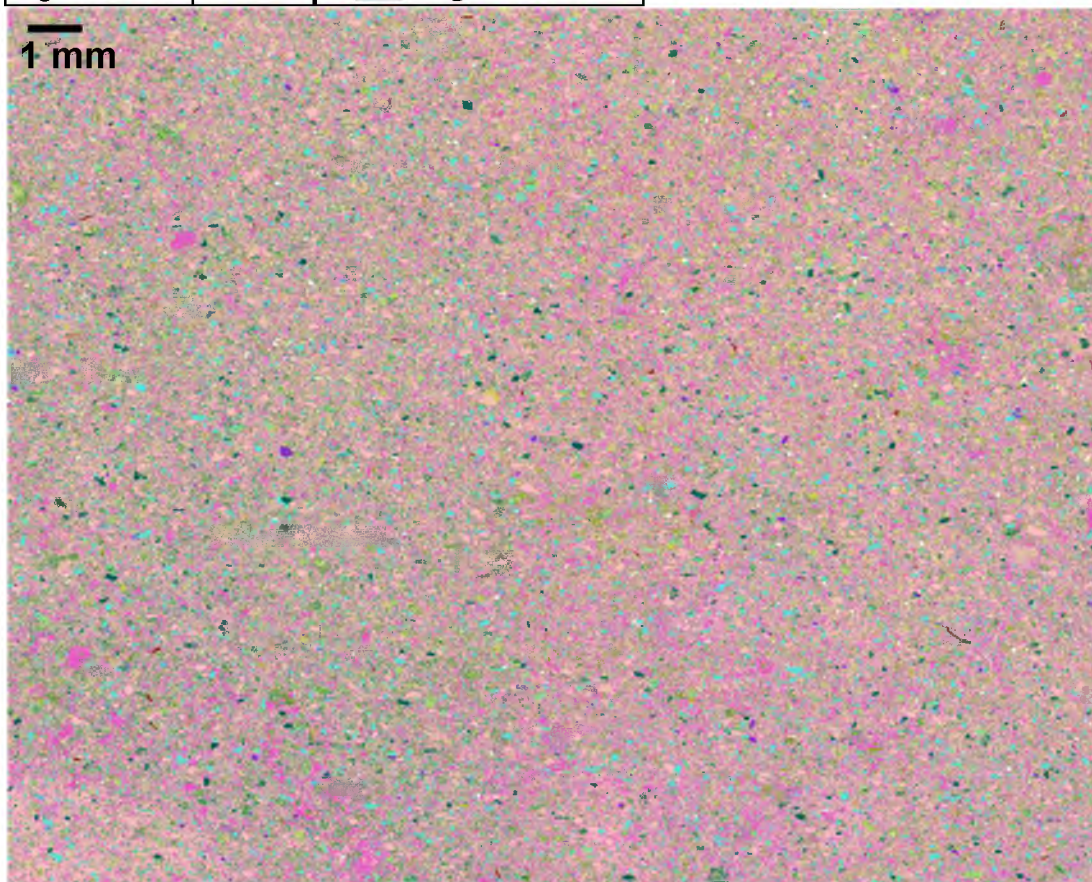
MC1 (McElmo Canyon)

Mineral Name	Area%	Mineral Name
Quartz	64.60	Quartz
Albite	13.37	Albite
Background	11.79	Background
Chlorite	5.20	Chlorite
Plagioclase	4.18	Plagioclase
Alkali Feldspar	3.27	Alkali Feldspar
Fe-oxides	3.00	Fe-oxides
Calcite	2.46	Calcite
Clinoptilolite	1.63	Clinoptilolite
Smectites	1.54	Smectites
Kaolinite	0.44	Kaolinite
Barite	0.18	Barite
Apatite	0.04	Apatite
Analcime	0.04	Analcime
Biotite	0.01	Biotite
Organic Matter	0.01	Organic Matter
Other	0.01	Other



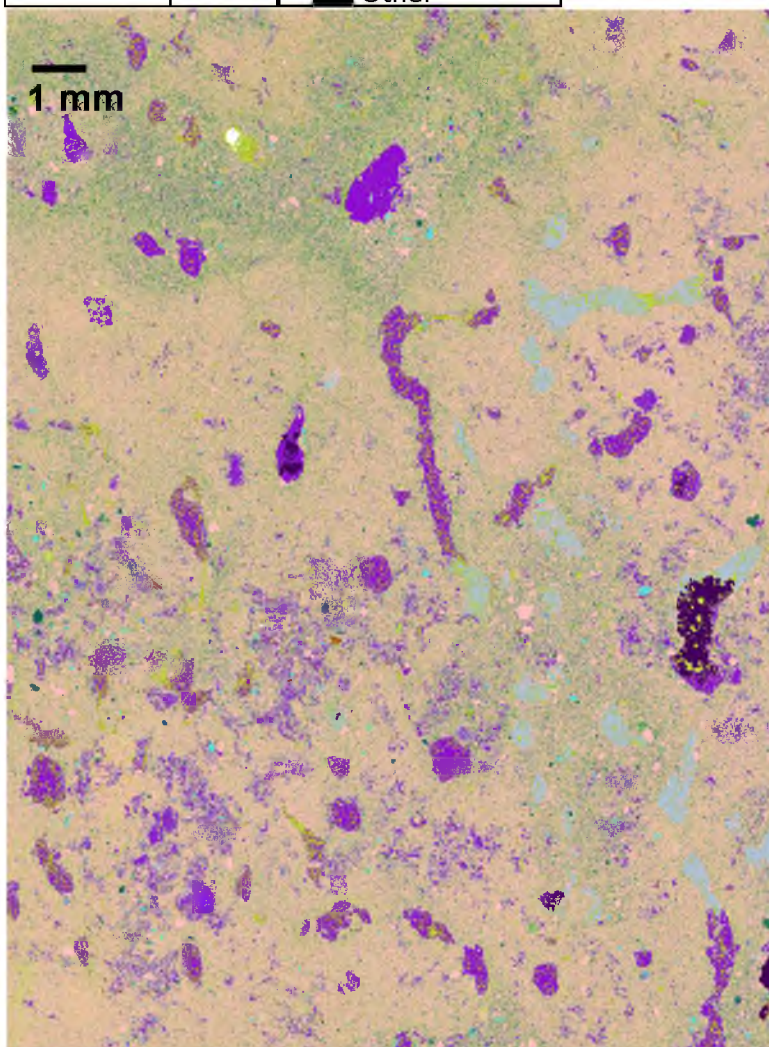
MZ18 (Montezuma Creek)

Mineral Name	Area%	Mineral Name
Quartz	33.42	Quartz
Apatite	20.05	Apatite
Chlorite	14.19	Chlorite
Alkali Feldspar	8.86	Alkali Feldspar
Plagioclase	8.68	Plagioclase
Calcite	6.09	Calcite
Smectites	4.06	Smectites
Background	3.63	Background
Fe-oxides	2.32	Fe-oxides
Albite	1.81	Albite
Clinoptilolite	0.21	Clinoptilolite
Analcime	0.11	Analcime
Other	0.10	Other
Biotite	0.08	Biotite
Barite	0.02	Barite
Organic Matter	0.01	Organic Matter



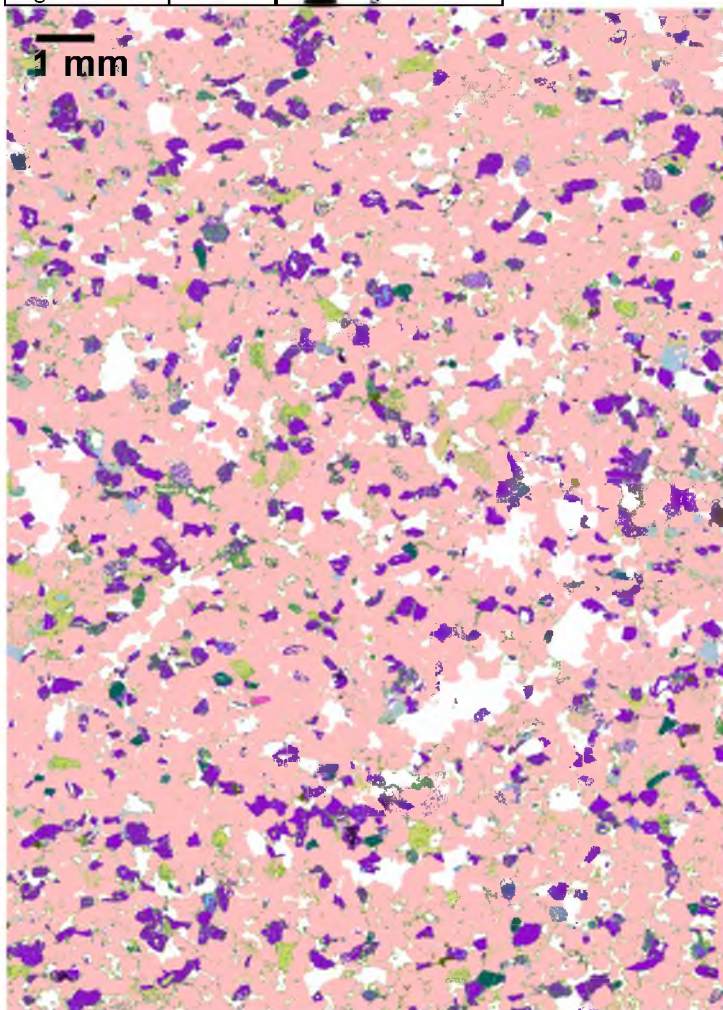
MZ3 (Montezuma Creek)

Mineral Name	Area%	Mineral Name
Quartz	52.26	Quartz
Chlorite	15.43	Chlorite
Alkali Feldspar	8.02	Alkali Feldspar
Albite	8.01	Albite
Clinoptilolite	4.91	Clinoptilolite
Plagioclase	4.33	Plagioclase
Fe-oxides	2.35	Fe-oxides
Smectites	2.16	Smectites
Calcite	1.78	Calcite
Barite	0.56	Barite
Background	0.27	Background
Biotite	0.08	Biotite
Analcime	0.05	Analcime
Pyrite	0.02	Pyrite
Apatite	0.02	Apatite
Organic Matter	0.02	Organic Matter
Other	0.01	Other



RG1 (Rattlesnake Gulch)

Mineral Name	Area%	Mineral Name
Quartz	73.49	Quartz
Background	17.38	Background
Albite	10.70	Albite
Chlorite	5.72	Chlorite
Alkali Feldspar	3.08	Alkali Feldspar
Clinoptilolite	2.55	Clinoptilolite
Plagioclase	1.94	Plagioclase
Calcite	1.10	Calcite
Smectites	0.43	Smectites
Barite	0.31	Barite
Kaolinite	0.25	Kaolinite
Fe-oxides	0.16	Fe-oxides
Biotite	0.08	Biotite
Analcime	0.08	Analcime
Apatite	0.06	Apatite
Other	0.04	Other
Organic Matter	0.02	Organic Matter



MZ17 (Montezuma Creek)

Mineral Name	Area%	Mineral Name
Quartz	48.07	Quartz
Chlorite	21.15	Chlorite
Smectites	6.71	Smectites
Alkali Feldspar	6.69	Alkali Feldspar
Clinoptilolite	6.44	Clinoptilolite
Albite	5.72	Albite
Plagioclase	3.99	Plagioclase
Background	1.96	Background
Calcite	0.67	Calcite
Fe-oxides	0.35	Fe-oxides
Analcime	0.07	Analcime
Apatite	0.06	Apatite
Other	0.04	Other
Barite	0.02	Barite
Kaolinite	0.01	Kaolinite
Biotite	0.01	Biotite
Organic Matter	0.01	Organic Matter



APPENDIX E

WHOLE ROCK ANALYSIS

Whole rock analysis (WRA) lists the weight percentages of major elements (identified as oxides) and trace elements concentrations in parts per million. ALS Chemex in Reno, Nevada performed the analyses using induced coupled mass spectroscopy. All sample localities and descriptions are given in Appendix A.

Justensen Flats Samples

	SiO ₂	Al ₂ O ₃	Fe ₂ O ₃	CaO	MgO	Na ₂ O	K ₂ O	TiO ₂	MnO	P ₂ O ₅	SrO	BaO	C	S
DESCRIPTION	%	%	%	%	%	%	%	%	%	%	%	%	%	%
UT10-SRS-10Jn a	64.6	2.79	1.81	10.8	4.53	0.04	1.04	0.18	0.16	0.03	0.01	0.02	3.68	0.01
UT10-SRS-10Jn c	88.4	3.28	1.39	1.67	1.09	0.05	1.21	0.2	0.03	0.03	0.01	0.03	0.72	<0.01
UT10-SRS-10Jn e	84.3	3.61	7.05	1.51	0.99	0.08	1.48	0.14	0.09	0.03	0.01	0.03	0.56	<0.01
UT10-SRS-13Jn a	80.2	2.54	3.52	3.98	2.59	0.07	1.04	0.11	0.1	0.02	<0.01	0.03	1.56	0.01
UT10-SRS-13Jn d	81.2	3.45	3.46	3.05	2.06	0.07	1.46	0.1	0.1	0.01	0.01	0.04	1.21	<0.01
UT10-SRS-13Jn g	72.2	2.83	2.17	6.43	4.24	0.05	1.15	0.17	0.15	0.02	0.01	0.04	2.63	<0.01
UT10-SRS-13Jn j	75.5	2.89	3.87	5.45	3.19	0.06	1.11	0.09	0.14	0.02	0.01	0.05	2.08	0.01
UT10-SRS-13Jn m	73.4	3.08	2.73	5.62	3.66	0.06	1.22	0.1	0.12	0.02	0.01	0.05	2.25	<0.01
UT10-SRS-13Jn p	75	2.77	2.1	5.12	3.21	0.13	1.07	0.1	0.11	0.01	0.01	0.07	2.11	0.03
UT10-SRS-13Jn s	68.7	2.9	2	8.54	3.25	0.05	1.02	0.16	0.1	0.02	0.01	0.03	2.89	<0.01
UT10-SRS-13Jn v	69	2.91	2	7.3	4.31	0.06	1.09	0.22	0.14	0.02	0.01	0.04	2.95	<0.01
UT10-SRS-13Jn y	64.3	2.4	1.9	10.15	4.82	0.05	0.95	0.18	0.15	0.02	0.01	0.03	3.7	<0.01
UT10-SRS-13Jn 1b	62.8	2.35	2.1	10.85	5.14	0.06	0.88	0.24	0.16	0.03	0.01	0.04	3.81	0.01
	Ba	Ce	Cr	Cs	Dy	Er	Eu	Ga	Gd	Hf	Ho	La	Lu	Nb
	ppm	ppm	ppm	ppm	ppm	ppm	ppm	ppm	ppm	ppm	ppm	ppm	ppm	ppm
UT10-SRS-10Jn a	200	10.2	30	1.09	1.47	1.07	0.33	3.4	1.31	6.4	0.33	5.8	0.18	3.2
UT10-SRS-10Jn c	246	11.6	20	1.21	1.1	0.75	0.28	3.6	1.09	6.5	0.23	5.5	0.14	3.4
UT10-SRS-10Jn e	246	10	30	1.44	0.94	0.59	0.28	4.8	1	3.7	0.19	4.8	0.11	4.5
UT10-SRS-13Jn a	264	8	20	0.96	0.94	0.66	0.23	3.2	0.89	3.8	0.21	4	0.11	2.7
UT10-SRS-13Jn d	336	8	20	1.21	0.8	0.54	0.25	3.8	0.81	2.7	0.17	4	0.09	2.2
UT10-SRS-13Jn g	337	9.9	20	1.03	1.27	0.91	0.3	3.5	1.17	5.9	0.29	5.3	0.17	3.1
UT10-SRS-13Jn j	421	7.7	20	1.03	0.96	0.67	0.26	3.6	0.92	2.6	0.21	4.1	0.1	2.3
UT10-SRS-13Jn m	432	8.1	20	1.13	0.98	0.67	0.27	3.7	0.97	2.4	0.21	4.4	0.11	2.2
UT10-SRS-13Jn p	512	7.7	10	1.01	0.95	0.64	0.24	3	0.86	2.4	0.21	4.1	0.1	1.9
UT10-SRS-13Jn s	251	9.6	20	1.29	1.23	0.87	0.3	3.2	1.17	5.2	0.27	5.1	0.15	3.1
UT10-SRS-13Jn v	289	11.5	20	1.15	1.51	1.05	0.33	3.4	1.32	7.8	0.35	6	0.19	3.8
UT10-SRS-13Jn y	239	10.8	20	1.1	1.52	1.1	0.33	2.9	1.32	6.9	0.34	6	0.2	3.3
UT10-SRS-13Jn 1b	309	14.8	30	1.09	1.98	1.47	0.35	3.1	1.71	10.5	0.46	7.8	0.28	4.4

Nd	Pr	Rb	Sr	Sm	Sr	Ta	Tb	Th	Tm	U	V	W	Y	
ppm	ppm	ppm	ppm	ppm	ppm	ppm	ppm	ppm	ppm	ppm	ppm	ppm	ppm	
1.52	1.24	32.6	1.24	4	76.6	0.3	0.22	1.47	0.16	0.76	13	2	9.3	
UT10-SRS-10m a	UT10-SRS-10m c	UT10-SRS-10m e	UT10-SRS-10m a	UT10-SRS-10m d	UT10-SRS-10m e	UT10-SRS-10m g	UT10-SRS-10m h	UT10-SRS-10m i	UT10-SRS-10m j	UT10-SRS-10m k	UT10-SRS-10m l	UT10-SRS-10m m	UT10-SRS-10n	
5.2	1.4	35.2	1.15	3	81.4	0.2	0.17	1.77	0.12	0.67	11	2	6.4	
4.4	1.21	46.3	1	4	89.6	0.2	0.15	1.53	0.1	0.54	11	11	5.3	
3.8	1.04	33.3	0.84	2	66.5	0.2	0.14	1.27	0.1	0.64	11	10	5.6	
3.6	1	44.3	0.8	4	79.5	1.1	0.13	1.15	0.08	0.51	13	12	4.5	
4.9	1.36	35.4	1.1	2	76.4	0.2	0.19	1.47	0.15	0.63	14	2	7.9	
3.9	1.05	36.1	0.89	5	73.3	1.3	0.15	1.13	0.1	0.62	16	43	5.7	
4.1	1.13	38.9	0.91	3	74.7	0.1	0.15	1.17	0.11	0.49	13	2	5.8	
3.8	1.04	32.4	0.85	2	71.6	0.1	0.15	1.08	0.09	0.53	13	2	5.6	
5	1.34	32.4	1.12	1	82.9	0.2	0.19	1.37	0.13	0.68	15	2	7.3	
5.7	1.55	33.2	1.31	1	76.9	0.3	0.23	1.75	0.17	0.92	16	2	9.3	
5.7	1.55	29.5	1.3	1	82.8	0.2	0.25	1.64	0.17	0.89	14	2	9.3	
7.3	2.02	29.4	1.68	2	102	0.3	0.29	2.47	0.24	1.18	17	3	12.4	
Yb	Zr	As	Bi	Hg	Sb	Se	Te	LOI	Total	Co	Cu	Ni	Pb	Zn
ppm	ppm	ppm	ppm	ppm	ppm	ppm	ppm	%	%	ppm	ppm	ppm	ppm	ppm
1.13	257	10.6	0.12	0.17	0.011	0.5	0.01	14.65	100.5	5	27	7	12	77
UT10-SRS-10m a	UT10-SRS-10m c	UT10-SRS-10m e	UT10-SRS-10m a	UT10-SRS-10m d	UT10-SRS-10m e	UT10-SRS-10m g	UT10-SRS-10m h	UT10-SRS-10m i	UT10-SRS-10m j	UT10-SRS-10m k	UT10-SRS-10m l	UT10-SRS-10m m	UT10-SRS-10n	UT10-SRS-10n
0.88	257	6.2	0.13	0.27	0.012	0.3	0.01	3.57	101	1	12	7	7	23
0.7	148	15.4	0.14	0.3	0.026	0.3	0.01	5.45	99.7	5	27	9	7	58
0.58	105	10.3	0.07	0.21	0.015	0.3	0.01	4.88	99.9	5	27	8	10	53
1.03	226	17.2	0.22	0.47	0.021	0.4	0.01	10.25	99.7	5	31	7	9	69
0.65	101	41.6	1.48	2.45	0.046	0.4	0.03	7.68	100	6	23	9	7	69
0.69	94	20.7	0.2	0.29	0.014	0.3	0.01	8.75	98.8	3	17	8	8	60
0.66	94	9.2	0.09	0.16	0.01	0.3	0.01	8.54	98.2	5	11	7	7	53
UT10-SRS-13m p	UT10-SRS-13m s	UT10-SRS-13m v	UT10-SRS-13m y	UT10-SRS-13m b	UT10-SRS-13m d	UT10-SRS-13m e	UT10-SRS-13m f	UT10-SRS-13m g	UT10-SRS-13m h	UT10-SRS-13m i	UT10-SRS-13m j	UT10-SRS-13m k	UT10-SRS-13m l	UT10-SRS-13m m
0.92	207	10.7	0.08	0.13	0.011	0.3	0.01	11.15	97.9	4	4	8	6	51
1.21	304	18.9	0.09	0.17	0.008	0.3	0.01	11.7	98.8	4	48	8	6	71
1.19	274	11.9	0.78	0.29	0.01	0.4	0.02	14.85	99.8	5	25	7	7	77
1.69	421	7.7	0.45	0.26	0.012	0.4	0.02	14.95	99.6	5	20	8	8	73

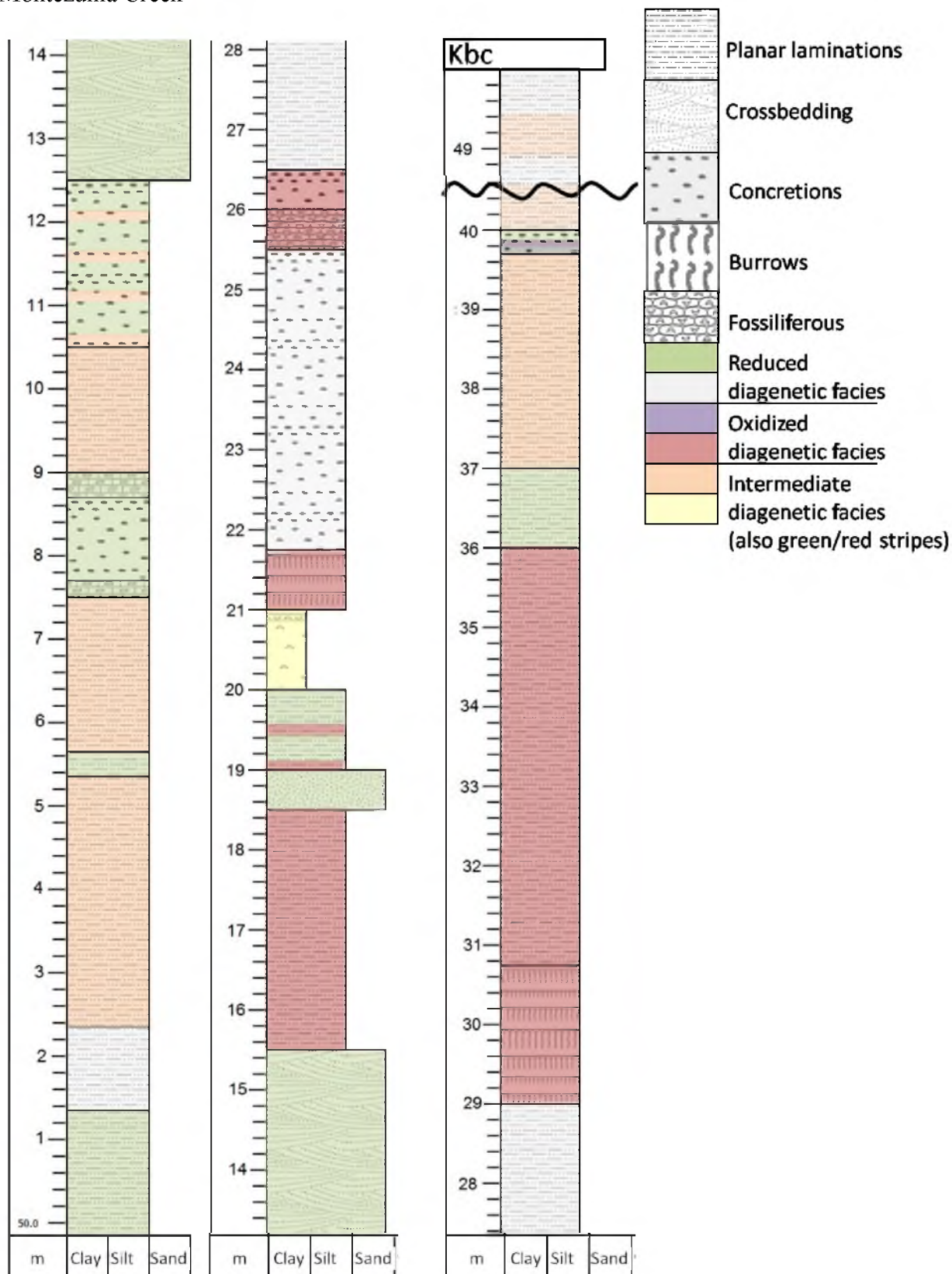
SAMPLE	ppm Sb	ppm Se	ppm Co	ppm Cu	ppm Ni	ppm Pb	ppm Zn
UT11-RG-1JMB	0.3	0.1	2	8	3	3	11
UT11-EC-1JMB	0.21	0.3	10	14	10	12	71
UT11-EC-2JMB	0.21	0.2	3	18	6	16	47
UT11-FP-2JMB	0.84	0.6	4	39	5	13	28
UT11-FP-3JMB	0.64	0.9	2	21	4	21	18
UT11-FP-5JMB	0.49	0.2	10	24	8	14	122
UT11-FP-7JMB	0.14	0.5	3	5	2	5	29
UT11-FPQ-1JMB.001	0.59	<0.2	1	11	<1	4	6
UT11-FPQ-1JMB.002	0.51	<0.2	3	9	1	25	27
UT11-FPQ-2JMB.001	0.68	3.7	5	11	2	32	36
UT11-FPQ-2JMB.002	0.17	<0.2	5	5	2	12	38
UT11-MZ-1JMB	9.78	59.5	16	21	4	77	17
UT11-MZ-2JMB	0.31	1.6	4	18	8	26	56
UT11-MZ-3JMB	0.44	0.5	7	15	5	16	58
UT11-MZ-4JMB	0.8	0.3	5	14	2	20	76
UT11-MZ-7JMB	0.19	<0.2	8	10	2	5	59
UT11-MZ-14JMB	0.34	0.2	3	8	2	21	48
UT11-MZ-15JMB	0.12	0.2	1	8	1	11	22
UT11-MZ-17JMB	0.2	<0.2	3	3	<1	19	53
UT11-MZ-18JMB	4.94	1.1	1	18	1	37	37
UT11-MZ-21JMB	0.16	0.7	3	7	2	21	56
UT11-MZ-22JMB	0.1	<0.2	2	12	1	19	50
UT11-MZ-23JMB	0.1	0.2	8	9	2	12	93
UT11-MZ-25JMB	0.15	16.7	6	11	4	4	68
UT11-MZ-27JMB	0.25	3.6	7	14	3	14	73
UT11-MZ-28JMB	0.23	1.2	3	9	1	26	56
UT11-MZ-29JMB	0.5	0.5	4	8	1	21	52
CO11-MC-1JMB.001	0.22	0.2	3	5	2	7	21
CO11-MC-1JMB.002	0.28	0.2	4	3	1	10	30
UT11-BH-5JMB	0.16	0.5	4	14	1	18	27
UT11-BH-9JMB	0.14	2	3	6	<1	16	20
UT11-BH-11JMB	0.13	5.8	5	12	4	21	56
UT11-BH-12JMB	0.91	0.7	5	29	6	10	43
UT11-BH-14JMB	0.13	0.3	5	9	2	19	59
UT11-BH-15JMB	1.74	0.3	2	17	2	18	26
UT11-BH-16JMB	0.2	0.7	2	5	<1	18	26
UT11-BH-17JMB	0.26	0.2	2	7	1	8	16
UT11-BH-18JMB	0.2	0.9	2	6	1	20	16
UT11-BH-19JMB	0.2	0.3	4	9	3	14	42
UT11-BH-23JMB	0.25	0.6	5	18	7	15	58
UT11-BH-24JMB	0.31	0.2	2	6	1	9	20
UT11-BH-27JMB	0.36	0.4	3	13	3	14	26
UT11-BH-28JMB	0.88	2.1	7	16	9	18	58
UT11-BH-31JMB	0.59	0.6	9	6	6	14	42
UT11-BH-32JMB	0.22	1.1	3	10	1	21	25
UT11-BH-33JMB.001	0.23	3	1	12	2	10	16
UT11-BH-33JMB.002	0.24	1.5	2	7	<1	12	15
UT11-TM-2JMB	13.4	0.2	3	14	<1	21	6
UT11-TM-3JMB	2.4	0.3	<1	6	1	10	7
UT11-TM-4JMB	0.28	1.4	<1	16	<1	14	7
UT11-TM-5JMB	0.22	0.5	2	7	1	21	28
UT11-EC-1JMB	0.21	0.3	10	14	10	12	71
UT11-EC-2JMB	0.21	0.2	3	18	6	16	47

APPENDIX F

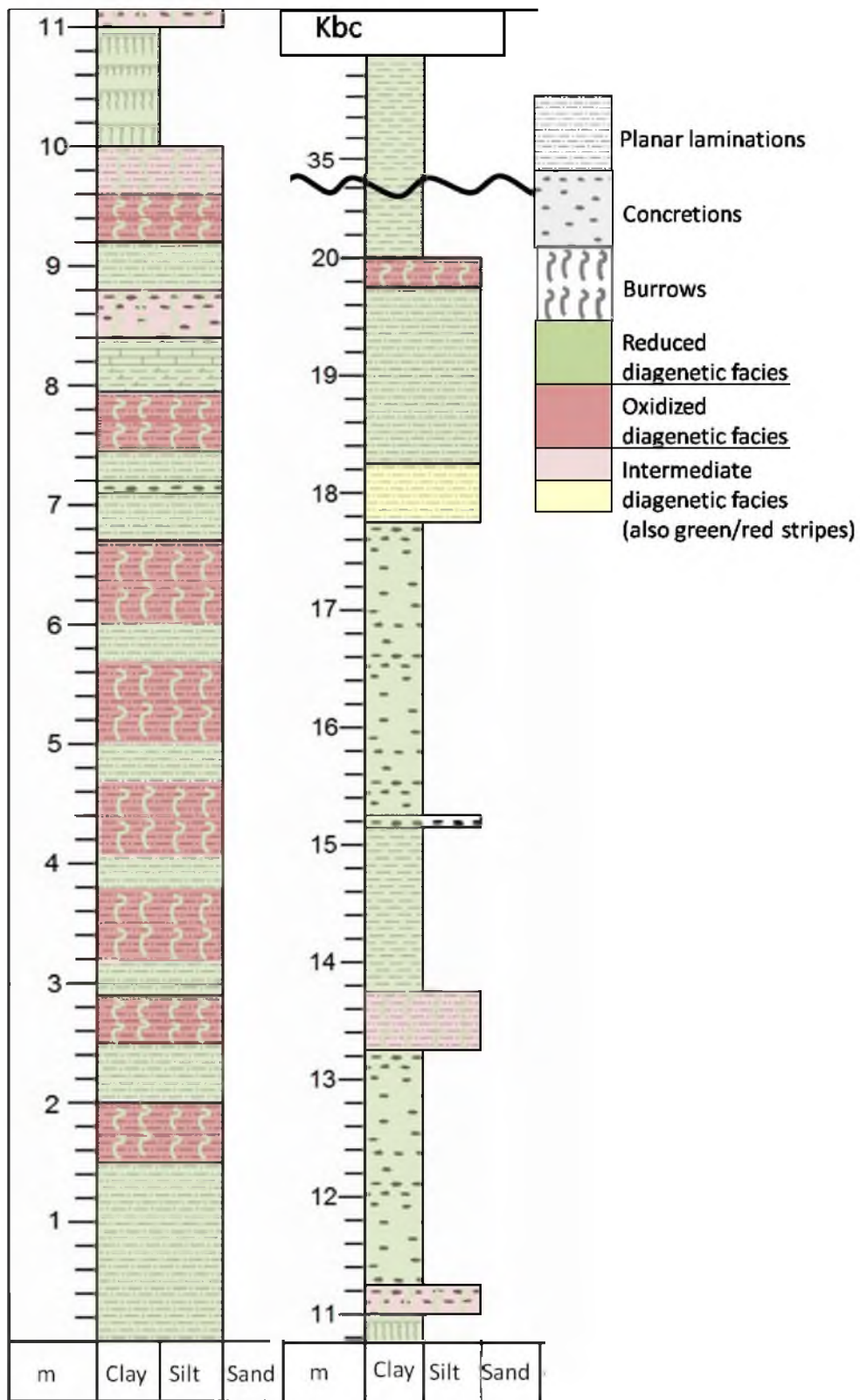
STRATIGRAPHIC SECTIONS OF THE BRUSHY BASIN MEMBER, JURASSIC MORRISON FORMATION

Stratigraphic sections were measured in meters in four locations: Montezuma Creek, Blue Hills (south and north sections) and Fruita Paleo Area. Localities are shown in Figure 2.1 and specific location coordinates are in Appendix A. Lithofacies and diagenetic facies are documented in detail. Colors indicate diagenetic facies where reds are oxidized, green and white are reduced and tan, yellow and orange are intermediate. Chapter 2 includes Munsell colors (from Munsell Rock Color Chart) of diagenetic facies and lithofacies detailed description and interpretation. Particular attention was paid to obvious biotic influences such as burrows, root traces (mottles), charophyte molds (vugs) and dinosaur and plant fossils. Fossiliferous horizons refers to the presence of permineralized bone and petrified wood.

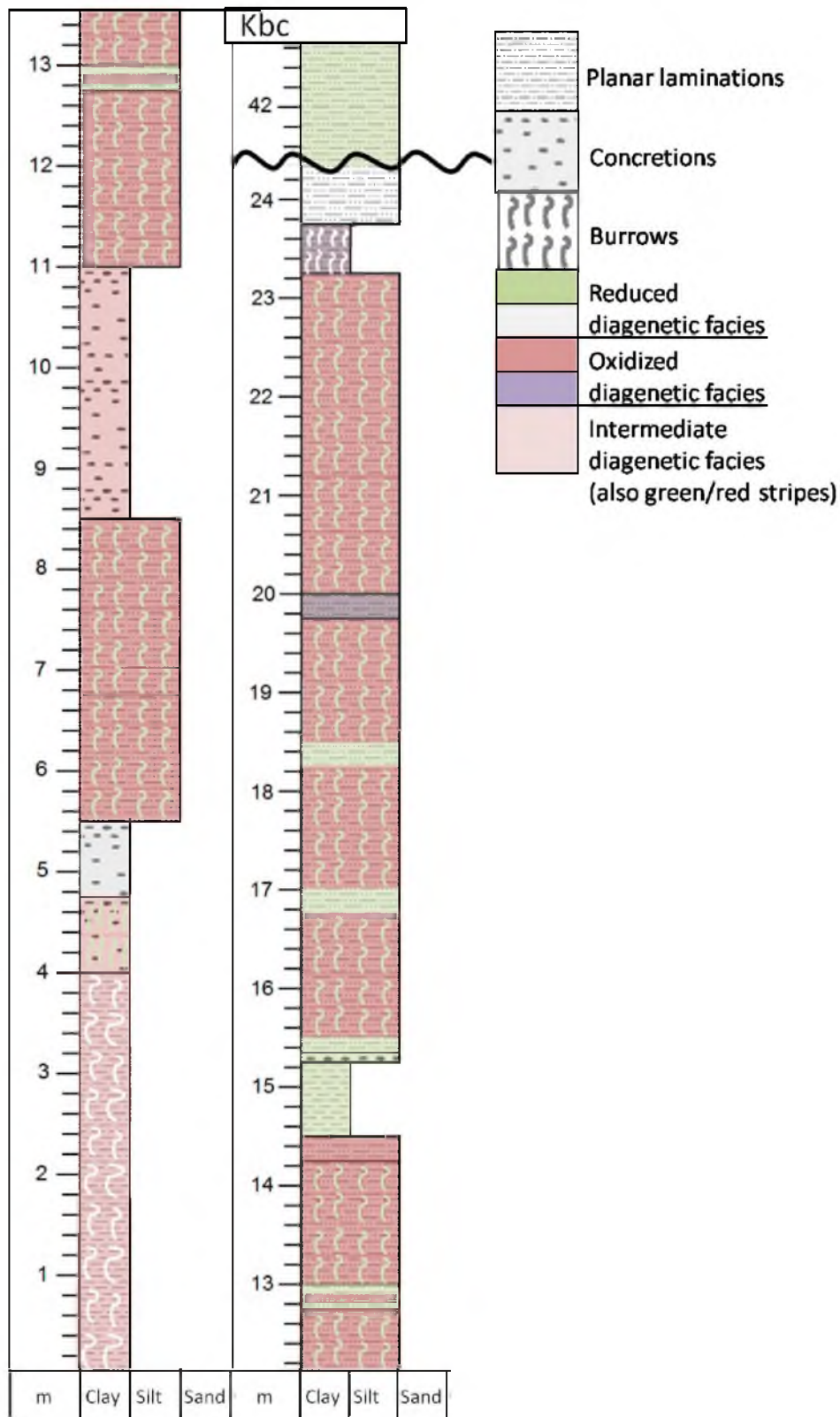
Montezuma Creek



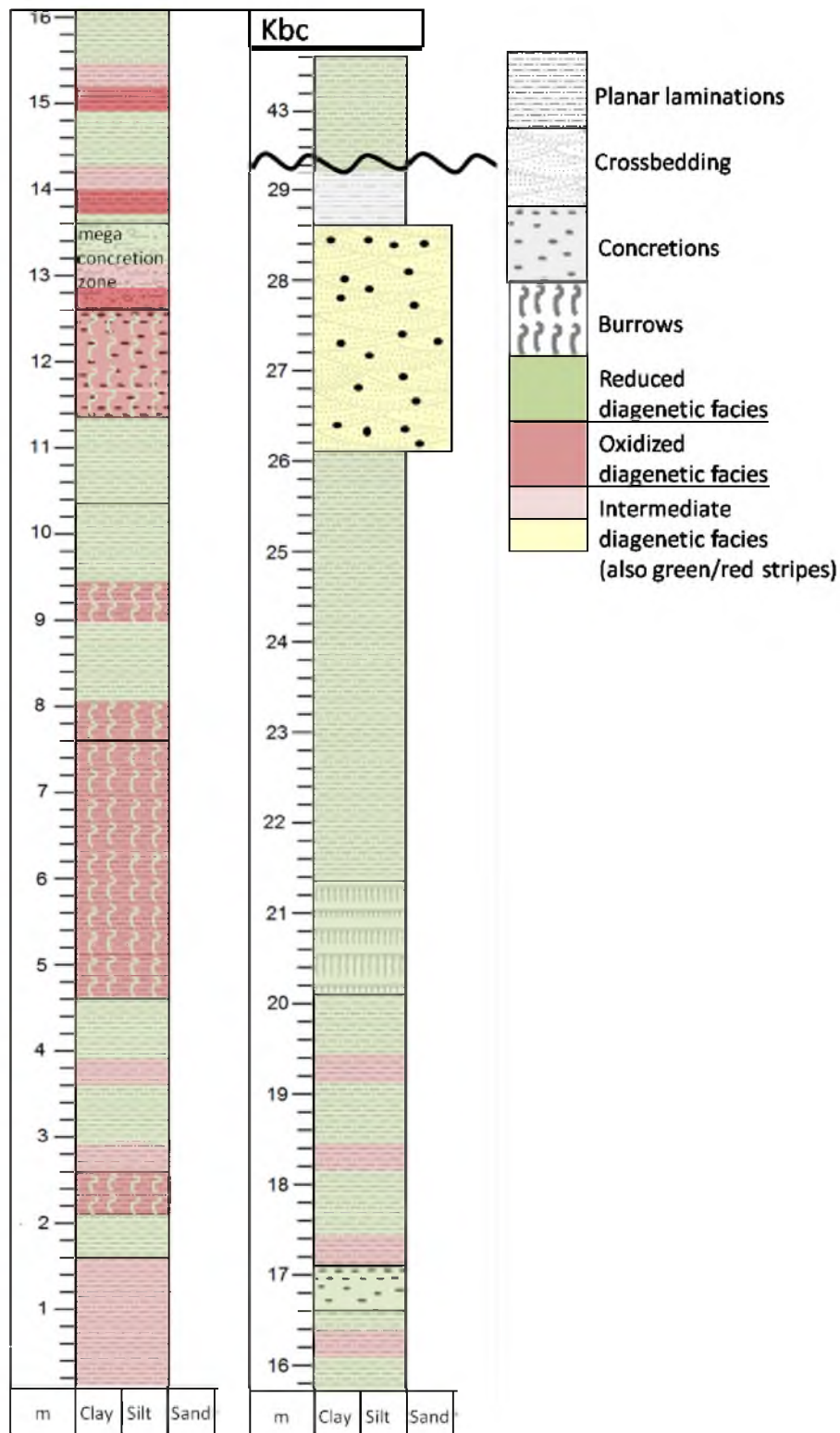
Blue Hills South



Blue Hills North



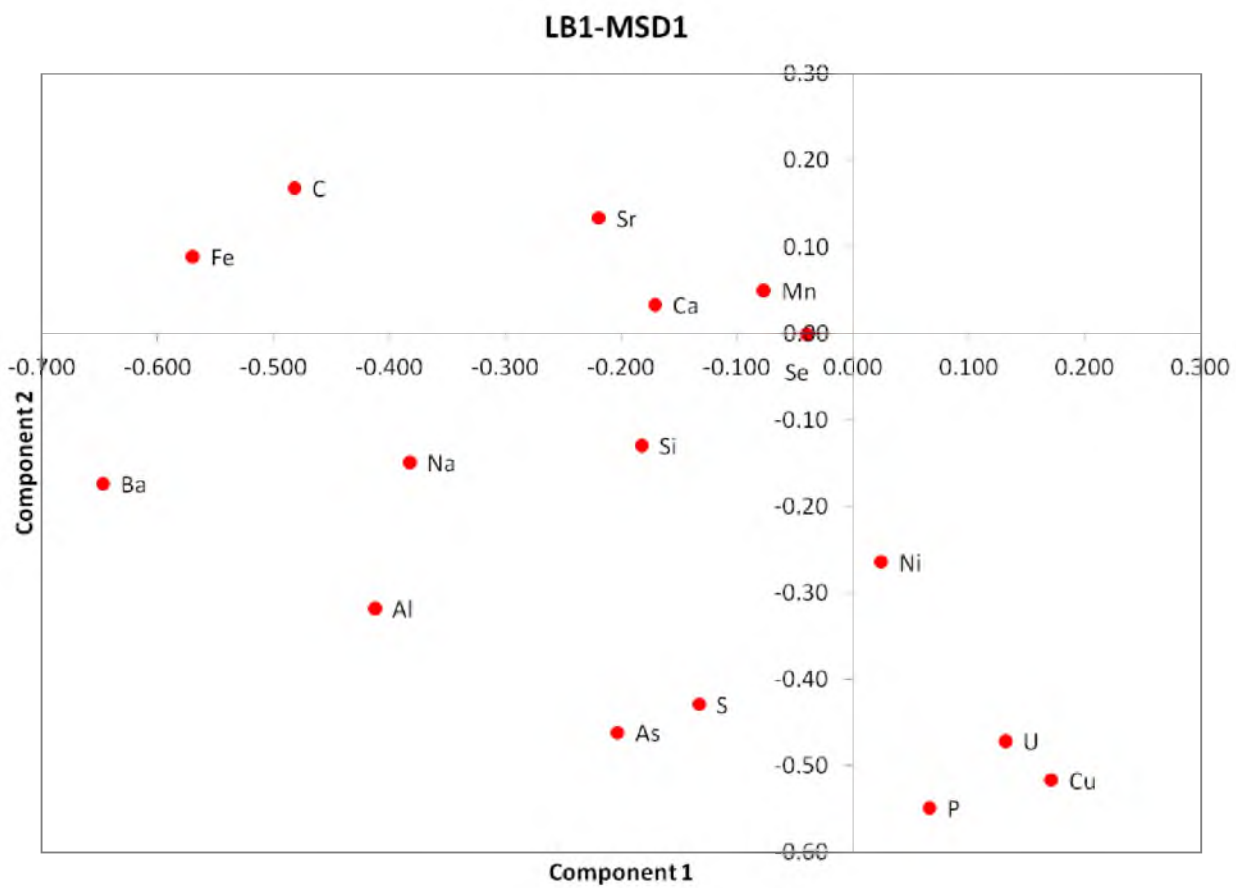
Fruita Paleo Area

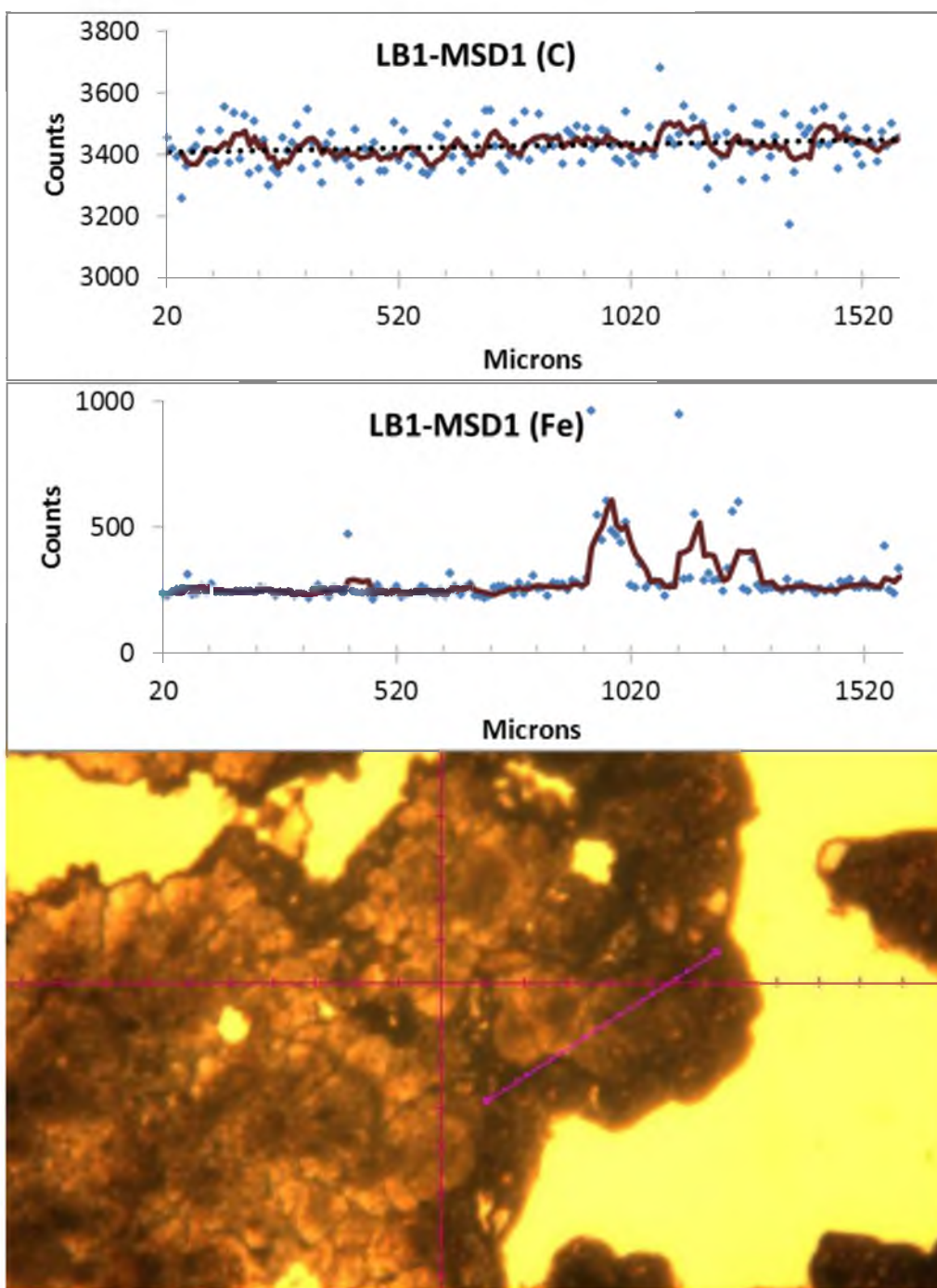


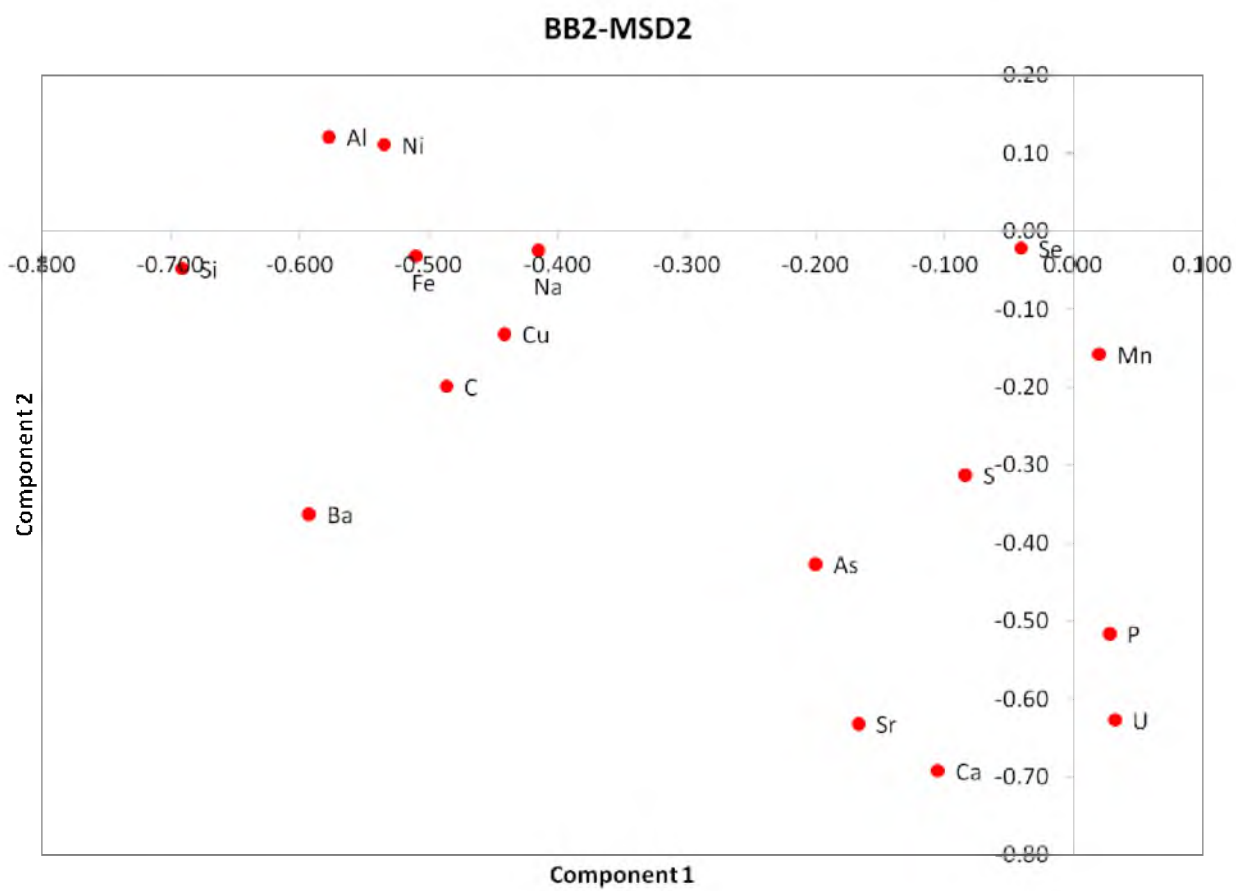
APPENDIX G

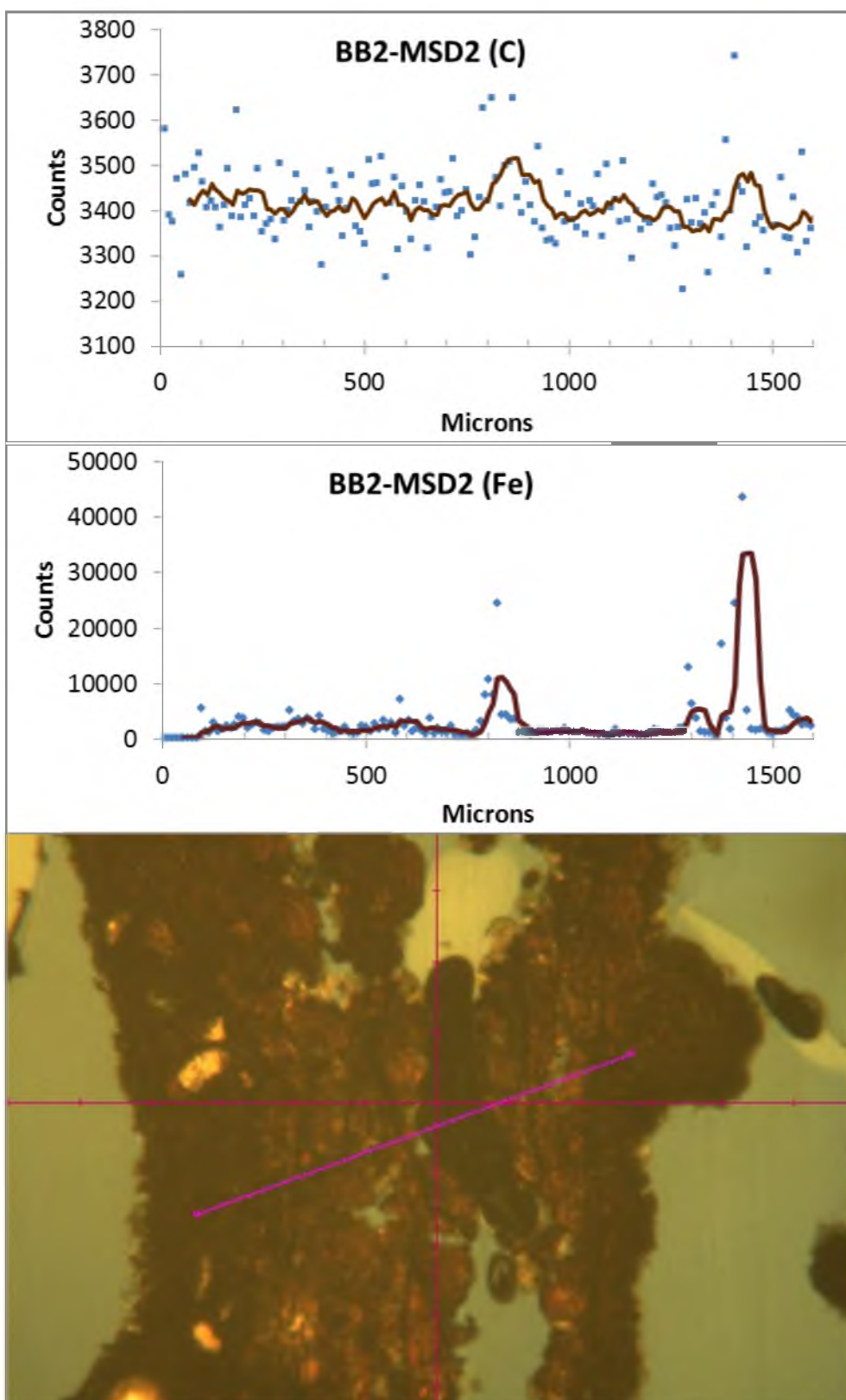
LASER ABLATION INDUCED COUPLED MASS SPECTROSCOPY

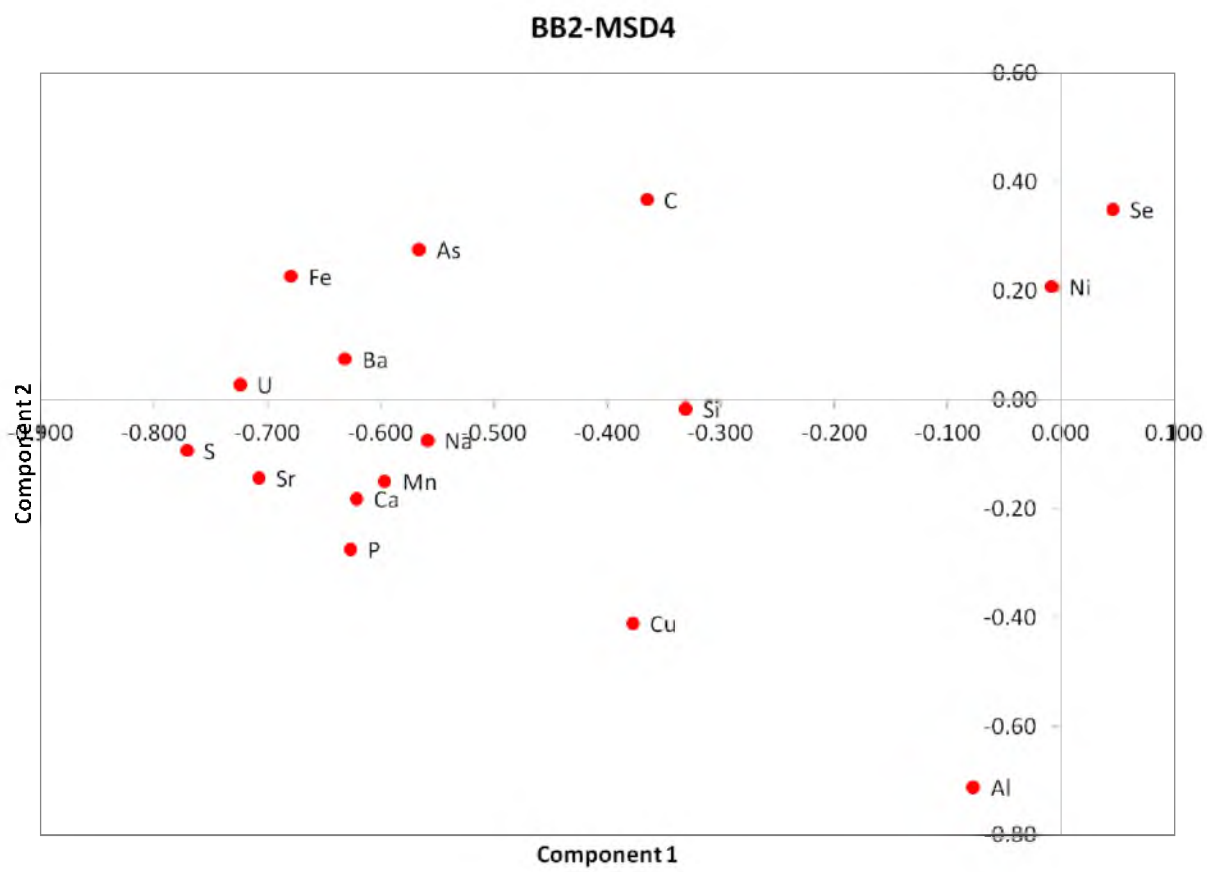
Principal component analysis (PCA) graphs show clusters of associated elements for each transect. Three groups are presented in the following order: 1) C, Fe, 2) C, S, Se and 3) anomalous correlations. Correlations are also compiled in Table 3.4. The appendix is arranged by the PCA graph for a selected sample first and then the graph of data acquired by Laser Ablation Induced Coupled Mass Spectroscopy (LA-ICP-MS) across 1600 μm transects of putative biological features showing concentrations of selected elements (carbon and iron). A photomicrograph showing features and transects analyzed is below the associated LA-ICP-MS graph; all transect lines in photos are $\sim 1600 \mu\text{m}$. The x axis in the LA-ICP-MS graphs represents counts (or concentrations) and the y axis corresponds to the distance along the transect, so maxima on the graphs show high concentrations at the corresponding point on the lines on the photomicrographs. LA-ICP-MS analysis was performed at the University of Utah under the guidance of Dr. Diego Fernandez and his laboratory assistants. Exact sample locations and descriptions are listed in Appendix A. Sample abbreviations correspond to locations as follows: LB=Little Bubbling Spring; BB=Big Bubbling Spring; CG=Crystal Geyser ($\sim 100\text{ka}$ terrace); MZ=Montezuma Creek; EC=Rattlesnake Gulch.

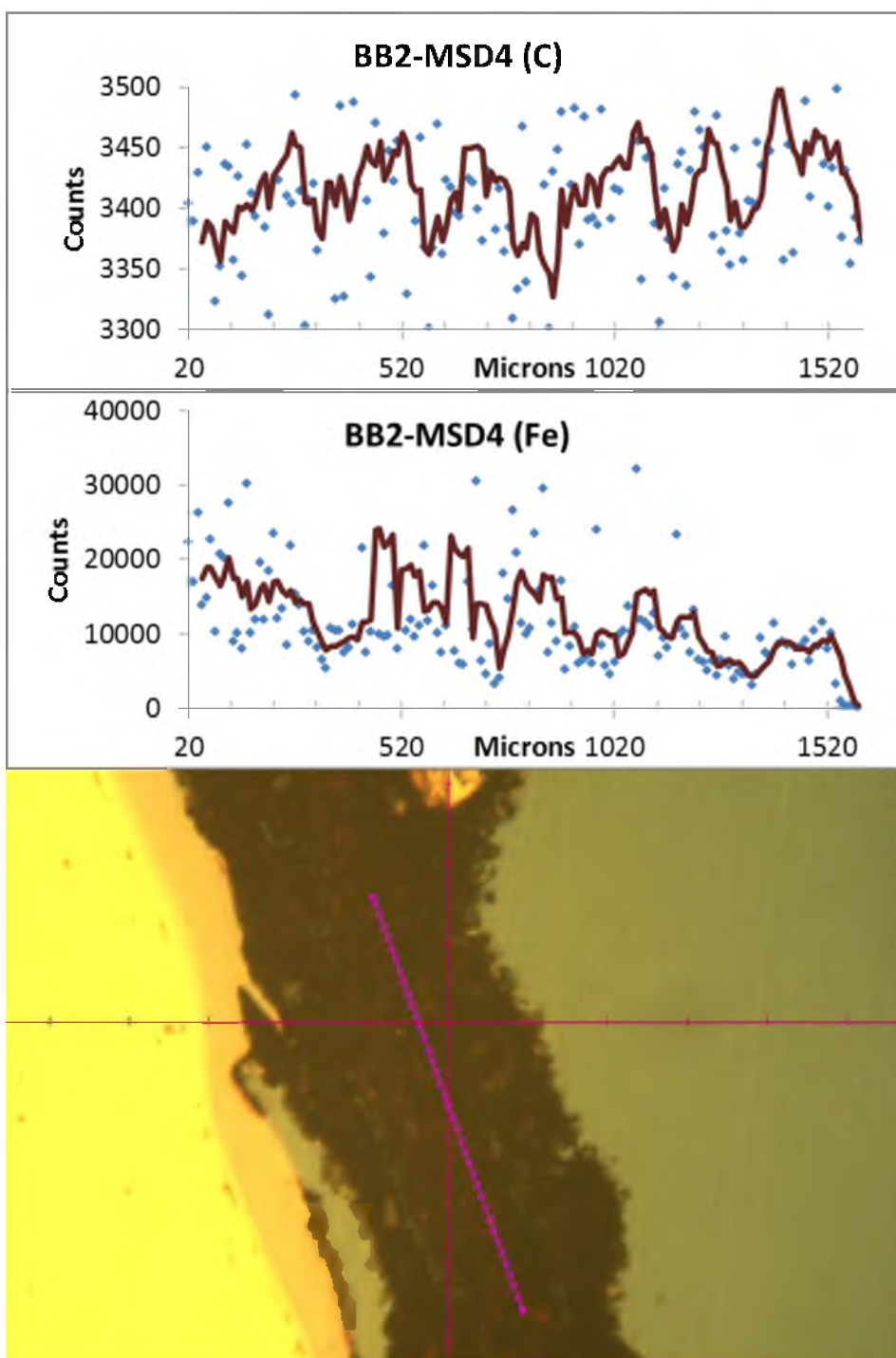
C, Fe Correlations

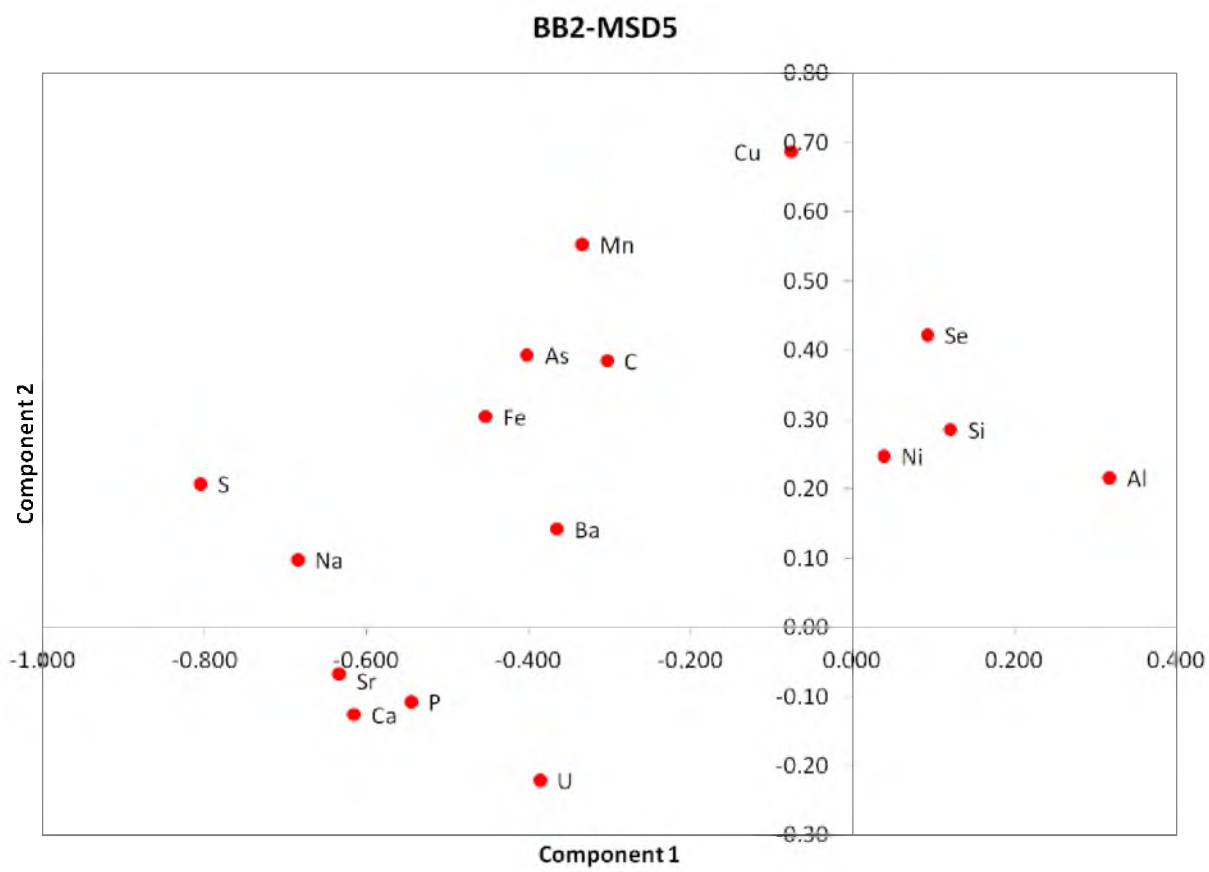


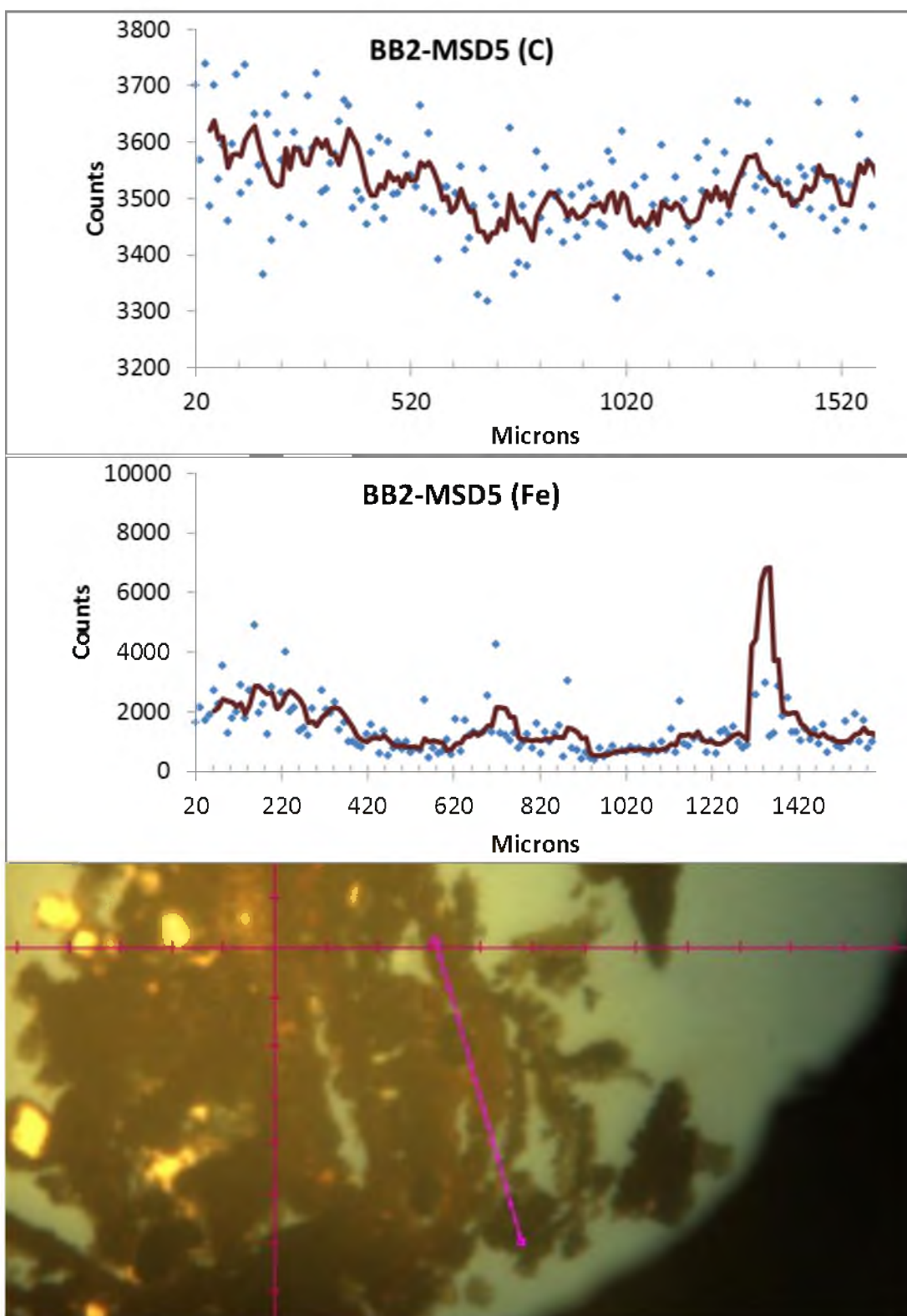


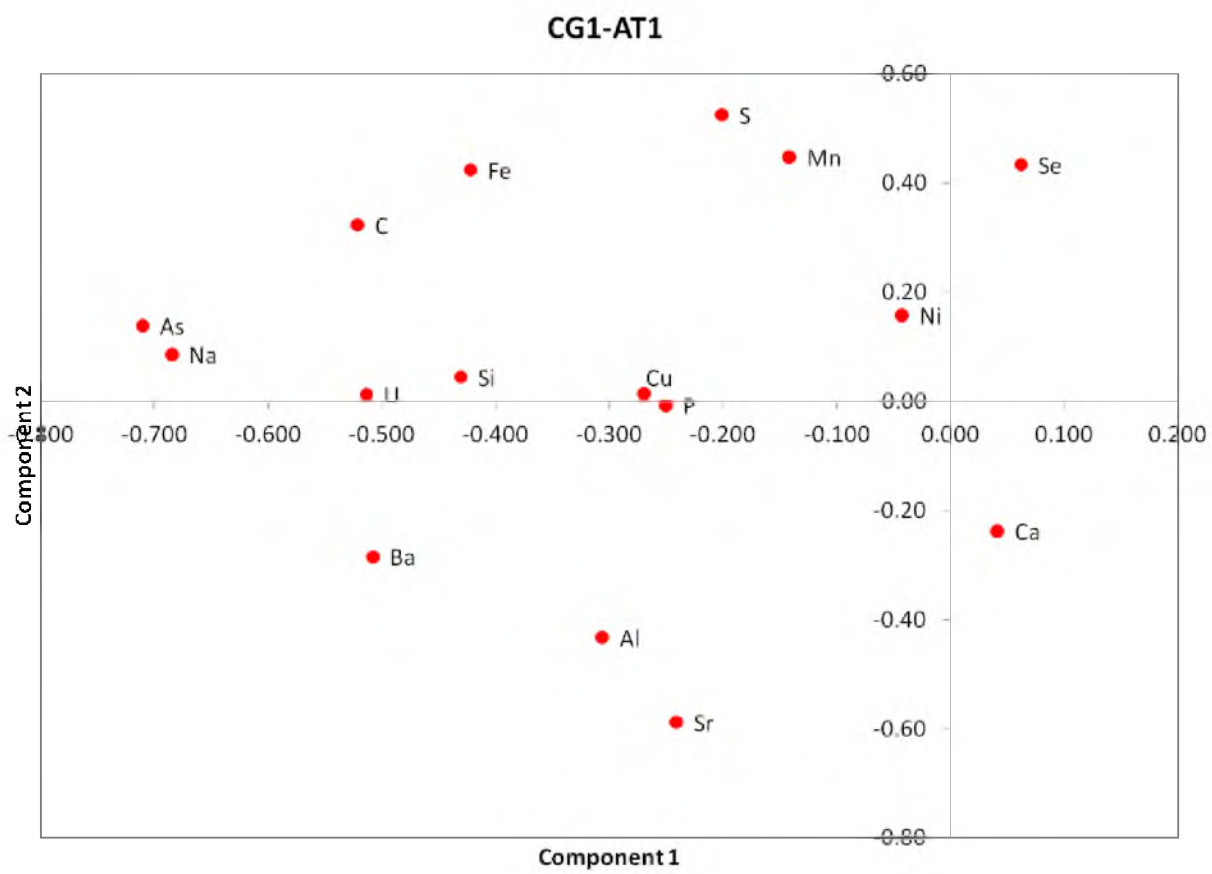


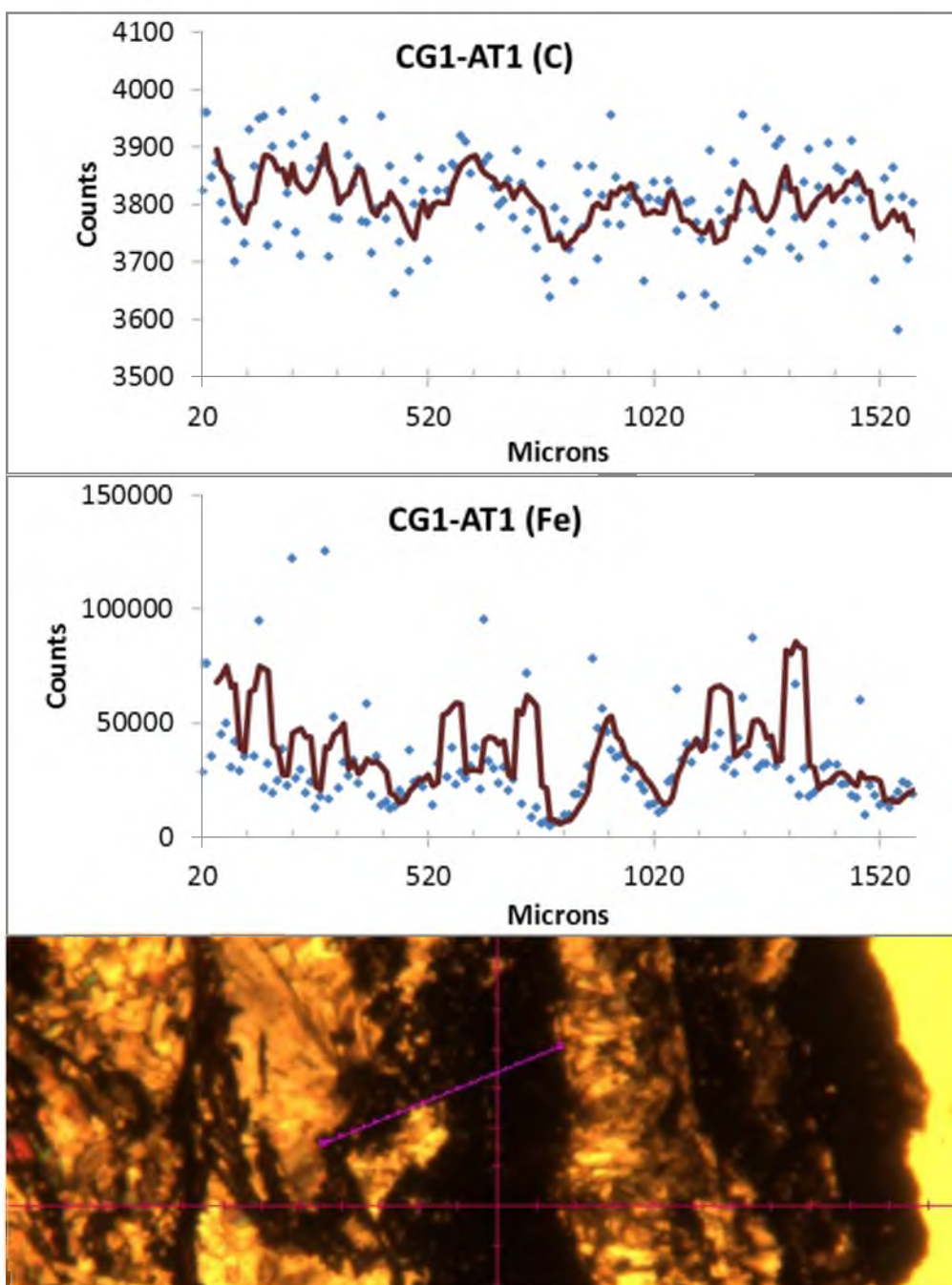


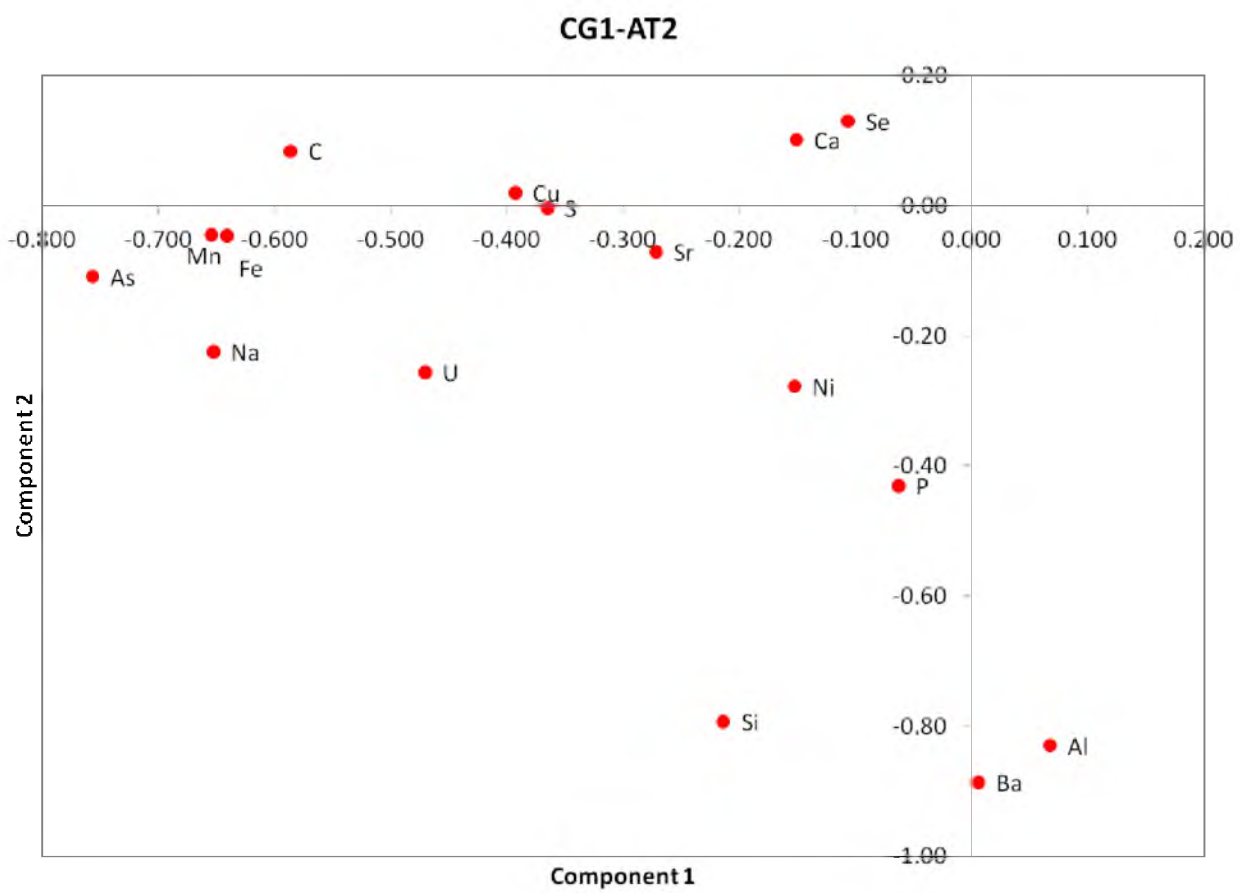


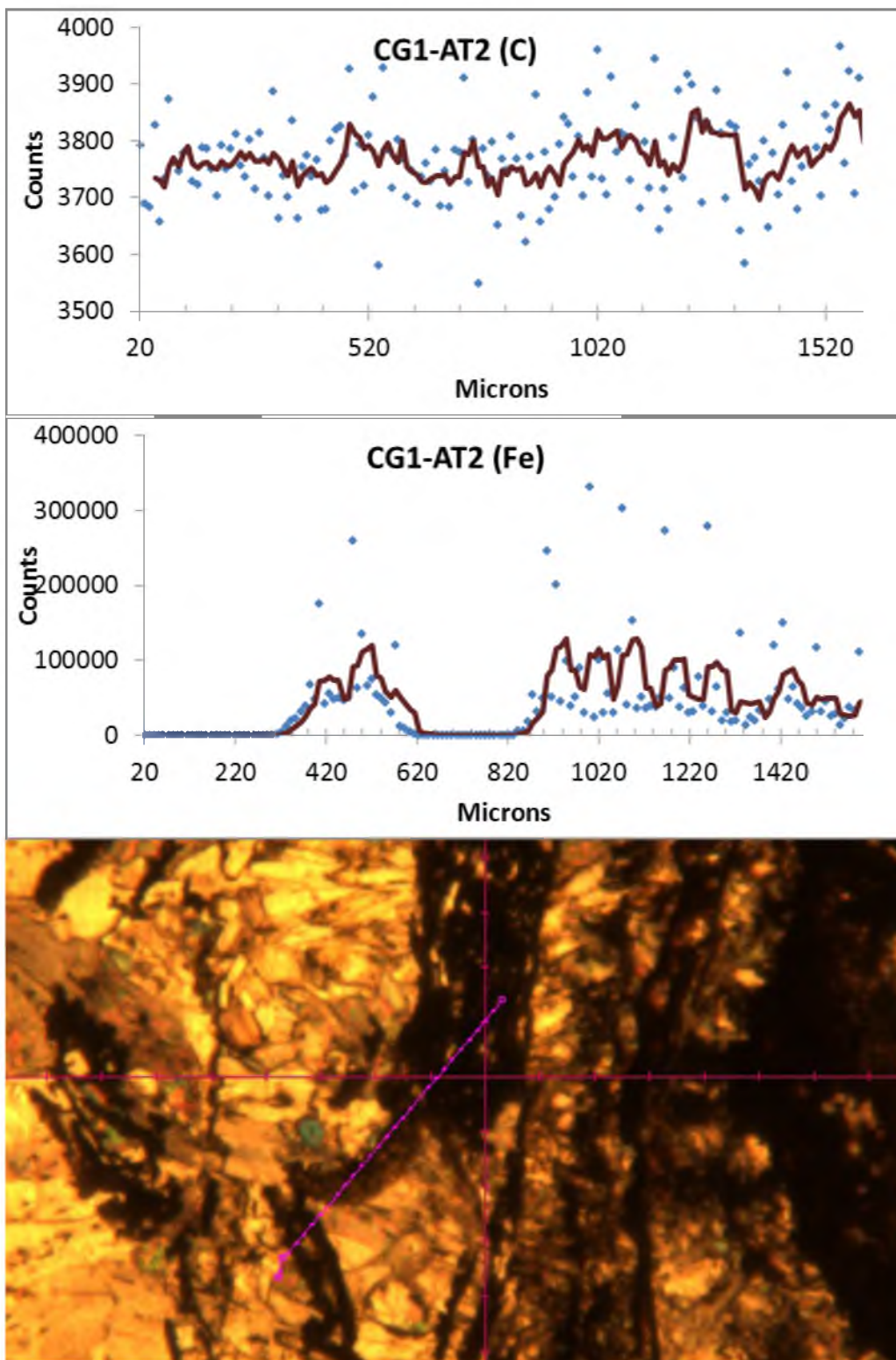


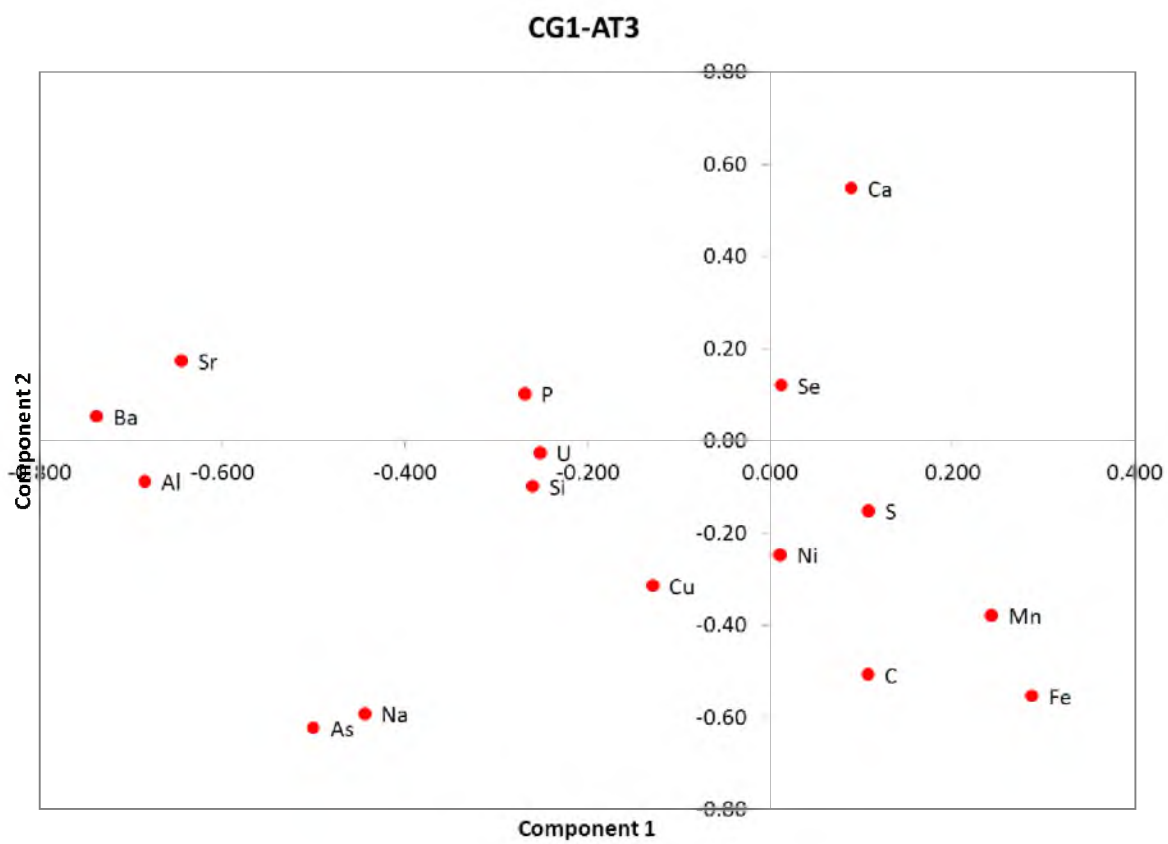


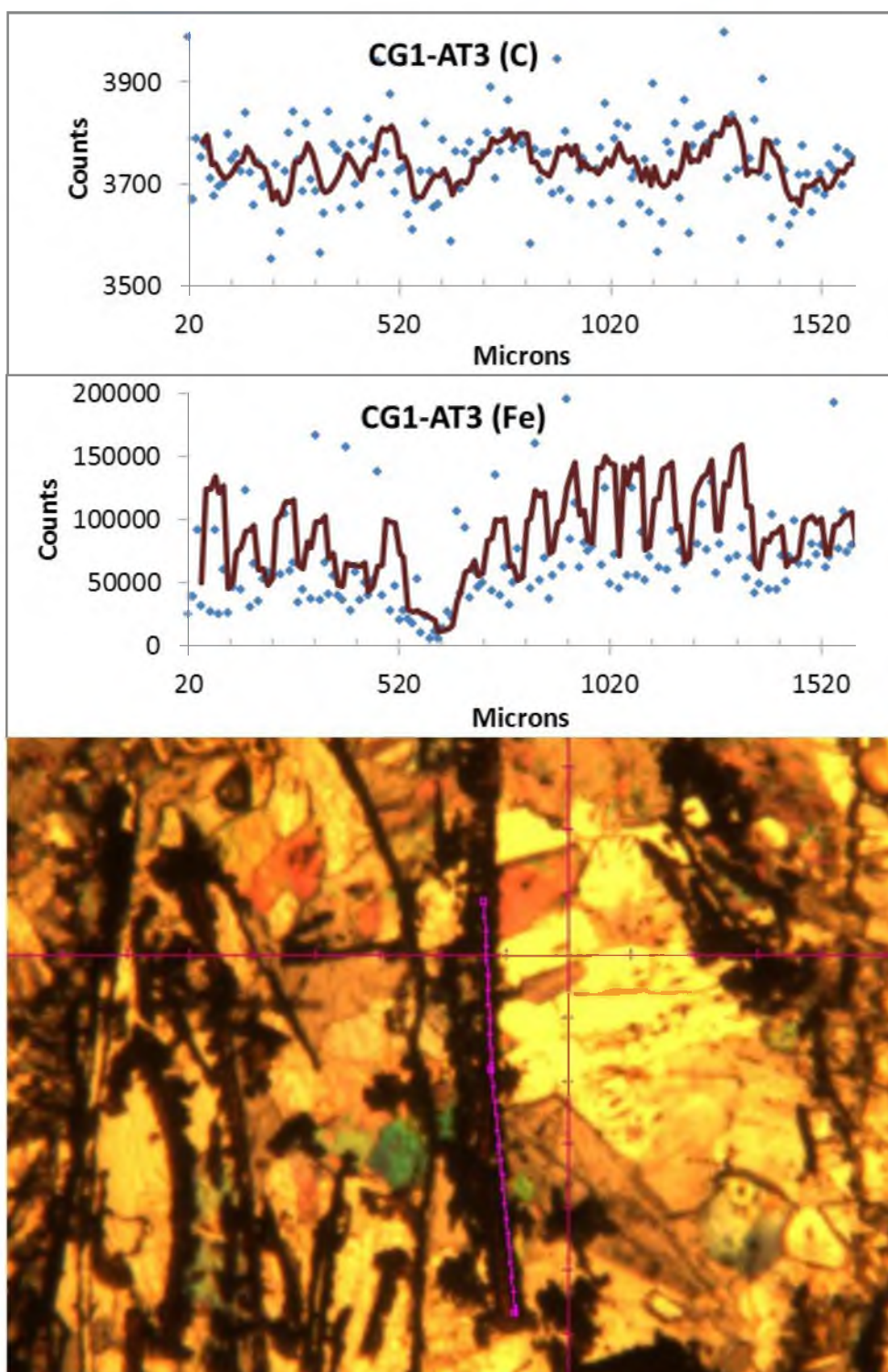


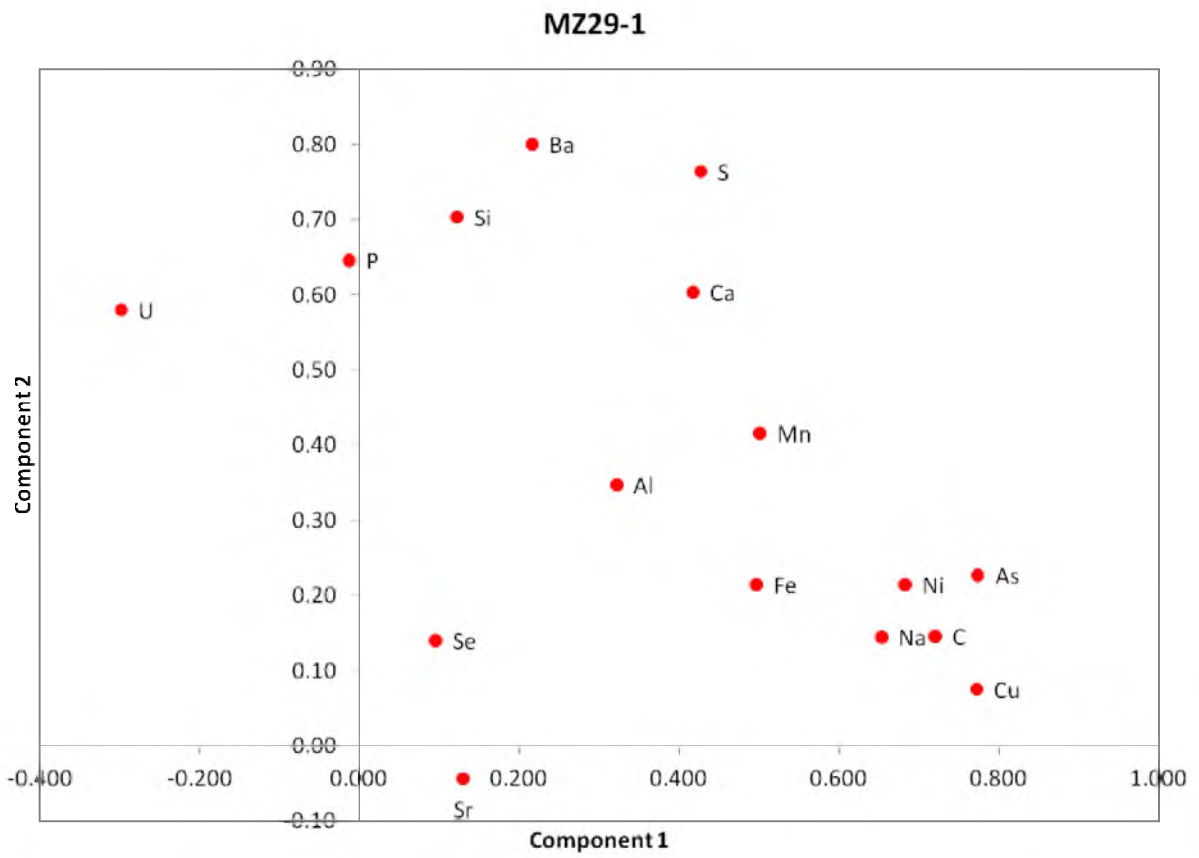


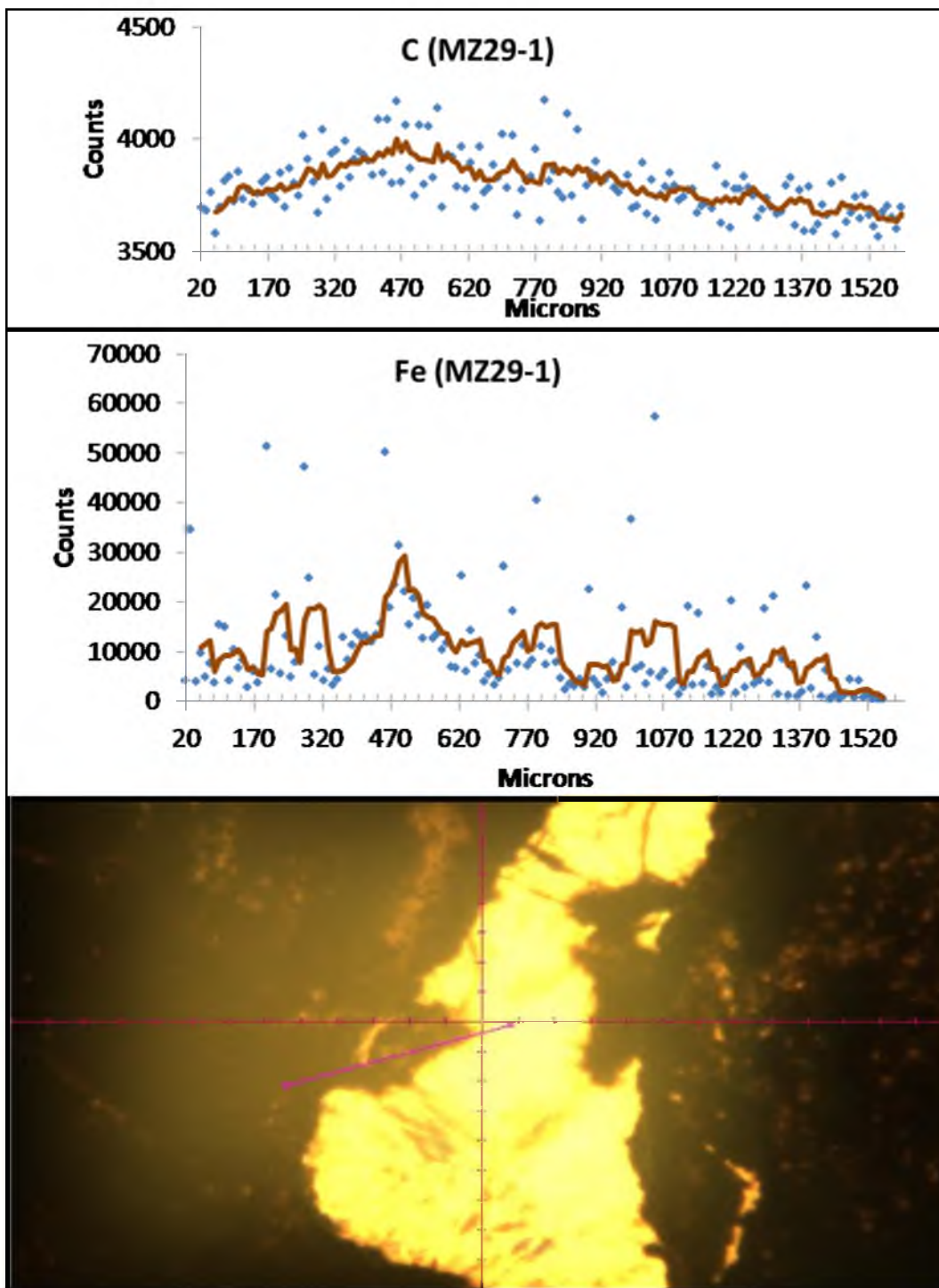


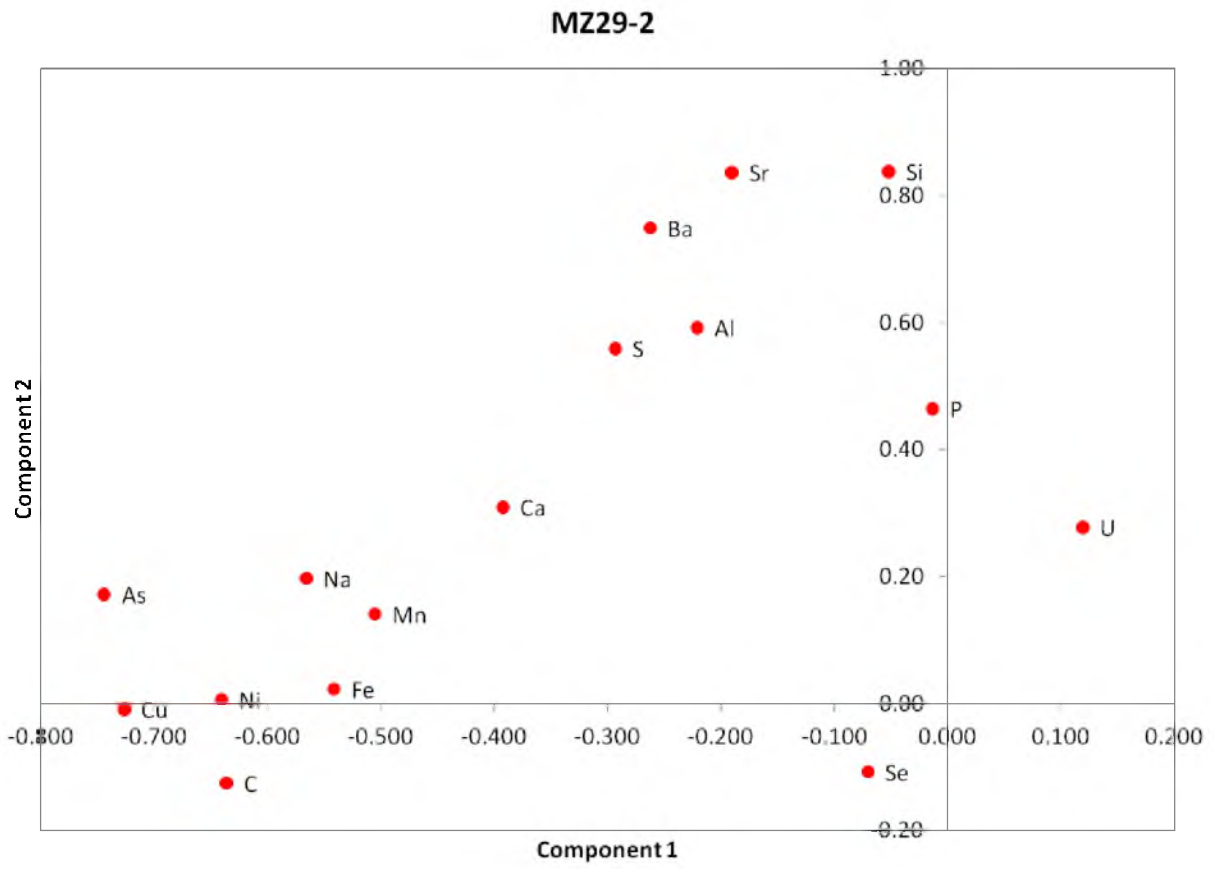


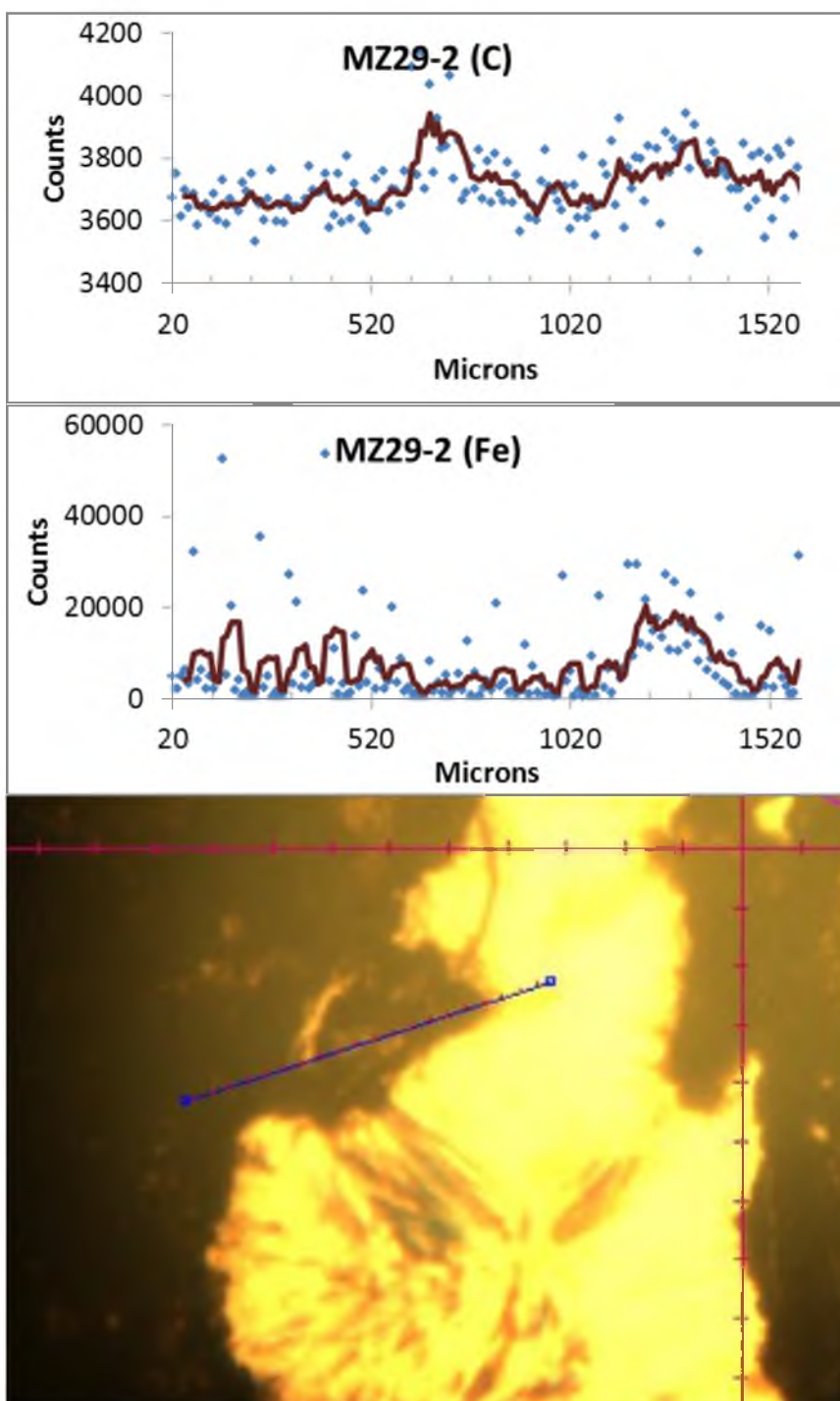


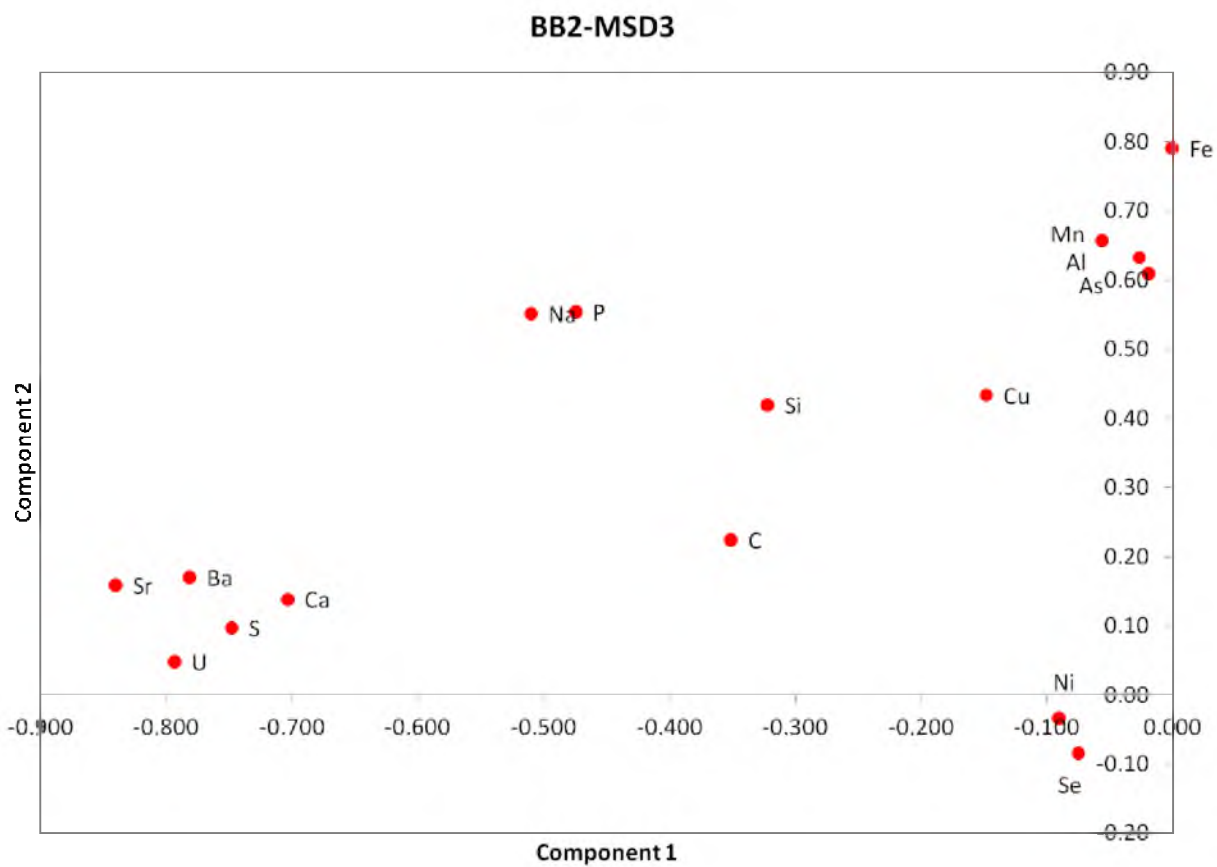




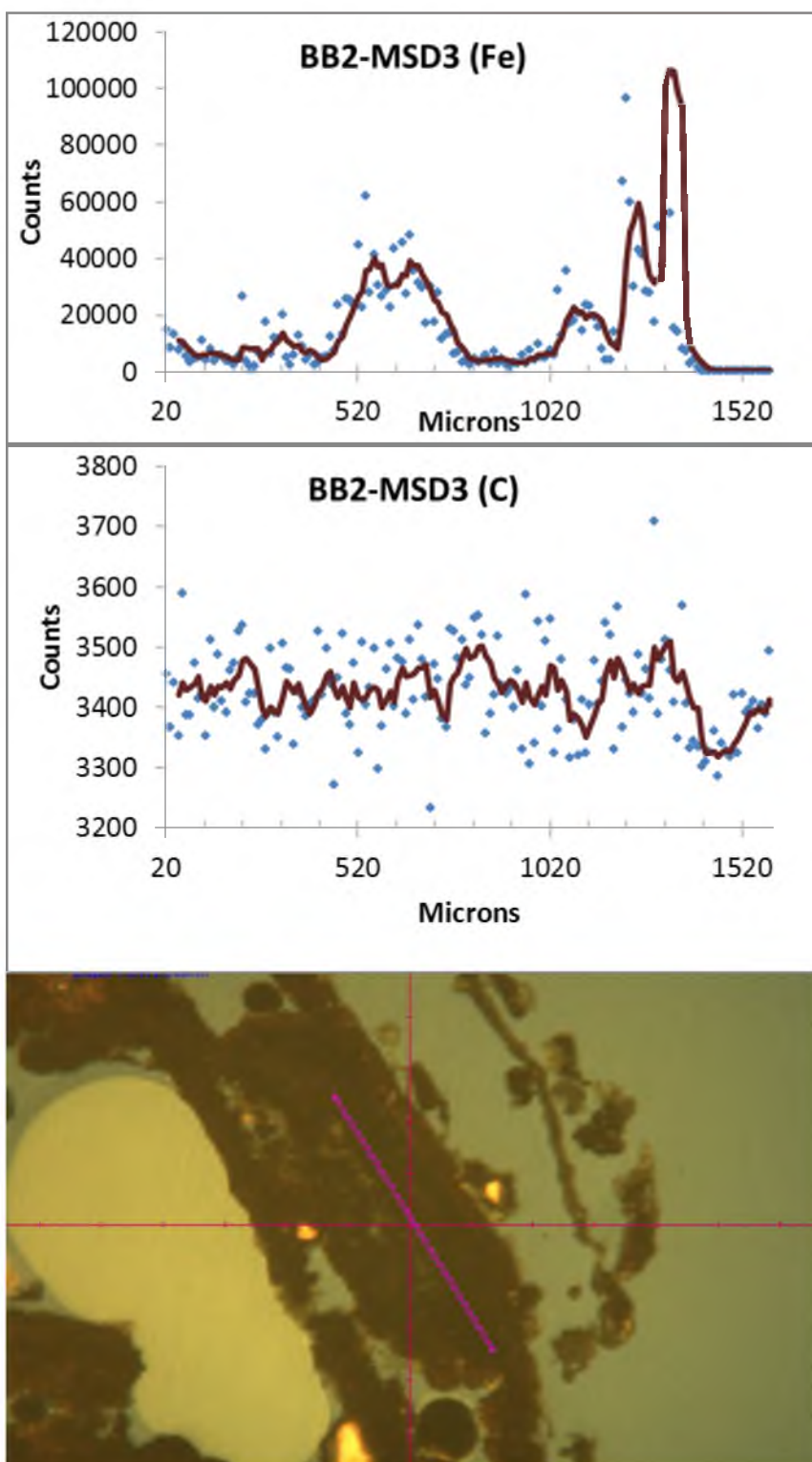


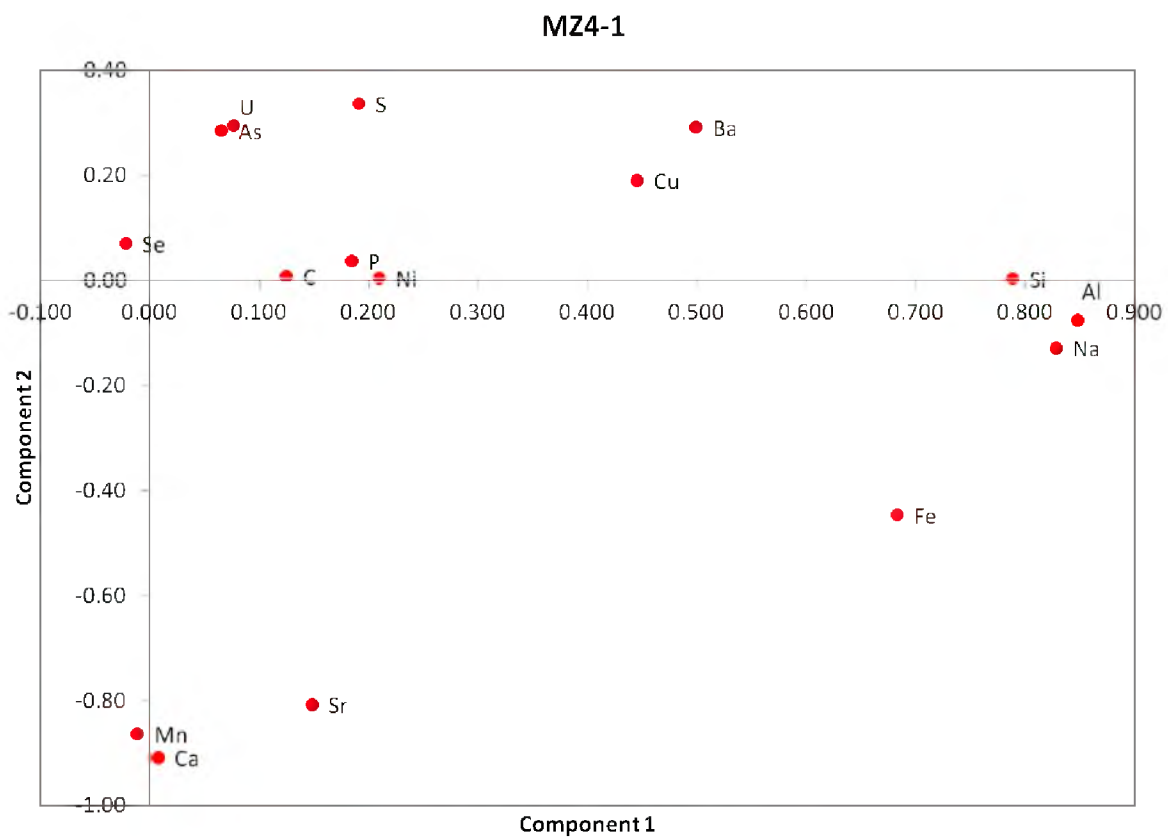


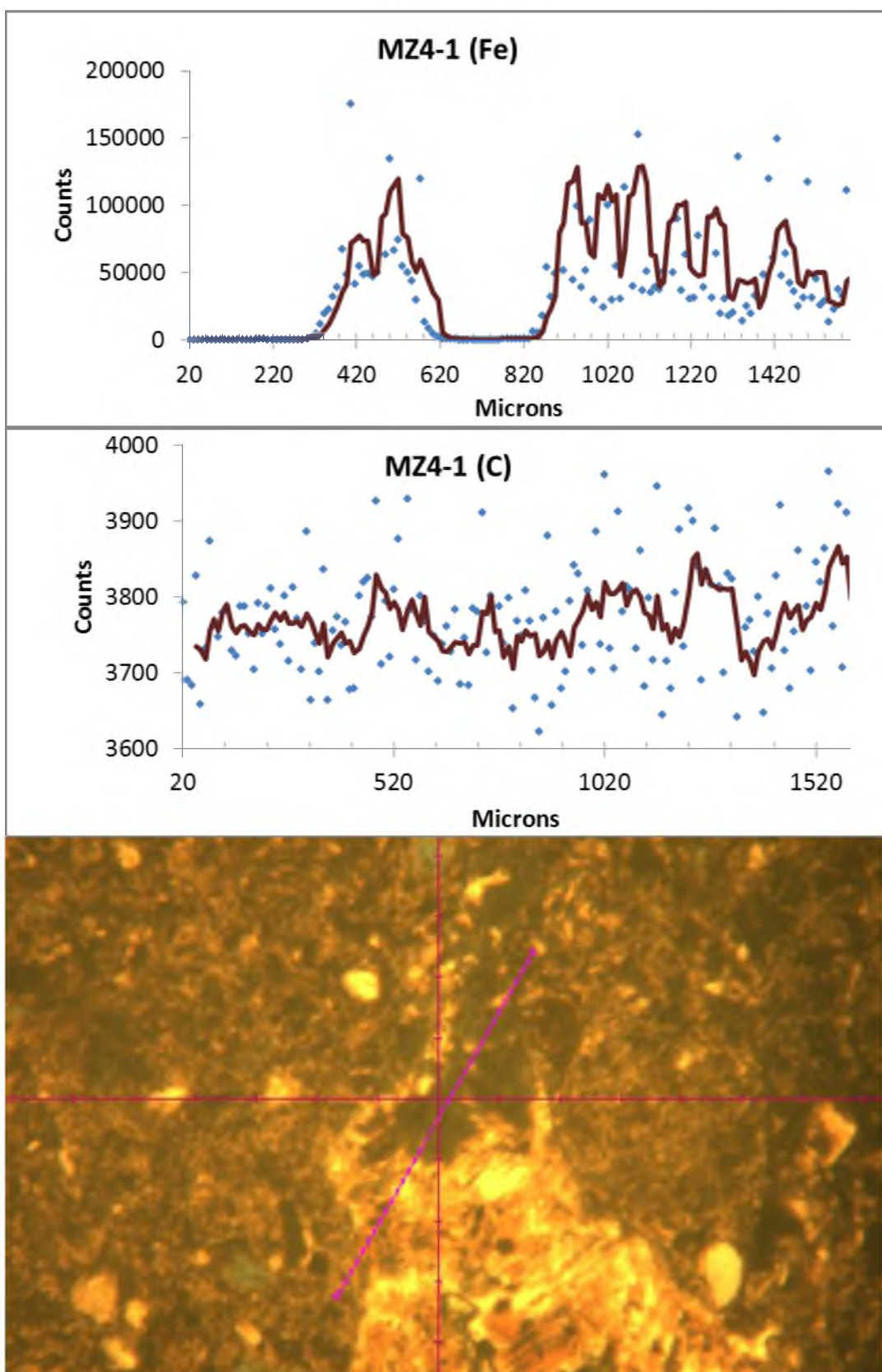


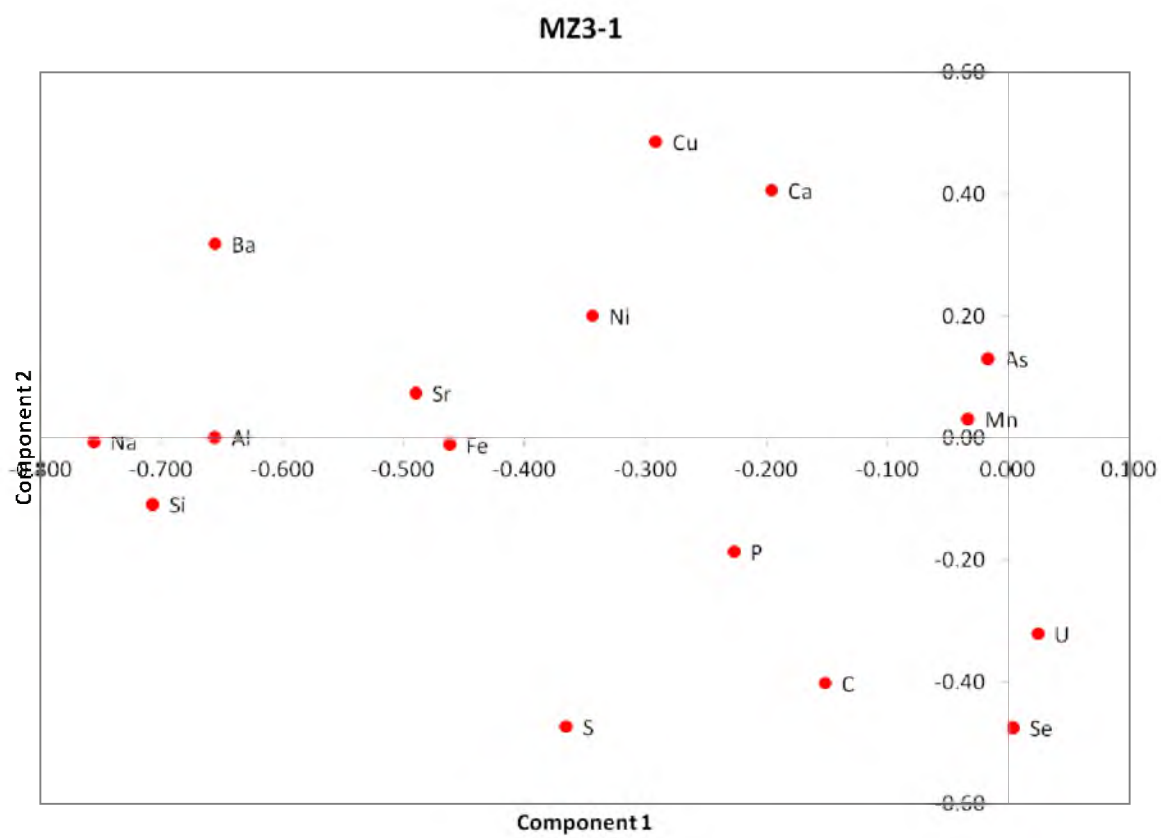
C, S, Se Correlations

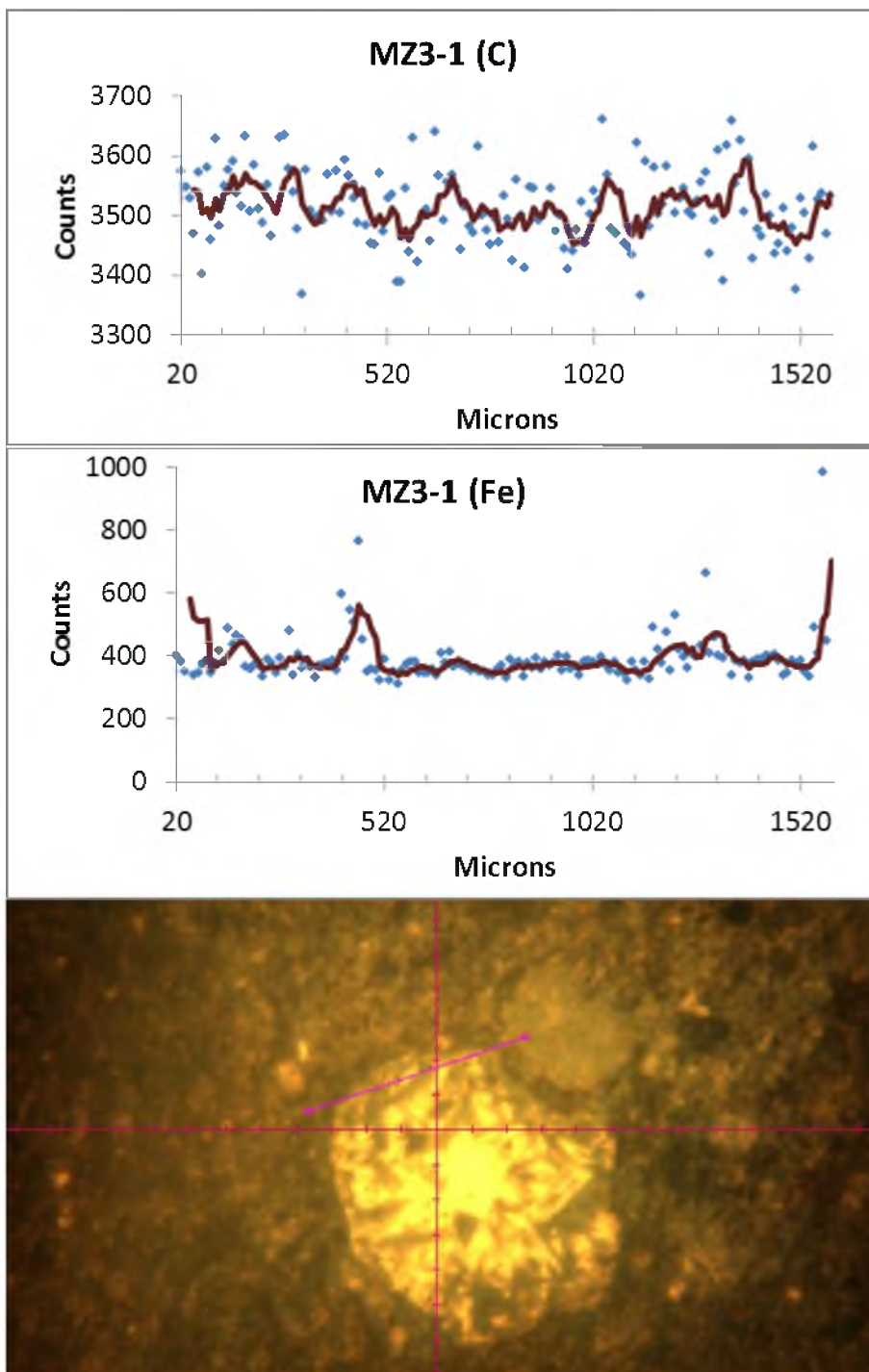
(C, S, Se is clustered about the X axis in this sample.)

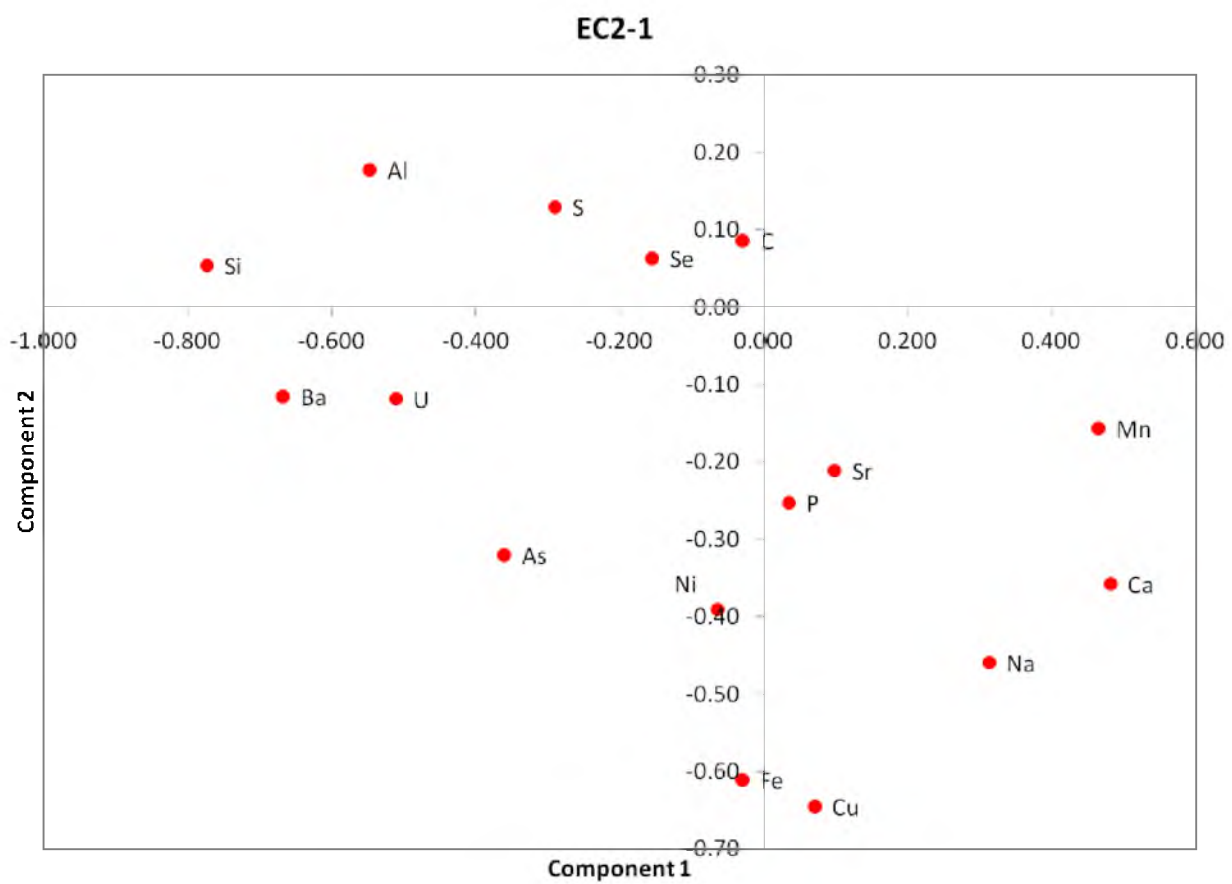


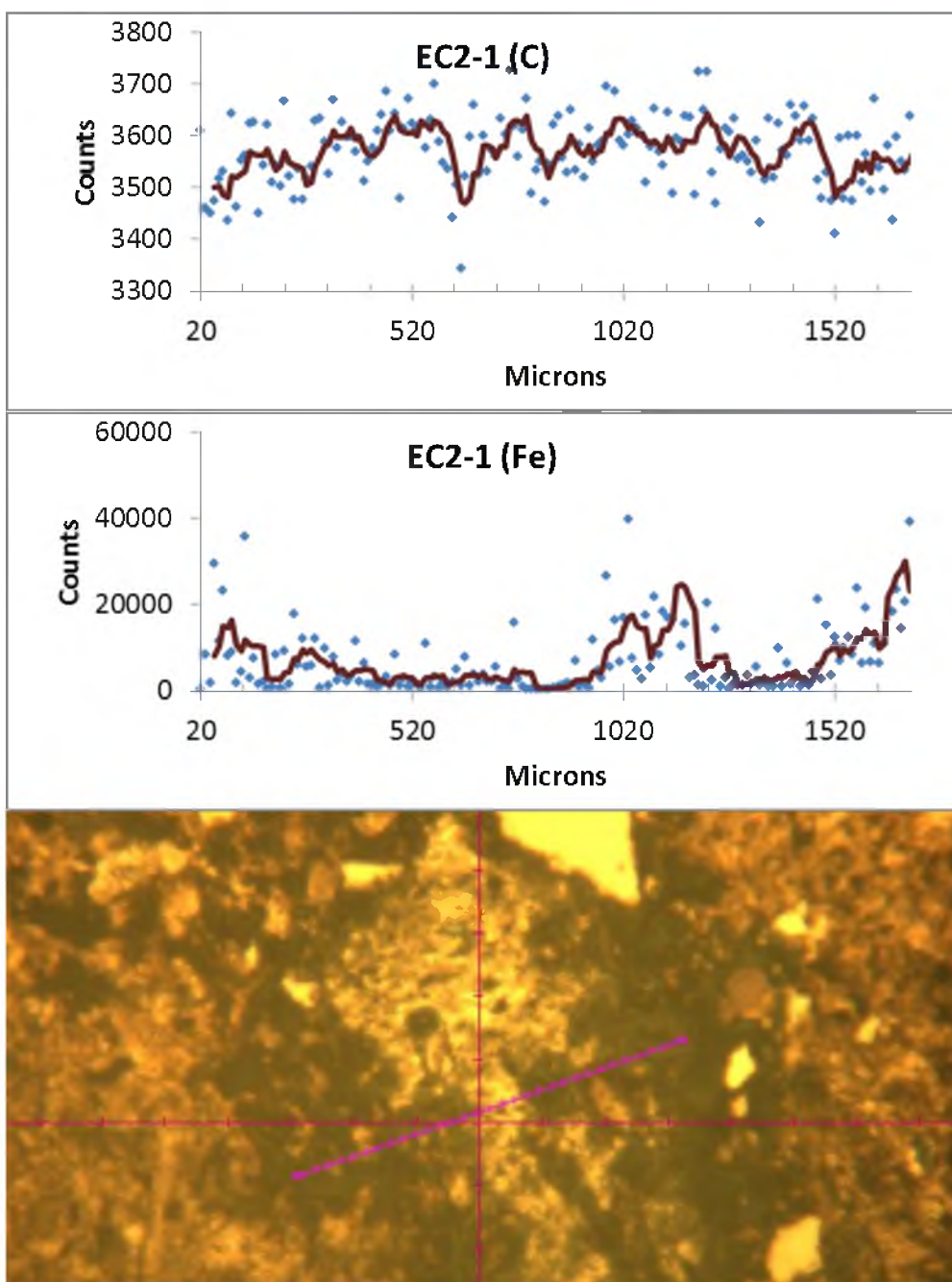


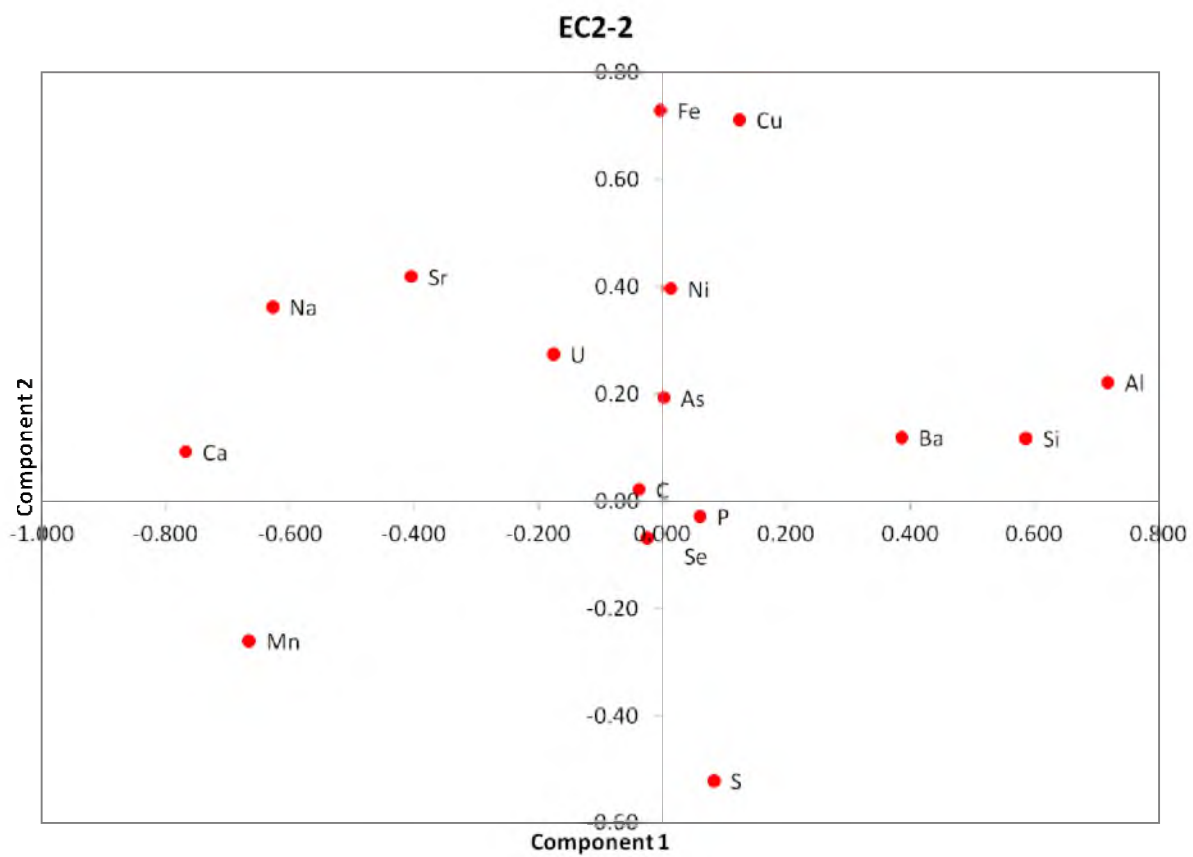


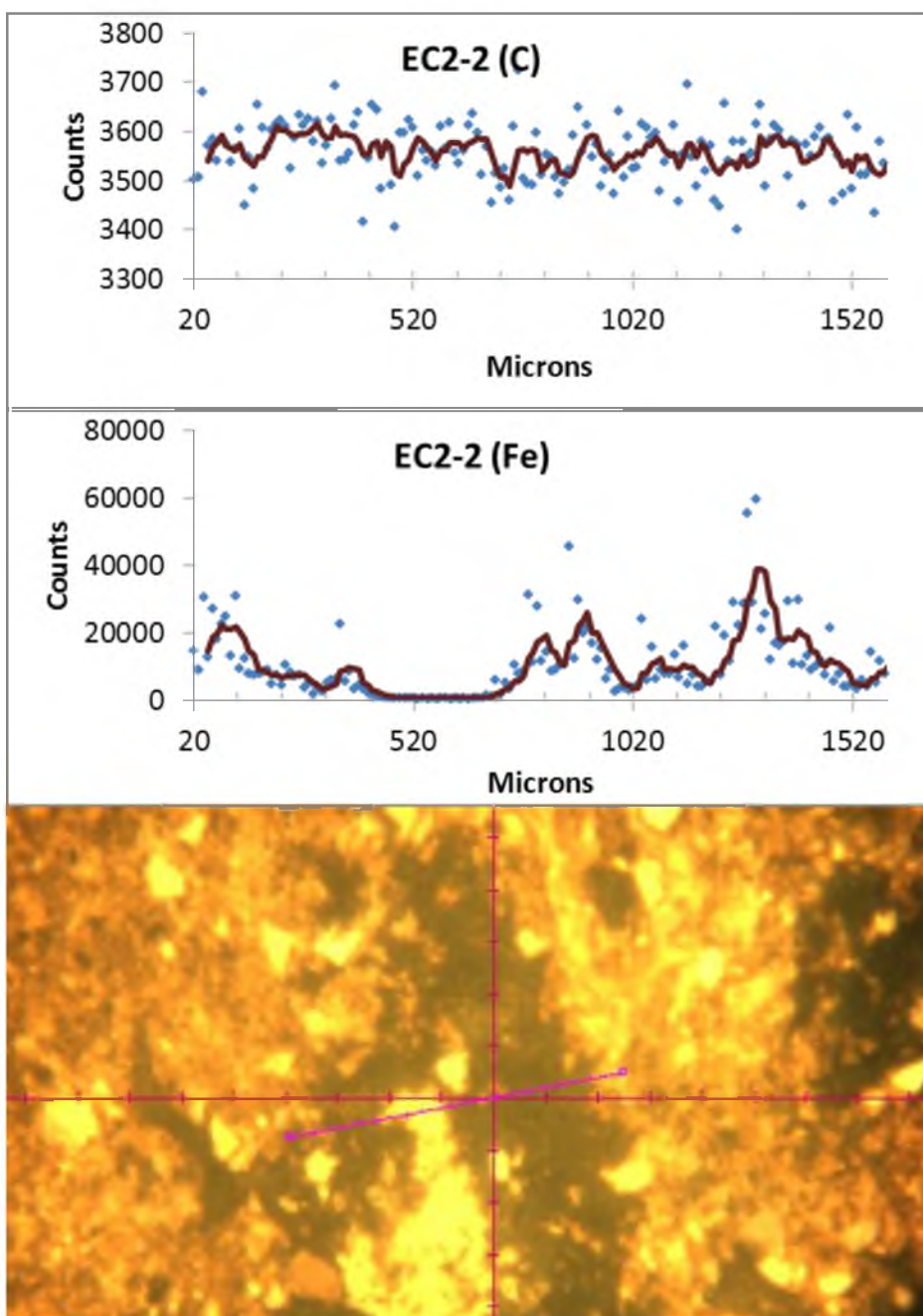


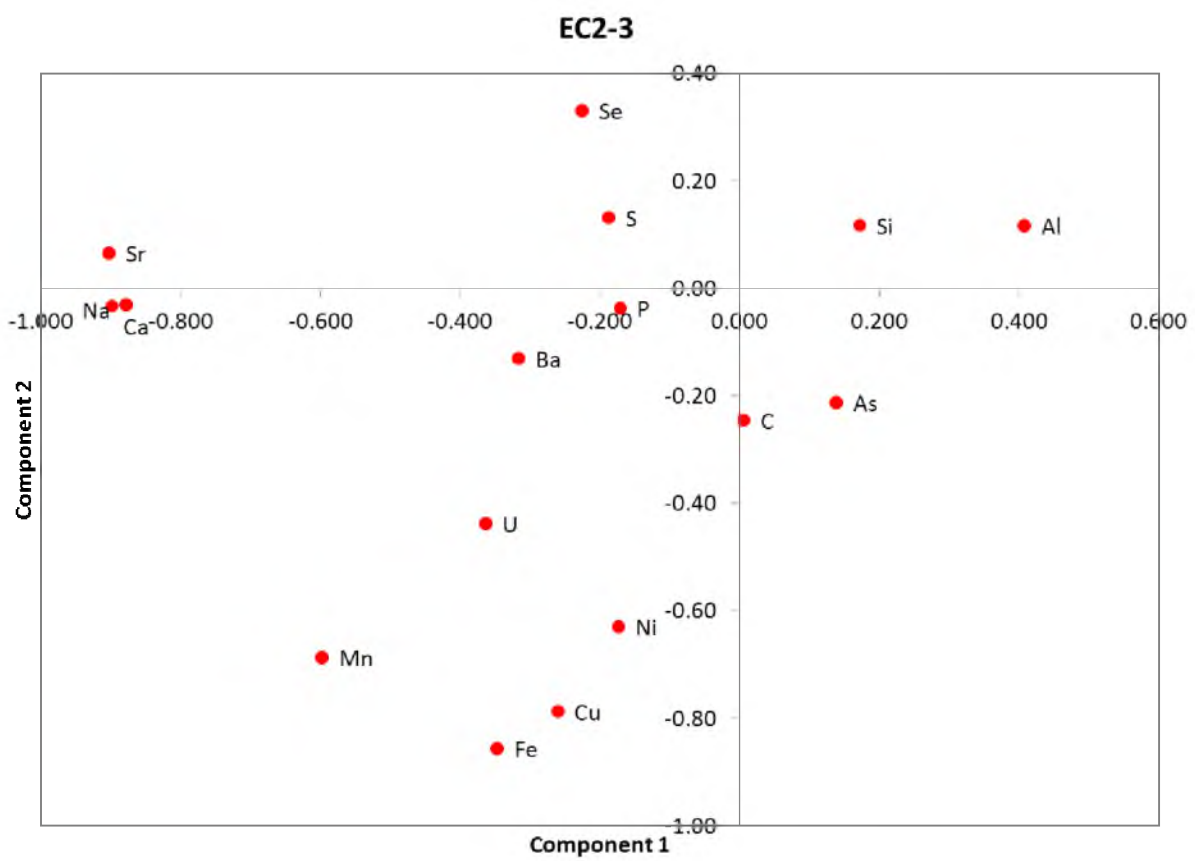


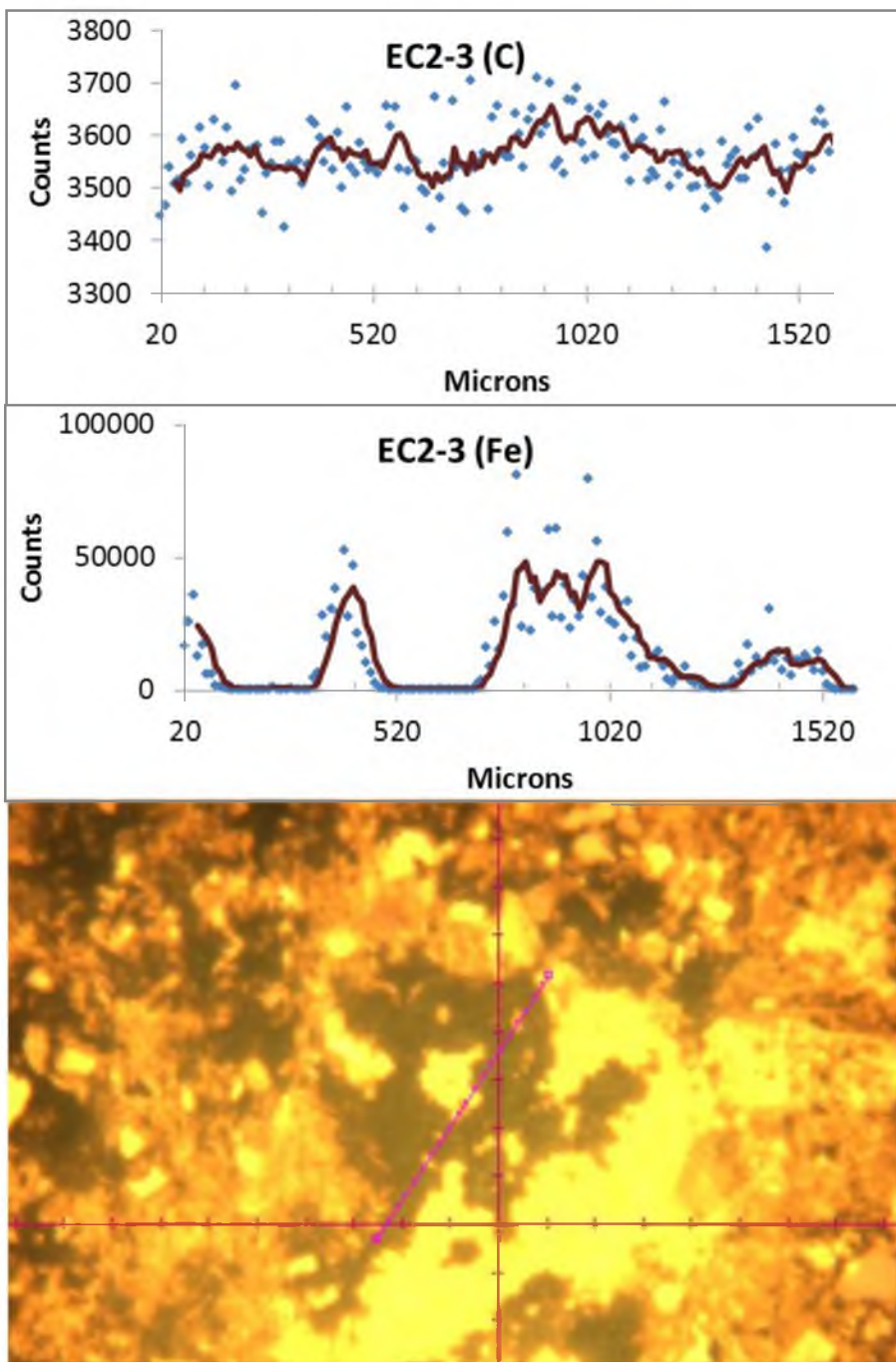


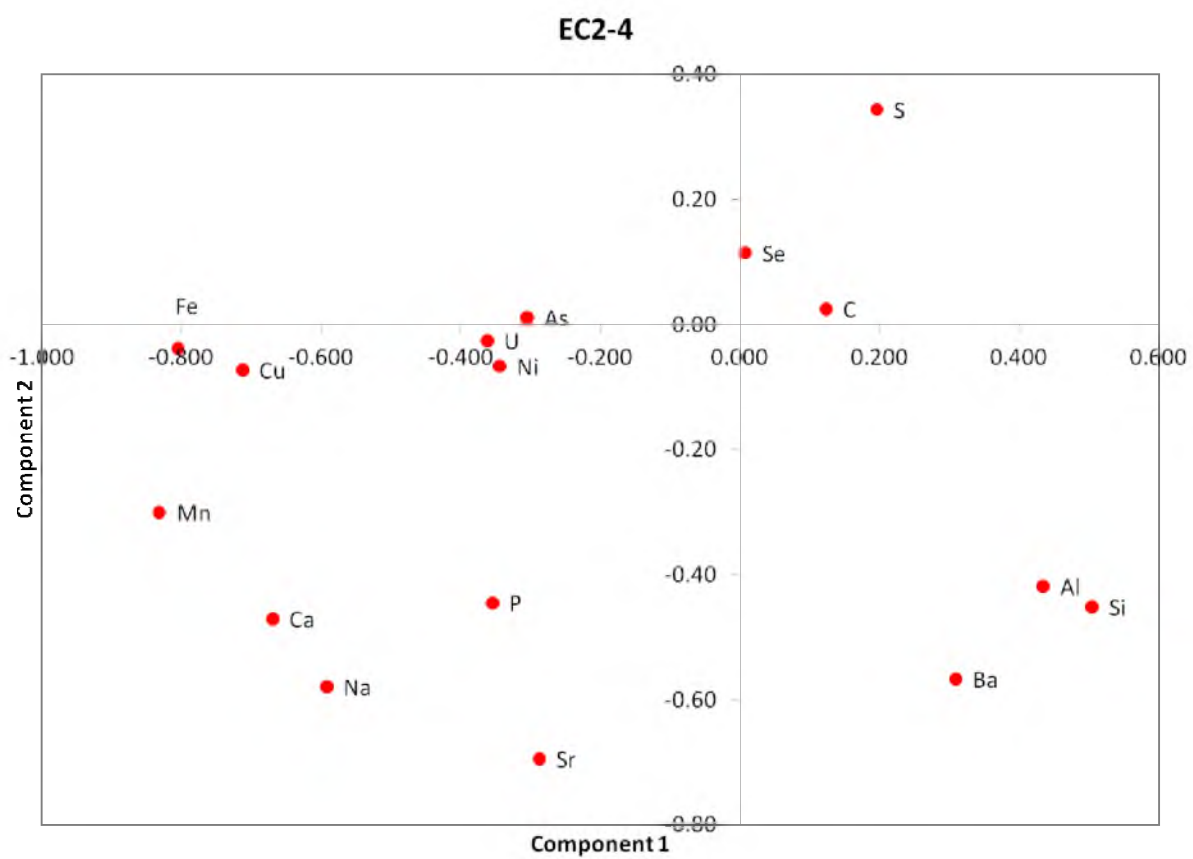


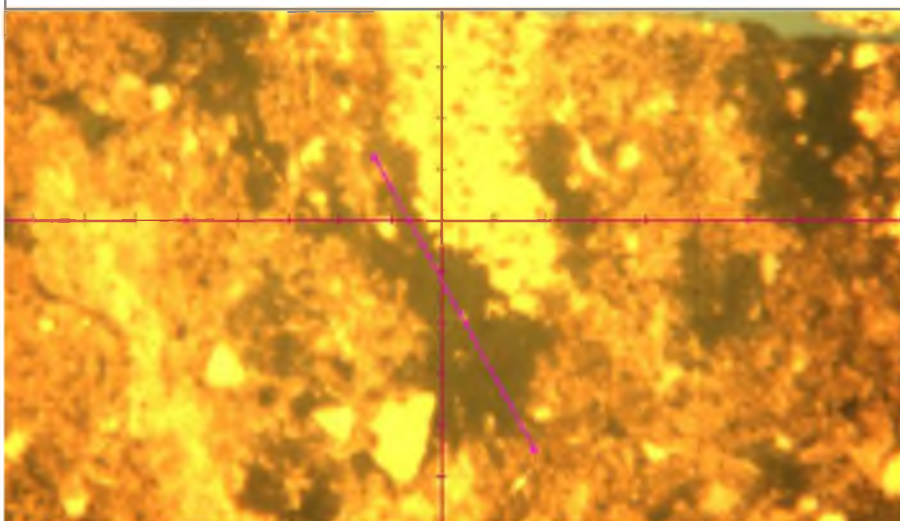
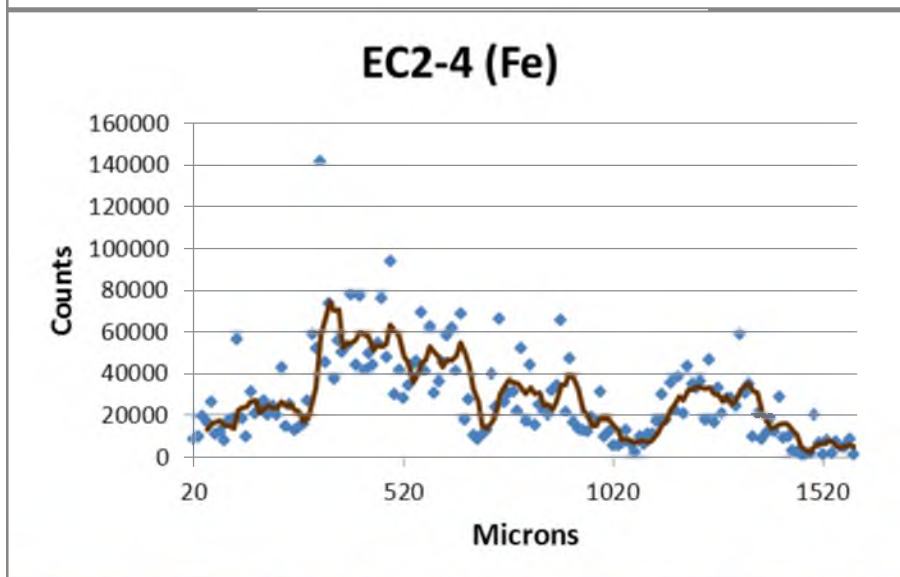
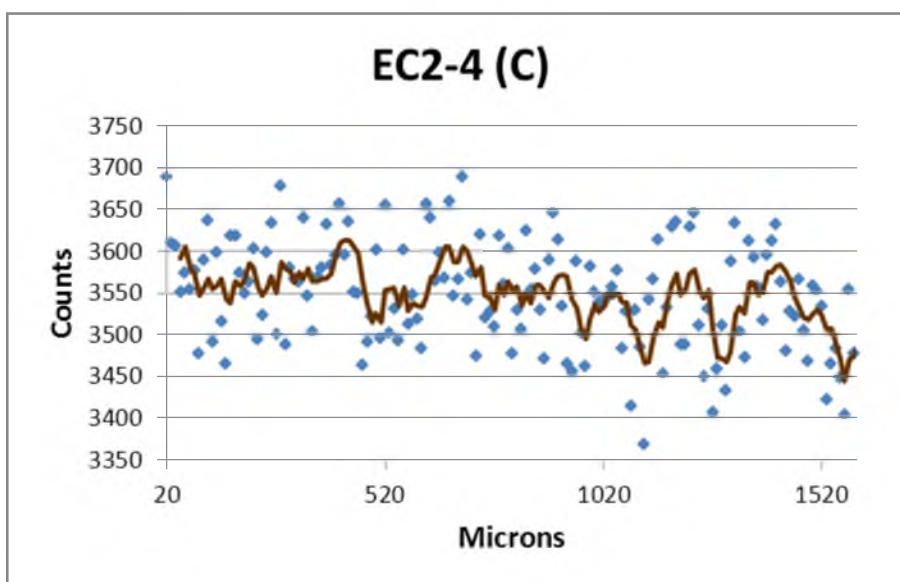


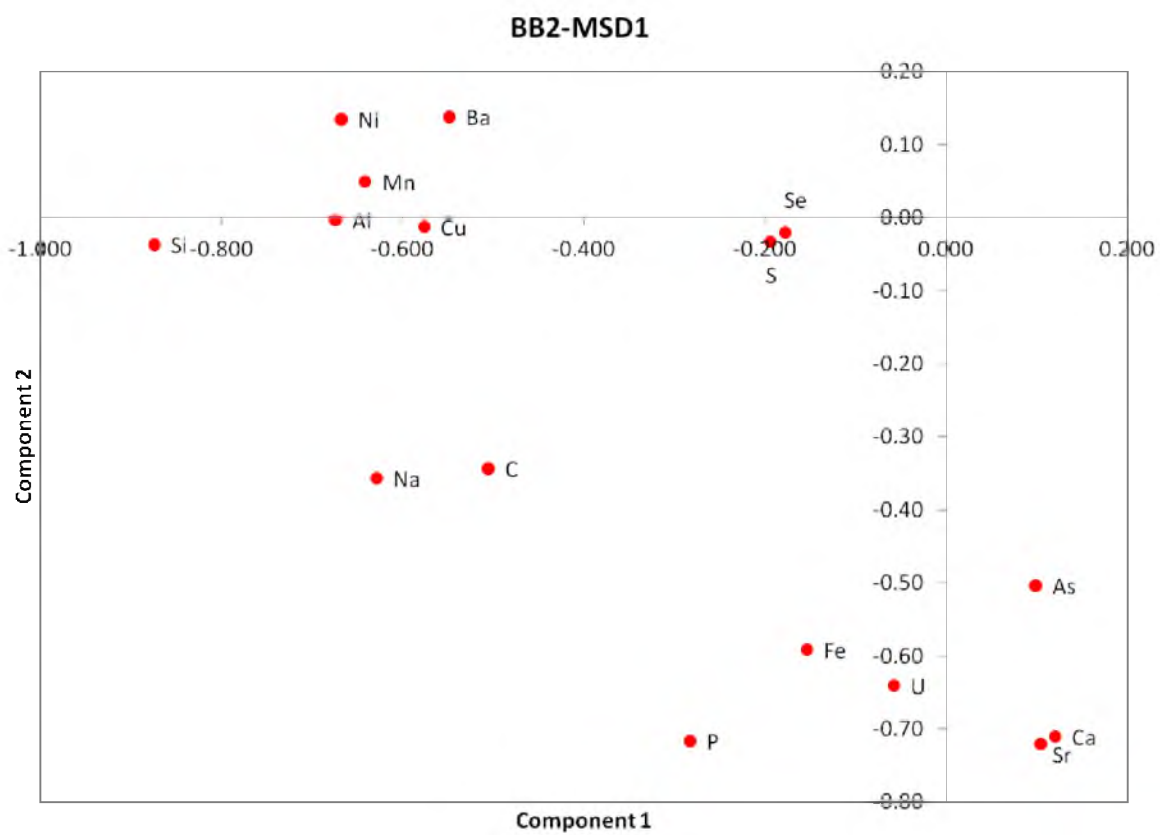


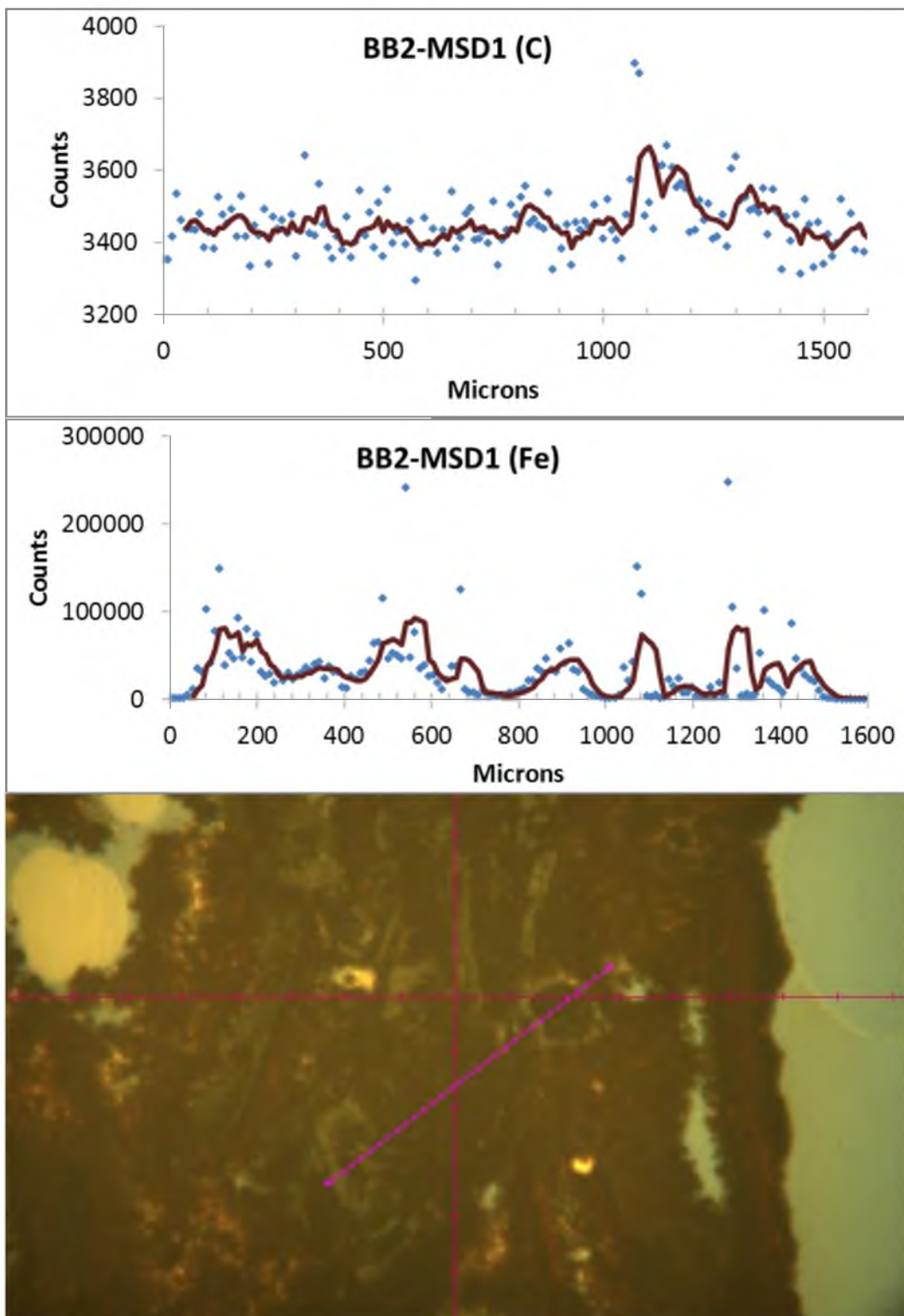


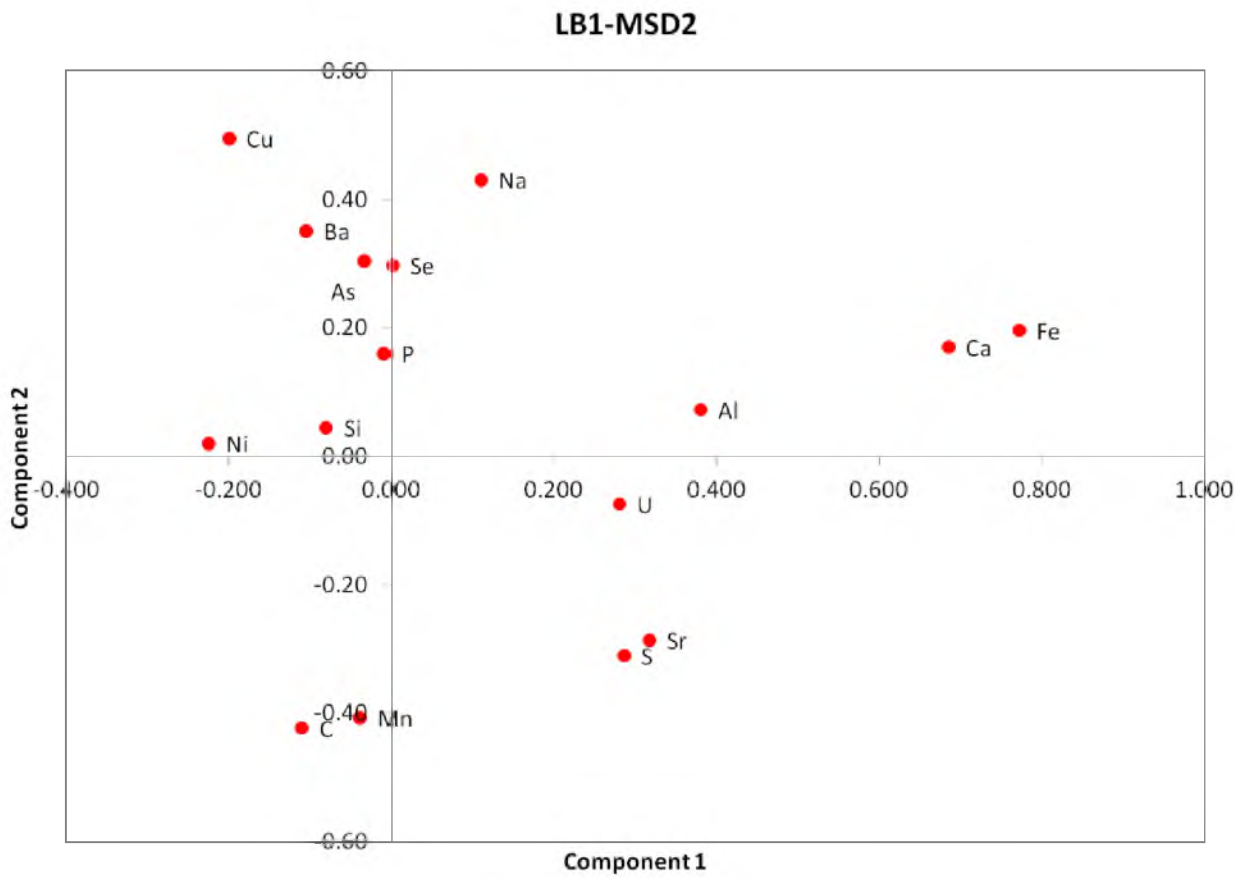


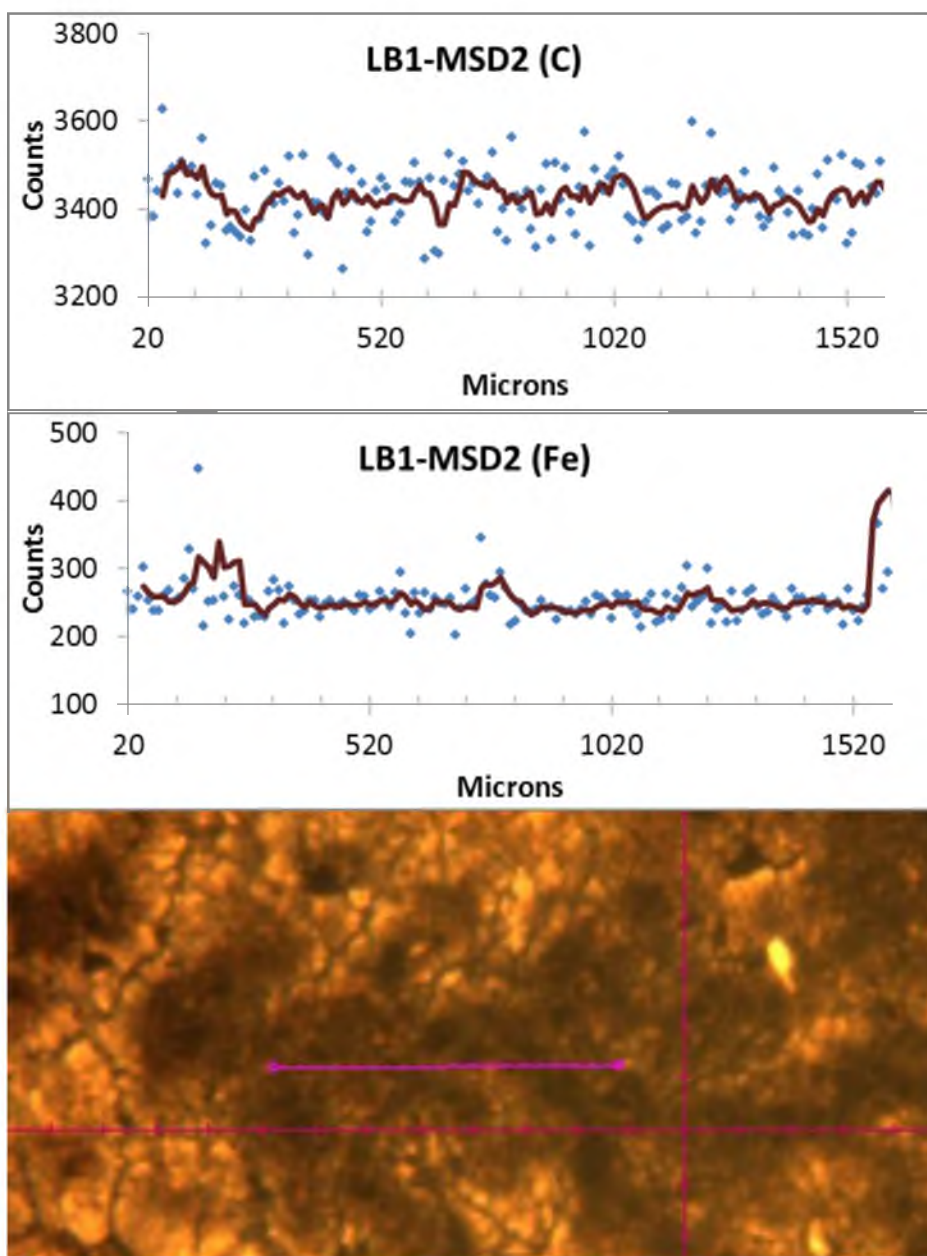


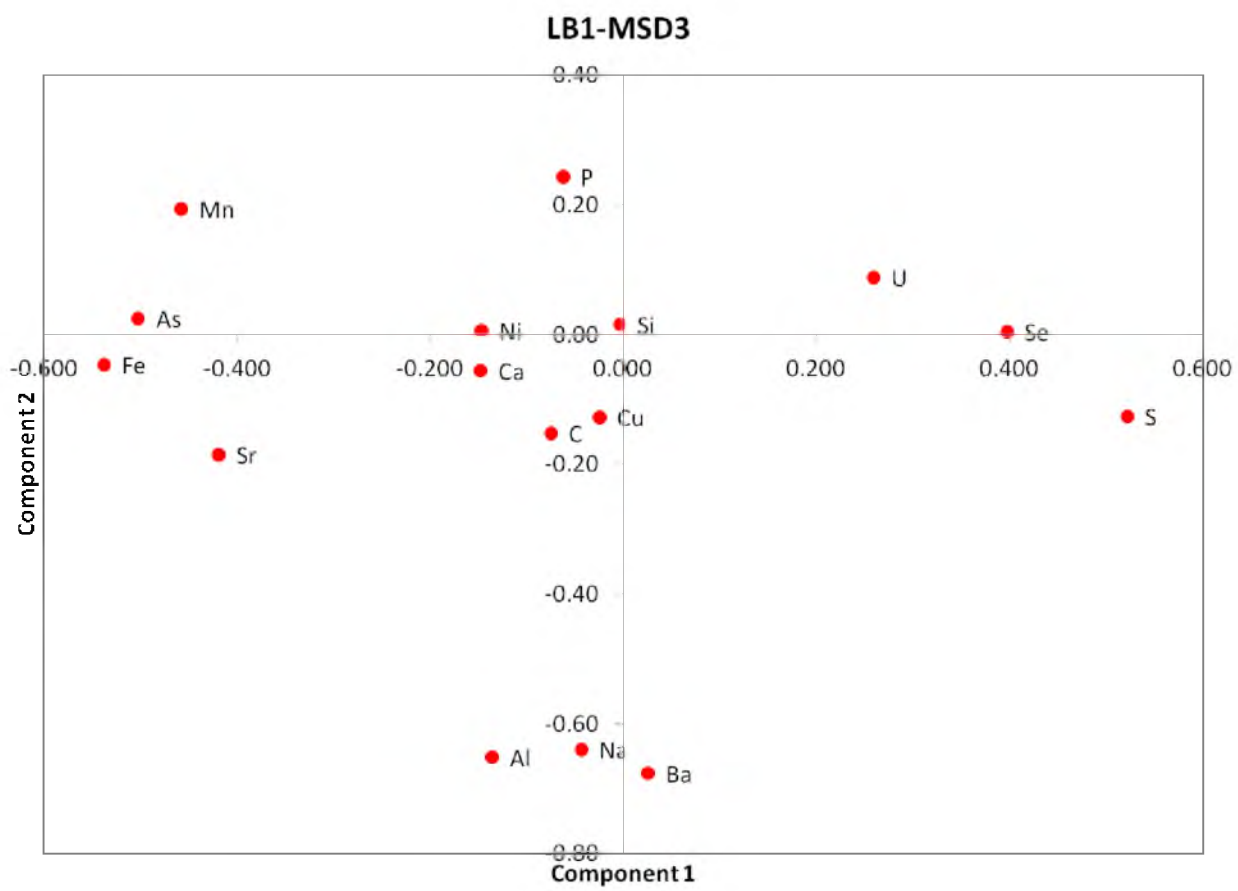


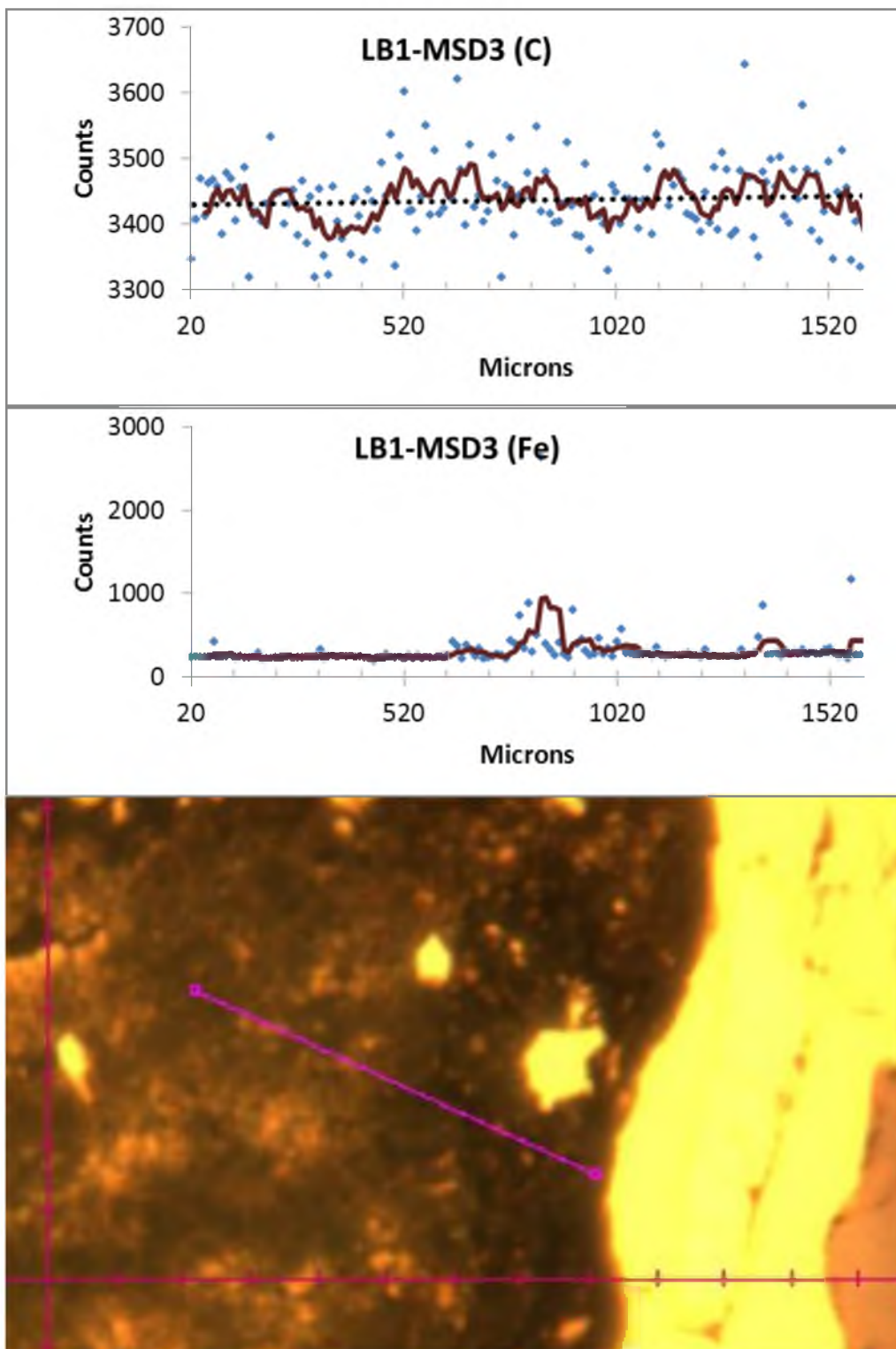
Anomalous Correlations

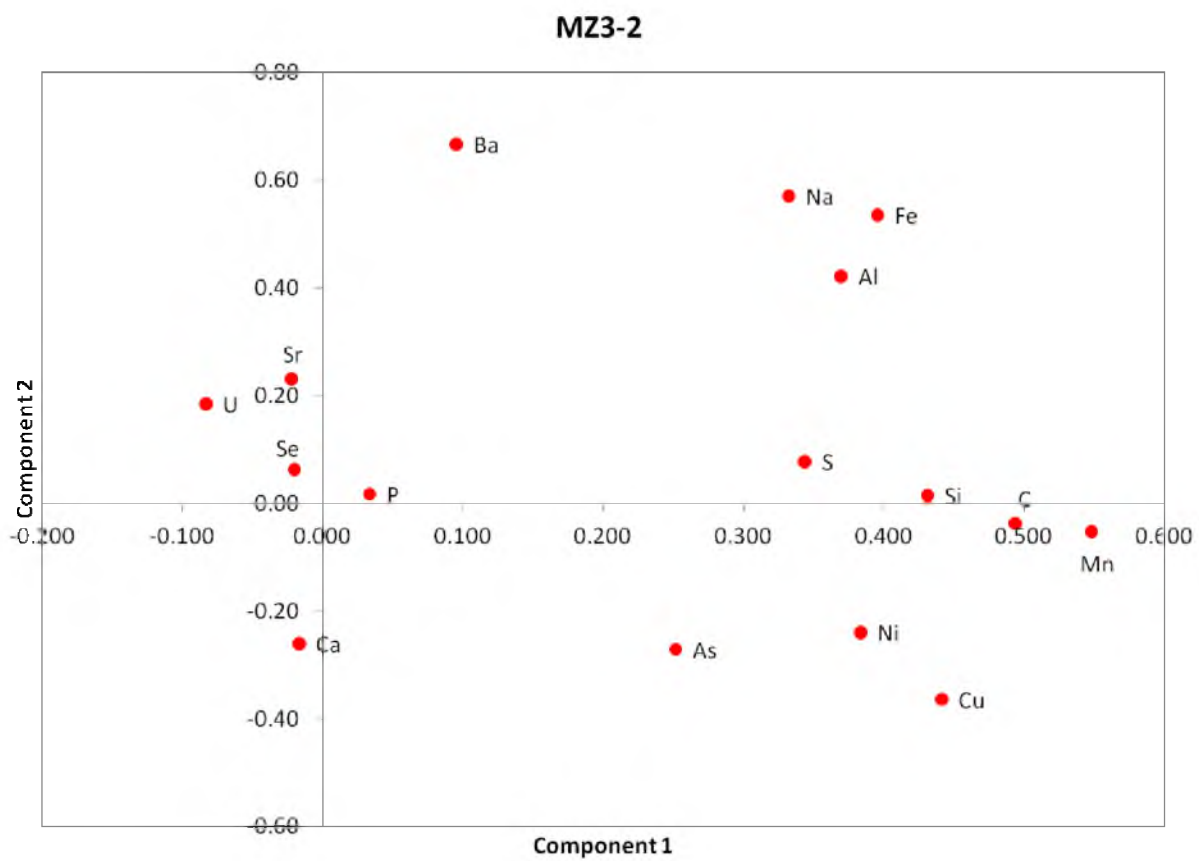


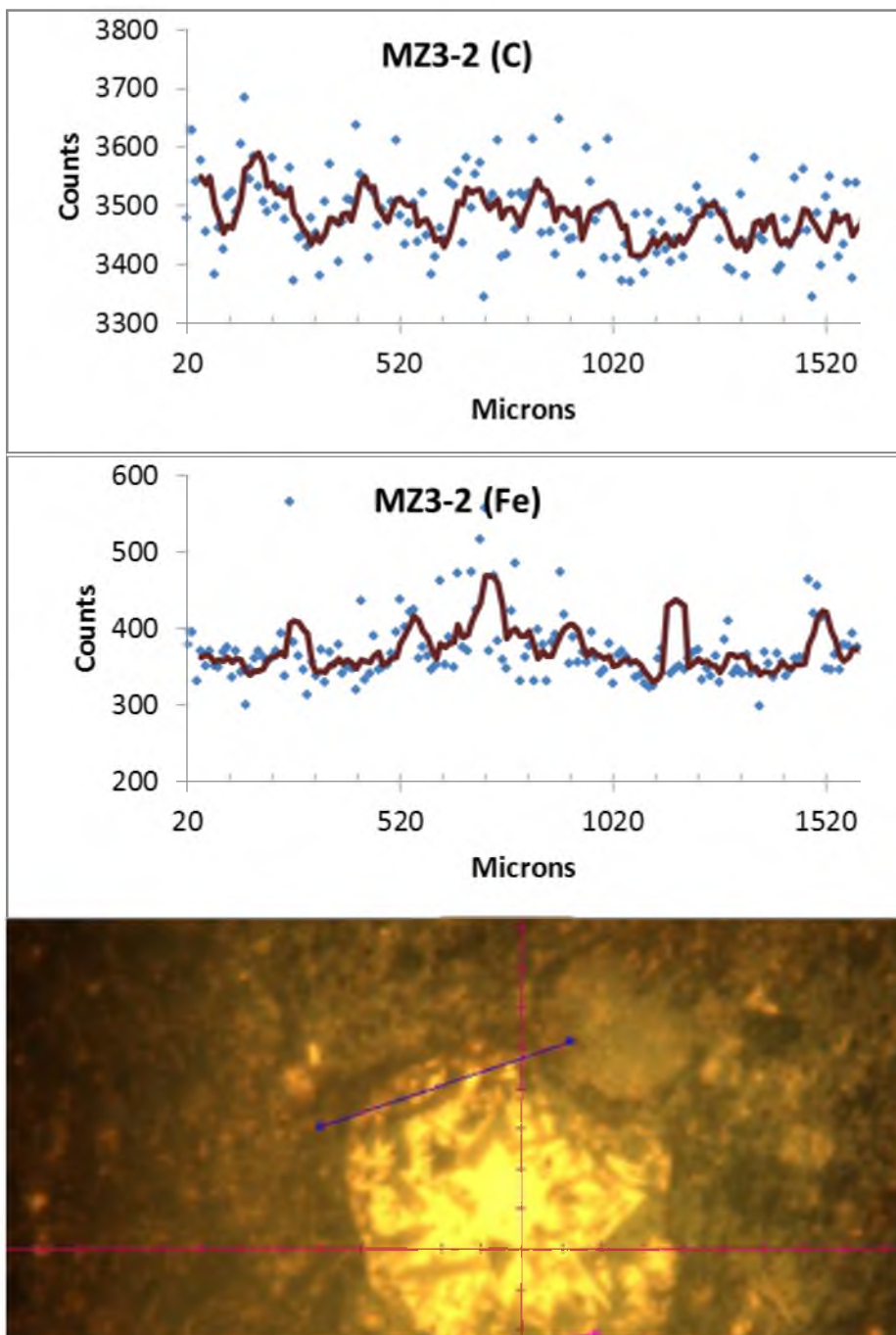


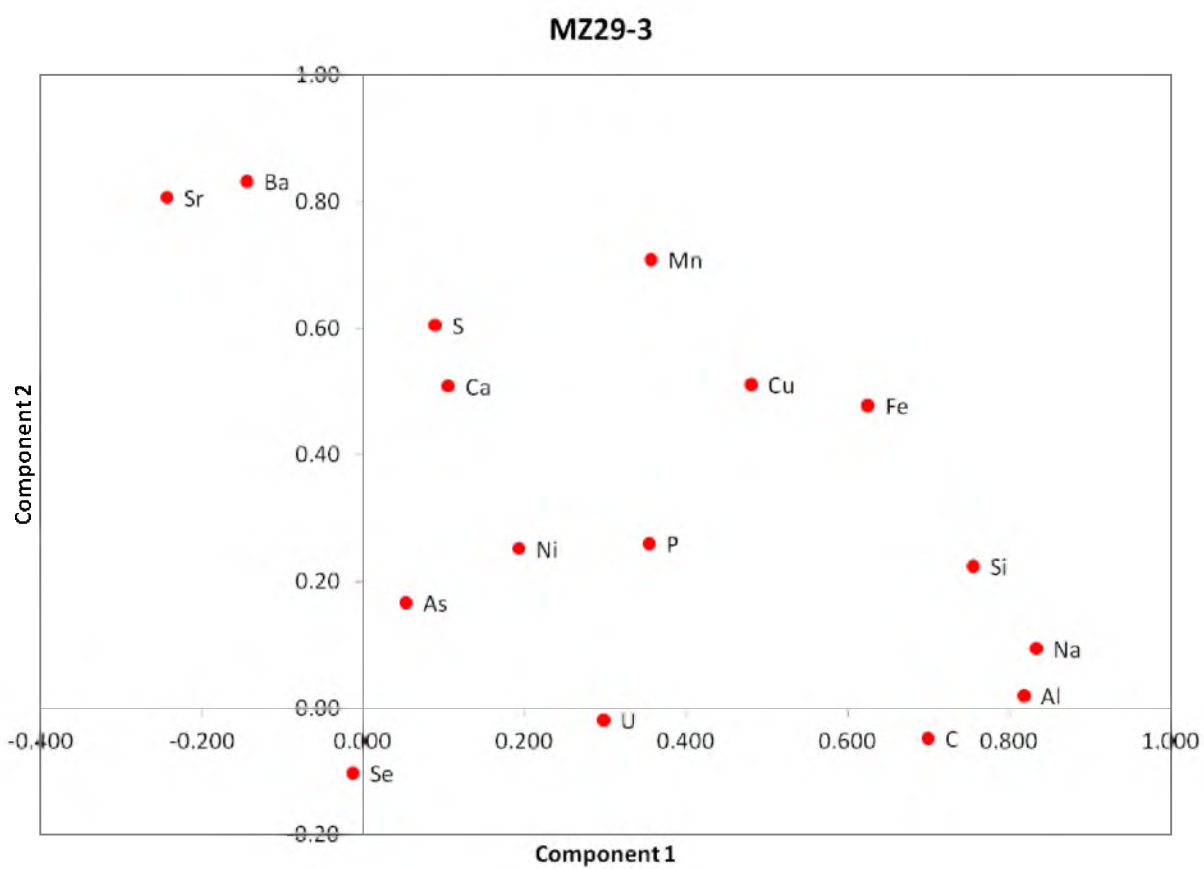


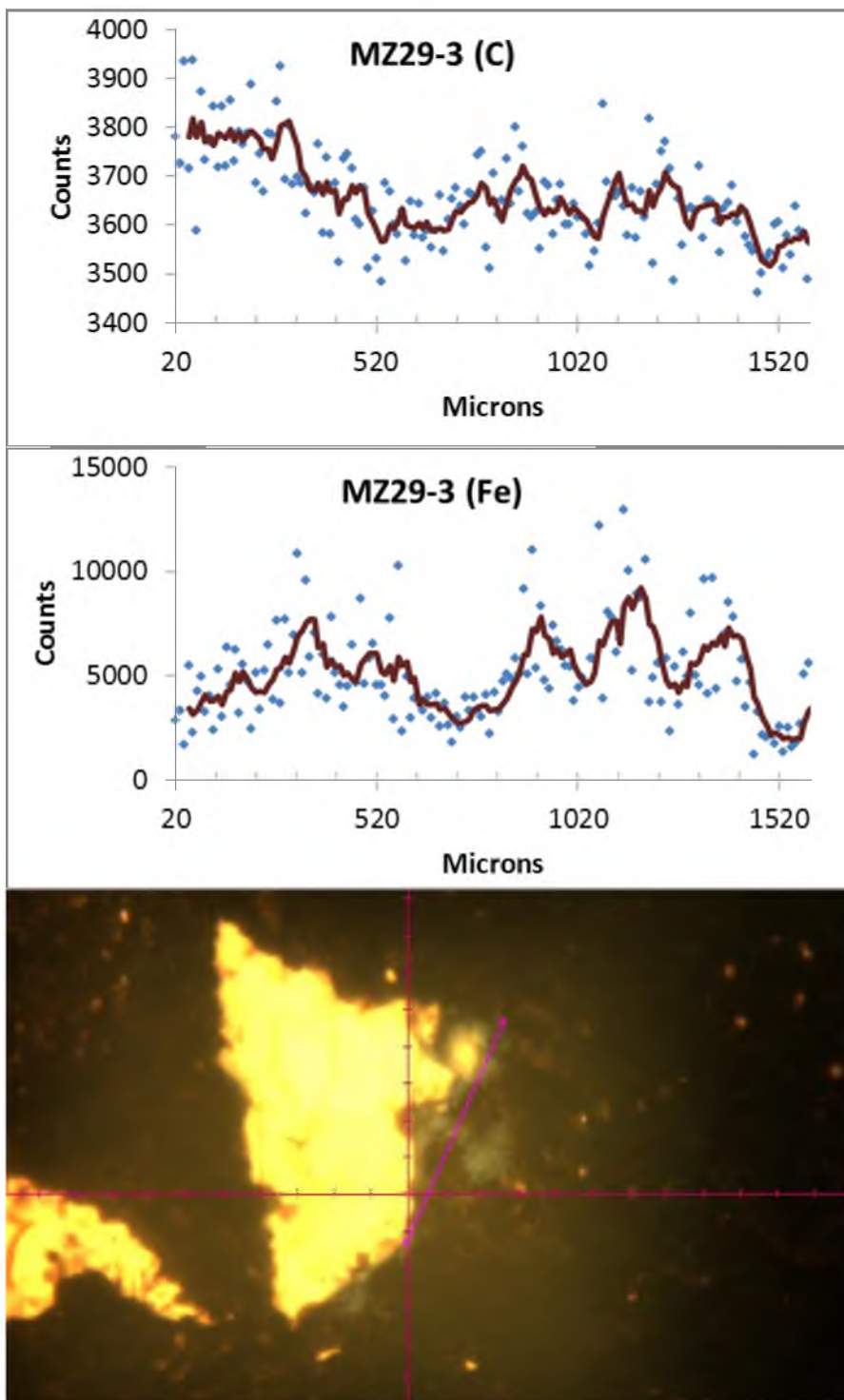












APPENDIX H

RAMAN SPECTROSCOPY

This section presents selected graphs of spectra acquired via confocal Raman spectroscopy using a 633nm wavelength, red laser performed in the Department of Chemistry at the University of Utah. Most graphs do not exhibit the subtle Raman signal because the spectrum is overwhelmed with fluorescence. Mineralogical and chemical features are identified where possible. Features are labeled with the mineral name or mineral group (e.g., iron (oxyhydr)oxide or silicates) or atomic bond (e.g., N=O, C=C) where identified. Identifications such as C=C indicate double bonds. Raman spectroscopy was performed in the Department of Chemistry at the University of Utah (using a 633nm laser), in the Department of Physics at the University of Utah (using a 325nm laser), and at University of Colorado at Boulder (using a 488nm wavelength).

